

Sheffield Hallam University

The structure and control of Ti₂N phases produced by unbalanced magnetron sputtering.

YANG, Shicai.

Available from the Sheffield Hallam University Research Archive (SHURA) at:

<http://shura.shu.ac.uk/20583/>

A Sheffield Hallam University thesis

This thesis is protected by copyright which belongs to the author.

The content must not be changed in any way or sold commercially in any format or medium without the formal permission of the author.

When referring to this work, full bibliographic details including the author, title, awarding institution and date of the thesis must be given.

Please visit <http://shura.shu.ac.uk/20583/> and <http://shura.shu.ac.uk/information.html> for further details about copyright and re-use permissions.

CITY CAMPUS POND STREET
SHEFFIELD S1 1WB

101 546 721 0



374109

Sheffield Hallam University

REFERENCE ONLY

ProQuest Number: 10701230

All rights reserved

INFORMATION TO ALL USERS

The quality of this reproduction is dependent upon the quality of the copy submitted.

In the unlikely event that the author did not send a complete manuscript and there are missing pages, these will be noted. Also, if material had to be removed, a note will indicate the deletion.



ProQuest 10701230

Published by ProQuest LLC (2017). Copyright of the Dissertation is held by the Author.

All rights reserved.

This work is protected against unauthorized copying under Title 17, United States Code
Microform Edition © ProQuest LLC.

ProQuest LLC.
789 East Eisenhower Parkway
P.O. Box 1346
Ann Arbor, MI 48106 – 1346

**The Structure and Control of Ti_2N phases
Produced by Unbalanced Magnetron Sputtering**

Shicai Yang

**A thesis submitted in partial fulfilment of the requirements
of Sheffield Hallam University for the degree of
Doctor of Philosophy**

September 1997

**Collaborating Organisation:
Surface Engineering Laboratory**



Advanced Studies

As part of my research studies I attended a number of both formal and informal research seminars presented at Sheffield Hallam University by discussion with academic staff from the Materials Research Institute and School of Science. I have also attended the following conferences and workshops.

- Hard Coatings by PVD Methods and Evaluation Techniques Work Shop, October 1992, Sheffield Hallam University
- 22nd International Conference on Metallurgical Coatings and Thin Films, April 1994, San Diego, California, United States of America
- The First Sheffield ABS Days, May 1995, Sheffield Hallam University
- 4th international Conference on Advances in Surface Engineering, May 1996, Newcastle upon Tyne, UK
- The Second Sheffield ABS Days, July 1996, Sheffield Hallam University
- The Institute of Physics Annual Congress on Surface Engineering: Fundamentals to Applications, March 1997, University of Leeds
- The Third Sheffield ABS Day Congress, May 1997, Sheffield Hallam University

Acknowledgements

The author is grateful to the following people and collaborating establishments for their helpful discussion and advice, especially to the supervisors for their red pen and utmost solicitude during the period of study.

- Dr. B. D. Lewis, Dr. J. Cawley, Professor J. S. Brooks, Materials Research Institute, Sheffield Hallam University, UK
- Dr. G. William, Electronic Department, University of Sheffield, UK
- Dr. I. Petrov, University of Illinois at Urbana-Champaign, Urbana, USA
- Dr. Ton Hurkmans, Hauzer Techno Coating Europe
- Mr. R. Day, Mr. G. Robinson, Staff of Surface Engineering Laboratory, Materials Research Institute, Sheffield Hallam University, UK
- Mr. R. Wainwright, Machine Tools and Manufacturing, School of Engineering, Sheffield Hallam University, UK
- Dr. L. Donohue, Dr. M. Ives, Dr. I. Wadsworth, and the research students of Materials Research Institute, Sheffield Hallam University, UK
- Research Student Bursary of the Materials Research Institute, Sheffield Hallam University, UK

Finally I would like to thank my wife and my son for making me laughing from hard working, and thank my mother for her constant contribution and selfless devotion throughout my life, education and research.

Contents

1. Abstract	6
2. Introduction	7
2.1 Hard coatings on the surface of materials	7
2.2 Technique to produce hard coatings	7
2.3 Summary of the work	9
References	11
3. Literature review	13
3.1 Glow discharge plasma	13
3.2 Sputtering and related events	16
3.3 Sputtering deposition techniques	19
3.3.1 D.C. diode sputtering	19
3.3.2 DC triode sputtering deposition	22
3.3.3 Magnetron sputtering deposition	23
3.4 Unbalanced magnetron sputtering deposition	25
3.5 Multi-cathode deposition system	27
3.6 Reactive sputtering	29
3.7 The principle of the film deposition	32
3.7.1 Nucleation and growth	32
3.7.2 The microstructures of the sputtering-deposited film	34
3.7.3 Characteristics of films	36
3.8 Hard coating systems	41
3.8.1 Classification of hard coatings	41
3.8.1.1 The first generation of hard coatings	41
3.8.1.2 The second generation of hard coatings	43
3.8.1.3 The third generation of hard coatings	45
3.8.2 Ti ₂ N coatings	47
3.9 Summary of this chapter	51
References	52
4. Experimental Techniques	58
4.1 Coating system	58
4.2 Coating procedure	61
4.2.1 Sample preparation	61
4.2.2 Coating procedure	62
4.3 X-ray Diffraction (XRD)	63
4.4 Scanning Electron Microscope (SEM)	67
4.5 Glow Discharge Optical Emission Spectrometer (GDOES)	69
4.6 Adhesion measurement of hard coatings	71
4.6.1 Scratch adhesion test	72
4.6.2 Rockwell indentation adhesion test	74
4.7 Hardness measurement of hard coatings	75
4.7.1 Hardness test using Vickers indenter	75
4.7.2 Hardness measurement using Knoop indenter	77
4.8 Roughness test of coatings	78
4.9 Thickness measurement of coatings	80
4.10 Preparation of samples for analysis	81
4.10.1 Fracture cross-section for analysis of scanning electron microscope	81
4.10.2 Cross sectional preparation for transmission electron microscope	81
References	83

5. Process study of TiCN hard coatings-----	84
5.1 Experiment arrangements-----	84
5.2 Hysteresis TiN coating process-----	84
5.2.1 N ₂ partial pressure and titanium plasma density dependent on N ₂ flow rate-----	86
5.2.2 Concentration depth profile of the stepwise films-----	88
5.2.3 XRD analysis of the stepwise TiN films-----	89
5.2.4 SEM results-----	91
5.2.5 Discussion hysteresis TiN coating-----	92
5.3 Hysteresis TiC coating process arrangements-----	93
5.3.1 Specimen preparation and experiment parameters-----	93
5.3.2 Methane partial pressure dependent on CH ₄ flow rate-----	93
5.3.3 Concentration depth profile of hysteresis TiC coatings-----	94
5.3.4 XRD results-----	95
5.3.5 SEM results-----	97
5.3.6 Discussion hysteresis TiC coating-----	98
5.4 TiCN Coating-----	99
5.4.1 Experimental parameters and arrangement-----	99
5.4.2 The variation of N ₂ /CH ₄ pressure ratio dependent on N ₂ /CH ₄ flow ratio---	100
5.4.3 Composition dependent on the reactive gas pressure ratio-----	101
5.4.4 Hardness results-----	102
5.4.5 XRD results-----	104
5.4.5.1 TiCN coatings deposited at 240°C-----	104
5.4.5.2 TiCN coatings deposited at 340°C-----	109
5.5 Triple layer TiCN coating-----	114
5.5.1 Experiment-----	114
5.5.2 GDOES result-----	115
5.5.3 XRD result-----	116
5.5.4 SEM and hardness result-----	117
5.6 Discussion of chapter 5-----	117
5.7 Conclusion of chapter 5-----	119
References-----	119
6. Uniform Ti-N coatings deposited at 350°C-----	130
6.1 Experimental parameters and arrangement-----	130
6.2 Results of composition dependent on nitrogen partial pressure-----	131
6.2.1 Stepwise coating-----	131
6.2.2 Uniform Ti-N coatings-----	132
6.3 XRD analysis of the coating-----	133
6.3.1 Compositional Stepped Coating-----	133
6.3.2 Coatings of Uniform Composition-----	135
6.4 Thickness and hardness results of uniform Ti-N coatings-----	141
6.5 Scanning Electron Microscopy-----	141
6.6 Investigation of cutting test of the coated high speed steel drills-----	142
6.6.1 Composition and phase analysis of the coatings using GDOES and XRD---	142
6.6.2 Physical properties of sub-stoichiometric Ti-N films and drilling test-----	143
6.7 Discussion of chapter 6-----	144
6.8 Conclusion of chapter 6-----	147
References-----	148
7. Process study of static Ti-N coatings deposited at 480°C-----	156
7.1 Experimental arrangement of the static deposition process-----	156
7.2 Experimental results-----	157
7.2.1 Composition dependence on the nitrogen partial pressure-----	157

7.2.2 Crystal phases dependent on composition of the coatings-----	158
7.2.3 Thickness, micro hardness, and adhesion measurement-----	166
7.2.4 Surface roughness dependence on composition of the films-----	169
7.3 Discussion of chapte 7-----	170
7.4 Conclusion of chapter 7-----	172
References-----	173
8. Investigation of $\epsilon\text{Ti}_2\text{N}$ films using substrate table rotation-----	181
8.1 Experimental arrangement-----	181
8.2 Composition and hardness as a function of substrate rotation-----	182
8.3 Crystal phase dependent on nitrogen gas flow and substrate rotation-----	184
8.3.1 X-ray diffraction pattern from coatings using 70 sccm nitrogen gas flow rate--	184
8.3.2 X-ray diffraction pattern from coatings using 75 sccm nitrogen gas flow rate--	188
8.3.3 X-ray diffraction pattern from coatings using 80 sccm nitrogen gas flow rate--	192
8.4 Cross sectional structure of the $\epsilon\text{Ti}_2\text{N}$ films-----	198
8.4.1 Cross sectional analysis using SEM-----	198
8.4.2 Cross sectional investigation using TEM-----	198
8.4.2.1 Results from sample deposited using three fold rotation-----	198
8.4.2.2 Result from sample deposited using one fold rotation-----	203
8.5 Discussion of chapter 8-----	206
8.6 Conclusion of chapter 8-----	210
References-----	211
9. Investigation of practical applications of $\epsilon\text{Ti}_2\text{N}$ films-----	223
9.1 Result of using pin-on-disc sliding wear test-----	223
9.1.1 Experimental program-----	223
9.1.2 Result of pin-on-disc sliding wear test-----	224
9.2 Result of thermal stability of $\epsilon\text{Ti}_2\text{N}$ film-----	226
9.3 Electrochemical corrosion test of the $\epsilon\text{Ti}_2\text{N}$ film-----	229
9.3.1 Experimental-----	229
9.3.2 Result of electrochemical corrosion test-----	230
9.4 Investigation of the practical performance of the $\epsilon\text{Ti}_2\text{N}$ coated drills-----	233
9.4.1 Result of drilling test using simple cooling-----	234
9.4.2 Result of drilling test using enhanced cooling-----	237
9.5 Discussion of chapter 9-----	240
9.6 Conclusion of Chapter 9-----	241
References-----	242
10. Discussion and conclusion of the deposition of pure $\epsilon\text{Ti}_2\text{N}$ films-----	243
10.1 Discussion-----	243
10.1.1 TiCN coatings-----	243
10.1.2 Ti_2N coatings-----	243
10.2 Conclusion-----	246
10.3 Future work-----	246
References-----	247
Appendix 1-----	248

1. Abstract

Physical vapour deposition (PVD) techniques used for the application of advanced surface engineering materials have been developed over many years, but only in about the last 10 years has the unbalanced magnetron sputtering (UBMS) PVD technique been developed and emerged as one of the most promising techniques for depositing reliable and high quality films used in industrial production.

Hard coatings have been studied for many years for the purpose of improving the performance of various tools, mechanical parts, and engineering components. The most studied binary hard coatings (such as stoichiometric titanium nitrides and titanium carbides) and the ternary hard coating (such as titanium carbonitride) have been developed for wear resistance for many years. Although many investigations have been made into the production of coatings with stoichiometric phases, it is both scientifically and commercially interesting to investigate the production and reproducibility of the pure titanium sub-nitride Ti_2N films.

The first results in chapter 5 describe work carried out to investigate the effect of nitrogen and carbon concentration within the films and was a prelude to the main activity of the development of Ti_2N films using commercial conditions.

The work for Ti_2N was carried out without substrate rotation in the UBMS coating process. The static deposition processes were studied to give a better understanding of the effect of partial pressures on the compositions of the Ti-N films. The phase development as a function of the composition of the films was investigated. The main contribution during this procedure was to achieve a suitable range of nitrogen partial pressure by which the films containing pure Ti_2N phase were produced using a UBMS deposition technique. The nitrogen content of the film was very sensitive to variation in nitrogen partial pressure and the nitrogen concentration influenced the phases developed in the films. The reproducibility of the pure Ti_2N phase was also discussed in this initial work.

A series of extensive experiments were conducted to investigate the formation of Ti_2N phase in the UBMS deposition processes using one to three fold rotations. The nitrogen partial pressure of the deposition process was basically determined from the results of the initial work. The effect of substrate rotation on the film composition during processing was studied. In general the film deposited using substrate rotation consisted of different composition using the same chamber condition in one process in which the nitrogen content of the coating increased from one fold rotation to three fold rotation. The film containing dominant ϵTi_2N phase could be produced on a sample using three fold rotation in a process whilst the multiphase compositions ($\alpha TiN_{0.3} + \epsilon Ti_2N$) were developed on the sample using the one and two fold rotations in the same process.

Characteristics of the ϵTi_2N films and the films containing multiphase compositions were investigated using transmission electron microscopy (TEM), scanning electron microscopy (SEM), glow discharge optical emission spectrometer (GDOES), X-ray diffraction (XRD), and a variety of mechanical testing instruments. The ϵTi_2N films have very smooth surface, very dense and fine columnar structure, relatively high hardness, and excellent adhesion with the substrate. The drilling tests using coated high speed steel drills compared the coatings containing ϵTi_2N phase with those containing a single TiN phase and showed excellent wear resistant results.

2. Introduction

2.1 Hard coatings on the surface of materials

For many years, people have been looking for materials which have low wear rate, corrosion resistance, and attractive appearance. It was made clear by some researchers^(1,2,3,4,5,6) that the protection of materials by hard coatings is one of the most important and versatile means of improving component performance.

Hard bulk materials, such as ceramics, are relatively brittle, as indicated by their low transverse rupture strength; therefore their use for abrasive wear application is limited because of the necessity for both hardness and toughness. This problem can be addressed by depositing hard coatings on ductile bulk materials⁽⁷⁾. The coated high-speed steel drills⁽⁸⁾, for example, have both increased tool life and achieved higher cutting speed than the un-coated drills. In fact, hard coating and substrate can be designed as a composite producing excellent performance which can not be obtained by either coating or substrate alone⁽⁹⁾.

2.2 Technique to produce hard coatings

Hard coatings can be produced by a number of techniques; vapour deposition, for example, is one of the most developed techniques. Many advanced techniques are combined in the vapour deposition process. In general, the coatings are produced in a vacuum chamber and glow discharge plasma is used in order to improve the coating properties.

The vapour deposition process can be divided into chemical vapour deposition (CVD) and physical vapour deposition (PVD). In the CVD process^(10,11,12), the coating materials are thermally decomposed and chemically reacted with other gases or vapours to form a film on the hot substrate surface. The CVD process can produce a wide range of coatings with excellent adhesion at moderate deposition rates. However the process must be performed at a relatively high temperature, which limits the

application to certain substrate materials, such as high speed steel, because of its high deposition temperature of 1000 °C.

In the PVD process^(13,14,15), the chamber is under vacuum conditions and the glow discharge plasma is one of the techniques used in the process. The basic PVD process techniques include evaporating and the sputtering process. Each technique can be used in some specific condition and has its own special process parameters. The PVD family tree is given in Fig 2.2.1 to facilitate evaluation of the PVD techniques.

Many natural materials can be deposited on the surface of various solid substrates by a PVD process in which the coating is produced by condensation of atomic vapours in a high vacuum on to the substrate surface. In the glow discharge process, ion beam techniques can be used to increase the kinetic energy of the coating particles, which produces excellent adhesion and improves chemical reaction without a high substrate temperature (less than 500°C). Magnetron technology is also widely used where enhanced ionisation is produced⁽¹⁶⁾. Therefore PVD process, TiN phase formed by reactive ion plating for example, with application of glow discharge and ion beam techniques is extremely versatile in the composition of coatings and substrate materials⁽¹⁷⁾.

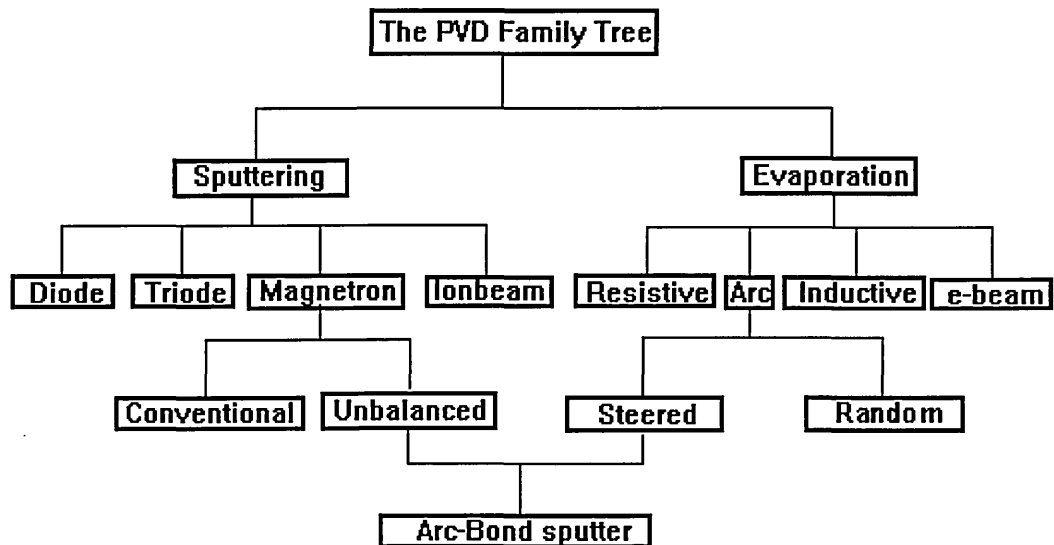


Fig 2.2.1 The PVD family tree

Deposition by evaporation is a process in which the vapour of coating atoms is produced from the surface of liquid or solid materials by means of joule heating which can be conducted by resistive, arc, inductive, and electron beam heating. The vapour can be deposited onto the substrate to form a film.

Sputtering deposition is one of the most studied PVD processes^(18,19) and is widely used for industrial application. In the sputtering deposition procedure the target surface is under bombardment of energetic particles such as ions and neutrals, then target materials, mainly atoms, are ejected in the process of momentum transfer. Therefore films can then be formed by the ejected atoms on the substrate surface which is placed facing the target. One of the most optimised sputtering deposition process involves use of unbalanced magnetron sputtering techniques^(20,21,22,23,24), and recently the combination of unbalanced magnetron sputtering and steered arc evaporation techniques has made a good contribution to industrial coating techniques⁽²⁵⁾.

2.3 Summary of the work

The work reported here, some TiCN, but primarily the Ti-N coatings (especially Ti₂N films deposited using an UBMS deposition technique) were considered for the study of the fundamental coating process. The aim is to investigate the effect of process parameters such as reactive gas partial pressure, temperature, and substrate table rotations, on the composition and properties of the coatings.

It is known that binary TiN and TiC coatings^(26,27,28,29,30,31,32) can be deposited on various substrates to improve wear and corrosion resistance. But the use of binary TiN and TiC was limited in some extremely high load and high temperature applications due to problems of brittleness, hot hardness, and thermal stability. In some recent reports^(33,34,35,36), ternary TiCN was considered to improve the performance of coatings which can not be achieved by either the binary TiN or the binary TiC alone.

Therefore, the work was started to investigate the process parameters by which TiCN hard coating can be produced.

As the interesting Ti_2N phase was found in the initial TiCN work, the research direction of this project was changed to study Ti-N films instead of TiCN coatings. The major work is focused on studying the effects of nitrogen partial pressure and substrate rotation on the phase compositions of Ti-N films in order to find process parameters to produce pure Ti_2N phase with sufficient reproducibility. It is very useful to obtain the process parameters by which the pure Ti_2N coating can be produced with sufficient reproducibility in order to make commercial application possible.

Analysis and characterisation have been carried out throughout the whole work. Scanning electron microscopy (SEM), transmission electron microscopy (TEM), X-Ray diffraction (XRD), glow discharge optical energy spectrometry (GDOES), Scratch, Rockwell, Vickers hardness, Roughness, calotest for thickness, wear resistant test, thermal stability and corrosion-erosion resistant test etc. have been used to establish the coatings produced and the properties of the coatings. The practical industrial application of the Ti_2N films has been carried out using a milling machine to test the coated high speed steel twist drills on the cast iron by dry cutting and on the austenitic stainless steel by wet cutting. The optimised process parameters were discussed in terms of the quality of Ti_2N films produced.

References

- (1) S. Bair, S. Ramalingam, and W.D. Winer, *Wear*, V.60 (1980)413-419
- (2) H.E. Hintermann, H. Boving, and W. Hanni, *Wear*, V.48(1978)225-236
- (3) T.P. Chang, H.S. Cheng, W.A. Chiou and W.D. Sproul, " A Comparison of Fatigue Failure Morphology Between TiN Coated and Uncoated Lubricated Rollers," Northwestern University, Evanston, Illinois, USA
- (4) B. Matthes, W. Herr, E. Broszeit and K.H. Kloos, etc, *Materials Science and Engineering*, A140(1991)593
- (5) H.Randhawa, *Thin Solid Films*, V153 (1987) 209
- (6) W.D. Sproul, *J. Vac. Sci. Technol.* A4 (1986) 2874
- (7) B. Bhushan and B.K. Gupta, *Handbook of Tribology (Materials, Coating, and Surface Treatments)*,McGRAW-HILL, INC.(1991)2.28
- (8) R. L. Hatschek, *American Machinist*, V 127, N 3, (1983) 129
- (9) D. S. Rickerby and A. Matthews, "Advanced Surface Coatings", 1991, Blackie & Son Limited
- (10) W.A. Bryant, *Journal of Materials Science*, V.12, (1977)1285-1306
- (11) B.N. Chapman, and J.C. Anderson, *Science and Technology of Surface Coatings*, Academic, New York (1974)169
- (12) H.E. Hintermann,*Thin Solid Films*, V.84 (1981)215-243
- (13) L.I. Maissel, and R. Glang, *Handbook of Thin Film Technology*, McGraw-Hill, New York (1970)
- (14) C.F. Powell, J.H. Oxley, and J.M. Blocher, *Vapor Deposition*, Wiley, New york (1966)
- (15) J.L. Vossen, and W. Kern, *Thin Film Process*, Academic Press, New York (1978)
- (16) J. Musil, S. Kadlec, J. vysokocil and V. Poulek, *Surf. Coat. Technol.*, V39/40 (1989)301
- (17) J.M. Molarius, A.S. Korhonen, and E.O. Ristolainen, *J. Vac. Sci. Technol.* A3(6) (1985)2419
- (18) J. Almeida, *Vacuum*, V39 (1989)717
- (19) M. Ahern, *Surf. Coat. Technol.*, V43/44 (1990)279
- (20) B. Window and N.Savvides, *J. Vac. Sci. Technol.*, A4 (1986)196
- (21) B. Window and N.Savvides, *J. Vac. Sci. Technol.*, A4 (1986)453
- (22) N.Savvides and B. Window , *J. Vac. Sci. Technol.*, A4 (1986)504
- (23) W.D. Sproul, P.J. Rudnik, K.O. Legg, W.-D. Münz, I. Petrov and J.E. Greene, *Surface and Coating Technology*, V56(1993)179
- (24) S.L. Rohde, L. Hultman, M.S. Wong and W.D. Sproul, *Surface and Coating Technology*, V50(1992)255
- (25) W.-D. Münz, D. Schulze and F.J.M. Hauzer, *Surface and Coating Technology*, V50(1992)169
- (26) R. Milovic, E.F. Smart, M.L.H. Wise, *Mater. Sci. Techgnol.* V2 (1986) 59
- (27) M. Tavi, K. Knuutila, O. Forsen, S. Ylasaari, *Key Eng. Mater.* V20 (1988) 1429
- (28) J.C. Knight, *Wear* V138 (1990) 239
- (29) J.S. Bull, P.R. Chalker, C.F. Ayres, D.S. Rickerby, *Mter. Sci. Eng. A* V139(1991) 71
- (30) T. Cho, D.G. Bhate, P.F. Woerner, *Surf. Coat. Technol.* V29 (1986) 239

- (31) D.L. Jiang, J.H. Wang, Y.L. Li, L.T. Ma, Mater. Sci. Eng. A V109 (1989) 401
- (32) J.C. Knight, T.F. Page, Thin Solid Films V193 (1990) 431
- (33) E. Bergmann, H. Kaufmann, R. Schmid, and J. Vogel, Surf. Coat. Technol. V42,(1990) 237
- (34) R. Bertocello, A. Casagrande, M. Casarin, A. Glisenti, E. Lonzone, L. Mirengi, and E. Tondello, Surface and Interface Analysis V18 (1992) 525
- (35) O. Knotek, F. Loeffler, G. Kraemer, Vacuum V43 (1992) 645
- (36) V. Hoffmann, Fresenius J. Anal Chem., 346 (1993) 165

3. Literature review

3.1 Glow discharge plasma

A plasma is a medium containing ions and electrons characterised by charge neutrality. It is increasingly employed in industry process, in particular in sputtering. One of the techniques for producing plasmas is to apply a high voltage to electrodes within a vacuum discharge chamber⁽¹⁾. The simplest electrodes are arranged as cathode and anode to provide a d.c. potential which ionises the gas under certain chamber conditions, known as d.c. diode glow discharge. The procedure of d.c. glow discharge can be described by the level of the potential between the electrodes against the level of the current as shown in fig 3.1.1, which gives a number of states of voltage dependence on current level.

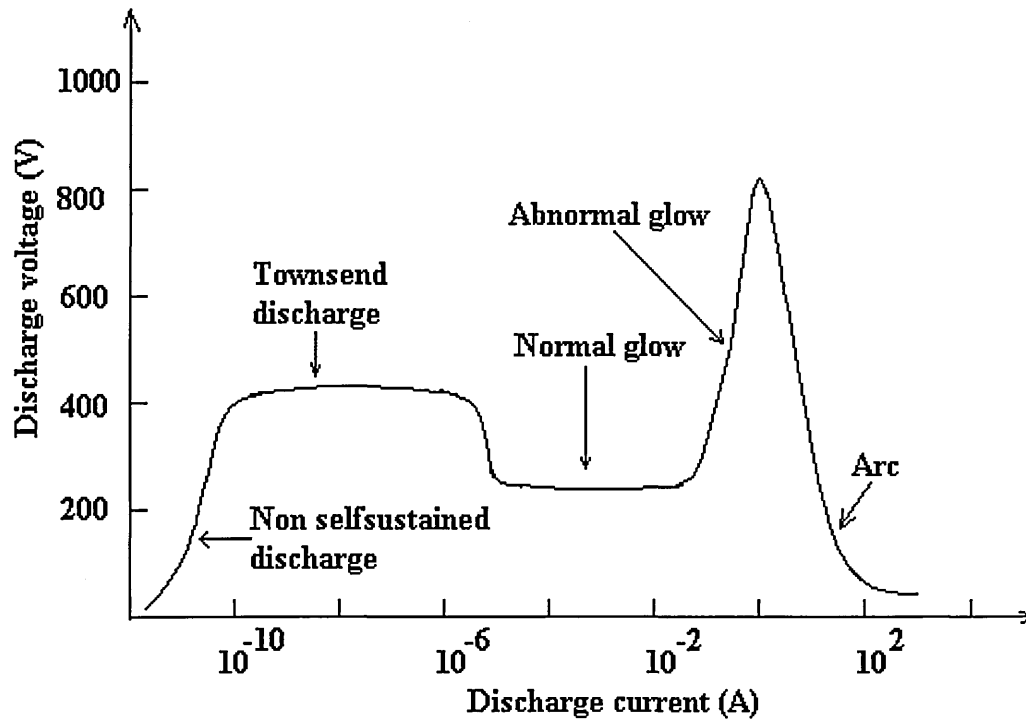


Fig 3.1.1 Diode glow discharge procedure: voltage/current relation

When the current is at a very low level, the amount of ionisation is not high enough to sustain the discharge unless some external energy is used to produce more ionisation,

and this region is known as non self-sustained discharge. If the voltage applied between the electrodes is sufficiently high, the electrons emitted by the cathode can obtain sufficient energy to produce more ionisation (breakdown) which causes the discharge to become self-sustaining; this region is known as Townsend discharge⁽²⁾. There is no appreciable space charge between the anode and cathode in the Townsend discharge and the electric field is more or less uniform across the electrodes. However if the discharge current is allowed to increase by increasing the dissipated power, the ions begin to collect near the cathode to form a localised space charge, which results in more energetic ion bombardment on the cathode. As there are more secondary electrons emitted from the cathode, the wholly maintained glow discharge is achieved accompanied by a fall of the voltage to a minimum. This region is defined as the normal glow discharge, which gives a few distinct regions between the electrodes of the discharge chamber as shown in fig 3.1.2

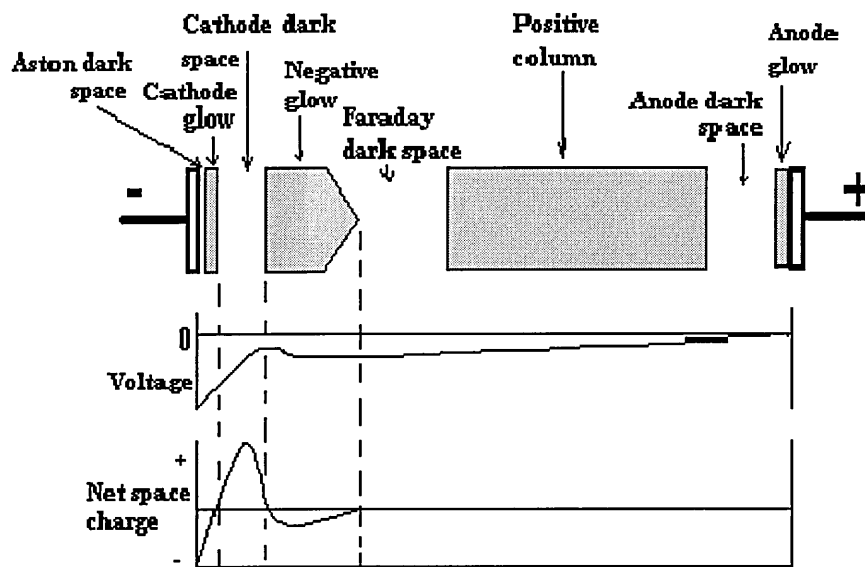


Fig 3.1.2 Physical regions in glow discharge

Directly adjacent to the cathode is the Aston dark space, where electrons leave the cathode with a very small initial energy which is not high enough to cause gas

excitation. The next is the cathode glow region caused by neutralisation of the positive ions as well as the negative ions. Beyond the cathode glow region is the cathode dark space in which positive ions are accumulated to form space charge. Most of the voltage is dropped in this region to provide the accelerating force driving the ions to the cathode. The thickness of this region is approximately the mean distance travelled by a secondary electron from the cathode before it makes a ionisation collision. The secondary electrons produced by ion bombardment on the cathode are accelerated in the cathode dark space to obtain sufficient energy to cause ion-electron pairs (plasma) which result in the formation of a negative glow region next to the cathode dark space. The electrons eventually lose most of the energy by a series of ionisation and excitation collisions, and finally no longer make any more ions. Since no more ions are produced, the electrons begin to accumulate in this region to form a slightly negative space charge. The next regions are the Faraday dark space, positive column, anode dark space and anode glow. However for sputtering process the space charge free positive column, the actual plasma expands through all rest of the vacuum chamber.

In the state of normal glow discharge for argon, the thickness of cathode dark space (pd) is 0.3 torr centimetre, which is independent of discharge current⁽³⁾. In the normal glow state the cross section of the glow does not cover all of the cathode area, as the current density is too low for a sufficient sputtering rate, and the potential is also too low to produce high sputtering yield. When the power dissipation is continually increased, the glow will eventually cover all the complete cathode area and the current density begins to increase with the voltage. This state is defined as abnormal glow discharge in which the thickness of cathode dark space can be expressed as:

$$pd = A + \frac{BF}{V - E} \text{-----} \quad 3.1.1$$

where A, B, E, and F are constants dependent on electrode material and geometry, as well as the gas composition. In the abnormal glow state, high electric field and high

current density result in a large number of energetic ions bombarding the cathode and therefore, the sputtering yield and sputtering rate are high enough to deposit film efficiently. It is for this reason that most of PVD sputtering deposition systems commonly employ abnormal glow discharge⁽⁴⁾. If the voltage increases even more, the cathode dark space will decrease in size, and the current density will rise to accelerate ions to energy levels high enough to cause emission of thermal electrons from the cathode accompanied by a large drop in voltage. This state is known as arc discharge.

In an arc discharge, the cathode (target) is bombarded by an high current density and low voltage arc which produces cathode spot (a small active emitting area on the target surface) randomly moving across the target surface if no external magnetic field is added. This is known as the random cathode arc. The cathode spot produces a high speed plasma jet which contains a high proportion of multiply charged ions, besides neutral particles and macro droplets of the evaporated target materials^(5,6,7,8). A technique has been developed to use external magnetic field in order to control the movement of the cathode spot. The external magnetic field can be produced by either the permanent magnets array⁽⁹⁾ or the electromagnetic coils⁽¹⁰⁾ arranged behind the cathode. Therefore the cathode spot is steered according to a predetermined orbit. This is known as the steered cathode arc. The steered arc has advantage on the reduction of the macro droplets and efficient use of the target materials as compared with the random cathode arc and therefore the steered arc technique is very commonly used in the commercial PVD systems.

3.2 Sputtering and related events

Sputtering is an atom separation process in which the surface of the target is undergoing energetic particle bombardments resulting in materials being ejected from the target surface due to the momentum transfer between the incident particles and the atoms on the surface of the target. Grove⁽¹¹⁾ was the first person to find the sputtering

phenomenon using a glass discharge tube in which the cathode material was discovered deposited on the surrounding glass wall.

The erosion of target material in sputtering is measured by sputtering yield (Y). Y is defined⁽¹²⁾ as the mean number of removed atoms from the surface of target per incident particle:

$$Y = \frac{\text{removed atoms}}{\text{incident particles}} \quad \text{-----} \quad 3.2.1$$

The incident particles may be ions, neutral atoms, neutrons, or electrons as well as energetic photons. However the measurements of Y are generally made using ion beam techniques which supply the desired ions with a certain energy since they are easy to produce and accelerate in glow discharge. For the necessary technology to produce a well defined ion beam the reader is referred to Freeman⁽¹³⁾.

The sputtering yield is a function of the energy of the incident ions⁽¹⁴⁾. When the energy of an ion is increased from a threshold energy (about 10 to 30eV), the sputtering yield rises rapidly. From about 100eV upwards, the sputtering yield increases almost linearly with increasing ion energy; at the same time the values begin to be large enough for deposition of films⁽¹⁵⁾. The sputtering yield can be expressed⁽¹⁶⁾ as:

$$Y = \frac{3\lambda \alpha E_i}{4\pi^2 U} \quad \text{-----} \quad 3.2.2$$

where E_i is the energy transferred in a binary collision, α is a function of the colliding atom masses, $\lambda = 4mm_i / (m + m_i)^2$ and U is the surface binding energy of the target. When the ion energy is increased even more, the dependence of Y on the incident energy is less than linear and this is associated with increasing penetration of the incident ion which reduces the sputtering effect and thus decreases the sputtering yielding. The sputtering is also dependent on the angle of the incident ions as shown

in Fig 3.2.1 where θ is measured from the surface normal of the target. In general, the yield reaches a maximum at an angle θ_{\max} which is between 60° and 80° dependent on incident ions with a certain energy and the target materials. For large angles, the yield decreases rapidly due to the increase in reflection as the direction of incidence approaches the glancing angle.

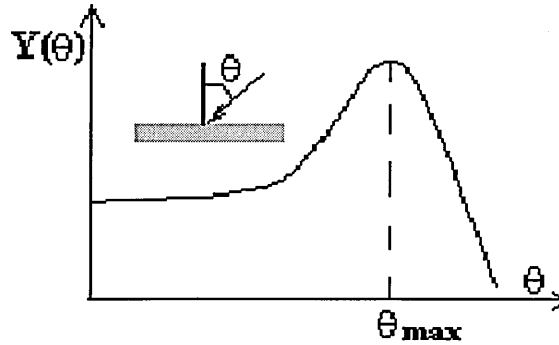


Fig 3.2.1 Sputtering yield dependence on ion incident angle

During a sputtering process, it is estimated that only up to 1% of the incident ion energy is consumed to produce ejected atoms and secondary electrons, while 75% contributes to target heating, and the remainder is associated with accelerating the secondary electrons crossing the dark space and then dissipated through collision with the substrate. The impinging of incident ions resulting in a series interaction occurring at the target surface⁽¹⁷⁾ as shown in Fig 3.2.2, which includes liberation of neutral atoms, back-scattering, X-ray emission, photon generation, secondary electron emission, and desorption of gas atoms from the target surface. Several processes occurring in the target include amorphisation, implantation, compound formation, cascade generation, local heating and the creation of point defects.

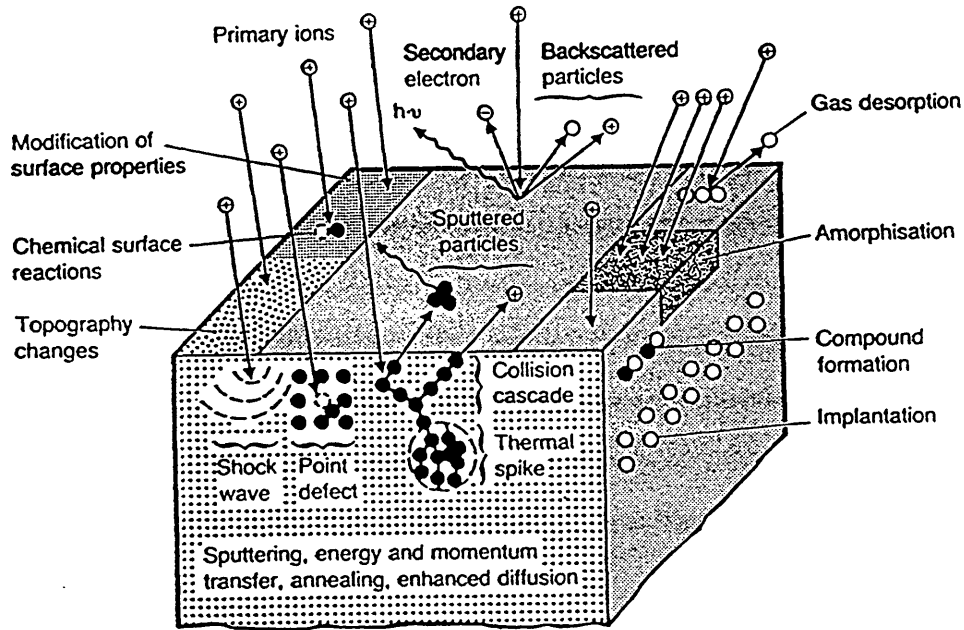


Fig 3.2.2 Interaction between incident ions and surface atoms of the target

The sputtering process used for surface coating has advantages over other processes due to less restriction in use of target materials (range from low melting point to high melting point, and from conducting to insulating materials if RF power is used). In addition the sputtering process can produce films, at a relative low temperature as compared with CVD, with thickness uniformity over large areas, and with smooth surface (no spitting as in thermal evaporation and no droplets as in arc deposition).

3.3 Sputtering deposition techniques

3.3.1 D.C. diode sputtering

The planar dc diode sputtering deposition configuration is the simplest sputtering process as shown in Fig 3.3.1⁽¹⁸⁾. The target is connected to a negative voltage controlled power supply and faced to the substrate where the film is growing. The abnormal glow discharge

is employed in the process to ensure that the cross section of the glow covers all of the target area to give uniform target sputtering as well as substrate coating. The cathode is either connected to a negative voltage with a dc power used to sputter a conducting target, or to a rf power source if an insulating target is to sputter. A conducting plate is attached at the back of the target to serve as the target cooling channel. The working gas is introduced to provide a medium in which a glow discharge can be initiated and maintained. A reactive gas can also be introduced in order to produce compound coatings. The substrate is placed as an anode which can be either earthen or biased with a negative voltage.

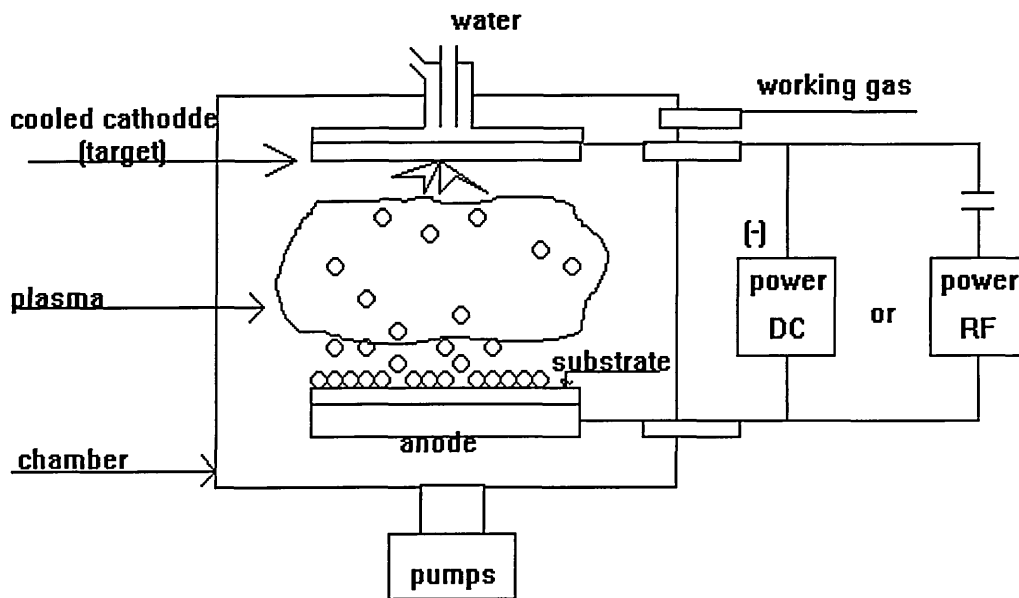


Fig 3.3.1 Sputtering deposition configuration

The sputtering yield of a target is dependent on both the characteristics of the target materials and the incident ion energy and mass. The effect of ion mass on sputtering yields of several materials is shown in Table 3.3.1⁽¹⁹⁾. Argon is the inert gas most commonly used as a sputtering medium in sputtering deposition system since its mass is high enough to produce a high sputtering yield and its price is low compared with other inert gases.

Table 3.3.1 Sputtering yield of elements at 500eV

element	Al	Ti	V	Cr	Zr	Nb	Mo	Ta	W
He(ion)	0.16	0.07	0.06	0.17	0.02	0.03	0.03	0.01	0.01
Ne(ion)	0.73	0.43	0.48	0.99	0.38	0.33	0.48	0.28	0.28
Ar(ion)	1.05	0.51	0.65	1.18	0.65	0.60	0.80	0.57	0.57
Kr(ion)	0.96	0.48	0.62	1.39	0.51	0.55	0.87	0.87	0.91
Xe(ion)	0.82	0.43	0.63	1.55	0.58	0.53	0.87	0.88	1.01

The dc diode sputtering deposition procedure is shown in fig 3.3.2. A plasma is produced by means of glow discharge when a sufficient potential (500-5000V) is applied between the cathode/anode pair. The substrate (anode) can be earthen or biased up to -1000V. The primary ions from the negative glow plasma are accelerated in the dark space and move towards the target. There is also a high probability for charge exchange collisions before the accelerated ions strike at the target, and so the target is under bombardment of number of ions and atoms with energy less than the applied potential. Most of the incident energy is transferred to heat the target. Only a small part of the energy is subjected to the collision cascades to produce the sputtered atoms forming as a coating flux towards the substrate. The substrate is also under the bombardment of particles from the plasma, such as energetic neutrals, ions and fast electrons ⁽²⁰⁾.

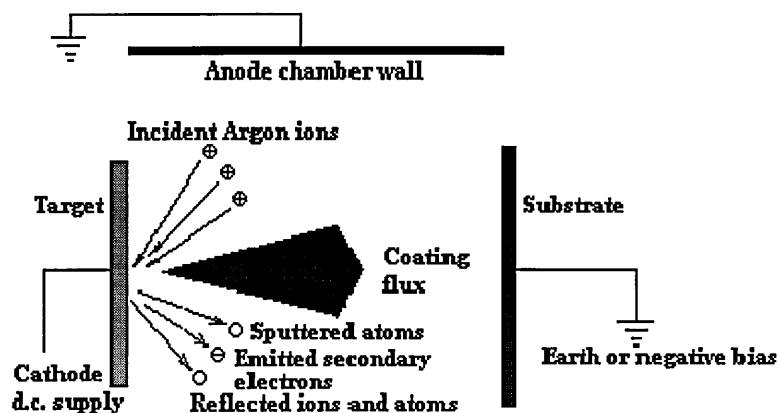


Fig 3.3.2 D.C. diode sputtering diagram

The disadvantages of diode sputtering deposition are that the process has to be operated at high voltage levels as well as in a high pressure range (5 to 100 mtorr) because the ionisation required for sputtering falls rapidly with decreasing pressure. As the back diffusion of the sputtered atoms to the target becomes a serious problem when the pressure is above 20 mtorr⁽²¹⁾, the sputtering process is very inefficient. Also the high pressure will cause a high background of undesirable impurities which may be incorporated during film growing⁽²²⁾ due to the back streaming of the diffusion pump. The advantage of dc diode sputtering is its simplicity, and therefore the techniques to improve the performance of sputtering deposition are still based on diode sputtering.

3.3.2 DC triode sputtering deposition

The dc triode sputtering technique (fig 3.3.3) employs a thermionical electron emitter (hot filament) to increase ionisation so that high ionisation at lower pressure or at reduced discharge voltage can be achieved^(22,23). The improvements of triode sputtering as compared with the diode process are the low pressure with gas throughput which leads to low background of impurity, the high deposition rate (up to 600Å/min), and low discharge voltage (<500V). However as the hot filament not only emits electrons but also results in contamination to the deposition, it is difficult to scale-up for industrial process, particularly for temperature sensitive and reactive processes⁽²⁴⁾.

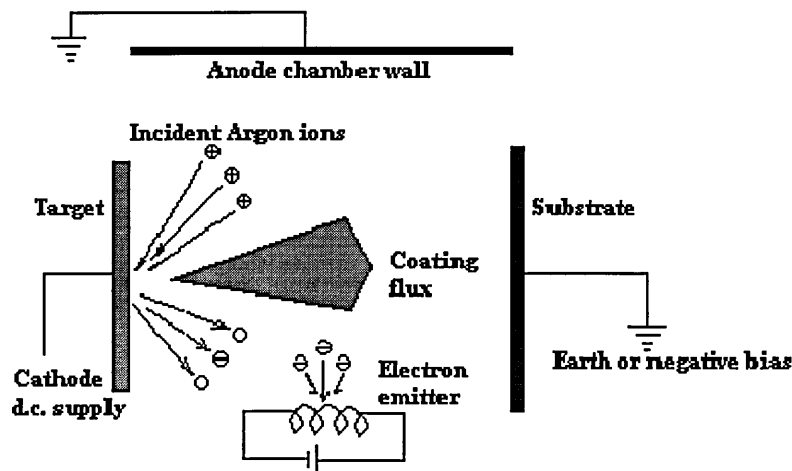


Fig 3.3.3 dc triode sputtering

3.3.3 Magnetron sputtering deposition

The discovery of magnetic enhanced ionisation was first made by Penning⁽²⁵⁾ in 1936. However the beginning of magnetron sputtering as an effective process for the deposition of metal and composite films can only be traced back to 1970^(26, 27, 28, 29). Many different magnetron configurations have been developed, such as cylindrical magnetrons, hollow cathodes, and planar magnetrons. However the most often used for practical applications is the rectangular planar magnetron^(26, 30). This technique was reviewed and discussed by Waits⁽²⁶⁾ and Thornton⁽³¹⁾. In general the magnetron effect can be described as a closed $E \times B$ drift path to confine the electron during glow discharge, so that enhanced ionisation and high sputtering rates could be achieved.

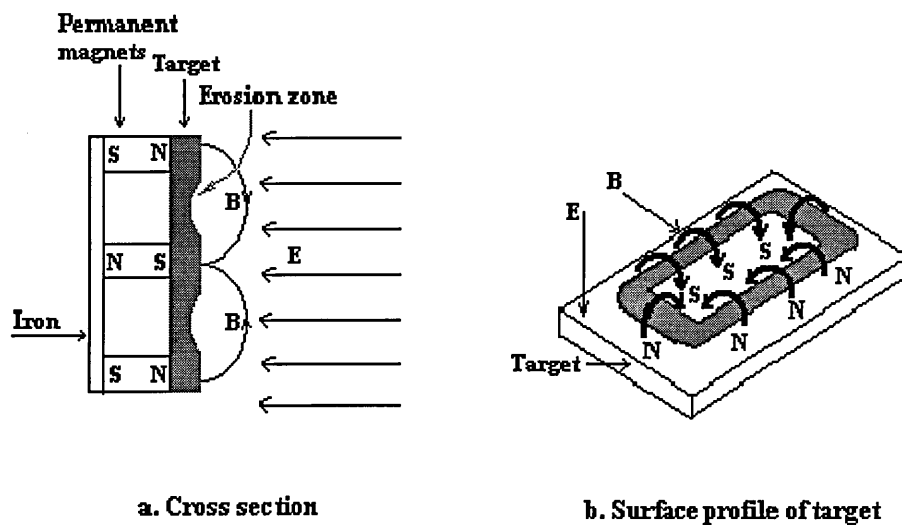


Fig 3.3.4 Arrangement of magnetron sputtering

Magnetron sputtering is designed so that the permanent magnets are arrayed to produce a region in front of the target surface where the locus of magnetic field lines (200 to 500 G) parallel to the target surface is a close path as shown in fig 3.3.4⁽³²⁾. A

charged (q) particle with a velocity (V) travelling in the magnetic field (B) is affected by a force (F) written as:

$$F = qV \times B \text{ -----3.3.1}$$

This force significantly influences the movement of electrons rather than that of ions since an ion is too heavy to be affected quickly. The electrons moving non parallel to the magnetic field will be subjected to a force $BeV\sin\theta$ vertical to the lines of magnetic force. Also the motion of electrons is coupled with a velocity $V\cos\theta$ parallel to the magnetic field. Hence the electrons are moving in helical paths around the lines of magnetic force. The radius (r) of the helix can be expressed as

$$r = \frac{m_e V \sin\theta}{Be} \text{ ----- 3.3.2}$$

The radius of the helix decreases with increasing magnetic field. Since an electron travels on a curved path instead of on a straight line, it will go a relatively long distance before escaping from the glow discharge region. Therefore more ionisation collisions will be produced to contribute to the ion density which results in a high sputtering rate (>500nm/min) .

The advantages of conventional magnetron sputtering deposition as compared with those of conventional diode and triode techniques are the higher deposition rate, lower re-sputtering from the substrate and the chamber, reduced substrate heating during deposition, and the stability of a process operating in a large pressure range so that the deposition parameters can be fully controlled.

The disadvantage of conventional magnetron sputtering deposition is that the electrons are only confined in the vicinity of the target and the ionisation falls rapidly with increasing target to substrate distance⁽³³⁾. When the distance from the target increases, the ion bombardment on the substrate decreases rapidly, which causes the

formation of inferior films with voids distributed along grain boundaries⁽³⁴⁾. The way to increase ion bombardment in the conventional magnetron sputtering is to apply a high bias voltage. However the high voltage may lead to the energy of the ions being too high and as a result the generation of more defects within the grains. Thus high stresses in the film are unavoidable, which also results in poor film quality⁽³⁵⁾. It is advantageous in many applications to increase the ion current density while maintaining a reduced bias voltage to keep the ion energy at a desirable range. An unbalanced magnetron has been invented which provides this kind of ion bombardment.

3.4 Unbalanced magnetron sputtering deposition

The concept of the unbalanced magnetron was first introduced by Window and co-workers^(36,37,38) in 1986. In a magnetron sputtering source, the magnetron is considered unbalanced in that some of its poles are strengthened (usually the outer poles) so that the intensities of magnetic flux through the pole facing to the outer poles are not comparable with that through the pole facing to the inner pole.

The modes of plasma localisation of balanced magnetron sputtering (BMS) and unbalanced magnetron sputtering (UBMS) are given in fig 3.4.1. In the UBMS mode, some of the electrons are trapped in the vicinity of the target and their function is as the same as that in BMS mode. The other electrons, however, are not fully trapped, and can gyrate along the magnetic field lines to the substrate region. Because of the need to maintain the electrical neutrality within the highly conducting plasma, the ions and electrons diffuse together⁽³⁹⁾. Thus the plasma is expanded towards the substrate region, and the ions in the plasma can be used to bombard the substrate by applying a bias on the substrate. Even at a low bias potential, UBMS provides a ratio of ion to deposited atoms of up to 2:1, which is much higher than that (0.25:1) produced by BMS. The ion (with a certain energy range) bombardment can help to

fill in voids and to transfer energy to surface atoms for increasing their mobility, both of these effects will produce dense films^(34, 40).

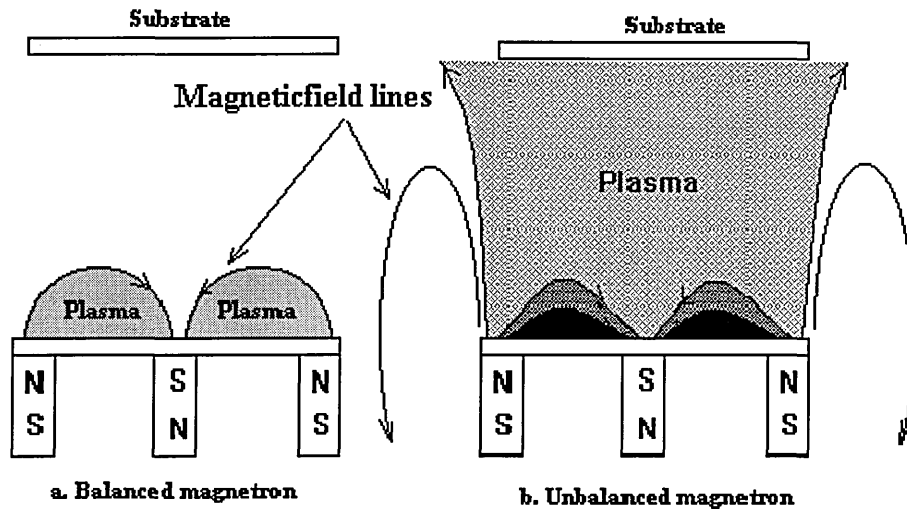


Fig 3.4.1 Magnet arrangements

There is no doubt that UBMS based on a single cathode provides enhanced low-energy ion bombardment during the deposition process, leading to improved quality of films. However there are still short-comings which need to be solved when this technique is considered for use in an industrial scale process. One is that the substrate current density is a sensitive function of the position in front the target⁽⁴¹⁾; the substrate current density decreases rapidly as the distance is increased from the centre of the target towards the outer edge. Another is that the sputtering is a line of sight process in which even if the substrate could be rotated to coat all sides, it would be coated from one direction at a time, which means that one side of the part would be in the shadow area where the arrival rate and energy of the target atoms would be very low, causing porous film structure and inferior film quality⁽⁴²⁾. These short-comings could be largely alleviated with the development of multi-cathode deposition systems using substrate rotation mechanisms.

3.5 Multi-cathode deposition system

Opposed cathode sputtering systems^(34,43,44) have been used for many years and more recently four cathode coating systems^(45,46) have been introduced to coat a variety of components such as cutting tools and decorative pieces. In a multi-cathode coating system, the components will be coated from more than one side at the same time and therefore, the shadow effect will be reduced or eliminated.

The opposed cathode unbalanced magnetron arrangement is the initial multi-cathode sputtering coating system as seen fig 3.5.1⁽⁴⁴⁾ in which the magnetic field lines of the facing poles are closed.

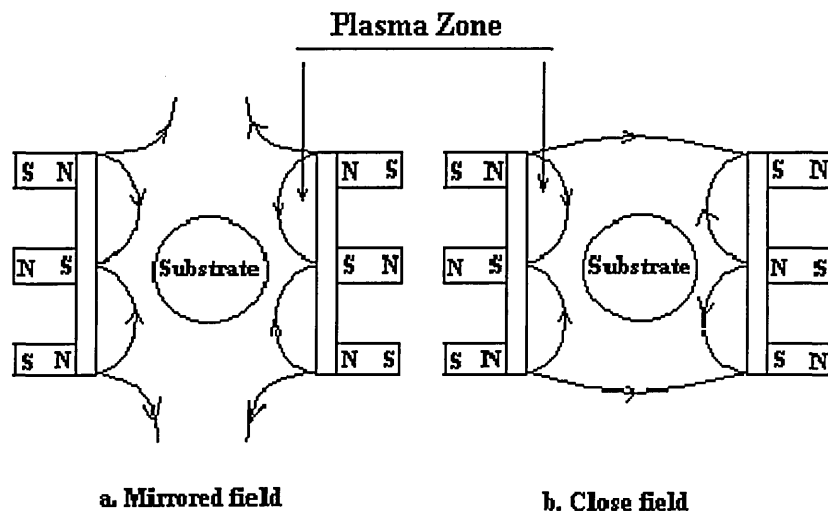


Fig 3.5.1 Opposed unbalanced magnetrons puttering coating system

In the mirrored field array, the plasma density is only high around the substrate when the distance of the cathodes is narrow enough where the plasma zones overlap. If this is not the case, the field lines at the mid-position are directed to the chamber walls causing the escape of the electrons from the plasma region and therefore leading to low ion density. In the close field however, the perpendicular division (respect to the

surface of the target) of the magnetic field lines links up and closes the fields between two targets⁽⁴⁷⁾ which produces an effective magnetic trap to confine the electrons in the region between the two cathodes. The high density of electrons results in high density of ions. In the close field geometry, the ion current density is up to 5mAcm^{-2} which is, at identical cathode distance, more than twice as high as that in the mirrored field geometry⁽⁴⁸⁾. Therefore it is common that the magnetic field geometry of the multi-cathode system is arranged as closed fields.

To alleviate the shortcomings of the single cathode system, multi-cathode systems have been considered and developed^(49,50,51,52). The industrial implementation of unbalanced magnetron sputtering coating technology has achieved great progress since the ABSTM⁽⁴⁶⁾(arc bond sputtering) coating system was introduced⁽⁴⁶⁾ (see fig 3.5.2).

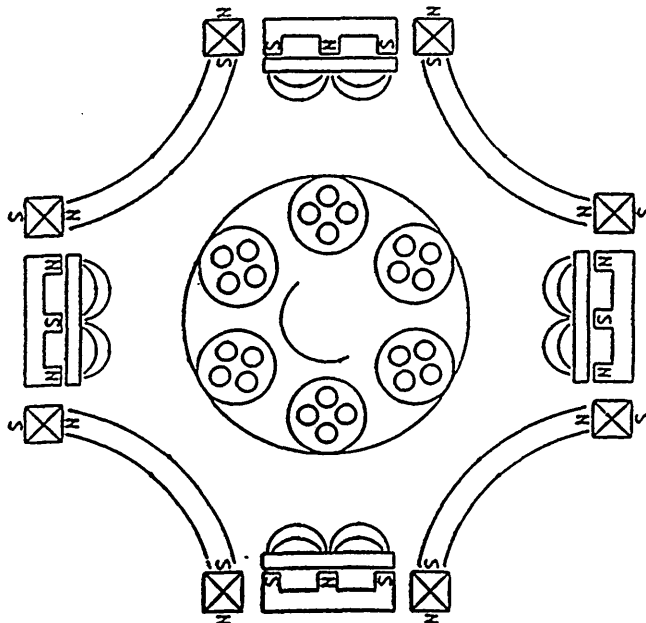


Fig 3.5.2 Four cathode geometry of ABS coater

This coater uses four cathodes with a combination of permanent unbalanced magnets, and electromagnets which can enhance the unbalanced magnetron effect. The substrate table is connected to rotating gears which make the substrate operate in threefold planetary rotation to obtain uniform deposition and to mitigate the shadow

effect. Both the unbalanced magnetron sputtering and the steered arc techniques can be used in one process. This coater performs an etching process to implant the metal ions into the substrate surface by using the steered arc prior to the unbalanced magnetron sputtering coating. As there is a titanium rich gradient interface produced between substrate and film, the adhesion between coating and substrate system is increased enormously⁽⁵³⁾ which gives the ABS coater more competitive application in industry than other coating systems.

3.6 Reactive sputtering

Reactive sputtering is a process in which the reactive gas is introduced into the glow discharge chamber to combine with the metal vapour flux to produce compound film at the substrate surface^(54,55,56). Deposition of titanium nitride film is an example of how nitrogen is introduced as the reactive gas which is partially ionised in the plasma. The formation of titanium nitride takes place on the substrate surface. This procedure can be explained using a hysteresis curve⁽⁵⁷⁾ as shown in fig 3.6.1

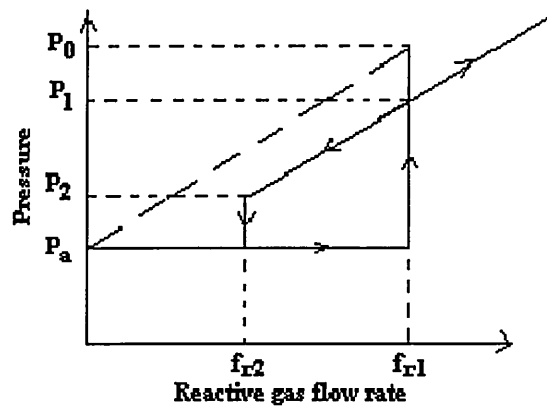


Fig 3.6.1 Hysteresis curve of reactive sputtering

P_a is a constant pressure maintained by the argon flow f_a , the dashed line means linear increase in P results from increasing f_a since $Q = SP$, where Q is the total flow rate, and S is the pumping speed.

When a reactive gas flow, fr , is increased, P remains almost constant at the initial value (P_a) until a flow rate fr_1 where P increases to a new value (P_1) which is defined as an equilibrium state. If no sputtering took place the value of P at this total flow rate would be P_0 and $\Delta P = P_0 - P_1$ is the reduction in pressure due to the reactive sputtering. Once the equilibrium state is established, the P is linearly changed with the variation of fr . The difference ΔP for the system pressure with and without reactive sputtering is constant unless the fr is reduced to the value fr_2 where the ΔP increases and system pressure decreases from P_2 to the initial value, P_a .

There are two states presented in the hysteresis curve. In state A, the total pressure is almost unchanging with the reactive gas flow fr . In state B, the total pressure varies linearly with fr but is lower by ΔP than the total pressure measured without sputtering taking place. The state A can be considered as that in which all the reactive gas is consumed being incorporated in the deposited film and the atomic ratio of reactive atoms to sputtered metal in the films increases with fr . In state B, a constant volume of reactive gas is consumed which is independent of fr and a stable compound film is produced as there is an excess of reactive gas. The consumed rate of reactive gas in the two states can be expressed as:

$$Q_a = fr \text{ -----} 3.6.1$$

$$Q_b = (fr_1 - fr_2) \frac{P_0 - P_1}{P_1 - P_2} \text{ -----} 3.6.2$$

The change from state A to state B may be explained using a target poisoning mode⁽⁵⁸⁾ to describe the formation of a compound on the surface of the metal target. As both the secondary electron emission and the sputtering yield of the compound are often much lower than that of pure metals⁽⁵⁹⁾, the deposition rate and ionisation in the plasma are reduced. The transition stage can be described further using the hysteresis loops for reactive sputtering⁽⁶⁰⁾ (fig 3.6.2).

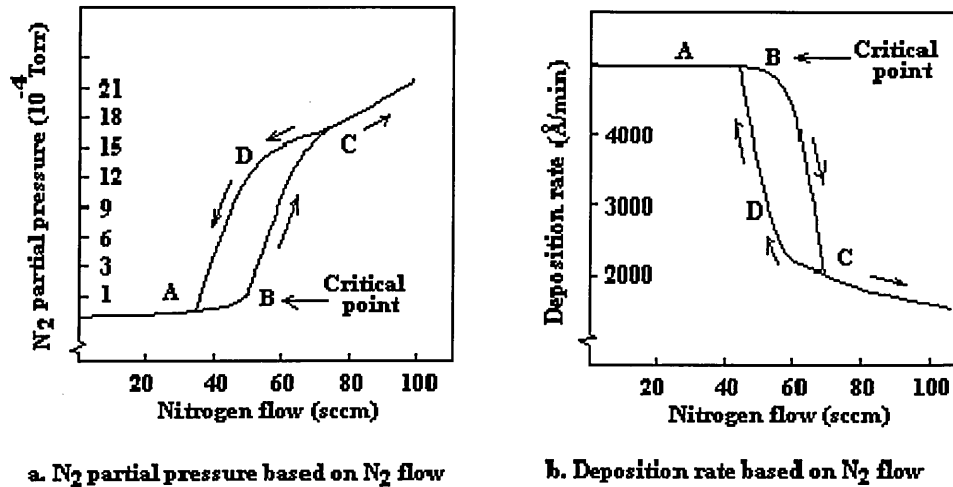


Fig 3.6.2 Nitrogen partial pressure and deposition hysteresis loops for reactive sputtering (sccm defined as standard cubic centimetres per minutes)

The hysteresis loop can be explained as following a path from $A \rightarrow B \rightarrow C \rightarrow D \rightarrow A$ where B is the critical point at which compound film begins to form on the surface of the target and the nitrogen partial pressure suddenly rises to a high point C and the deposition rate drops rapidly. Any further increasing nitrogen flow from point C will cause a linear increase in nitrogen partial pressure and a decrease in deposition rate. When the nitrogen flow is decreased after reaching point C, the nitrogen partial pressure will not reduce according to the path it followed when increasing. The nitrogen partial pressure will stay at a high level until reaching point D, when the compound film on target surface is sputtered off. Then the nitrogen partial pressure decreases quickly to the original level. The deposition hysteresis loop also obeys the $A \rightarrow B \rightarrow C \rightarrow D \rightarrow A$ path.

As B is the critical point to produce stoichiometric film without losing more deposition rate many techniques have been developed to get reactive sputtering controlled at this range or to avoid the undesirable hysteresis effect. An automatic feed back controller was used continuously to control the reactive gas flow mode to produce stoichiometric compound films at high deposition rate⁽⁶⁰⁾. Pulsed nitrogen gas flow was used to

produce TiN at 50% of the metal deposition rate⁽⁶¹⁾. The hysteresis loop effect can be avoided if the pumping speed for reactive gas, S_r , is higher than a critical pumping speed, S_c ($S_r > S_c$)^(62,63). S_c is expressed as:

$$S_c = \left(-\frac{dS\phi_r}{dp_r}\right)_{\max} \text{-----} 3.6.3$$

where $S\phi_r$ is the gettered reactive gas flow rate by sputtered metal atoms, and p_r is the reactive gas pressure. As there is no sudden increase in the partial pressure, stoichiometric film can be produced using a mass flow controller to maintain the reactive partial pressure during the process.

3.7 The principle of the film deposition

3.7.1 Nucleation and growth

In the sputtering deposition process, the film material is sputtered to become atomic vapour flux moving towards the substrate where film grows due to condensation of the material from vapour to solid phase. The film growing procedure can be described in four stages^(64, 65): nucleation, island growth, coalescence, and continuous growth.

In the first stage, the incident atoms become adatoms on the substrate surface where they lose their excess energy for escaping the surface potential barrier (W) and then the adatoms will vibrate with a frequency ν and migrate along the surface⁽⁶⁶⁾ as seen fig 3.7.1 a. This is known as self-diffusion of an atom across a perfect surface. In a real substrate surface, there are many defects such as dislocations, monatomic steps, vacancies, and adatoms where the interface between nuclei and substrate is increased and therefore nucleation here has a higher probability than on a perfect surface⁽⁶⁷⁾. When the adatoms meet some defects such as the step in fig 3.7.1 b, they will stay there and have more chance to meet other adatoms to become aggregates or clusters which are more stable than single adatoms. This stage is known as nucleation. Once the cluster reaches a critical size r^* , the free energy corresponding to the cluster reaches a maximum as

described by the capillary model (see appendix 1). It means the value of $r < r^*$ relates to a unstable aggregate which tends to have a high probability of desorption, while the values of $r > r^*$ lead to a stable cluster which will become larger when it meets other aggregates or adatoms.

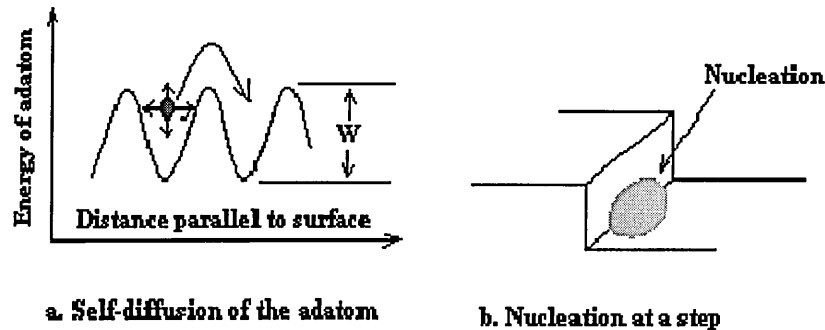


Fig 3.7.1 Behaviour of Adatom on the surface

The stage for island growth takes place once the establishment of nucleation is complete. The clusters begin to grow three dimensionally as expanding islands to occupy more surface area. When different islands meet each other, coalescence will take place among the islands and this leads to the enlarging of the island and an increase in the uncovered substrate area due to the resultant reduction in surface energy which acts to reduce the surface area to a minimum. As the orientation of growth for each island is different, the grain boundaries and defects are incorporated into the large islands. There are also similar events happening among the islands and nuclei. A nuclei will grow until it coalesces with its neighbour or an island and this incorporates immediately into the large island.

In the third stage, most regions of the substrate surface are covered by growing islands. As coalescence is continuously taking place among the islands, a network structure is formed on the substrate surface in which the deposited materials is separated by long, irregular, and narrow channels of width 50 to 200Å⁽⁶⁵⁾. The channels will be bridged and eventually filled while the deposition continues due to the nucleation occurring in these

channels and the nuclei grow and touch the sides of the channels to incorporate into the bulk of the film.

As the deposition continues, the channels are filled and all of the substrate surface is gradually covered by the bulk film. This stage is the growth of continuous film. The obvious preferred orientation occurring in this stage is commonly the columnar structure⁽⁶⁸⁾. The growth of continuous film can be classified as three modes^(69,70):

- (1) Layer-by-layer outlined (Frank van der Merwe) when the surface energy of the film material is lower than that of substrate material, and the strain energy in the film is small compared with the surface energy of the film materials.
- (2) Layer-by-layer fashion plus three dimensional clump (Stranski-Krastanov) when the surface energy of the film material is lower than that of substrate material, while the strain energy in the film is large compared with the surface energy of the film materials.
- (3) Three dimensional island growth (Volmer-Weber) when the surface energy of the film material is larger than that of substrate materials.

3.7.2 The microstructures of the sputtering-deposited film

A wide range of microstructures and physical properties are found in sputtering deposited films that are highly dependent on the incident coating flux, the nature of the substrate surface, and the substrate temperature. Classification of these microstructures can be normalised by the structure zone diagram based on the process pressure as well as the temperature ratio T/T_m where T is the substrate temperature and T_m is melting point of the deposition materials.

The early classic structure diagram was made by Movchan and Demchishin⁽⁷¹⁾ as shown in fig 3.7.2 a, where the structures are based on temperatures and divided into three zones. Zone 1 ($T/T_m < 0.26 - 0.3$) classifies the deposition by the condition of insufficient

adatom mobility, and therefore porous films with large spaced columns and domed tops are produced due to the shadow effect. Zone 2 ($0.25 - 0.3 < T/T_m < 0.45$) normalises the deposition controlled by surface diffusion resulting from increased adatom mobility, so that films with dense columns and smooth surfaces are deposited. Zone 3 ($T/T_m > 0.45$) classifies the high temperature deposition in which bulk diffusion becomes an important effect on the film structures and therefore films of equi-axed grains are produced.

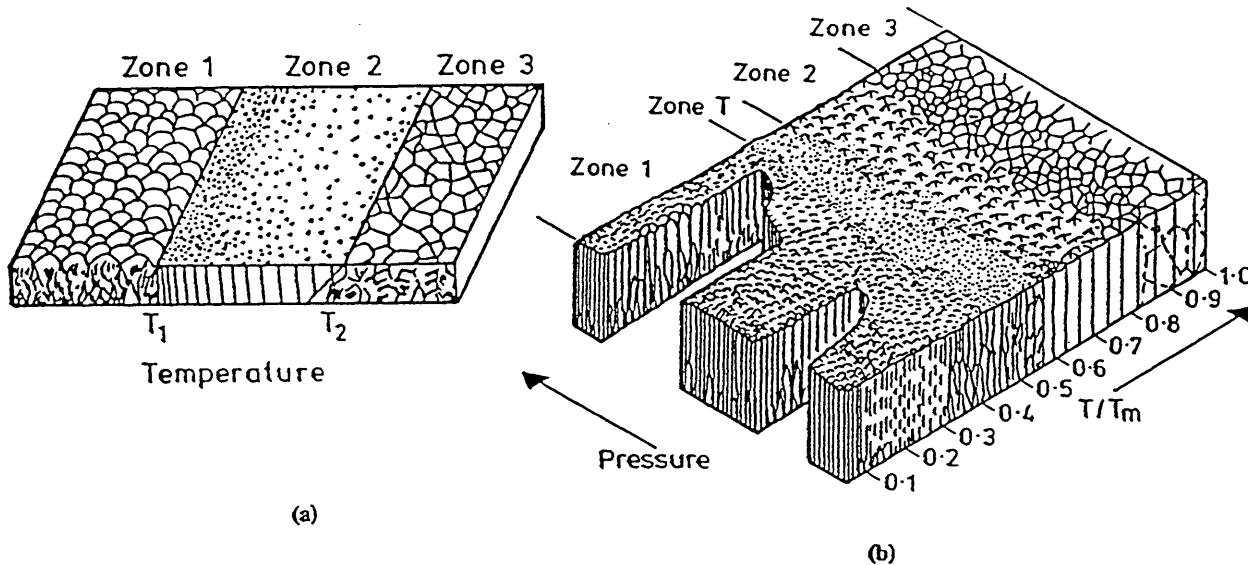


Fig. 3.7.2 Structure zone of the deposited films

The structure classification of the deposited films was improved by Thornton's zone diagram⁽⁷²⁾ by taking consideration of both temperature and total pressure (see fig 3.7.2 b). The diagram shows that columnar film with porous areas and voids located at the inter-grain boundaries is produced under conditions of low temperature and high pressure. This film structure is classified in the region of Zone 1 in which $T/T_m < 0.1$. At higher T/T_m (0.1 - 0.3) or lower pressure, the self-diffusion becomes appreciable and the coatings consist of dense columnar structures which are separated by conventional grain boundaries; this region is known as zone T (transition zone). At still higher T/T_m (0.3 - 0.5), sufficient surface mobility of the adatoms results in very dense film with fine columnar structures which are separated by real grain boundaries rather than porous areas and voids. This area is defined as zone 2, in which the film structure is less

influenced by the deposition pressure. When the substrate temperature is further increased (T/T_m range 0.5 - 0.75), the deposited films can still keep the columnar structure but the surface tends to become faceted because of the low energy (30 - 50eV) ion bombardment. At very high temperature ($T/T_m > 0.75$), the surface structure consists of relatively flat grain tops and film with equi-axed crystal grain structure can be produced if the temperature is high enough.

The last model of the structure zone was made by Messier⁽⁷³⁾ to take consideration of the effects of bias voltage as well as temperature. The effect of substrate bias voltage incorporates the adatom mobility induced by the energetic ion bombardments. This model specifies the zone T which hardly exists in the region between zone 1 and zone 2 without the ion bombardment (no bias voltage). However the width of zone T increases with the bombardment energy due to the zone 1 decreasing in width while the boundary of zone 2 remains almost the same (see fig 3.7.3)

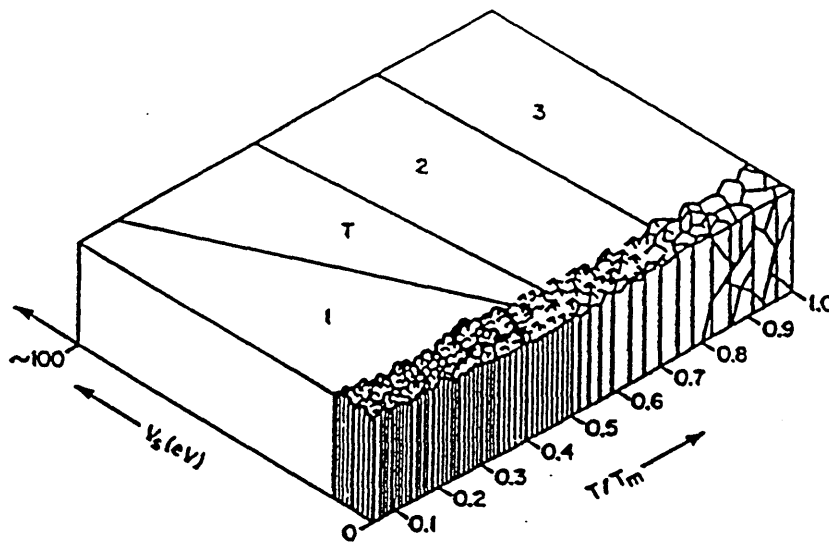


Fig 3.7.3 Structure model showing the effect of bias voltage and temperature

3.7.3 Characteristics of films

The packing density is one of the most important film parameters which relates to the microstructure of the films. This parameter can be expressed⁽⁷⁴⁾ as:

$$P = \frac{\text{Volume of the solid part of the film (columns)}}{\text{Total volume of the film (columns plus voids)}} \text{-----3.7.1}$$

It is common in a PVD deposition process that the film has columnar structure⁽⁷²⁾. The simplest model of this columnar structure can be specified as three patterns⁽⁷⁵⁾, using hexagonal array as shown in fig 3.7.4.

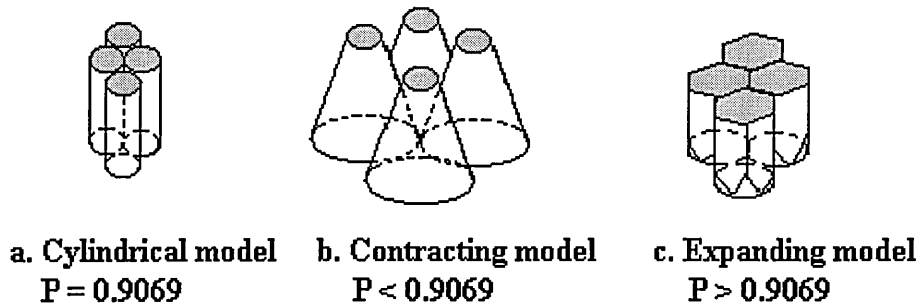


Fig 3.7.4 Columnar patterns of films

The pattern of the columnar structure is considered to have closely packed circular bases and cross-sectional areas expanding, contracting, or remaining constant in the direction of growth. The cylindrical model is calculated to have a packing density equal to 0.91, while the P for contracting or expanding models is less than or greater than 0.91 respectively.

In a real situation, especially for deposited film with low adatom mobility and even a single column or grain has the same density as that of the bulk materials, the packing density of the film is generally less than that of bulk materials due to the occupation of the porous areas and voids in the grain boundaries as well as the inter-space between columns. The loose packed film can be made dense using high temperature deposition to increase the adatom mobility⁽⁷⁶⁾, or using an ion assistance process to apply low energy ion bombardment during growth⁽⁷⁷⁾. Both experiments and computer simulations have been carried out to investigate the microstructure of the deposited film affected by ion

bombardment⁽⁷⁸⁾; they show that high density films are achieved by energetic ion bombardment, and both the energy of ions and the ion to atom arrival ratio closely influence the development of densification.

Hardness is also an important film parameter which can be expressed as the Hall-Petch^(79,80) formula

$$H = H_0 + Kd^{-1/2} \text{-----} 3.7.2$$

where H is hardness, H₀ the intrinsic hardness of a single crystal, d the grain size, and K the materials constant. The hardness for the coating, however, is not only dependent on the grain size but also the texture, porosity, residual stress, etc., which are affected by the process parameters⁽⁸¹⁾. In general the hardness is determined by the inter-atomic forces and the operative deformation mechanism. The materials exhibit high intrinsic hardness due to the high cohesive energy, short bond length, and high degree of covalent bonding⁽⁸²⁾.

In practice, hardness of the coating is not the only parameter selected for the applications due to the complex function of film/substrate system as shown in fig 3.7.5⁽⁸³⁾. The important parameters considered to achieve better performance are the elastic modulus, thermal expansion, crystal structure and chemical compatibility of the coating and substrate materials⁽⁸¹⁾.

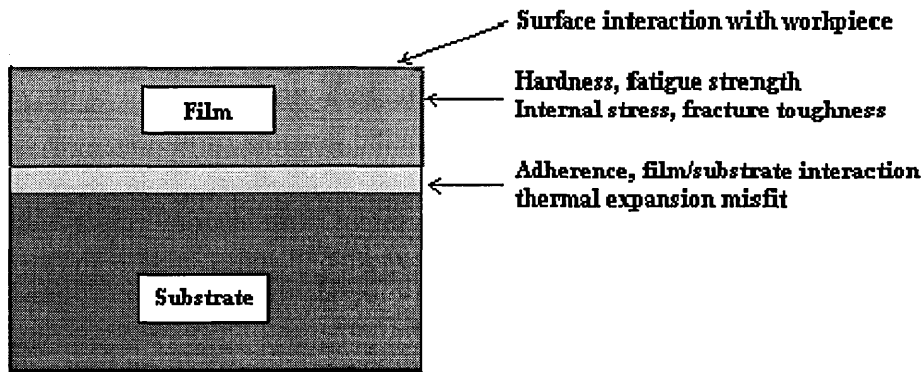


Fig 3.7.5 Film/substrate system

In an application with a high loading intensity, the imposed strain results in a stress discontinuity at the substrate/coating interface if the elastic modulus of the coating and the substrate are different⁽⁸⁴⁾. During a bending test of TiC coated high speed steel sample as shown in fig 3.7.6, the stress discontinuity at the coating/substrate interface is caused by the difference in the Young's modulus of the coating and the substrate material when an external force acts the coating/substrate system. It is very common that interface failure is caused by stresses. Therefore the stresses should be made as small as possible by choosing coating/substrate combinations⁽⁸¹⁾.

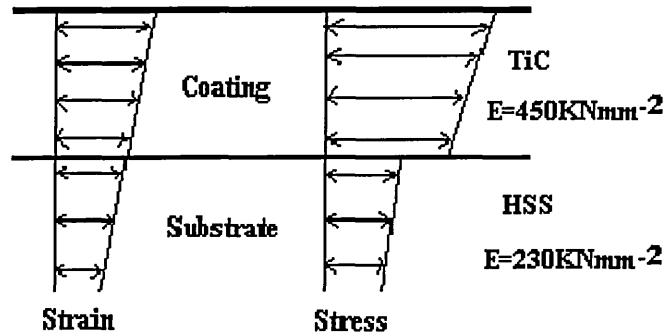


Fig 3.7.6 Strain/stress distribution of coating/substrate system

Coating deposited using PVD techniques often exhibits residual stress which can be catalogued as intrinsic stress and thermal stress^(85,86,87). The intrinsic stress can be calculated as:

$$\sigma = KRE^{1/2} \text{-----} 3.7.3$$

where, K is the constant for material, R the ion to atom arrival ratio, and E the ion energy. The generation of intrinsic stress is caused by the formation of defects and microstructure mismatch between coating and substrate. The intrinsic stress is sensitively influenced by the deposition parameters such as substrate temperature, pressure, angle of incidence, deposition rate and distance from substrate to source^(88,89,90)

In most cases, the effects of these parameters are interdependent, especially with respect to the substrate temperature, which greatly affects the diffusion of the point defects, and the formation of the microstructure, as well as the thermal stress.

The thermal stress results from mismatch of the thermal expansion coefficients between the coating and the substrate. Therefore the deposition temperature and the cooling rate during a process result in stresses being introduced into the film/substrate system. The relation can be expressed⁽⁹¹⁾ as:

$$\sigma_{th} = \frac{E_f}{1-\nu_f} (\alpha_f - \alpha_s)(T_s - T_a) \text{-----3.7.4}$$

where, E_f and ν_f are the Young's modulus and Poisson's ratio of the coating. α_f and α_s are the thermal expansion coefficients of the coating and substrate. T_s and T_a are the deposition temperature and the room temperature respectively.

The contribution of the thermal and intrinsic stresses to the residual stress in the film can be considered as a function of T/T_m ⁽⁹²⁾ where T(K) is the substrate temperature during the deposition process and T_m is the melting point of the film material as shown in Fig 3.7.7.

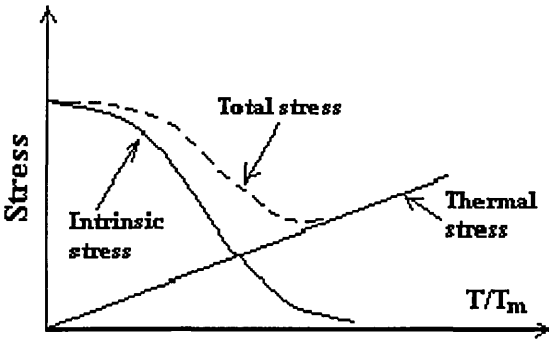


Fig 3.7.7 Contribution of the intrinsic and thermal stresses

At low T/T_m , the intrinsic stress is the dominant stress. When T/T_m reaches about 0.25 to 0.3 the intrinsic stress is no longer the major factor while the thermal stress begins to take effect. At $T/T_m > 0.3$ the thermal stress becomes the dominant. The total stress, therefore, could be at a minimum at an intermediate T/T_m as a result of the combination of intrinsic and thermal stresses.

3.8 Hard coating systems

3.8.1 Classification of hard coatings

Hard coatings have been used primarily as wear resistant layers on cutting tools, mechanical contact parts, and decorative appearances on various components. One of the important parameters influencing the wear behaviour is the hardness of the coating. A hard coating on the substrate can reduce wear by preventing ploughing on both a macro and a micro scale and therefore is particularly useful in abrasive environments. Also the hard coating can lead to low friction since the load is well supported by the hard coating to reduce the shear strength⁽⁹³⁾ of the real contact area. The development of hard coatings can be described as having three generations⁽⁹⁴⁾.

3.8.1.1 The first generation of hard coatings

The first generation of hard coatings can be catalogued as binary compounds of transitional metal nitrides, carbides, and borides in which the properties of hard coating are dependent on the single metal-non-metal compounds. As is known from Hägg's rule⁽⁹⁵⁾, the structure of transitional metal nitrides, carbides, and borides is determined by the ratio of the atomic radius, $R=r/r_m$, where r is the atomic radius of the interstitial element while r_m is the atomic radius for the transitional metal. A simple structure, such as the NaCl structure, will be formed if R is less than 0.59. If R is more than 0.59 however, very complicated structures which may consist of more than 100 atoms per unit cell will be produced.

Hardness is one of the important properties of hard coatings. In general the hardness is dependent on the chemical bonding characters of the coating compounds⁽⁹⁶⁾ These bonding characters can be classified as covalent bonding (C), metallic bonding (M), and ionic bonding (I). The properties for these bonding materials are given in table 3.8.1 which shows that none of these materials can have all the properties at the highest level. If hardness is at a maximum, some degree of brittleness and lower adherence is unavoidable.

Table 3.8.1 Physical properties of materials dependent on bonding

Level	Hardness	Brittleness	Melting point	Stability ΔG	Thermal expansion coefficient	Adherence to metallic substrate	Interaction tendency	Multilayer suitability
High	C	I	M	I	I	M	M	M
↓	M	C	C	M	M	I	C	I
Low	I	M	I	C	C	C	I	C

In the initial stage of hard coating engineering, mononitrides^(97,98,99,100,101,102) and monocarbides^(103,104,105,106,107) were produced as coating materials to improve both wear and corrosion behaviour. Titanium nitride was the most studied nitride coating material which could be deposited by both CVD and PVD. TiN coatings were widely used for wear protection films due to the high hardness (2000 to 2300 kg/mm² on average) and chemical stability, and for decorative films due to their golden colour. The hardness of TiN coatings was a function of the N/Ti ratio in the coating, and the highest was achieved⁽¹⁰⁸⁾ when the N/Ti ratio was close to 0.6. Titanium carbide was also the most studied hard coating material. The hardness of TiC coating was in general higher (2500 to 3000 kg/mm²) than that of TiN coating due to the more pronounced covalent bonding⁽¹⁰⁹⁾. Apart from the high hardness, TiC coating also possesses fine single phase microstructures and a low coefficient of friction and therefore is generally considered as a wear resistant material. At the present, even through many groups of other binary nitride, carbide, and boride coatings have been developed, TiN and TiC coatings are still widely used in industrial applications.

3.8.1.2 The second generation of hard coatings

In many wear applications, the tribology components are often imposed in terms of severe constraining, bending, and sliding which cause the coating to fail due to the demands of both hardness and toughness of the coatings, as well as the adherence between coating and substrate. In cutting applications, for example, very high forces and high temperature develop in the vicinity of the cutting tip or edge^(110,111). Because of the high temperature at the cutting edge, TiN coating starts to oxidize at 500°C⁽¹¹²⁾, and the TiO₂ is formed. As the TiO₂ is sheared off immediately by the mechanical motion of the chip, the substrate is exposed resulting in further heating, oxidation and wear⁽¹¹³⁾. When the temperature increases above 400°C, the hardness of the TiC coating decreases rapidly due to the formation of TiO₂⁽¹¹⁴⁾ resulting in porosity and cracks.

The second generation of hard coatings was developed to meet the demand for hardness and toughness of the coating, as well as to cope with the adherence between coating and substrate. This type of coating consists of multi-component materials which can be produced in two ways⁽¹¹⁵⁾.

One is to substitute the metal lattice of the binary metal based compounds with another metal element to form solid solutions resulting in strengthening and optimising of the properties of the hard coatings. In TiN compounds for example, the lattice of titanium can be partially replaced by Al, or Nb to form TiAlN or TiNbN hard coatings^(116,117,118) which enormously improve the high temperature oxidation resistance and the wear resistance as compared with TiN films.

Another is to vary the concentration of the non-metallic elements to change the valence electron concentration (VEC) which results in a change of mechanical and physical properties. Hardness, for example, is a function of the VEC as shown in fig 3.8.1⁽⁹⁶⁾.

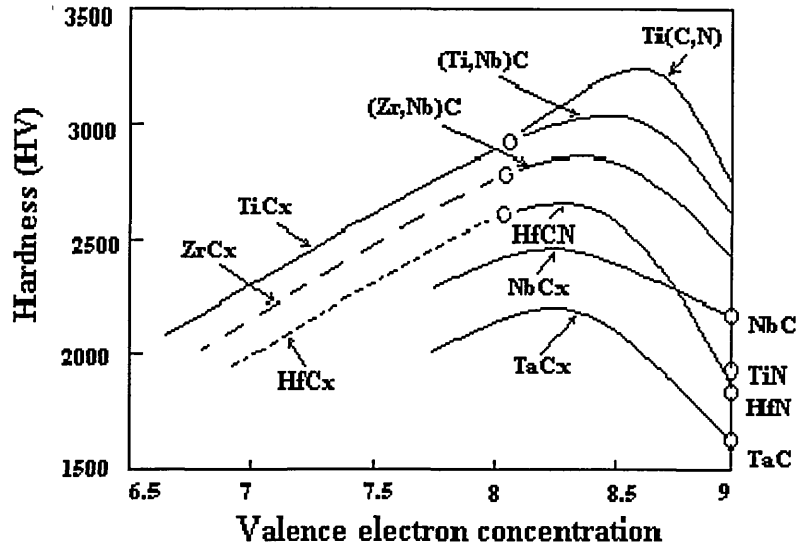


Fig 3.8.1 Hardness as a function of VEC

In general, hardness tends to be the maximum when VEC is about 8.4 to 8.5. The ternary TiCN coating is an example which shows physical properties superior to either TiN or TiC binary hard coatings. Many techniques have been developed to produce TiCN coatings. C ion implantation on the PVD TiN coating⁽¹¹⁹⁾ was used to produce a TiCN top layer which reduced the friction coefficient of the coating and reduced fretting wear damage. Plasma assisted CVD⁽¹²⁰⁾ was used to deposit TiCN coatings in the temperature range less than 450 °C. The arc process was applied⁽¹²¹⁾ to form TiC and TiCN coatings. In this work acetylene was used as the carbon containing gas and the titanium reacted with carbon at a temperature of approximately 500 °C. The pure TiC coating tended to spall because of the high internal compressive stress. The TiCN coating, however, had less internal stress and therefore good adhesion between coating and substrate could be obtained. High precision bearings were deposited with multi-layer (TiC, TiCN, TiN) coatings using the CVD process⁽¹²²⁾. The coated samples showed no trace of wear after 1000 hours operating while the un-coated samples were observed to have obvious wear traces. The interface composition of TiN and TiCN hard coatings on high speed steel was investigated⁽¹²³⁾. As acetylene was used as the carbon containing source, the hydrogen atoms and ions could react with oxygen at the interface to produce H₂O

which was desorbed from the surface at temperatures below 400 K. The TiCN coatings had better adhesion ($L_c = 50$ N) than the TiN coating ($L_c = 40$ N) since there was less oxygen intensity at the interface. The arc evaporation technique was used⁽¹²⁴⁾ to study the TiCN coatings. It could be seen from this research that the composition of TiCN coatings was dependent on the $CH_4:N_2$ ratio and the total pressure in the coating chamber. The composition and microstructure of TiCN and TiN coatings were investigated⁽¹²⁵⁾. These coatings consisted of NaCl type single phase with very fine and dense microstructure. The microhardness of TiCN coated specimens was significantly harder (Hv 1000 more) than that of TiN coated samples. Thus the TiCN coatings, as discussed above, could be used in the wear resistant applications.

3.8.1.3 The third generation of hard coatings

At present considerations have been made to develop the third generation (multilayer or superlattice) of hard coatings. These coatings can be produced as two types: metal/ceramic multilayers such as Ti/TiN, and ceramic/ceramic multilayers such as TiN/NbN.

The quality of structure strengthening for the multilayered coatings can be attributed to three parameters⁽¹²⁶⁾: sharpness of the interface, period length (Λ) in the direction normal to the layers, and refining effect of the grains. In a multilayered situation, the three parameters are related each other. The flow stress of the coating materials depends on the thickness of each layer, sharpness of interface boundaries, and flow stress of individual layers⁽¹¹⁵⁾. The grain refining effect is caused by breaks in the growth and nucleation process when the deposition changes from one layer to another according to Wulff's law⁽¹²⁷⁾

$$\gamma/h = \text{constant} \text{-----} 3.8.1$$

3.8.2 Ti₂N coatings

Stoichiometric hard titanium nitride films have been used for many years as decorative, wear and corrosion resistant layers on a wide range of components. The reason is that titanium nitride is very stable over a large composition range⁽¹³³⁾. Toth uses a phase diagram Fig 3.8.3⁽¹³³⁾ to explain the phase compositions of Ti-N system. The TiN phase includes the stoichiometric composition, and a broad composition range extending from about 30 to over 50 at % N. The α Ti(N) phase also occupies a large composition range distributing from 0 to about 20 at % N. The pure ϵ Ti₂N phase, however, is only located at a very narrow composition range about 33 at % N. This special composition range for ϵ Ti₂N phase has been reviewed by Wriedt⁽¹³⁴⁾ who pointed out that the probable composition range of Ti₂N is between 31 and 33 at % N, while N rich and N deficient Ti₂N coexist with δ TiN and α Ti(N) respectively.

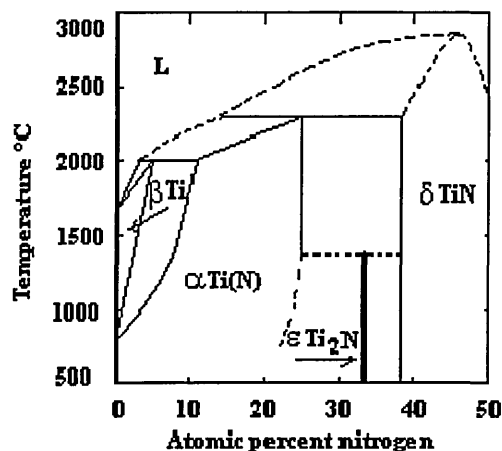


Fig 3.8.3 Phase diagram of Ti-N system

It is often difficult to produce pure Ti₂N films because the concentration of nitrogen critically influences the formation of a single ϵ Ti₂N phase. In a process of sputtering depositing Ti-N films for example, the nitrogen partial pressure affects the nitrogen concentration of the film in two different stages as shown in fig 3.8.4, which refers

to Sundgren⁽¹³⁵⁾. The concentration range for the Ti₂N films is located at the first stage in which any small change in nitrogen partial pressure will result in a large change of nitrogen concentration in the film. If the partial pressure can not be accurately controlled in a PVD process, there is less chance of developing the Ti₂N phase.

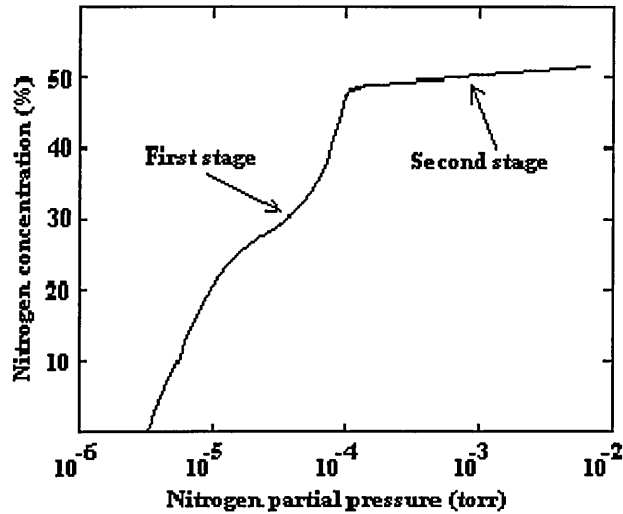


Fig 3.8.4 Nitrogen concentration dependence on N₂ partial pressure

In the PVD coating process, the development of phase composition of the film is determined by the combined parameters. Matthews⁽¹³⁶⁾ used an assisted ion plating technique to investigate the Ti-N compounds and found that a certain ionisation efficiency (>0.6%) was necessary to develop the Ti₂N phase. Molarius^(137,138) found that a low deposition rate a_D (about 0.25nm/s) is beneficial for producing Ti₂N films. Poulek⁽¹³⁹⁾ applied a combined parameter, S_E , to control the growth of the Ti₂N phase. The S_E is defined as

$$S_E = \left(\frac{I_s U_s}{a_D} \right) T_s \text{-----} 3.8.2$$

where I_s , U_s and T_s are substrate current, voltage and temperature. a_D is the deposition rate. This parameter represents the energy delivered to the growing film.

It arises in the case when $S_E \geq S_t$, where S_t is the threshold energy (10^6J/cm^3) under the condition of $T_s = 820\text{K}$ in order to stimulate the growth of Ti_2N film. Czerwiec⁽¹⁴⁰⁾ investigated Ti-N films using diode sputtering and found that the development of phase composition is a function of both the ratio of nitrogen gas flow/working gas flow and the distance from substrate to the sputtering target. Stappen⁽¹⁴¹⁾ concluded that a higher substrate temperature ($T_s \geq 500^\circ\text{C}$) is essential for depositing Ti_2N films. Investigation of substrate temperature (T_s) and deposition rate (a_D) was made by Poulek and co-workers⁽¹⁴²⁾ as shown in fig 3.8.5 in which the T_s is a function of the a_D . The ϵ Ti_2N phase only appears in the area in which a certain temperature has to be attained with an upper limitation of the deposition rate.

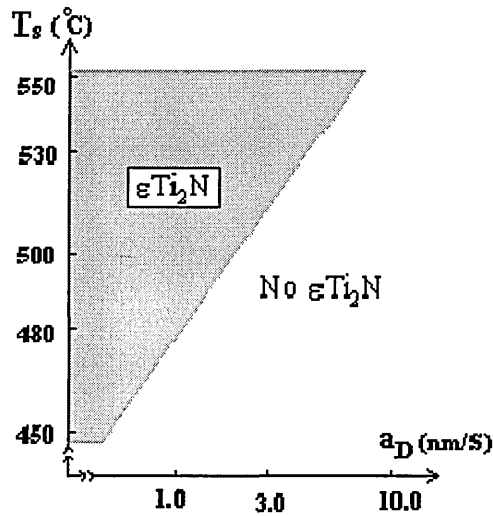


Fig 3.8.5 T_s dependence on a_D

In a PVD process, the parameters mentioned above for growth of $\epsilon\text{Ti}_2\text{N}$ films are often cross related. The condition used for one kind of process can not simply be applied to another kind of process. Ahern⁽¹⁴³⁾ found that Ti_2N phase developed at a higher deposition rate (up to $0.25 \mu\text{m/min}$) and lower substrate temperature (less than 350°C), which is the opposite of Poulek's result. Musil and co-workers⁽¹⁴⁴⁾ investigated the deposition of under-stoichiometric TiN_x films using a magnetron

sputtering technique and found that the transition from $\alpha\text{Ti(N)}$ phase to the δTiN_x is direct, without an $\epsilon\text{Ti}_2\text{N}$ phase and this case may be due to that they missed the right composition under their deposition conditions. In fact the development of $\epsilon\text{Ti}_2\text{N}$ phase in the growing film is cross-affected by the deposition process parameters, such as temperature, ion density around the growing film, and the geometry of the target and substrate system.

The reported properties of films containing Ti_2N phase are often conflict in the value over a wide range. Both enhanced hardness^(145,146,147,148) and reduced hardness^(149,150) due to the occurrence of Ti_2N phase have been reported. Table 3.8.2 gives the hardness values of films containing $\text{Ti}_2\text{N} + \text{TiN}$ phases as well as TiN phase from the references. As the reported values have been derived from different processes, there is no obvious relation between the highest hardness and the Ti_2N phase. As Sundgren⁽¹⁵¹⁾ has pointed out, high hardness is mainly caused by specific microstructures that can develop rather than by the Ti_2N phase itself.

Table 3.8.2 Hardness of the films containing different phases

	Film phase		References
	$\text{Ti}_2\text{N} + \text{TiN}$	TiN	
Hardness (kg/mm^2)	1300 - 2800	340 - 1900	Nakamura ⁽¹⁵²⁾
	2000 - 2300	1700 - 2200	Sato ⁽¹⁵³⁾
	2500 - 2800	625 - 1200	Jacobsson ⁽¹⁵⁴⁾
	2000 - 2800	1200 - 2000	Yoshihara ⁽¹⁵⁵⁾
	2500	1800	Matthews ⁽¹⁵⁶⁾
	1700	1700 - 2200	Sundgren ⁽¹⁵⁷⁾
	3000	2500	Ikeda ⁽¹⁵⁸⁾
	1500 - 1700	2200	Poulek ⁽¹⁵⁹⁾
	4500	1800 - 3500	Roth ⁽¹⁶⁰⁾

It is very common that the reported films containing Ti_2N phase^(143,155,161) are mainly of multi-phase composition, $\text{Ti}+\text{Ti}_2\text{N}$, $\text{Ti}+\text{Ti}_2\text{N}+\text{TiN}$, or $\text{Ti}_2\text{N}+\text{TiN}$. Although stoichiometric or close to stoichiometric titanium nitride films are most

commonly used for wear resistant coatings on cutting tools to extend their life time, Substoichiometric TiN films containing Ti_2N phase may be also the candidate used for the wear and the corrosion resistant Ikeda⁽¹⁵⁸⁾ claimed that multi-phase composition titanium nitride films containing Ti_2N phase have superior wear resistance characteristics, i.e., the flank wear of TiN coated cutting tools was more than 0.1mm after 10 minutes cutting performance whilst that of the Ti_2N coated tools was less than 0.05 mm using the same cutting condition. Poulek reported⁽¹⁴²⁾ that film containing Ti_2N phase have a very smooth surface as examined the coating surface morphology using electron microscopy and Stappen⁽¹⁴¹⁾ reported that the Ti_2N film has lower stress as the positions of X-ray diffraction peaks from the film are very close to the tabulated values referred to JCPDS file and good adherence as critical load (L_c) was more than 40 N using scratch test.

In general, Ti-N films containing the Ti_2N phase have composition from 20 to 33 at % N, but the single Ti_2N phase is present in only at composition of approximately 33 at % N⁽¹⁵⁷⁾. In fact, the structure of Ti_2N coatings is critically dependent on the growth conditions^(142, 143, 147, 161, 162) which cause the poor control of process parameters and insufficient reproducibility.

3.9 Summary of this chapter

The basic principles and properties related to glow discharge plasma, the unbalanced magnetron sputtering deposition process and the film growing have been discussed in this chapter. The literature survey also details the first, second, and third generation of coatings. The statistics of the deposited films containing Ti_2N phase have given in this chapter and the problems connected with depositing Ti_2N films have been discussed

References

- (1) B. Chapman, "Glow Discharge Processes", John Wiley & Sons, (1980) 79
- (2) F. I. Boley, "Plasma-Laboratory and Cosmic", D. Van Nostrand Company, INC. (1966)64
- (3) R.W. Berry, P.M. Hall, and M.T. Harris, "Thin Film Technology", Van Nostrand Reinhold Company New York, 1968
- (4) B. Chapman, "Glow Discharge Processes", John Wiley & Sons, (1980) 95
- (5) I.G. Brown, X. Godechot, IEEE Trans. Plasma. Science, V19(1991)715
- (6) R. L. Boxman, S. Goldsmith, Surface and Coating Technology, V52(1992)39
- (7) J. E. Daalder, Journal of Physics, D: V9(1976)2379
- (8) C. N. Tai, E. S. Koh, K. Ahari, Surface and Coating Technology, V43/44(1990)324
- (9) S. Ramalingam, U.S. Patent # 4763477, 1987
- (10) J. R. Morrison, U.S. Patent # 4724058, 1988
- (11) W.R. Grove, Phil. Trans. Roy. Soc. London, V142 (1852)87
- (12) R. Behrisch, Sputtering by Particle Bombardment I, Springer-Verlag Berlin Heidelberg New York 1981
- (13) J.H. Freeman: In Ion Implantation ed. By G. Dearnaley, J.H. Freeman, R.S. Nelson, J.Stephen (North-Holland, Amsterdam 1973)P.225
- (14) R.V. Stuart and G.K. Wehner, J. Appl. Phys. V33, (1962)2345
- (15) M. Konuma, Film Deposition by Plasma Techniques, Springer-Verlag (1992)111
- (16) B. Chapman, "Glow Discharge Processes", John Wiley & Sons, (1980) 181
- (17) C.R. Weissmantel, Deposition of Metastable Films by Ion Beam and Plasma Techniques, Proc. 9th Int. Vacuum Congress and 5th int. Conf. On Solid Surface (Madrid), 26 Sept-1 Oct (1983)229
- (18) B. Bhushan and B.K. Gupta, Handbook of Tribology (Materials, Coating, and Surface Treatments),McGRAW-HILL, INC.(1991)9.59
- (19) J.L. Vossen and J.J. Cuomo, Glow Discgarge Sputtering Deposition, Thin Film Process, J.L. Vossen anf W. Kern, ed., Academic Press (1978)12
- (20) B. Chapman, "Glow Discharge Processes", John Wiley & Sons, (1980) 209
- (21) B.J. Stocker, Journal of Applied Physics, V32 (1961)465
- (22) T.C. Tisone and J.B. Bindell, Journal of Vacuum Science Technology, V11 (1974) 519
- (23) S.L. Rohde, S.A. Barnett and C.H. Choi, Journal of Vacuum Science Technology, A7 (1989)2273
- (24) J.M. Molarius, A.S. Korhonen, E.O. Ristolainen, J. Vac. Sci. Technol. A3(6) (1985)2419
- (25) F.M. Penning, Physica, V3 (1936)873
- (26) R.K. Waits, Journal of Vacuum Science Technology, V15 (1978)179
- (27) S. Swann, Journal of Vacuum Science Technology, A5 (1987)1750
- (28) J.J. Cuomo and S.M. Rossnagel, Journal of Vacuum Science Technology, A4 (1986)393
- (29) P.S. Mcleod and L.D. Hartsough, Journal of Vacuum Science Technology, V14 (1977)263

- (30) J. Almeida, Vacuum, V39 (1989)717
- (31) J.A. Thornton and A.S. Penfold, Journal of Vacuum Science Technology, V15 (1978)171
- (32) M. Konuma, Film Deposition by Plasma Techniques, Springer Verlag Berlin Heidelberg, (1992)133
- (33) S. Kadlec, J. Musil, W.-D. Münz, G. Hakansson, and J.-E. Sundgren, Surface & Coating Technology, V39/40 (1989)487-497
- (34) I. Petrov, L. Hultman, U. Helmersson, J.-E. Sundgren, and J.E. Green, Thin Solid Films, V169 (1989)299
- (35) J.-E. Sundgren and H.T.G. Hentzell, J. Vac. Sci. Technol. A4(5) (1986)2259
- (36) B. Window and N. Savvides, Journal of Vacuum Science and Technology, A4 (1986)196
- (37) B. Window and N. Savvides, Journal of Vacuum Science and Technology, A4 (1986)453
- (38) N. Savvides and B. Window, Journal of Vacuum Science and Technology, A4 (1986)504
- (39) B. Window and G.L. Harding, Journal of Vacuum Science and Technology, A8 (1990)1277
- (40) J.E. Greene, S.A. Barnett, J.-E. Sundgren and A. Rockett, in Ion Beam Assisted Film Growth, edited by T. Itoh (Elsevier, Amsterdam, 1988), Chap. 5
- (41) S.L. Rohde, I. Petrov, W.D. Sproul, S.A. Barnett, P.J. Rudnik and M.E. Graham, Thin Solid Films, V193/194 (1990)117
- (42) S. Schiller, E. Beister, J. Reschke and G. Hoelzsch, J. Vac. Sci. Technol., VA5(1987)2188
- (43) W.-D. Münz, J. Vac. Sci. Technol., VA4(1986)2717
- (44) W.D. Sproul, P.J. Rudnik, M.E. Graham and S.L. Rohde, Surface and Coatings Technology, V43/44(1990)270-278
- (45) W.-D. Münz, F.J.M. Hauzer, D. Schulze and B. Buil, Surface and Coatings Technology, V49/44(1991)161-167
- (46) W.-D. Münz, D. Schulze and F.J.M. Hauzer, Surface and Coatings Technology, V50(1992)169-178
- (47) W.D. Sproul, P.J. Rudnik, M.E. Graham and S.L. Rohde, Surface and Coating Technology, V43/44 (1990)117
- (48) S.L. Rohde, L. Hultman, M.S. Wong and W.D. Sproul, Surface and Coating Technology, V50 (1992)255
- (49) D.G. Teer, Surface and Coating Technology, V35 (1988)901
- (50) D.G. Teer, Surface and Coating Technology, V39/40 (1989)565
- (51) S. Kadlec, J. Musil, V. ValVoda, W.-D. Münz, H. Petersein and J. Schroeder, Vacuum, V41 (1990)2233
- (52) W.D. Sproul, P.J. Rudnik, M.E. Graham and S.L. Rohde, Surface and Coating Technology, V43/44 (1990)270
- (53) W.-D. Münz, Surface and Coating Technology, V48 (1991)81
- (54) W. Fleischer, D. Schulze, R. Wilberg, A. Lunk and F. Schrade, Thin Solid Films, V63 (1979)347
- (55) U. König, Surface and Coating Technology, V33 (1987)91
- (56) L. Hultman, W.-D. Münz, J. Musil, S. Kadlec, I. Petrov and J.E. Greene, Journal of Vacuum Science Technology, A9 (1991)434

- (57) M.H. Francombe and J.L. Vossen, "Physics of Thin Films", V14 (1989)3
- (58) W.D. Sproul, P.J. Rudnik and C.A. Gogol, *Thin Solid Films*, V171 (1989)171
- (59) J.E. Sundgren, B.O. Johansson and S.E. Karlsson, *Thin Solid films*, V105 (1983)353
- (60) W.D. Sproul, *Surface and Coating Technology*, V33 (1987)73
- (61) A.J. Aronson, D. Chen and W.H. Class, *Thin Solid Films*, V72 (1980)535
- (62) J. Musil, S. Kadlec, J. Vyskocil and V. Poulek, *Surface and Coating Technology*, V39/40 (1989)301
- (63) T. Serikawa and A. Okamoto, *Thin Solid Films*, V101 (1983)1
- (64) E. Bauer and H. Poppa, *Thin Solid Films*, V 12 (1972)167
- (65) D.W. Pashley, M.J. Stowell, M.H. Jacobs and T.J. Law, *Philosophical Magazine*, V10 (1964)127
- (66) M. Prutton, *Surface Physics*, Oxford University Press, (1983)104
- (67) G. Hass and R.E. Thun, *Physics of Thin Films*, Academic Press, New York and London V4 (1967)
- (68) P. Ding, Z. Ni, S. Zhou and F. Pan, *Surface and Coating Technology*, V49 (1991)203
- (69) A. Zangwill, *Physics at Surface*, Cambridge University Press, 1988
- (70) E. Bauer and H. Poppa, *Thin Solid Films*, V12 (1972)167
- (71) B.A. Movchan and A.V. Demshishin, *Fiz. Metal. Metalloved.* V28 (1969)653
- (72) J.A. Thornton, *Journal of Vacuum Science Technology*, V11 (1974) 666
- (73) R. Messier, A.P. Giri and A. Roy, *Journal of Vacuum Science Technology*, A2 (1984) 500
- (74) H.A. Macleod, *Journal of Vacuum Science Technology*, A4 (1986)418
- (75) *Thin Solid Films*, V57 (1979)173
- (76) K.H. Müller, *Journal of Applied Physics*, V58 (1985)2573
- (77) P.J. Martin, R.P. Netterfield and W.G. Sainy, *Journal of Applied Physics*, V55 (1984)235
- (78) K.H. Guenther and K.H. Müller, *Journal of Vacuum Science Technology*, A7 (1989)1436
- (79) E.O. Hall, *Proc. Phys. Soc. London*, V643 (1951)747
- (80) N.J. Petch, *J. Iron Steel Inst. London*, V173 (1953)25
- (81) J.E. Sundgren and H.T.G. Hentzell, *Journal of Vacuum Science Technology*, A4 (1986)2259
- (82) E.A. Almond, *Vacuum*, V34 (1984)835
- (83) H. Holleck, *Journal of Vacuum Science Technology*, A4 (1986)2661
- (84) B. Kramer, *Thin Solid Films*, V108 (1983)117
- (85) D.S. Rickerby, G. Eckold, K.T. Scott, and A.M.B. Golder, *Thin Solid Films*, V154 (1987)125
- (86) D.S. Rickerby, *Journal of Vacuum Science Technology*, A4 (1986)2809
- (87) O. Knotek, R. Elsing, G. Kramer, F. Jungblut, *Surface and Coating Technology*, V46 (1991)265
- (88) D.W. Hoffman and J.A. Thornton, *Thin Solid Films*, V40 (1977)355
- (89) D.W. Hoffman and J.A. Thornton, *Journal of Vacuum Science Technology*, V16 (1979)134
- (90) D.W. Hoffman and J.A. Thornton, *Thin Solid Films*, V40 (1977)355
- (91) J.F. Nye, *Physical Properties of Crystals*, Clarendon Press, Oxford (1985)

- (92) J.A. Thornton and D.W. Hoffman, *Thin Solid Films*, V171 (1989)5
- (93) K. Holmberg, *Surf. and Coat. Technol.*, 56 (1992) 1
- (94) A. Leyland, K.S. Francey and A. Matthews, *Surface Engineering*, V7 (1991)207
- (95) L.E. Toth, *Transition Metal Carbides and Nitrides*, Academic Press New York, 1971
- (96) H. Holleck, *Journal of Vacuum Science Technology*, A4 (1986)2661
- (97) W.D. Sproul, *Thin Solid Films*, V107 (1983)
- (98) B.E. Jacobsson, R. Nimmagadda and R.F. Bunshah, *Thin Solid Films*, V63 (1979)333
- (99) J.E. Sundgren, *Thin Solid Films*, V128 (1985)21
- (100) W.D. Sproul, P. J. Rudnik, M.E. Graham, *Surf. and Coat. Technol.*, 39 (1989) 355
- (101) Y. Sun, T. Bell, *Mater. Sci. and Eng.*, A140 (1991) 419
- (102) M. Ives, J. Cawley, J.S. Brooks, *Surf. and Coat. Technol.* 61 (1993) 127
- (103) B.E. Jacobsson, R.F. Bunshah and R. Nimmagadda, *Thin Solid Films*, V54 (1978)107
- (104) R.F. Bunshah and A.C. Raghuram, *Journal of Vacuum Science Technology*, V9 (1972)1385
- (105) I.T. Ritchie, *Thin Solid Films*, 73 (1980) 65
- (106) H.M. Gabriel, K.H. Kloos, *Thin Solid Films*, 118 (1984) 223
- (107) K. Upadhya, *Mater. Sci. and Eng.*, A140 (1991) 549
- (108) O. Johansson, J.E. Sundgren, J.E. Green, A. Rockett, and S.A. Barnett, *J. Vac. Sci. Technol.*, A3 (1985)303
- (109) J.E. Sundgren and H.T.G. Hentzell, *J. Vac. Sci. Technol.*, A4 (1986) 2259
- (110) E.A. Almond, *Vacuum*, V34 (1984)835
- (111) B. Kramer, *Thin Solid Films* V108 (1983)117
- (112) M.V. Stappen, L.M. Stals, M. Kerkhofs and C. Quaeys, *Surface and Coating Technology*, V74/75 (1995)629
- (113) J.M. Molarius, A.S. Korhonen, E. Harju and R. Lappalainen, *Surface and Coating Technology*, V33 (1987)111
- (114) M. Tamura and H. Kubo, *Surf. and Coat. Technol.*, 49 (1991)194
- (115) C. Subramanian and K.N. Strafford, *Wear*, V165 (1993)85
- (116) J.R. Roos, J.P. Celis, E. Vancoille, H. Veltrop, S. Boelens, F. Jungblut, J. Ebberink and H. Homberg, *Thin Solid Films*, V193/194(1990)547
- (117) W.-D. Münz, *Werkstoffe und Korrosion*, V41, (1990)753
- (118) W.-D. Münz, T. Hurkmans, G. Keiren, and T. Trinh, *Journal of Vacuum Science & Technology*, A11, (1993)2583
- (119) J.R. Roos, J.P. Celis, M. Franck, and H. Pattyn, *Surf. and Coat. Technol.* , V45 (1991)89
- (120) K.T. Rie, A. Gebauer, *Mater. Sci. and Eng.*, A139 (1991) 61
- (121) O. Knotek, F. Loeffler, and G. Kraemer, *Vacuum* V43 (1992) 645
- (122) C.H. Zhong, P.Z. Xian, L.J. Zhong, T.H. Huei, S.X. Kun, and F.Y. Wen, *ASTM Special Technical Publication N1195* (1993) 71, Publ. by ASTM Philadelphia, PA, USA
- (123) E. Roman, J.L. Desegovia, A. Alberdi, G. Calvo, and J. Laucirica, *Mater. Sci. and Eng.*, A163 (1993) 197

- (124) E. Damond, and P. Jacquot, *Mater. Sci. and Eng.*, A140 (1991) 838
- (125) R. Bertoncello, A. Casagrande, M. Casarin, A. Glisenti, E. Lanzoni, L. Mirengi, and E. Tondello, *Surface and Interface Analysis*, V18 (1992)525
- (126) Xue Zengquan, Wu Quande and Li Hao, *Thin Film Physics (in Chinese)*, Electronic Industrial Publisher, (1991)208
- (127) R.F. Huang, L.S. Wen, L.P. Guo, J. Gong, B.H. Yu and H. Bangert, *Surface and Coating Technology*, V50 (1992)97
- (128) Z. Renji, L. Ziwei, C. Zhouping and S. Qi, *Wear*, V147 (1991)227
- (129) U. Helmesson, S. Todorova, S.A. Barnett, J.-E. Sundgren, L.C. Markert and J.E. Greene, *Journal of Applied Physics*, V62 (1987)481
- (130) P.B. Mirkarimi, L. Hultman and S.A. Barnett, *Applied Physics Letters*, V57 (1990)2654
- (131) M. Shinn, L. Hultman and S.A. Barnett, *J. Mater. Res.*, V7 (1992)901
- (132) Data Sheet from Balzers, Balzers Verschleibschutz GmbH, Am Ockenheimer Graben 41, D-55411 Bingen
- (133) L.E. Toth, *Transition Metal Carbides and Nitrides*, Academic Press, New York, 1971
- (134) H.A. Wriedt and J.L. Murray, *Bulletin of Alloy Phase Diagrams*, V. 8 (1987)378
- (135) J.-E. Sundgren, B.-O. Johansson and S.-E. Karlsson, *Thin Solid Films*, V105 (1983)353
- (136) A. Matthews and D.G. Teer, *Thin Solid Films*, V72(1980)541
- (137) J.M. Molarius, A.S. Korhonen and E.O. Ristolainen, *Journal of Vacuum Science Technology*, A4 (1986)2686 A3 (1985)2419
- (138) J.M. Molarius, A.S. Korhonen, H. Kankaanpaa and M.S. Sulonen, *Journal of Vacuum Science Technology*, A4 (1986)2686
- (139) V. Poulek, J. Musil, R. Cerny and R. Kuzel, *Thin Solid Films*, V170 (1989)L55
- (140) T. Czerwiec, M. Remy and H. Michel, *Instruments and Methods in Physics Research B37/38*(1989)701
- (141) M.V. Stappen, K.D. Bruyn, C. Quaeyhaegens, L. Stals, V. Poulek, *Surface & Coating Technology*, V74-75 (1995)143
- (142) V. Poulek, J. Musil, V. Valvoda and Dobiasova, *Materials Science and Engineering*, A140(1991)660
- (143) M. Ahern and M.S.J. Hashmi, *Surface and Coating Technology*, V50(1992)249
- (144) J. Musil, S. Kadlec, J. Vyskocil and V. Valvoda, *Thin Solid Films*, V167 (1988)107
- (145) B.E. Jacobson, R. Nimmagadda and R.F. Bunshah, *Thin Solid Films*, V63 (1979)333
- (146) H. Yoshihara and H. Mori, *Journal of Vacuum Science Technology*, V16 (1979)1007
- (147) T. Roth, E. Broszeit and K.H. Kloos, *Surface and Coating Technology*, V36 (1988)765
- (148) T. Ikeda and H. Satoh, *Thin Solid Films*, V159 (1991)99
- (149) G. Farges, J.C. Pivin and F. Pons, *Surface and Coating Technology*, V35 (1988)231
- (150) H. Wulff, A. Lunk and R. Basner, *Vacuum*, V41 (1990)2201

- (151) J.-E. Sundgren, Thin Solid Films, V128 (1985)21
- (152) K. Nakamura, K. Inagawa, K. Tsurvoka and S. Komiya, Thin Solid Films, V40 (1977)155
- (153) T. Sato, M. Tada, Y.C. Huang and H. Takei, Thin Solid Films, V54 (1978)61
- (154) B.E. Jacobsson, R. Nimmagadda and R.F. Bunshah, Thin Solid Films, V63 (1979)333
- (155) H. Yoshihara and H. Mori, J. Vac. Sci. Technol., V16(1979)1007
- (156) A. Matthews and D.G. Teer, Thin Solid Films, V73 (1980)367
- (157) J.-E. Sundgren, B.-O. Johansson, S.-E. Karlsson and H.T.G. Hentzell, Thin Solid Films, V105 (1983)367
- (158) T. Ikeda and H. Satoh, Thin Solid Films, V195(1991)99
- (159) V. Poulek, J. Musil, V. Valvoda and R. Cerny, Journal of Physics, D21 (1988)1657
- (160) T. Roth, E. Broszeit and K.H. Kloos, Surface and Coating Technology, V36 (1988)765
- (161) M. Kiuchi, K. Fujii, H. Miyamura, K. Kadono, M. Satou and F. Fujimoto, Nuclear Instruments and Methods in Physics Research B37/38 (1989)701
- (162) T. Czerwiec, M. Remy and H. Michel, Surf. Coat. Technol., V59 (1993)91

4. Experimental Techniques

4.1 Coating system

The HTC 1000-4 ABS industrial coating system⁽¹⁾ used for the study of the hard coating process is manufactured by Hauzer. This system has an octagonal cross section vacuum chamber (Fig 4.1.1) which consists of stainless steel (25 mm thick). Four cathodes are assembled orthogonally on two large chamber doors which can be opened from two sides to provide maximum accessibility to the interior, the targets and the substrate holders. The diagonal distance between cathodes is 1 m of which combined with the same chamber height gives a chamber capacity approximately 1 m³ with a load capacity of 500 kg. Each cathode is equipped with a water cooled copper plate which is connected to a target (600x190x12 mm³) to provide excellent thermal flux transmission from the target.

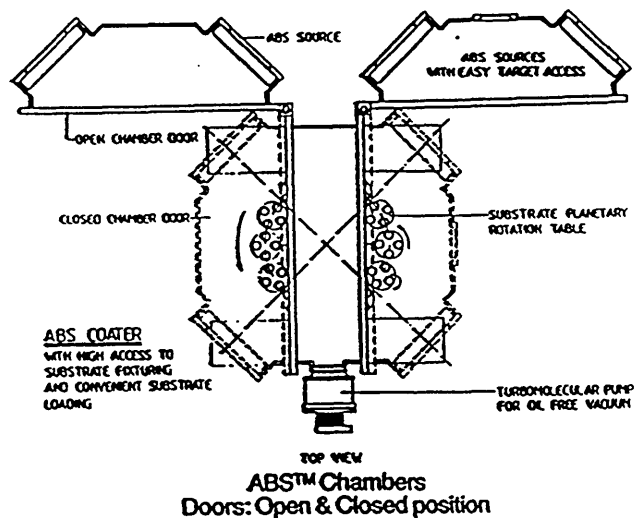


Fig 4.1.1 ABS coater chamber

The pumping instruments for this system are two Balzers TPH 2200 turbomolecular pumps with oil-lubricated bearing and inert-gas sealing, in combination with a roots pump with a pumping speed of 500 m³/h and a rotary-vane pump with a

pumping speed of 250 m³/h. The turbo-molecular pumps are flanged to the vacuum chamber with two 250 mm VAT high vacuum gate valves to allow the pumps to run at full speed even when the chamber is open. The nominal pumping speed of the turbo-molecular pumps is 4400 l/s to achieve a base pressure of 10⁻⁵ mbar with a leak rate less than 5x10⁻² Pa.l./s, and to keep a constant pressure of 10⁻³ mbar range during a reactive coating process in which a large amount of working gas and reactive gas is introduced into the chamber.

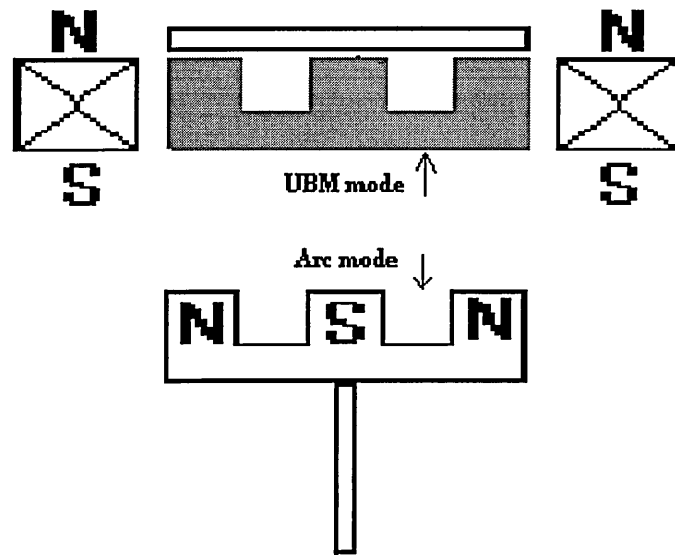


Fig 4.1.2 Magnetron movement for UBM and Arc mode

The cathode can accept powers of more than 10 W/cm² to provide an adequate deposition rate. SmCo is used as the permanent magnet material. The magnets are arranged to function as an unbalanced magnetron by reinforcing of the outer magnet poles. The degree of unbalance is made adjustable by electromagnets which are assembled surrounding each cathode with an electromagnetic coil (Fig 3.5.2) concentrically around each target outside the vacuum chamber to generate a magnetic field of up to 10,000 ampere turns. The geometry of the magnets for the four cathodes is designed as a close field to confine the plasma around the substrate leading to high bias current density (5 mA/cm²) even at a distance of up to 30cm^(1, 2)

away from the targets during a process. The UBM cathode can be converted to an arc mode by a suitable movement of the permanent magnets away from the target using compressed air as shown in Fig 4.1.2. The power supply of the target includes arc mode (high current-low voltage) which provides current /voltage values of 100A/80V, and magnetron mode (low current-high voltage) which supplies current/voltage values of 40A/750V. The maximum power for each target is 10KW.

The substrate holders (six or twelve) assembled as satellites on the turntable are designed to have three fold planetary rotations during a coating process. In general, small pieces such as drills go through three fold rotations, large pieces such as hob cutters run as two fold rotations. For even larger components such as casting molds, single rotation can be used. The turntable with its load of tools can be moved in or out of the chamber using a carriage to keep loading time as short as possible. The turntable and its substrate are directly linked to the bias voltage supply which provides up to -1200V for high voltage etching and 0 to 200V for coating processes. Four large internal radiant heaters give substrate heating up to 450 °C in one hour which combines with the powerful pumps of the ABS coating system to give a base pressure of 10^{-5} mbar with very low water vapour partial pressure a short time after loading the main chamber. In addition the heaters can be also used to control the substrate temperature precisely during a deposition process regardless of whether other process parameters change or not.

This system is controlled and monitored by a Mitsubishi SPS control unit which supervises all important switching and operating functions, interlocking and process sequences. During a deposition process, the nitrogen flow can be controlled by a P.I.D. (proportional integrating differential) control unit with feedback function using the total chamber pressure as the input variable measured by a Leybold Viscovac gauge. The chamber total pressure is also monitored from atmospheric to 1×10^{-1} mbar by a pirani gauge and from 1×10^{-1} mbar to 1×10^{-5} mbar by a Balzer's ion gauge. The gas flow is adjusted by piezo-electric valves and the gas purity (Ar or N₂) is 99.999%. Two thermocouples assembled on the rotating turntable are used to

monitor the substrate temperature. A differentially pumped Hiden quadrupole mass spectrometer residual gas analyser is used to monitor any gas partial pressure during a coating process.

4.2 Coating procedure

4.2.1 Sample preparation

The specimens chosen to be coated are flat M2 high speed steel and Austenitic stainless steel cylindrical disks (ϕ 30mm \times 10mm) and 6mm Presto high speed steel drill blanks and drills. The flat samples are mechanically finished to 1 μ m polish. The substrate cleaning procedure is shown in table 4.2.1

Table 4.2.1 Sample cleaning procedure

Step	Function	Medium	Temp. (°C)	Ultrasonic	Time (min)
1	Preliminary degreasing	2% HT107A+HT107B in tap water	60	Yes	3
2	Rinse	Tap water	RT	No	0.5
3	Acid etch	1.0% HT017 in tap water	RT	Yes	1
4	Rinse	Tap water	RT	No	0.5
5	Degreasing	2% Bannerclean 16 in tap water	70	Yes	3
6	Rinse	Tap water	RT	No	0.5
7	Final degreasing	2% Bannerclean 13 in tap water	70	Yes	3
8	Rinse	Tap water	RT	No	0.5
9	Rinse	De ionised water	RT	Yes	3
10	Final rinse	De ionised water	RT	No	1
11	Drying	Hot air dryer	100	No	5-10

Step 1 is used to clean up organic and inorganic contamination left on the sample from the initial mechanical preparation. Step 3 is used to clean the rust and oxidation off the sample (especially on high speed steel samples) and this step has to be carefully monitored to avoid over etching on the metal surface and pitting corrosion of high speed steel. Steps 5 and 7 are used to remove inorganic

The etching stage uses a steered arc to produce highly charged metal ions (Me^{+1} , Me^{+2} or Me^{+3}) which are implanted to the substrate surface due to a bias potential of up to -1200V. As there is a gradient rich titanium interface between substrate and coating the adherence is enormously improved⁽²⁾. The etching is also an effective clean process since contamination on the sample surface can be knocked off by the energetic ions.

The coating stage uses unbalanced magnetron sputtering mode. The time for deposition is dependent on the type of load, the rotation status of the substrate, the coating material, and the employment of target power. The typical deposition rate for titanium nitride is 2.5 μm /hour.

Finally the cooling stage takes about one and half hours to let the temperature down from 450 to 200°C.

4.3 X-ray Diffraction (XRD)

X-ray diffraction is used regularly in materials science to assist better understanding of crystal structures and orientations. Diffraction is a process by which an X-ray is scattered by a regular array of centres as shown in fig 4.3.1, such that reinforcement of the radiation takes place in very specific directions. The process is dependent on the symmetry of the scattered centres, their orientations and the wave length of the X-ray used.

Bragg regarded a crystal as consisting of a series of parallel planes of atoms. At a given angle θ , the scattering of all atoms in one plane may be shown to be in phase, giving constructive interference. This can apply to all planes separately. Taking two parallel planes as example, the path difference between incident beam I and diffraction beam II can be given as, $uv + vw = 2d\sin\theta$. The equation for the path

difference equal to $n\lambda$ for constructive interference is known as Bragg's law, which is expressed as

$$n\lambda = 2d\sin\theta \text{-----} 4.3.1$$

Where n is an integer, λ is the wave length of X-ray, and d is the interplanar space.

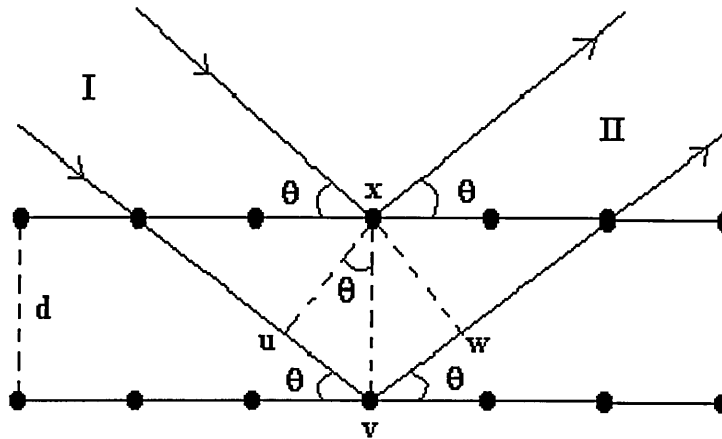


Fig 4.3.1 X-ray diffraction diagram

Many X-ray methods have been developed, such as the X-ray diffractometer, powder camera and flat plate camera. However the most commonly used method to analyse PVD films is the X-ray diffractometer, shown in fig 4.3.2. The diffractometer consists of a monochromatic X-ray source, a specimen table which sits at the centre of the diffractometer, and a counter used to detect the intensity of the diffraction beam. The X-ray source generates a monochromatic X-ray beam which radiates a flat sample supported by the specimen table. The specimen rotates on its axis by an angle θ while the diffracted beam is detected by the counter which is mechanically coupled to the table to rotate around the same axis by an angle of 2θ to maintain the Bragg condition. The result is a profile of the intensity of the X-ray counts as a function of diffraction angle 2θ . The profile is a series of peaks at positions and intensities characteristic of the unit cell of the specific phase which presents in the crystalline sample.

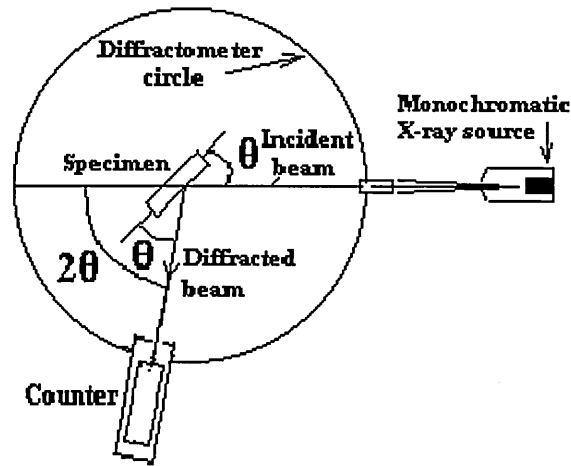


Fig 4.3.2 Diagram of X-ray diffractometer

The major uses of the diffractometer are determination of lattice parameters, crystal structure, lattice strain, grain size and preferred orientation, as well as identification of unknown phases or mixtures of phases.

The lattice parameter can be calculated from the Bragg law equation 4.3.1. Taking a cubic crystal as an example, the lattice parameter can be written as

$$a = d\sqrt{(h^2 + k^2 + l^2)} \text{----- 4.3.2}$$

The identification of unknown phases can be made using comparison with the powder diffraction file system⁽³⁾ in which any one powder pattern is classified in terms of inter-planar spacings (d) and relative intensities. A given crystalline substance always exhibits a characteristic diffraction pattern, i.e. a fingerprint of the substance to be identified. According to the Hanawalt method, each substance can be characterised by the d values of the three strongest lines, d₁, d₂, and d₃ for the first, second and third strongest line respectively. These together with their relative intensities are normally sufficient to characterise any compound.

The determination of preferred orientation can be made using calculations of texture by the inverse pole figure method. The preferred orientation is related to a specific axis which is perpendicular to the surface of the specimen. Under standard Bragg-Bretano conditions, diffraction takes place only from planes parallel to the surface of the specimen, when the specimen surface and counter are inclined at angles θ and 2θ respectively to the X-ray beam. In a powder specimen, the planes are randomly oriented, the characteristic of the phase is specified by the relative intensity of each reflection which is randomly oriented. In coatings however, the planes are not oriented at random. For example, TiN films can grow with either {111} or {110} planes preferred orientation. If the intensities are measured from the (hkl) reflections of the coating, its preferred orientation or texture can be determined using the inverse pole figure technique in which **P** can be expressed⁽⁴⁾ as

$$P = \frac{I_{hkl} / R_{hkl}}{\left[\frac{1}{n} \sum_0^n (I_{hkl} / R_{hkl}) \right]} \text{-----4.3.3}$$

Where I_{hkl} is the measured diffraction intensity corresponding to the (hkl) reflection, R_{hkl} is the diffracted intensity for the same reflection in a standard random specimen which can be obtained from the JCPDS files, and n is the numbers of reflection considered. If **P** exceeds unity, the (hkl) planes are oriented parallel to the surface more than in the random case. Therefore the preferred orientation can be estimated using this formula.

The determination of lattice strain and grain size can be made by measurement of strain broadening. The relationship among them can be expressed as⁽⁵⁾:

$$\frac{\beta \cos \theta}{\lambda} = \frac{1}{\epsilon} + \frac{4\sigma \sin \theta}{\lambda} \text{-----4.3.4}$$

Where β is the true broadening, λ is wave-length of X ray, ϵ is the grain size, σ is the lattice strain, and 2θ is the angle of diffraction peak. Broadening measurements

are made from the peak profiles. The true broadening β is determined from the observed broadening B , and instrumental broadening b , by the following relationship:

$$\beta = \sqrt{(B-b)\sqrt{(B^2 - b^2)}} \text{-----4.3.5}$$

Instrumental broadening was determined using a silicon standard.

4.4 Scanning Electron Microscope (SEM)

The SEM is a very common tool used for examination of a wide range of coating characteristics. In general a SEM consists of 6 components: electron gun, vacuum pumps, electromagnetic lenses, scan coil and scan generator, sample chamber and display screen (CRT) as shown in fig 4.4.1.

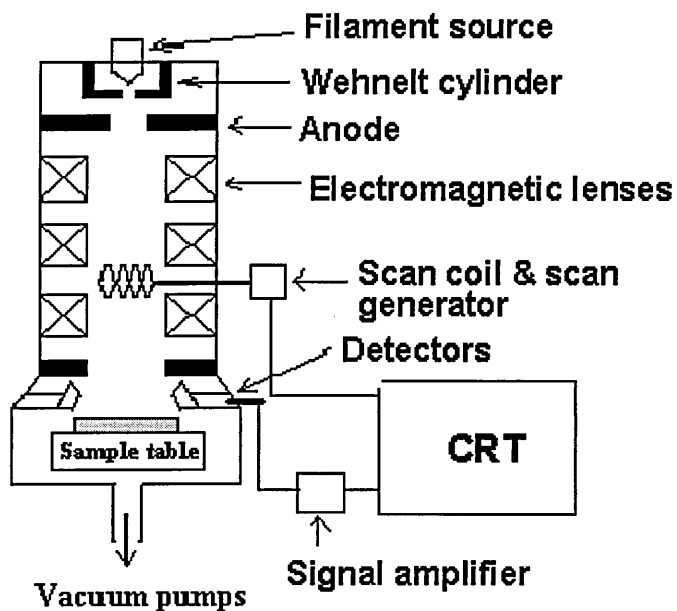


Fig 4.4.1 Diagram of scanning electron microscope

The electron gun is usually a tungsten filament, heated to 2,700 °C during operation, which emits electrons which are accelerated towards the anode by a high positive potential from 1 to 50 kV. The electron beam is primarily focused using a Wehnelt cylinder which is applied a small negative bias voltage to give a source (typically 50 µm in diameter) of electrons for the microscope.

The electromagnetic lenses demagnify the source of electrons to spot sizes from 4 nm to 1 µm based on the applied magnification. A pair of deflector coils scan the focused electron spot across the sample surface to form a raster. The electron spot on the display monitor, cathode ray tube (CRT) is scanned in synchronisation with the electron spot on the sample surface. Electrons from a point of the sample surface are collected by a detector, the signal from which is sent to the grid of the CRT, so that the signal from the sample surface controls the brightness of the electron spot on the CRT. Since the contrast on the sample surface varies from point to point, an image of the surface is produced on the CRT. The image from the CRT is taken point by point using a camera. The typical magnification ranges for SEM are 100 to 300,000. The magnification of the image can be calculated as

$$\text{Magnification} = \frac{\text{Side length of CRT}}{\text{Side length of raster on sample}} \text{----- 4.4.1}$$

The most commonly utilised signal interaction between the electrons and the sample surface in a SEM are secondary electrons, back-scattered electrons, and characteristic X-rays, as shown in fig 4.4.2.

The ejection of secondary electrons results from collisions between the loosely bonded outer electrons of the atoms in the sample and the incident electron beam. Secondary electron images give the topographic contrast which arises from local variation in both surface tilt and relief on the sample surface, resulting in corresponding point to point variations in the electron signal.

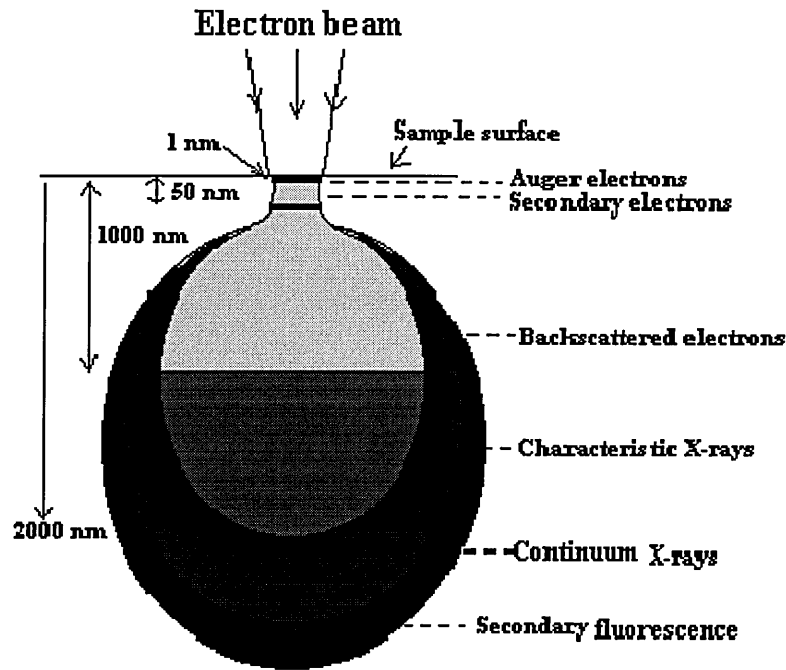


Fig 4.4.2 Interaction between electrons and specimen

Backscattered electrons are reflected electrons from the incident electron beam. The number of electrons reflected from the sample surface is a function of both its atomic number and orientation with respect to the electron beam, which gives atomic number and topographical contrast respectively. A atomic number contrast enables phase with different compositions to be imaged on the sample surface. Regions of higher atomic number show brighter whilst those of lower atomic number appear darker.

4.5 Glow Discharge Optical Emission Spectrometer (GDOES)

A GDOES consists of a glow discharge source and an optical spectrometer as shown in fig 4.5.1. The glow discharge source is a cathode and anode system operating under vacuum condition. The cathode is made by a flat sample with a size of more

than 4 mm in diameter. The anode is a hollow cylindrical metal tube. When a potential exists between cathode and anode under a controlled low argon pressure in a vacuum environment, uniform glow discharge sputtering on the sample surface, and the excitation and ionisation of the sputtered atoms in the glow discharge tube can be obtained. An enhanced optical emission is subsequently produced whilst the sputtered atoms return to their ground state from a state of excitation and ionisation. The wave-lengths of the emitted photons provide fingerprint information about the elements present within the sample and the intensity of the related emission lines is proportional to the number of sputtered atoms, hence the elemental concentration of the sample can be obtained.

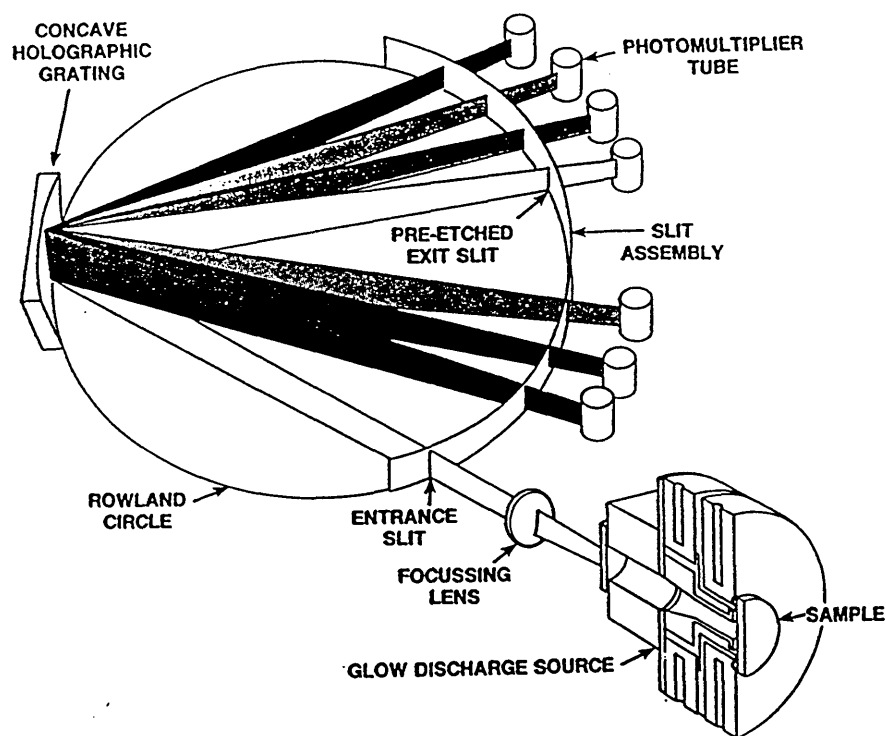


Fig 4.5.1 Diagram of glow discharge optical emission spectrometer

The optical spectrometer consists of a concave holographic grating, a Rowland circle, and photo-multiplier tubes. The light emitted from the glow discharge source is primarily focused by passing through the optical spectrometer onto a concave holographic grating by which the light is diffracted and hence the photons of a

certain wave-length reach a certain pre-etched slit around the Rowland circle which contains the grating and a series of pre-etched slits. The photo multiplier tubes are positioned behind the pre-etched slits to detect the intensity of the photons passing through the slits.

GDS-750 QDP is the GDOES instrument used for the elemental quantitative depth profile analysis of the coated samples. This machine consists of a glow discharge lamp producing a uniform cathode sputtering and a 750 mm spectrometer to measure the optical spectrum ranging from 150 to 456 nm; it can detect up to 44 elements. Composition and distribution of elemental depth profiles are calculated using a LECO 386 computer with LECO graphical-user-interface software^(6,7) which makes both operation and analysis simple and easy to control.

4.6 Adhesion measurement of hard coatings

Hard coatings produced by either PVD or CVD offer the improvement of surface properties of a component or cutting tools resulting in reliable performance and significant extension of tool life over uncoated materials. It is important to understand the relationship between the properties of the coatings and the substrate in order to ensure the improvement of the surface performance. In general many of these surface properties are only useful in certain applications. However, the relevance to a wide range of applications can be characterised by a few fundamental properties⁽⁸⁾. One of these fundamental properties is the coating/substrate adhesion. Methods to measure the coating/substrate adhesion can be summarised⁽⁹⁾ as pull-off, indentation and shockwave loading, and scratch test. Among them scratching may be the most widely used method to give qualitative measurements of the adhesion level of the coating/substrate system.

4.6.1 Scratch adhesion test

The scratch test involves a Rockwell indenter being drawn across the coated surface under a stepwise or continuously increasing load as shown in fig 4.6.1 thus the deformation of coating/substrate interface can be assessed. The level of the coating adhesion is characterised by the critical load, L_c , which is defined as the minimum load at which the failure of coating/substrate adhesion can be observed.

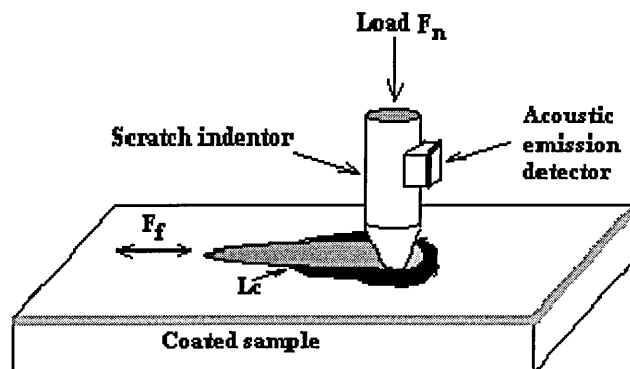


Fig 4.6.1 Diagram of scratch test

A well developed scratch tester consists of an integrated optical microscope, an acoustic emission detector, and a device to measure the friction force, F_f in the scratching direction. The microscope (light or electron) can be used to observe the point on the scratch channel where the failure of coating adhesion takes place. Also it can be used to identify any coating damages and detachments. The acoustic emission detector identifies a failure by monitoring the amount of cracks, which will increase dramatically upon failure. The friction force is monitored to look out for a sudden change in friction as the indenter penetrates to the substrate.

There are two sets of parameters, instrument related intrinsic parameters and sample related extrinsic parameters⁽¹⁰⁾, which have to be carefully considered in order to give the right L_c value.

The intrinsic parameters include loading rate, scratching speed, indenter radius and diamond tip wear. The L_c increases as loading rate increases, and it decreases as the scratching speed increases. However the L_c could be independent of the loading rate dL/dt and scratching speed dx/dt provided that dL/dx remains constant. The changing in L_c against dL/dx increases for the lower dL/dx values (0-100 N/mm) because the probability of encountering a defective adhesive region increases as dL/dx decreases. In general the lowest L_c is found for a manual loader since $dL/dx = 0$. The manual scratch test is dependent on the scratch speed, whilst the automatic scratch test is dependent on both dL/dt and dx/dt . For the automatic scratch test, the recommended dL/dx value is 10N/mm. The indenter's tip radius affects the critical load because the decrease of average pressure is proportional to the radius squared. Therefore larger tip radius will result in larger critical load. In practice the recommended tip radius is 200 μm . The diamond tip wear is a function of the sample hardness, increasing with hardness of both the surface and the substrate. There could be progressive increases in diamond tip wear without any change in critical load. However once the diamond tip damage increases noticeably, it does affect the critical load and the damaged diamond has to be replaced by a new one since the diamond tip is not reproducible.

The extrinsic parameters relate to substrate hardness, coating thickness, coating roughness, substrate roughness, and frictional characteristics between the indenter and the surface. As the critical load is linked to the degree of deformation, a greater load is needed for the harder substrate to cause the same deformation. For the same reason, the thicker coating needs higher loading on the indenter to deform it. The roughness of the coating should be less than 0.3 μm in order to avoid damage caused by the surface defects. The substrate roughness also affects the value of L_c . Increasing substrate roughness accompanies decreasing critical load. The friction coefficient between indenter and coating influences the critical load. In general, higher friction results in lower value of L_c .

The instrument used here for the scratch adhesion test is a ST200 tester manufactured by Teer Coating Service Ltd. This machine consists of a Rockwell diamond indenter of tip radius 200 μm . Measurements can be carried by either continuous mode using increasing load from 0 to 100 N at a dL/dX of 10N/mm, or stepwise mode using dx/dt of 10 mm/min with a 5 N increase in load for each step. The critical load is measured using an optical microscope equipped with a sample stage adjusted by a manometer.

4.6.2 Rockwell indentation adhesion test

The Rockwell indentation adhesion test employs a Rockwell-C diamond indenter which makes a point indentation with a load of 150 kg onto the coating/substrate composite system. The level of adhesion is measured by comparing the deformation profile of coating/substrate around the indentation with the adhesion criteria developed by the Union of German Engineers, Verein Deutscher Ingenieure (VDI), as shown in fig 4.6.2.

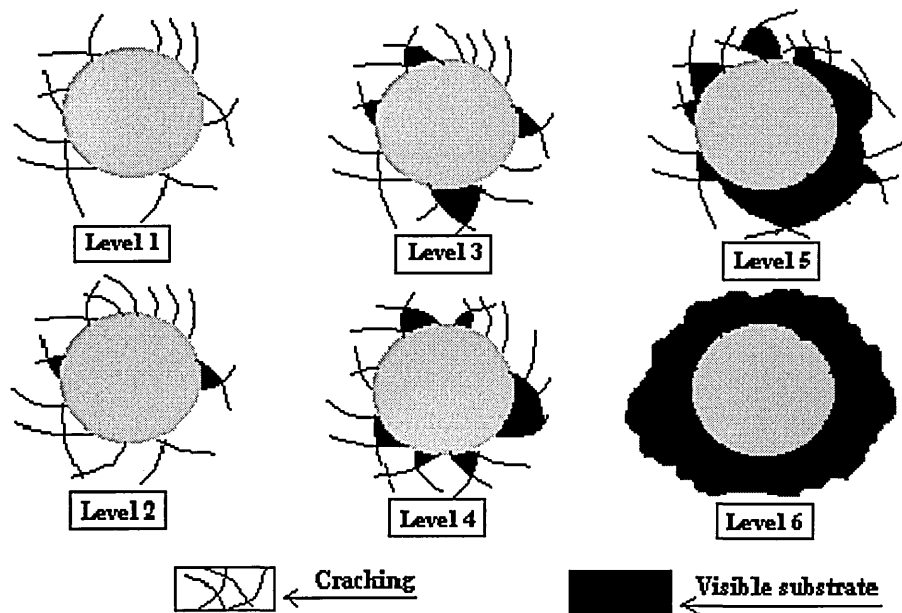


Fig 4.6.2 Adhesion judgement using Rockwell-C indentation

The classification of the adhesion judgement has been made under these conditions: the substrate hardness is not less than Rc 54, the coating thickness is not more than 5 μm , and the optical microscope is set at a magnification of x100 to observe the deformation of the coating/substrate system. There are 6 levels describing the resistance to propagation of cracks along the coating/substrate interface. Level 1 to level 4 (Rc-1 to Rc-4) are acceptable coating adhesions at which only cracks or small regions of spallation appear around the indentation whilst level 5 and level 6 (Rc-5 and Rc-6) are not acceptable adhesions at which large areas of spallation are found around the indentation.

The Rockwell indentation adhesion test results presented here were performed on high speed steel substrate of Rc-64 deposited with films of 1 to 5 μm thickness using a standard Rc indenter.

4.7 Hardness measurement of hard coatings

Hardness is also one of the fundamental properties of hard coatings, emphasising the importance of performance of coating for wear resistant applications. The measurement of coating hardness is carried out using a calibrated machine which forces a diamond indenter of specific geometry, under loading, into the surface of the coating and measures the length of the diagonal of the indentation. In general the depth of the indentation must be less than one tenth of the coating thickness⁽¹¹⁾. At the present the most widely used indentors are the Vickers indenter and the Knoop indenter.

4.7.1 Hardness test using Vickers indenter

The Vickers indenter is a highly polished, pointed, square-based pyramidal diamond with face angle of 136° , as shown in fig 4.7.1. The four faces of the indenter are

equally inclined to the axis of the indenter and meet at a sharp point. The line of junction between opposite faces (offset) should be not more than 0.5 μm in length.

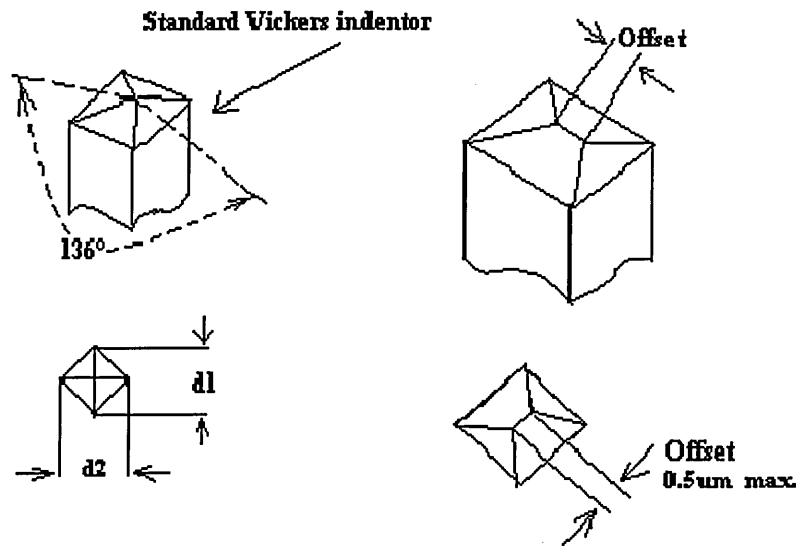


Fig 4.7.1 Diagram of Vickers indenter

The Vickers hardness number (Hv) is obtained by dividing the applied load in kilogram force by the surface area of the indentation in square millimetres calculated from the measured diagonals of the indentation. The equation can be expressed as

$$H_v = P/A = 2P \sin(\theta/2) / d^2 = 1.8544 P/d^2 \text{-----} 4.7.1$$

where P is load in kg and d is the average diagonal length in mm. Even though the hardness test is very simple, the operator must pay careful attention to each step during a measurement in order to avoid unnecessary error data or damage of the indenter. The surface of the test sample must be perpendicular to the axis of the direction of the load application. If the sample needs to be mounted, soft mounting materials can be used under the condition that the material has to be of sufficient rigidity so that there is no movement of the sample during load application. The

indenter comes close to the sample at a speed of between 15 and 70 $\mu\text{m/s}$. The time for the full test load should be 10 to 15 seconds. The test machine should be located in an area as free from vibrations as possible, especially for test loads less than 100g.

The Fischerscope H100V is used for Hv hardness testing of coatings with measurement of indentation depth under load. The load on the indenter can be varied from one to one hundred grams force to fit different applications.

4.7.2 Hardness measurement using Knoop indenter

The Knoop indenter is a highly polished, pointed, rhombic-based pyramidal diamond with included longitudinal edge angle of 172° and 130° as shown in fig 4.5.2. The four faces of the indenter are equally inclined to the axis of the indenter and meet at a sharp point. The line of junction between opposite faces (offset) should be not more than $1.0 \mu\text{m}$ in length for indentations greater than $15 \mu\text{m}$ in length.

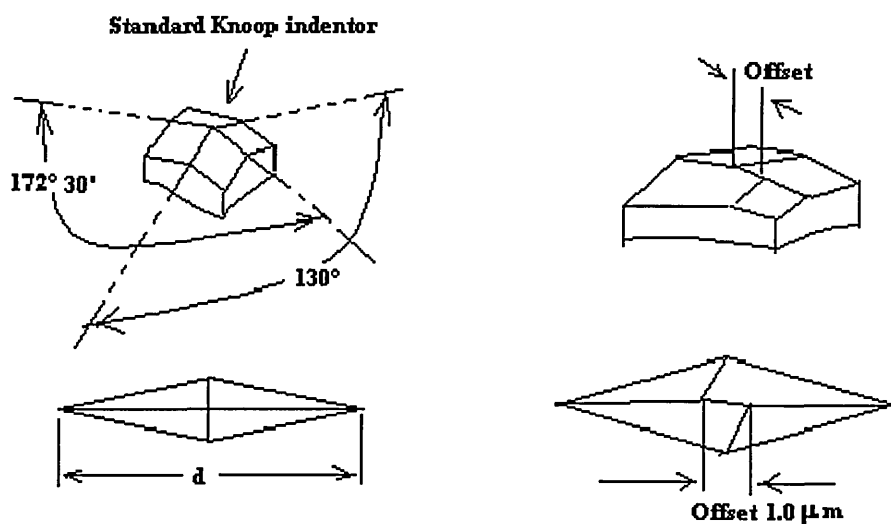


Fig 4.7.2 Diagram of Knoop indenter

The Knoop hardness number (Hk) is obtained by dividing the applied load in kilogram force by the projected area of the indentation in square millimetres calculated from the measured long diagonals of the indentation. The Knoop hardness number can be written according to the following equation

$$Hk = P/A_p = P/d^2c = 14.229 P/d^2 \text{-----} 4.7.2$$

where P is the applied load in kg force, A_p is the projected area in mm², d is the length of long diagonal in mm, and c is the indenter constant relating projected area of the indentation to the square of the length of the long diagonal. The careful approach described in 4.5.1 for proper use of the Vickers indenter is also required for correct hardness tests using the Knoop indenter.

The Mitutoyo MVK-H21 tester is used to measure the HK micro-hardness. This machine can apply two types of loads on the indenter for different uses. The low load is from one to twenty-five grams force, whilst the high load is from fifty to two thousand grams force.

4.8 Roughness test of coatings

Surface roughness is a very important parameter of coatings to determine the characteristics for decorative, friction, corrosion resistant, and wear resistant applications. In general, a flat surface having irregular peaks or waves is regarded as a curved or rough surface. For a PVD film, the roughness arises either during the sample preparation or the coating process. Practically, the properties of film roughness can be measured according to their origin. A very widely used technique for roughness measurement employs a diamond tipped stylus (2 μm in radius) to contact the sample surface and detect its variations as shown in fig 4.8.1.

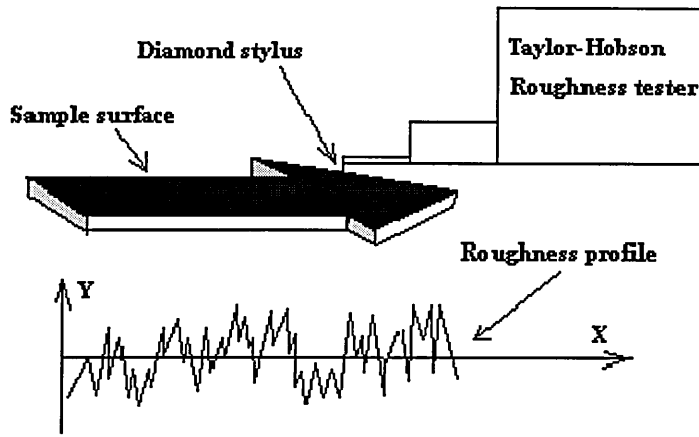


Fig 4.8.1 Diagram of roughness measurement

As the stylus travels along the surface, the variation of the surface topography is detected and coupled to a linear variable differential transformer which gives the roughness profile of the sample surface. The most commonly used roughness parameters are arithmetic average roughness (Ra), ISO 10 point height average roughness (Rz), and maximum peak to valley of roughness (Rt). The Ra can be written as

$$Ra = \frac{1}{L} \int_0^L |Y| dX \text{ -----4.8.1}$$

where L is the travel length along the X direction and Y is the variation of the surface topography. The Rz can be expressed as

$$Rz = \frac{1}{5} \left(\sum_{i=1}^5 Y_{pi} + \sum_{i=1}^5 Y_{vi} \right) \text{ -----4.8.2}$$

where Y_{pi} is one of the 5 highest peaks whilst Y_{vi} is one of the 5 lowest troughs. Rt is given as

$$Rt = Rp + Rv \text{ -----4.8.3}$$

where R_p is the highest peak and R_v is the lowest troughs.

The machine used for roughness measurement is the Rank Taylor-Hobson 120L surface texture measuring instrument which has a resolution of 10 nm for a 6 mm measuring range.

4.9 Thickness measurement of coatings

The thickness of the coatings is measured using a calotest as shown in Fig 4.9.1. A grinding ball is rotated on the coating surface where a diamond suspension is inserted as grinding material between the sphere and the coating. A layer annulus is produced as the material is abraded. The thickness of the coating, t , is calculated as

$$t = \frac{1}{2} \left[\sqrt{4R^2 - d^2} - \sqrt{4R^2 - D^2} \right] \text{-----4.9.1}$$

where t is the thickness of the coating, R is the radius of the grinding ball, d is the inside diameter of the abraded layer annulus, and D is the outside diameter of the abraded layer annulus.

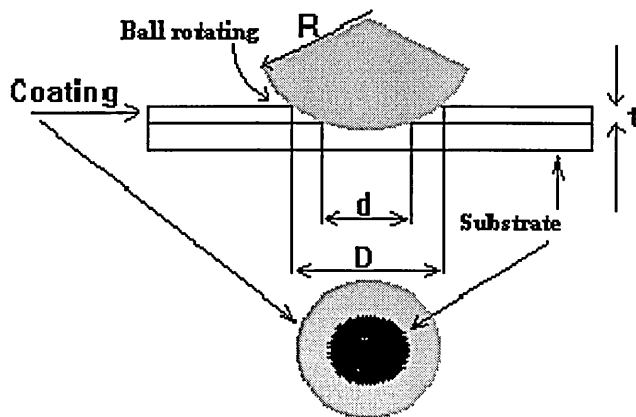


Fig 4.9.13 Geometrical principle of the calotest

4.10 Preparation of samples for analysis

Most of the analytical techniques need no sample preparation other than flat samples with standard cleaning such as air jet, acetone, or methanol to remove dust and trifling contamination. However, coated specimens used for cross sectional analysis have to be carefully prepared in order to get successful results reflecting the real structure and composition of the tested samples.

4.10.1 Fracture cross-section for analysis of scanning electron microscope

Columnar morphology and grain structure of the coatings are often investigated using fractured samples. Coated high speed steel drill blanks are the most typical samples used for this analysis. The preparation procedures are the following:

- A deep slit (~2/5 of diameter of drill blank) is cut into the side of the sample opposite to the coated surface using an Accutom rotary saw
- The cut sample is put in liquid nitrogen to be quenched for two to three minutes.
- The sample is clamped at the bottom and a uniform load is applied to the top to cause an even fracture along the slit.
- Gold plating on the fractured surface may be used to avoid the contrast between coating and substrate being too great.
- The fractured sample is then mounted vertically on a metal sample holder.

4.10.2 Cross sectional preparation for transmission electron microscope

The transmission electron microscope is a very useful tool for examining a coating's cross sectional structure. However specimen preparation for the cross sectional structure analysis is in fact a time consuming task. In general the specimen preparation procedure is the following:

- Specimens are cut into $0.5 \times 1.2 \times 3.0 \text{ mm}^3$ slices as shown in fig 4.10.1 a.

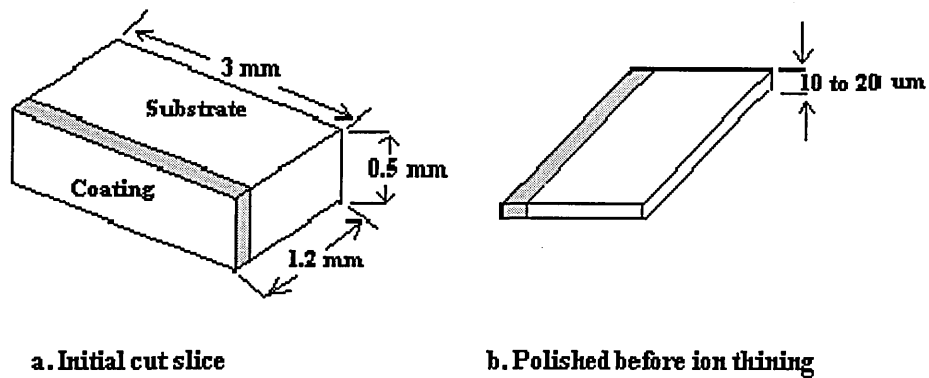


Fig 4.10.1 Specimen preparation for TEM analysis

- Sectioned slices are mechanically ground and polished on one side to a thickness of $100 \mu\text{m}$ and a finish of $1 \mu\text{m}$.
- The reverse side is further thinned and polished to make a foil with thickness of 10 to $20 \mu\text{m}$ and a finish of $1 \mu\text{m}$ as shown in fig 4.10.1 b.
- Final thinning for electron transmission is performed using argon ion beam thinning at an incident angle to the thinning surface from 0 to 5° , an accelerating voltage of 5 kV and a current of $7\text{-}10 \mu\text{A}$. The ion beam is only operated at $\pm 30^\circ$ normal to the coated surface in order to protect the coating/substrate interface from being damaged during the ion beam thinning stage.

References

- (1) W-D. Münz, D. Schulze, F. J.M. Hauzer, Surf. Coat. Technol., 50 (1992)169
- (2) W.-D. Münz, Surface and Coating Technology, V48 (1991)81
- (3) Powder Diffraction File, JCPDS International Centre for Diffraction Data, Swarthmore, PA 1991
- (4) P.T. Moseley, K.R. Hyde, B.A. Bellamy and G. Tappin, Corrosion Science, V24 (1984)547
- (5) G.K. Williamson and W.H. Hall, ACTA Metallurgical, V1 (1953)22
- (6) V. Hoffmann, Fresenius J. Anal Chem., 346 (1993)165
- (7) M. Ives, J. Cawley and J.S. Brooks, Surf. Coat. Technol., 61(1993)127
- (8) S.J. Bull and D.S. Rickerby, Br. Ceram. Trans. J., V 88 (1989)177
- (9) P.R. Chalker, S.J. Bull and D.S. Rickerby, Materials Science and Engineering, A140 (1991)583
- (10) P.A. Steinmann, Y. Tardy and H.E. Hintermann, thin Solid Films, V154 (1987)333
- (11) H. Buckle, in J.W. Westbrook and H. Conrad (eds.), The Science of Hardness testing and Its Research Applications, American Society for Metals, Metal Park, OH, (1973)453

5. Process study of TiCN hard coatings

5.1 Experiment arrangements

The TiCN coating experiments were arranged as three procedures: hysteresis TiN, hysteresis TiC, and TiCN deposition processes. The hysteresis deposition processes were used to study the effect of reactive gas flow rate on the reactive partial pressure under certain temperature condition during a deposition process. This gave a better understanding of the range of process parameter values by which stoichiometric composition films could be produced. The TiCN coating processes were conducted to investigate the effect of carbon and nitrogen concentration on the properties of TiCN films.

5.2 Hysteresis TiN coating process

The preparation of samples for deposition were described in chapter 4.2.1. The nitrogen gas flow rate was changed stage by stage during the deposition process as shown in fig 5.2.1. The nitrogen gas flow rate was increased from zero to a high level in a stepwise manner (20 minutes for each step) to give ranges of nitrogen gas partial pressure within the chamber during the process whilst the argon flow rate was kept at a constant value.

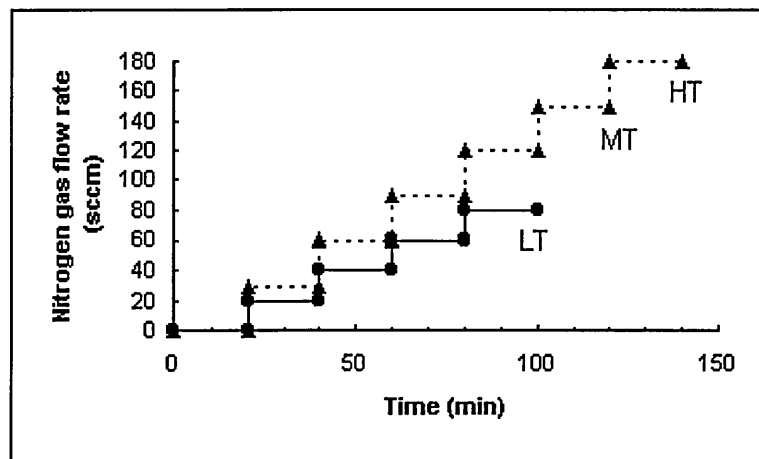


Fig 5.2.1 N₂ flow dependent on time in a process

There were three target power conditions, low target power (LP, 4×3 kW), mediate target power (MP, 4×5 kW) and high target power (HP, 4×10 kW) considered for the processes, which led to the film deposited at low temperature (LT, 180°C), mediate temperature (MT, 300°C) and high temperature (HT, 480°C) respectively. In LT deposition process, the change in nitrogen gas flow rate was 20 sccm (standard cubic centimetres per minutes) per step, while in MT and HT processes, the change in nitrogen gas flow rate was 30 sccm per step.

As there were no heaters used during these experiments, the substrate temperature was mainly dependent on the power supply of the targets. However, substrate bias voltage and the coil currents also affected the substrate temperature. The process parameters are recorded in table 5.2.1.

Table 5.2.1 Process parameters of stepwise TiN coatings

PN	Cathode power (kW)	Bias voltage (V)	Coil current (A)	Temperature (°C)
01	4x3	100	4x10	180 (LT)
02	4x5	120	4x10	300 (MT)
03	4x10	150	4x10	480 (HT)

The nitrogen partial pressure was measured by a differentially pumped mass spectrometer and calculated using the formula:

$$P_n = P_c \times \frac{p_n}{p_c} \text{-----5.2.1}$$

in which P_n and P_c are nitrogen partial pressure and total pressure in the coating chamber, p_n and p_c are nitrogen partial pressure and total pressure in the mass spectrometer. As the pumping speed of the mass spectrometer was different from the main chamber, the nitrogen partial pressure calculated using equation 5.2.1 is useful only for monitoring purposes. This partial pressure value will be called throughout this work as ‘‘reduced’’ partial pressure.

The relative titanium plasma density was measured using a Ti^+ optical emission monitor which was used to measure the signal intensity of the titanium optical emission from the target; hence the relative titanium plasma density was determined.

5.2.1 N_2 partial pressure and titanium plasma density dependent on N_2 flow rate

The reduced nitrogen partial pressure as a function of nitrogen gas flow rate is given in fig 5.2.2. In the initial stage the consumption of the nitrogen was proportional to the nitrogen gas flow rate. The nitrogen partial pressure started from a low value, about 0.6×10^{-4} mbar, and increased slowly with increasing nitrogen gas flow rate due to the increasing of nitrogen consumption in the deposition process. When the nitrogen partial pressure increased at a certain point, the consumption of nitrogen no longer increased with the nitrogen gas flow rate and therefore the nitrogen partial pressure suddenly increased quickly with a increase of nitrogen gas flow rate. This point is defined as an equilibrium point at which the consumption of the nitrogen and the sputtered titanium atoms from the target is balanced. As there was no increase of nitrogen consumption within the chamber with increasing nitrogen gas flow, the nitrogen partial pressure began to rise rapidly. It could be seen that the nitrogen partial pressures at any target power condition were changing almost linearly with the nitrogen gas flow rate before reaching the equilibrium point of nitrogen partial pressure. The critical nitrogen gas flow rate was 40 sccm for the equilibrium nitrogen partial pressure level using low power (LP) condition (4×3 kW), 60 sccm for that using medium power (MP) condition (4×5 kW), and 150 sccm for that using high power (HP) condition (4×10 kW). The equilibrium nitrogen partial pressures for LP, MP, and HP processes were 0.7, 0.8 and 1.0×10^{-4} mbar respectively. The total chamber pressure was kept constant within experimental accuracy (2.5×10^{-3} mbar) during the process before the equilibrium nitrogen partial pressure was achieved. Following this, the total chamber pressure was increased to a range of 2.7, 2.75 and 2.8×10^{-3} mbar respectively for the LP, MP, and HP coating processes.

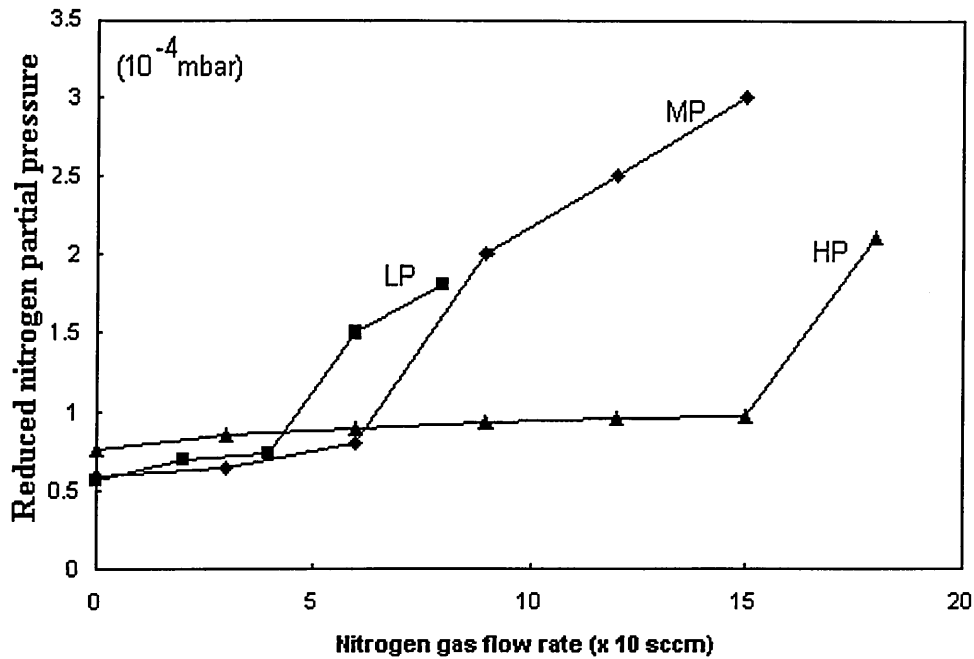


Fig 5.2.2 Reduced N₂ partial pressure dependence on N₂ gas flow rate

The titanium plasma density (which was measured using the Ti⁺ optical emission spectrometer) was changed corresponding to variations in nitrogen gas flow rate as shown in fig 5.2.3. When the gas flow rate was zero, the relative density of titanium plasma was 1. Then the plasma density decreased when the nitrogen gas flow rate was increasing. The change of titanium plasma density was almost linear until the nitrogen partial pressure reached an equilibrium point, following which the titanium plasma density reduced to a very low level when the nitrogen gas flow was increased further. After this point, as the target was fully poisoned, the titanium plasma density remained the same low level (over poisoned level) even though the nitrogen gas flow rate was further increased. The variation of plasma density mirrored the behaviour of nitrogen partial pressure dependent on the nitrogen gas flow rate. Under high power condition, the equilibrium point located at high nitrogen gas flow rate, while under low power condition, the equilibrium point located at low nitrogen gas flow rate.

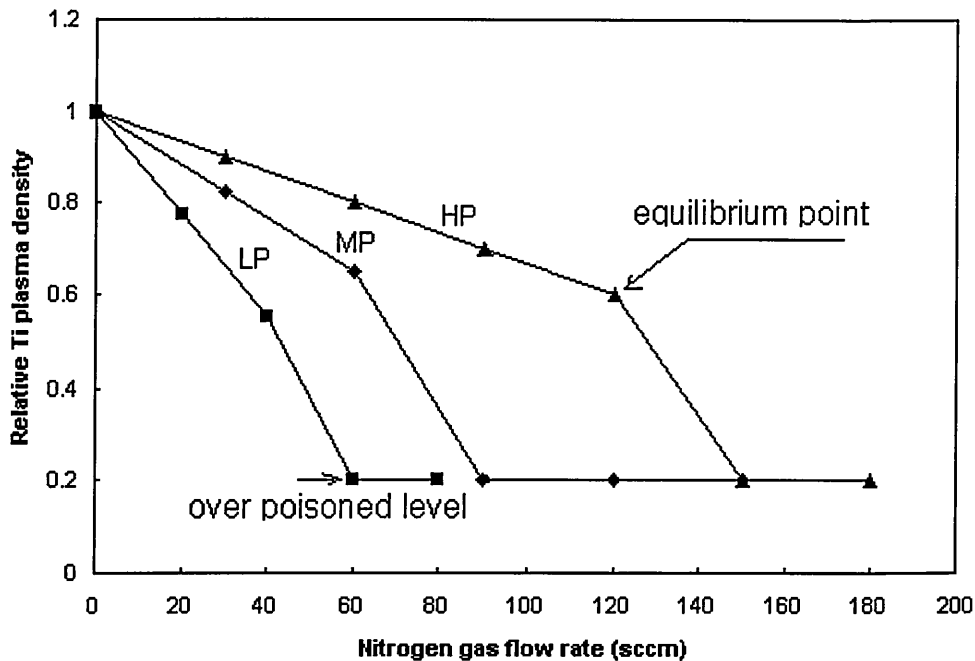


Fig 5.2.3 The relationship between Ti plasma density and N₂ flow rate

5.2.2 Concentration depth profile of the stepwise films

Concentrations of the films were estimated by GDOES calibration. It could be seen that an increase in nitrogen was accompanied by a decrease in titanium content from substrate/coating interface to the top surface of the coating as shown in fig 5.2.4,5,6. At a low target power condition, the elemental distribution depth profile of the coating showed different layers in the coating, over-stoichiometric composition ($N/Ti > 1$) at the top surface, then a thin stoichiometric composition ($N/Ti = 1$) layer at the middle, and then an under-stoichiometric layer ($N/Ti < 1$) with increasing titanium and decreasing nitrogen near the interface. At a medium power condition, the depth profile of the coating composition clearly showed three layers, stoichiometric composition at the top surface, under-stoichiometric composition with $Ti/N = 2$ at the middle, and then a titanium rich layer near the interface. At a high power deposition, the concentration depth profile of the film appeared to be a stepwise distribution. Stoichiometric composition appeared at the top surface, and then the elemental distribution was changing almost linearly with increasing titanium and decreasing nitrogen from the top surface to the coating/substrate interface.

(See page 120 and 121 for fig 5.2.4, 5, and 6)

Fig 5.2.4 Concentration depth profile of film deposited using low target power

Fig 5.2.5 Concentration depth profile of film deposited using medium target power

Fig 5.2.6 Concentration depth profile of film deposited using high target power

5.2.3 XRD analysis of the stepwise TiN films

X-ray diffraction patterns are shown in fig 5.2.7, 8, 9 for the stepwise coatings deposited low, medium, and high target power respectively. In general, these were multiphase compositions, Ti, $\alpha\text{TiN}_{0.3}$, $\epsilon\text{Ti}_2\text{N}$, and δTiN , developed in the coatings. These phases resulted from variation in composition from the coating/substrate interface to the top surface. Therefore it is reasonable to infer that the different phases reflect the compositions of the different layers distributed through the stepwise coating.

The XRD analysis of the stepwise TiN coatings is given in table 5.2.2 in which the types of coating (T), phases, (hkl) reflections, and the relative peak numbers (PN) were recorded. In the coating deposited using low target power as shown in fig 5.2.7, Ti, $\alpha\text{TiN}_{0.3}$, $\epsilon\text{Ti}_2\text{N}$, as well as δTiN phases were identified. There were diffraction peaks as marked from number 1 to number 11 for the film and those for the substrate. The strongest diffraction peak was an $\alpha\text{Ti(N)}$ (10.0) reflection as marked by peak number 1. The identified reflections were Ti (00.2), (10.1); $\alpha\text{TiN}_{0.3}$ (10.0), (11.0), and (20.1); $\epsilon\text{Ti}_2\text{N}$ (200), (111), and (002); δTiN (111) and (200).

In the coating deposited at medium target power as shown in fig 5.2.8, there were ten diffraction peaks for the film as well as the peaks for the substrate presented in the XRD pattern. $\epsilon\text{Ti}_2\text{N}$ (200) and (101) were the very strong diffraction peaks as marked by peak number 1 and 2. The reflections were Ti (11.2); $\alpha\text{TiN}_{0.3}$ (10.1); $\epsilon\text{Ti}_2\text{N}$ (101), (200), (210) and (002); δTiN (111), (200), (220) and (311).

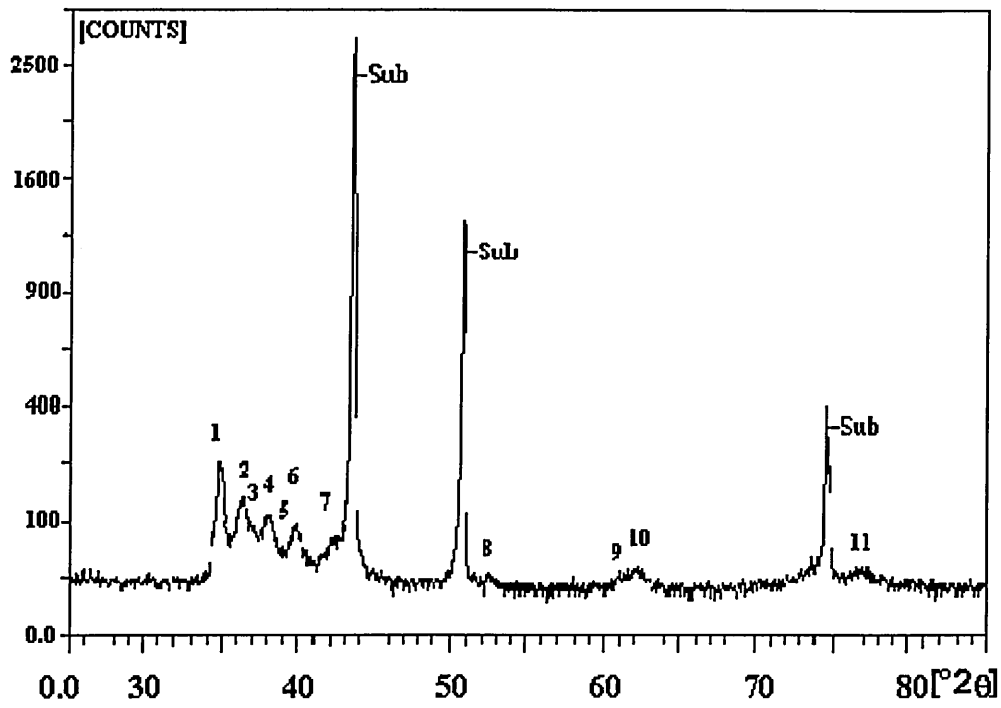


Fig 5.2.7 XRD pattern of the stepwise TiN coating deposited using low power

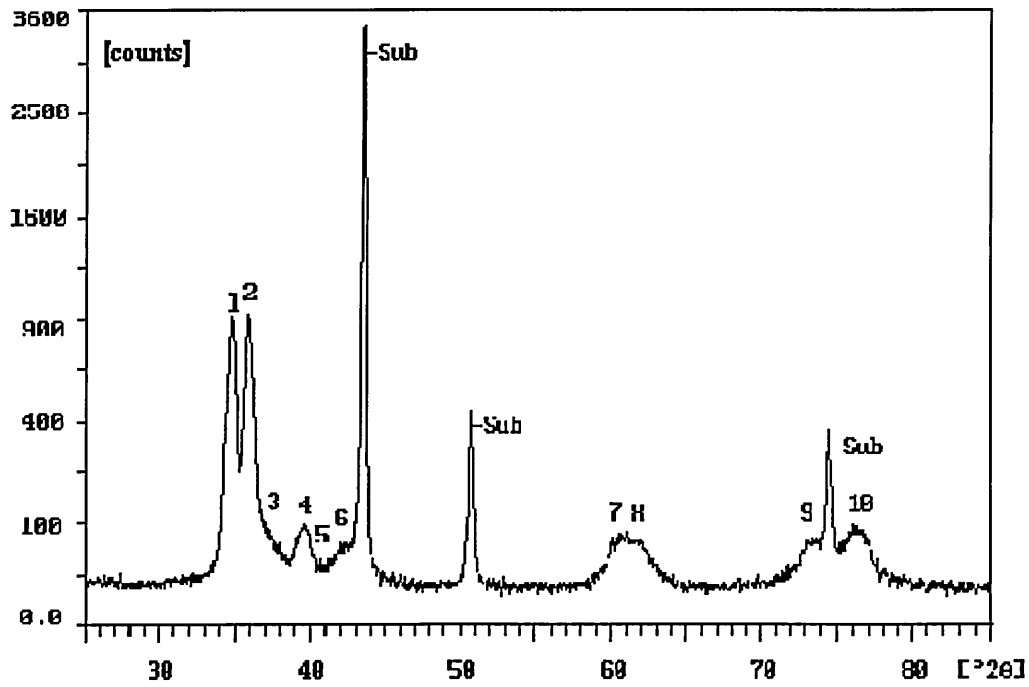


Fig 5.2.8 XRD pattern of the stepwise TiN coating deposited using medium power

There were twelve peaks presented in the diffraction pattern of the coating deposited using high target power as shown in fig 5.2.9. The strongest diffraction peak was δ TiN (111) as marked by peak number 2. The reflections corresponded to Ti (10.3) and (20.0); α TiN_{0.3} (10.1), (10.2), (10.3) and (00.4); ϵ Ti₂N (101), (002) and (202), δ TiN (111), (200), and (220).

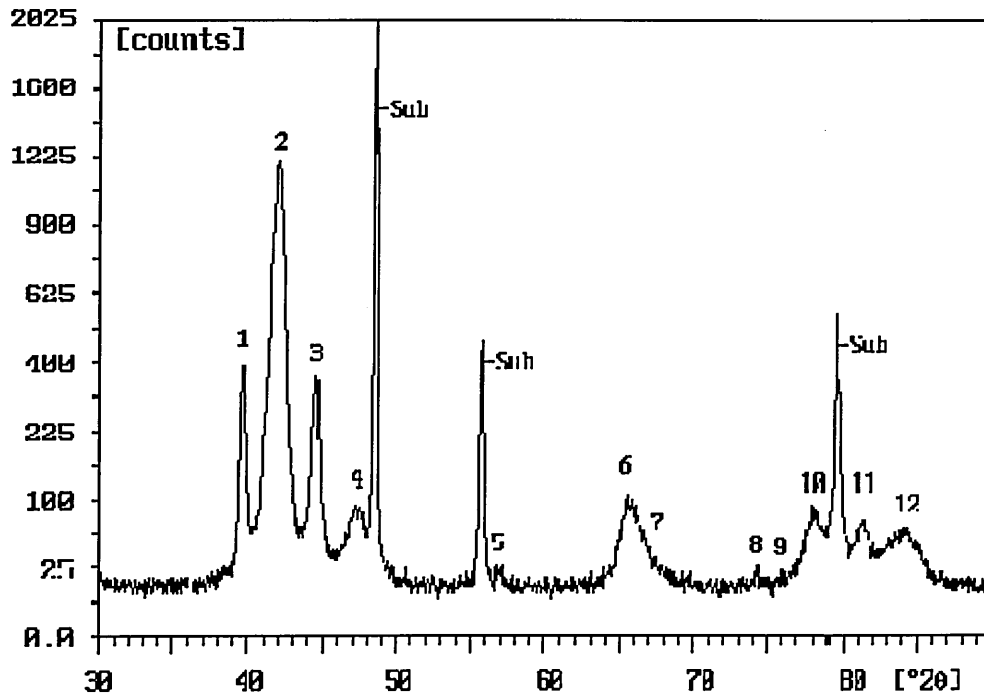


Fig 5.2.9 XRD pattern of the stepwise TiN coating deposited using high power

Table 5.2.2 XRD analysis of stepwise TiN coatings

T	Phase	Ti			α TiN _{0.3}			ϵ Ti ₂ N				δ TiN				
LP	hkl	002	101	102	100	110	201		200	111	002		111	200		
	PN	4	6	8	1	10	11		2	5	9		3	7		
MP	hkl	112			101				101	200	210	002	111	200	220	311
	PN	10			4				1	2	5	7	3	6	8	9
HP	hkl	103	200		101	102	103	004	101	002	202		111	200	220	
	PN	9	10		3	5	8	12	1	6	10		2	4	7	

5.2.4 SEM results

The fracture cross section of the stepwise TiN coatings examined using SEM are shown in fig 5.2.10 a, b, and c. The thickness was 0.5, 1.5, and 3.0 μ m for coatings deposited

using low, mediate and high target power respectively. In general, a columnar structure is formed in the coatings normal to the substrate surface. It was clear (see fig 5.2.10 b and c) that the column size varied throughout the depth of coating. Large column sizes were observed close to the film/substrate interface where the coating was rich in titanium, and near the top surface where the coating was rich in nitrogen. In the middle of the coating however, the grain size was very small which reflected a very dense film produced in this region.

(See page number 122 for fig 5.2.10)

Fig 5.2.10 SEM fracture cross sectional images of stepwise TiN coatings
a. deposited at LP, b. deposited at MP, c. deposited at HP

5.2.5 Discussion hysteresis TiN coating

Nitrogen partial pressure is a function of the nitrogen gas flow rate during a deposition process⁽¹⁾ and this function is basically dependent on the applied target power⁽²⁾. When the nitrogen gas flow is started, there is only small change in nitrogen partial pressure in the chamber because a large amount of nitrogen gas is combined with the sputtered titanium. As the nitrogen gas flow is increased to a certain level, the nitrogen partial pressure is suddenly increased because there is sufficient nitrogen in the chamber to form a compound on the surface of the target. This compound results in a large decrease of sputtering rate and therefore the consumption of nitrogen is also largely reduced. Hence there is a big jump in the nitrogen partial pressure. Higher target power leads to a high sputtering rate which results in large amount of sputtered titanium atoms to contribute the growing film and a large amount of nitrogen is needed during the formation of stoichiometric TiN film. Therefore high nitrogen gas flow is needed to keep the equilibrium nitrogen partial pressure in order to supply sufficient nitrogen combined with the sputtered titanium.

During a process titanium plasma density is linearly decreasing with increasing nitrogen gas flow rate before the equilibrium nitrogen partial pressure is achieved. This indicates

the titanium sputtering rate is linearly reduced in this stage. Afterwards, the sputtering rate falls to a lowest level because the titanium nitride formed on the target causes target poisoning and greatly reduces the sputtering yield.

Different nitrogen concentrations of the coating correspond to the different phase compositions⁽³⁾. Low nitrogen (less than 25 at % N), middle nitrogen (about 33 at % N), and high nitrogen (above 35 at % N) concentrations within the coating correspond the $\alpha\text{TiN}_{0.3}$, $\epsilon\text{Ti}_2\text{N}$ and δTiN phase compositions respectively. As the level of nitrogen partial pressure in a deposition process corresponds to the level of nitrogen concentration in the coating, low, middle, and high levels of nitrogen partial pressure could be used to deposit films containing $\alpha\text{TiN}_{0.3}$, $\epsilon\text{Ti}_2\text{N}$, and δTiN phase compositions respectively. Comparing with composition depth profile and the X-ray diffraction of the stepwise TiN coating, it is reasonable to say that the δTiN phase is formed at the top layer, $\epsilon\text{Ti}_2\text{N}$ phase is developed in the middle layer, $\alpha\text{TiN}_{0.3}$ phase is produced at the layer next to the coating/substrate interface.

5.3 Hysteresis TiC coating process arrangements

5.3.1 Specimen preparation and experiment parameters

The method and procedure of specimen preparation, experiment parameters and arrangements of stepwise TiC coatings were the same as that of stepwise TiN coatings (see chapter 5.2) except that methane (CH_4) was used as the reactive gas in the process instead of nitrogen.

5.3.2 Methane partial pressure dependent on CH_4 flow rate

The results are shown in fig 5.3.1 in which the background levels of reduced methane partial pressure for all the conditions of low power, LP (4×3 kW), mediate power, MP (4×5 kW), and high power, HP (4×10 kW) processes were almost the same at the initial depositing stage. Then the methane partial pressure was linearly increasing as the gas flow rate increased. When the gas flow rate reached a certain value (approximately 40

sccm in the LP process for example), the partial pressure began to rise rapidly with increasing methane flow rate. The higher target power process had lower methane partial pressure even through the introduced methane gas flow rate was the same as that in low target power process. This reflected the fact that more carbon was used during the high power process. The change of methane partial pressure dependent on the gas flow rate was smaller for the higher power process. The total chamber pressure was 2.5×10^{-3} mbar when the deposition process started, then the total pressure increased to 2.6, 2.65, and 2.7×10^{-3} mbar respectively for the LP, MP, and HP coating processes when the methane partial pressure began to change rapidly.

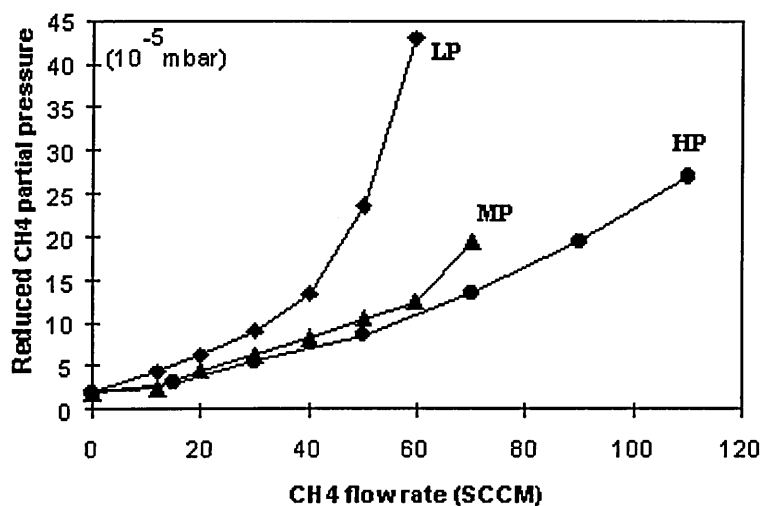


Fig 5.3.1 Reduced CH₄ partial pressure dependent on gas flow rate

5.3.3 Concentration depth profile of hysteresis TiC coatings

The elemental distributions in the depth of the coatings was estimated by GDOES as shown in fig 5.3.2, 3, and 4. It could be seen that an increase in carbon was accompanied by a decrease in titanium content from substrate/coating interface to the top surface of the coating. At low power process, the concentration within the coating showed clearly two layer's distribution. The over-stoichiometric composition ($C/Ti > 1$) from the top surface to the middle of the coating then a titanium richer layer ($C/Ti < 1$) from the middle to the coating/substrate interface. At Mp and HP conditions, the concentration

depth profile of the films appeared to be a stepwise distribution. Close to stoichiometric composition appeared at the top surface, and then the elemental distribution was changing almost linearly with increasing titanium and decreasing carbon from the top surface to the coating/substrate interface.

(See page 123 and 124 for fig 5.3.2, 3, and 4)

Fig 5.3.2 Concentration depth profile of stepwise TiC film deposited at LP

Fig 5.3.3 Concentration depth profile of stepwise TiC film deposited at MP

Fig 5.3.4 Concentration depth profile of stepwise TiC film deposited at HP

5.3.4 XRD results

There were four diffraction peaks for the film deposited at low power process as well as the peaks for the substrate as shown in fig 5.3.5. It can be seen that peak 1 (in the shoulder of peak 2) belongs to the reflection from Ti (10.0); peaks 2, 3, and 4 were TiC (111), (200), and (220) respectively. The strongest diffraction peak was TiC (111), thus indicating a {111} texture.

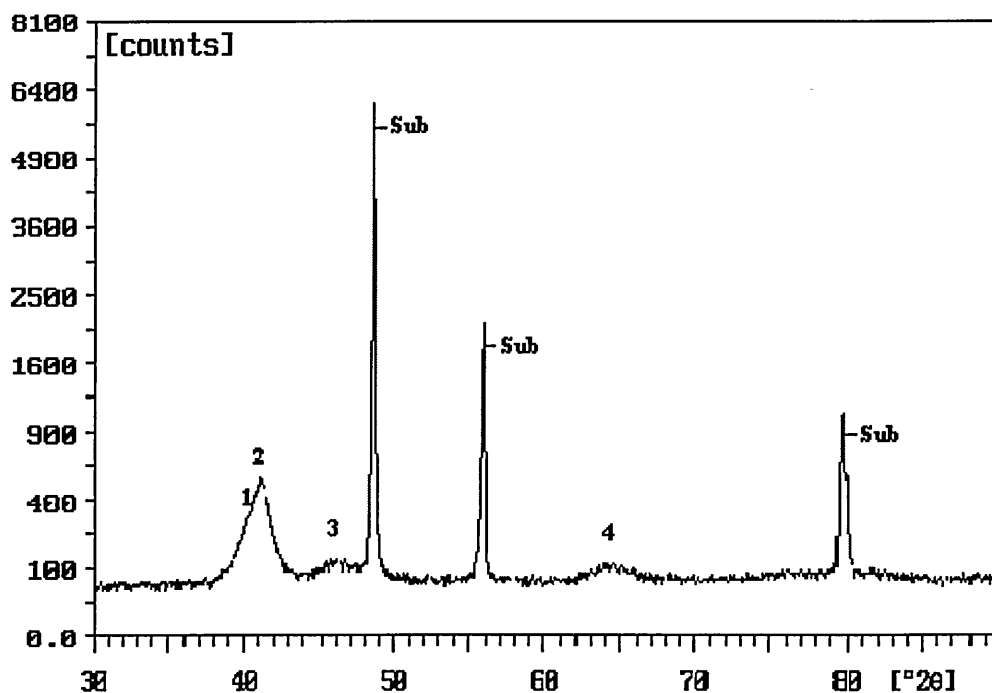


Fig 5.3.5 XRD pattern of the stepwise TiC coating deposited at LP

There were nine diffraction peaks identified in the film deposited at an intermediate power as shown in fig 5.3.6. Peaks 1, 3, 5, 7, and 9 were reflections from Ti (10.0), (00.2), (10.3), (20.0), and (20.1) planes, whilst peaks 2, 4, 6, and 8 were reflections from TiC (111), (220), (311), and (222) planes. The strongest diffraction peak was from Ti (10.0) plane. The overlapping of the diffraction peaks took place as the diffraction angle increased, which caused difficulties in identifying peaks.

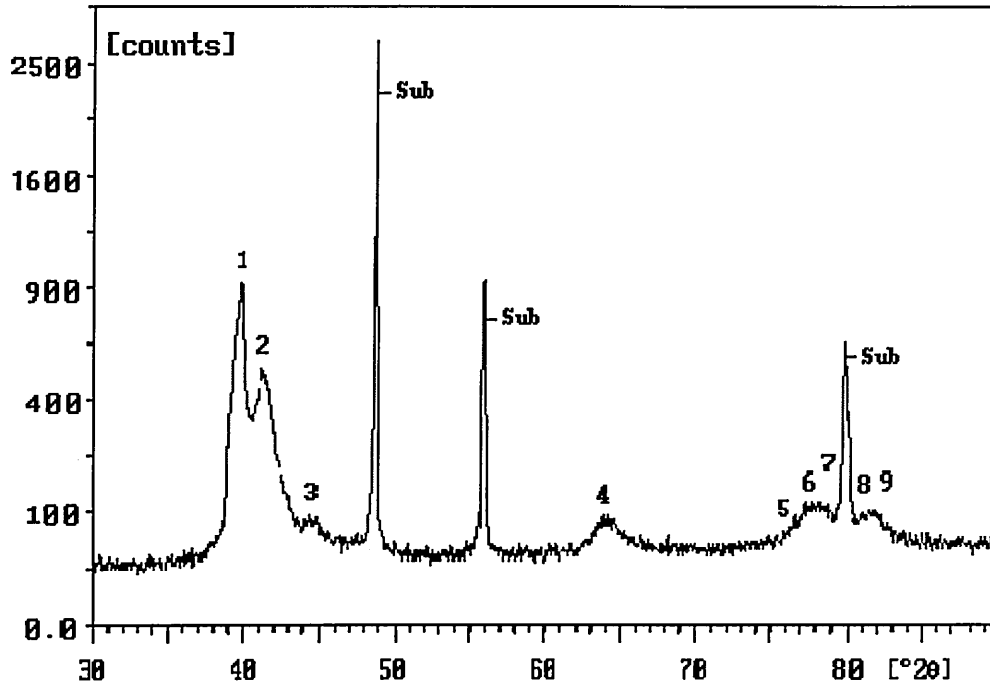


Fig 5.3.6 XRD pattern of the stepwise TiC coating deposited at MP

The XRD pattern of film deposited using high target power is shown in fig 5.3.7, in which eight diffraction peaks present in the film were identified. Peaks 1, 3, 4, 5, 7, and 8 were reflections from Ti (10.0), (00.2), (10.1), (20.0), (11.2), and (20.1) planes, whilst peaks 2 and 6 were reflections from TiC (111) and (222) planes. There were more titanium peaks present in the XRD pattern of coating deposited at high target power. The diffraction peaks were also sharper and had a higher intensity as compared with that of the XRD pattern from the coating deposited at a low power. The strongest diffraction peak was Ti (00.2).

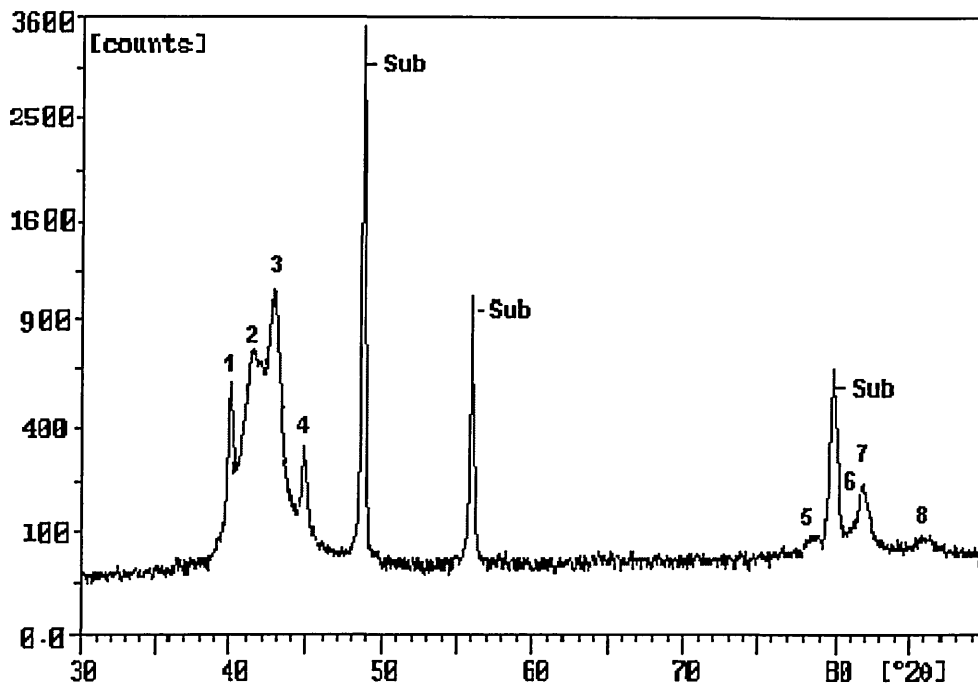


Fig 5.3.7 XRD pattern of the stepwise TiC coating deposited at HP

5.3.5 SEM results

The fracture cross sectional images of the TiC stepwise coatings deposited using a low, intermediate, and high power were examined by scanning electron microscopy figs 5.3.8 a, b, and c. It could be seen that a columnar structure was produced within the coatings and the column orientation was normal to the substrate surface. It was clear that the columnar size changed from the coating/substrate interface to the coating surface. The column size at the interface was larger than that at the top surface. This indicated that the TiC coating with high carbon concentration near the surface had fine columnar structure whilst the titanium rich TiC coating near the coating/substrate interface had coarse columnar grains. The columnar size was also dependent on the target power. The coating deposited using higher target power had a coarse columnar structure as compared with the film deposited using low target power. The thickness was approximately $1\mu\text{m}$ for the low temperature coating, and $2.5\mu\text{m}$ for the middle and high temperature coatings.

(See page 125 for fig 5.3.8)

Fig 5.3.8 SEM images of the stepwise TiC coatings deposited at a. LP, b. MP, c. HP

The outer edge images of the fracture cross section are shown in fig 5.3.9. Cone shaped defects grown from deposition during the cathodic arc etching stage can be seen on the coating surface. However, when the coating was deposited using high target power, this cone defect tended to be flattened and the top surface became more smooth.

(See page 126 for fig 5.3.9)

Fig 5.3.9 Outer edge images of the fracture cross section of the stepwise TiC coatings deposited at a. LP, b. MP, c. HP

5.3.6 Discussion hysteresis TiC coating

The process of using high target power leads to high plasma density and high deposition temperature both of which are beneficial to activate the carbons reacting with the sputtered titanium. As more methane is consumed in the high temperature coating process, the methane partial pressure is reduced. Therefore the high target power process had the lower methane partial pressure as compared with the low target power process using the same methane gas flow rate as seen from fig 5.3.1.

There are more diffraction peaks in the XRD pattern of coating deposited using high target power as compared with that of coating deposited using low target power. This may be attributed to the thickness of the coatings. High target power leads to high sputtering rate and hence the high deposition rate. The thickness of the coating deposited at high target power is less than 2.5 μm whilst the thickness of the coating deposited at low target power is only 1 μm . As the diffraction intensity contributed by the thicker coating is higher, more diffraction peaks could be identified because there is more chance of recording the weak diffraction signal.

The grain size of the TiC coating is a function of the composition. The carbon within the coating is increasing from the substrate/coating interface to the top coating surface. When the number of carbon within the coating is less than the number of the titanium atoms, the composition gradients and the chemical potential may develop. This may direct the migration of the pre-condensed deposits leading to formation of relatively large stoichiometric grains surrounded by substoichiometric regions and voided boundaries⁽⁴⁾. When the composition approaches to stoichiometry at the coating surface, the composition gradients and directed migration will decrease. This implies the small grains with dense grain boundaries will be formed⁽³⁾.

5.4 TiCN Coating

5.4.1 Experimental parameters and arrangement

The coating process was arranged to operate at two kinds of target power conditions, 4×5kW and 4×10kW which resulted the substrate temperatures at 240°C (LT) and 340°C (HT) respectively. There were five processes performed for each power condition. Argon flow was kept constant for every coating process. The chamber total pressure for TiCN coating process was chosen from the average value of the hysteresis TiN and TiC process. At low temperature (LT) process TiCN coating process, the total pressure was 2.70×10^{-3} mbar whilst the total chamber pressure was chosen 2.75×10^{-3} mbar for the high temperature (HT) process. The ratio of nitrogen gas flow rate to methane flow rate was not changed in a single process so that a uniform TiCN film could be produced. Uniform TiCN coatings with different compositions were deposited using different ratios of the reactive gas flow rate in the different coating processes. During a process the total pressure (which was contributed by argon, nitrogen and methane) was kept at a constant value which was expected in the range of the saturated pressure considered to produce stoichiometric TiCN, $(C+N)/Ti = 1$. The reactive gas flow rate was determined such that the contribution of introduced nitrogen and methane to the total chamber pressure which kept the total pressure at the considered value. The coating process parameters are given in table 5.4.1, and 2.

Table 5.4.1 Process parameters of TiCN coating in LT process

PN	Target power (kW)	Bias voltage (V)	Coil current (A)	CH ₄ flow rate (SCCM)	N ₂ flow rate (SCCM)	Ar ₂ flow rate (SCCM)	Total pressure (mbar)
LT01	4x5	120	4x10	15	50	110	2.65x10 ⁻³
LT02	4x5	120	4x10	25	48	110	2.65x10 ⁻³
LT03	4x5	120	4x10	29	38	110	2.65x10 ⁻³
LT04	4x5	120	4x10	36	28	110	2.65x10 ⁻³
LT05	4x5	120	4x 10	37	20	110	2.65x10 ⁻³

Table 5.4.2 Process parameters of TiCN coating in HT process

PN	Target power (kW)	Bias voltage (V)	Coil current (A)	CH ₄ flow rate (SCCM)	N ₂ flow rate (SCCM)	Ar ₂ flow rate (SCCM)	Total pressure (mbar)
LT01	4x10	150	4x10	36	87	110	2.75x10 ⁻³
LT02	4x10	150	4x10	46	75	110	2.75x10 ⁻³
LT03	4x10	150	4x10	56	53	110	2.75x10 ⁻³
LT04	4x10	150	4x10	67	32	110	2.75x10 ⁻³
LT05	4x10	150	4x 10	80	15	110	2.75x10 ⁻³

5.4.2 The variation of N₂/CH₄ pressure ratio dependent on the N₂/CH₄ flow ratio

It can be seen from fig 5.4.1 that the N₂/CH₄ pressure ratio was almost linearly changing with the ratio of nitrogen gas flow to methane flow. The major variation of reactive gas pressure ratio dependent on reactive gas flow ratio in both low and high temperature coating process was not very much different.

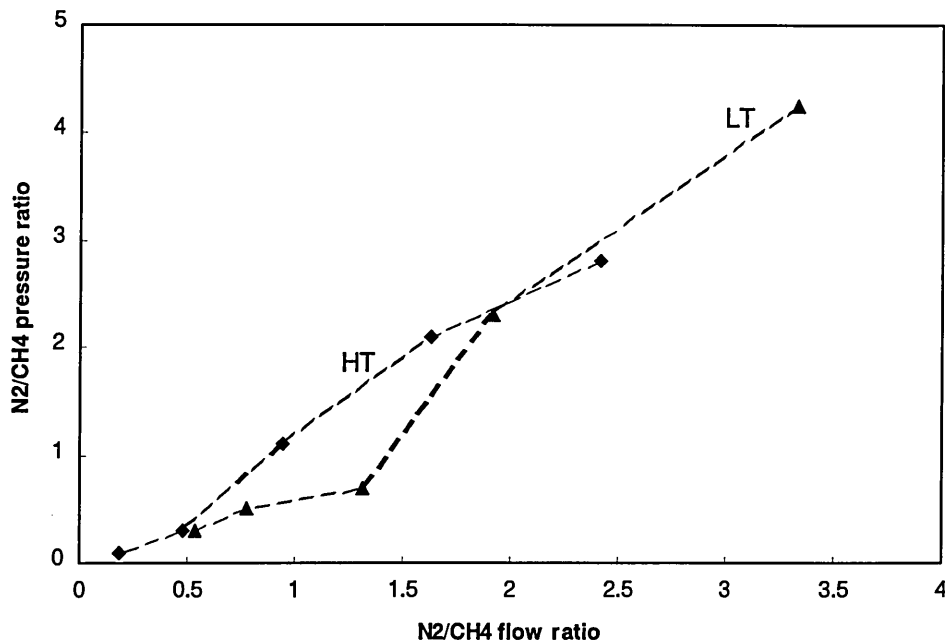


Fig 5.4.1 Ratio of reactive gas pressure dependent on reactive gas flow ratio

5.4.3 Composition dependence on the reactive gas pressure ratio

The elemental distribution with respect to depth of the coating was estimated using GDOES. In general, the coatings deposited in the low target power process, at low temperature (240°C), contained about 70 at % Ti and 30 at % (C+N), while the coatings deposited in high target power process, at high temperature (340°C), contained about 60 at % Ti and 40 at % (C+N) as shown in fig 5.4.2 and 3.

(See page 127 for fig 5.4.2 and 3)

Fig 5.4.2 Composition depth profile of TiCN film deposited at LT temperature

Fig 5.4.3 Composition depth profile of TiCN film deposited at HT temperature

The relationship between the ratio of N/C composition in the coating and the ratio of the corresponding reactive gas pressure in the coating process is significant. Almost linear variation of the nitrogen to carbon ratio in the coatings dependent on the change of

nitrogen gas pressure to methane pressure ratio in the process was found as shown in fig 5.4.4.

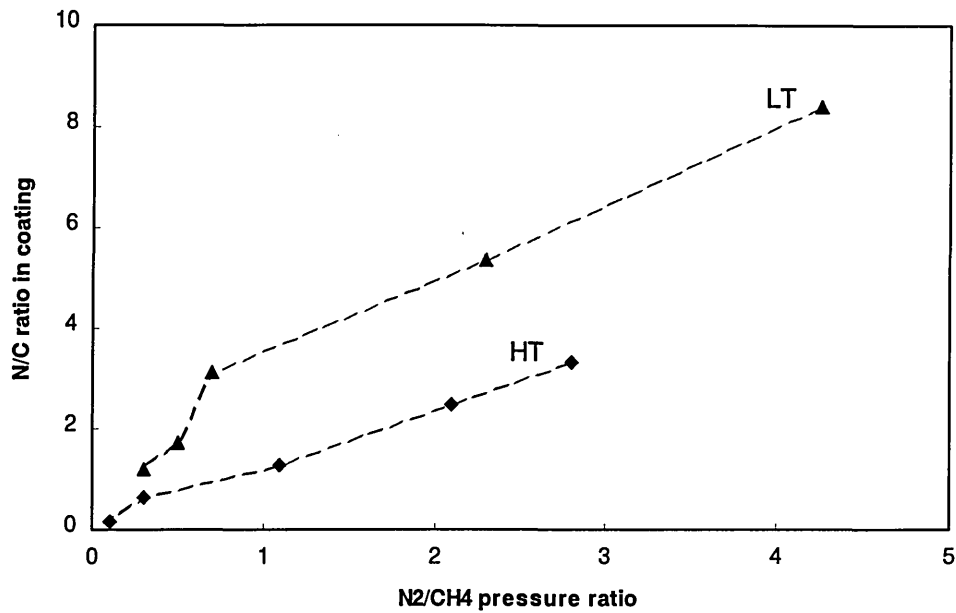


Fig 5.4.4 Concentration ratio in coatings dependence on reactive gas pressure ratio

The N/C ratio in coating deposited at a higher target power process was lower than that in coating deposited at a low target power process even through the nitrogen gas pressure to methane pressure ratio was kept at the same level. As high target power process led to high substrate temperature, thus it could give assumption that high carbon content coatings could be produced at high temperature conditions.

5.4.4 Hardness results

The hardness results as well as the atomic concentration of TiCN coatings deposited at low substrate temperature (LT, 240°C) are recorded in table 5.4.3. The coated stainless steel samples were found to have a hardness value varying from 1588 Hv for the lowest hardness to 2874 Hv for the highest hardness. The coated high speed steel samples were found to have hardness values varying from 1743 Hv for the lowest hardness to 3455 Hv for the highest hardness.

Table 5.4.3 Hardness results of TiCN coatings deposited at 240°C

PN	Concentration atomic (%)			Atomic Ratio		Hardness Load 25g (Hv)	
	N	C	Ti	N/C	(N+C)/Ti	SS	HS
LT01	25.2	3.0	71.8	8.4	0.39	2209	2549
LT02	29.4	5.6	65.0	5.25	0.54	2874	3455
LT03	22.7	7.3	70.0	3.11	0.43	2449	2790
LT04	15.3	8.9	78.0	1.71	0.31	2253	2533
LT05	10.9	9.1	80	1.20	0.25	1588	1743

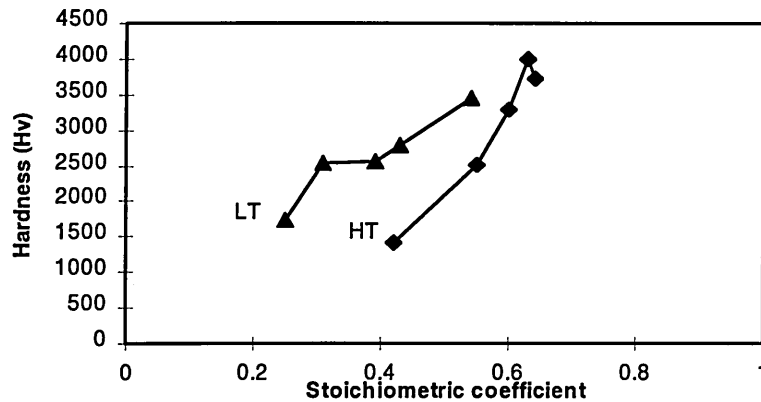
The values of hardness and atomic concentration of TiCN coatings deposited at high substrate temperature (340°C) are recorded in table 5.4.4. The coated high speed steel samples were found to have 1409 Hv for the lowest hardness, and 4003 Hv for the highest hardness as measured using 25g load on the indenter. When 50g load on the indenter was applied however, a much lower hardness value was measured in the same sample. This is because the coating is not thick enough to resist the penetration of the indenter with heavy load. As the indenter is close to the substrate, the measuring value is influenced more by the substrate and therefore a lower hardness value is recorded.

Table 5.4.4 Hardness results of TiCN coatings deposited at 340°C

PN	Concentration (%)			Atomic Ratio		Hardness (Hv) load 25g	hardness (Hv) load 50g
	N	C	Ti	N/C	(N+C)/Ti	HSS	HSS
HT01	30.0	9.0	61.0	3.33	0.64	3722	3411
HT02	27.6	11.2	61.2	2.46	0.63	4003	2548
HT03	21.2	16.4	62.4	1.29	0.60	3290	2689
HT04	14.0	21.6	64.4	0.65	0.55	2519	1607
HT05	4.0	25.6	70.4	0.16	0.42	1409	992

The relation between coating hardness and stoichiometric coefficient was shown in fig 5.4.5. The stoichiometric coefficient was defined as $(C+N)/Ti$. It was clear that the hardness was almost proportional to the stoichiometric coefficient. A higher

stoichiometric coefficient could result in higher hardness except for the measurement of samples from HT02 to HT01 in which the hardness reduced from Hv 4003 to Hv 3722 when the stoichiometric coefficient increased from 0.63 to 0.64.



**Fig 5.4.5 Hardness as a function of stoichiometric coefficient
25g load on the indenter**

5.4.5 XRD results

5.4.5.1 TiCN coatings deposited at 240°C

XRD traces for the samples LT01 to LT05 were shown in figs 5.4.6, 7, 8, 9 and 10 in which the carbon content in the coatings was increased from 3% to 9.1 at %. TiCN (111), (200), and (220) were found to be the main reflections. The interplanar spacings, diffracted intensity of the (hkl) reflections, random intensity according to standard XRD JCPDS files, lattice parameters, and textures are given in table 5.4.5. The interplanar spacing of the (200) reflection in samples from LT01 to LT05 were found systematically increased with the carbon content within the coatings. For the (111) and (220) reflections, however, the change in interplanar spacing with increasing carbon content in the films was not so systematic.

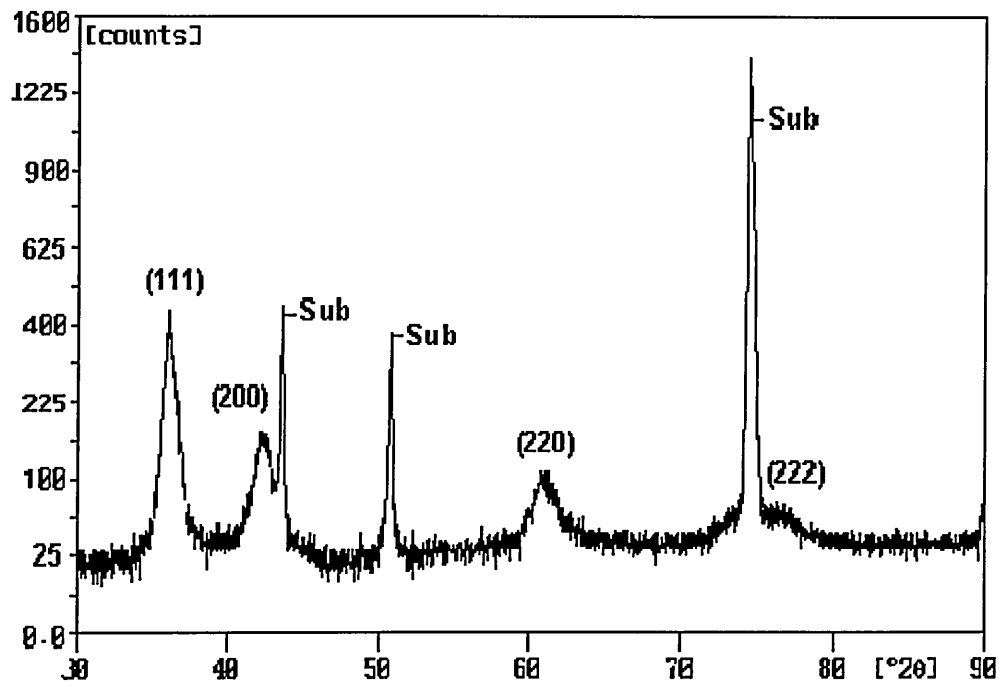


Fig 5.4.6 XRD pattern of TiCN coating from sample LT01

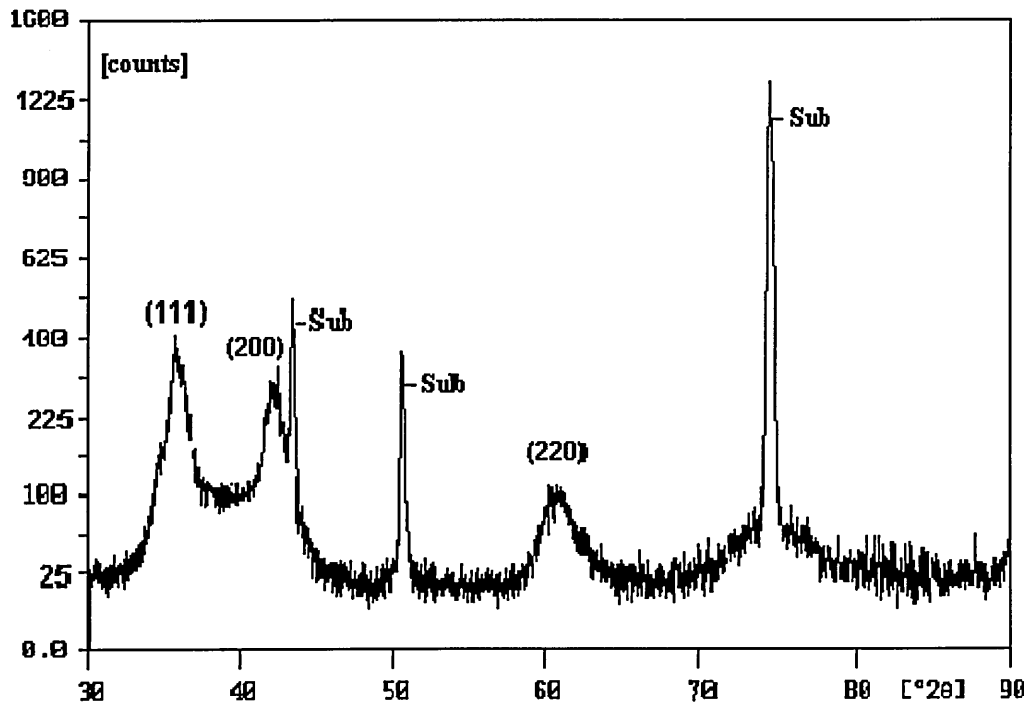


Fig 5.4.7 XRD pattern of TiCN coating from sample LT02

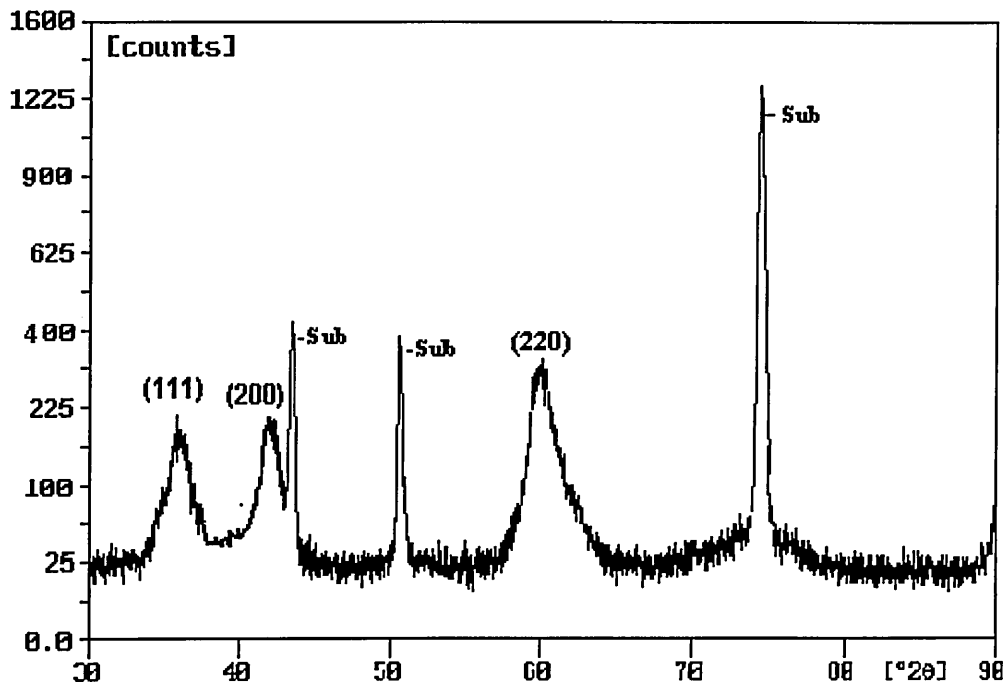


Fig 5.4.8 XRD pattern of TiCN coating from sample LT03

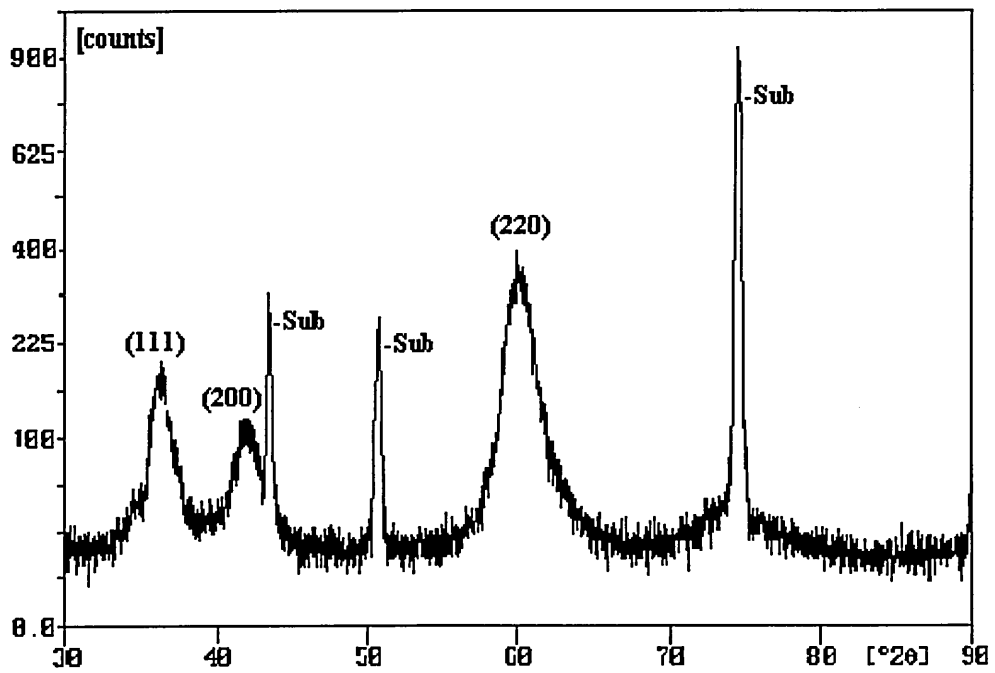


Fig 5.4.9 XRD pattern of TiCN coating from sample LT04

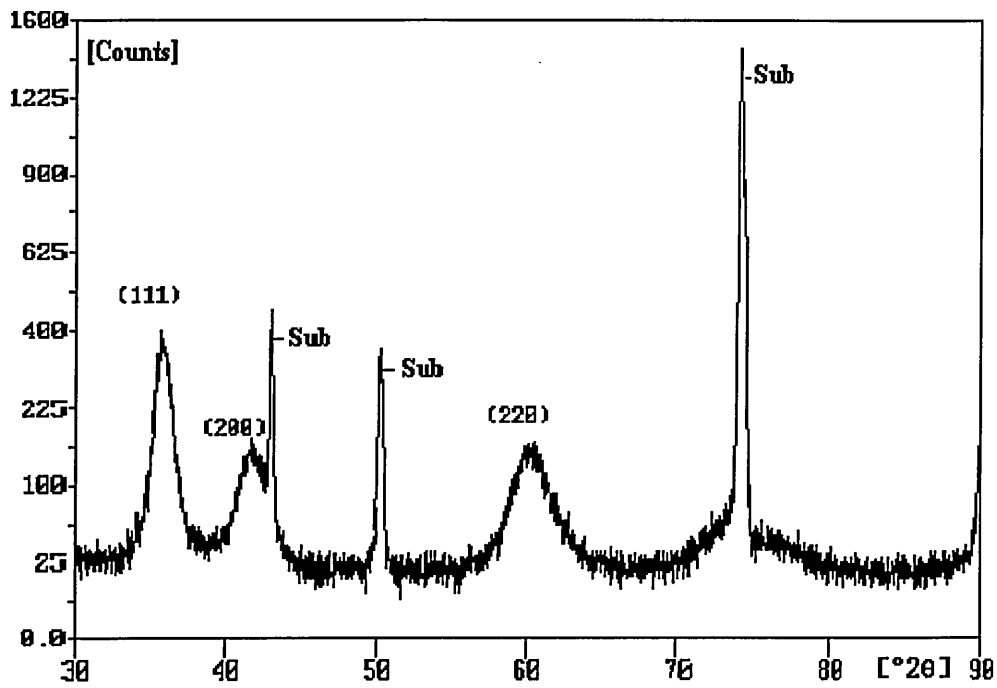


Fig 5.4.10 XRD pattern of TiCN coating from sample LT05

Table 5.4.5 Texture and lattice parameters of TiCN coatings at 240°C

PN	plane	I	I _R	T (%)	d(Å)	a (Å)	a* (Å)
LT01	111	444.18	46	62.6	2.484	4.302	4.26441 for TiC _{0.3} N _{0.7} and 4.29709 for TiC _{0.7} N _{0.3}
	200	209.19	100	13.6	2.136	4.272	
	220	146.76	40	23.8	1.518	4.293	
LT02	111	651.54	46	57.1	2.496	4.323	
	200	532.45	100	21.5	2.137	4.274	
	220	211.86	40	21.4	1.521	4.302	
LT03	111	276.98	46	24.3	2.494	4.320	
	200	278.89	100	11.3	2.150	4.300	
	220	637.42	40	64.3	1.537	4.347	
LT04	111	283.35	46	4.6	2.485	4.304	
	200	200.24	100	7.7	2.151	4.302	
	220	873.61	40	87.4	1.536	4.345	
LT05	111	538.36	80	48.5	2.500	4.330	
	200	288.47	100	11.9	2.161	4.322	
	220	382.26	60	39.6	1.534	4.339	

a* is the standard lattice parameter (TiC_{0.3}N_{0.7} or TiC_{0.7}N_{0.3})

It was observed that the texture varied as a function of composition as shown in fig 5.4.11. An increase in {220} component with a corresponding decrease in the {111} component was observed when carbon content, $C/(C+N)$, increased from 0.1 to 0.37. As the carbon content increased up to above 0.37, the {220} texture decreased whilst the {111} texture increased. The texture as calculated using the (200) planes did not exhibit greater variation as compared with that calculated using (111) and (220) planes.

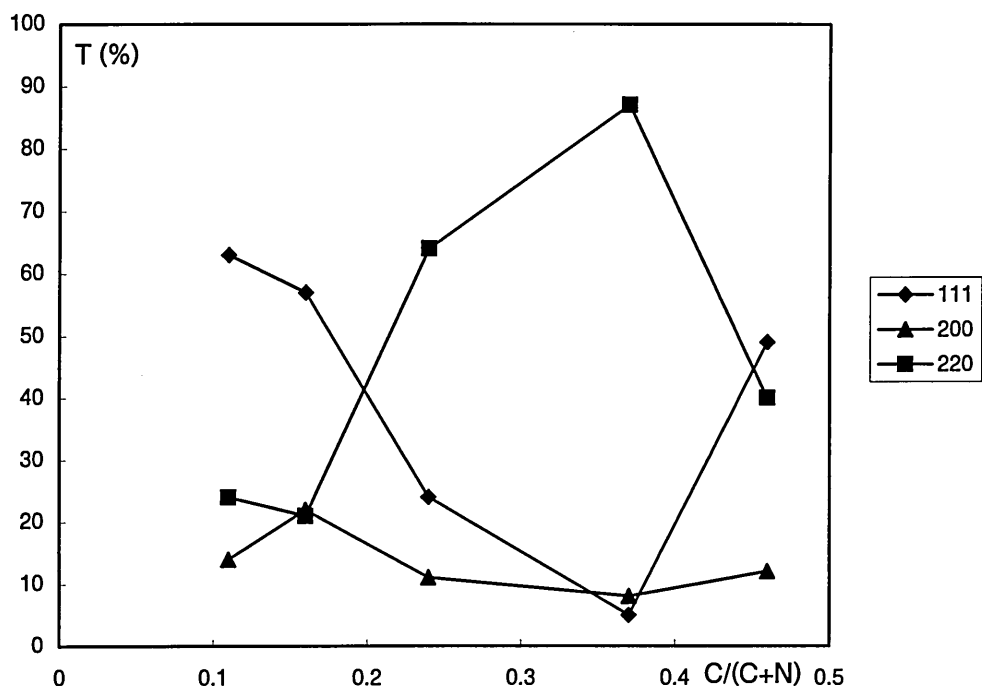


Fig 5.4.11 Texture coefficient dependence on composition of coating at 240°C

The lattice parameters as calculated from the experimentally determined interplanar spacings together with that of the JCPDS files are shown in fig 5.4.12 in which increased lattice parameters were found compared with those of the standard XRD JCPDS files. The lattice parameters calculated using interplanar spacings of (111) and (220) reflections were always larger than those calculated from the (200) reflection. The lattice parameters calculated using (200) reflection systematically increased with increasing carbon of the coating whilst those calculated from the (111) and (220) reflection did not show any systematic change with increasing carbon content.

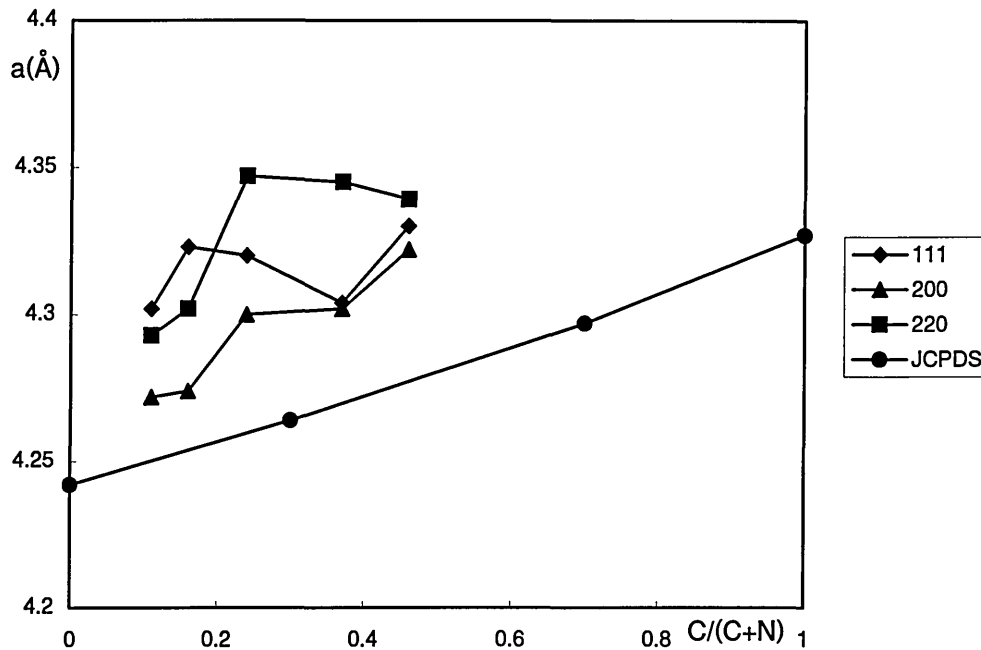


Fig 5.4.12 TiCN lattice parameter dependent on composition (deposited at 240°C)
 a, b, c, and d are standard lattice parameters of TiN, $TiC_{0.3}N_{0.7}$, $TiC_{0.7}N_{0.3}$, and TiC

5.4.5.2 TiCN coatings deposited at 340°C

The XRD patterns of TiCN coatings deposited at 340°C are shown in fig 5.4.13, 14, 15, 16, and 17 in which TiCN (111), (200), (220), and (311) were found to be the main reflections. It could be seen that in the films deposited at 340°C the carbon content had little effect on peak position. Table 5.4.6 shows the diffraction intensity of the relative (hkl) reflections, the random intensity according to standard XRD JCPDS files, the texture (T%), interplanar spacings, and the relative lattice parameters.

The texture as a function of composition $C/(C+N)$ is given in fig 5.4.18 in which it can be seen that the intensity of the {220} texture was at a maximum and the {111} texture a minimum at a carbon content of $C/(C+N) = 0.45$.

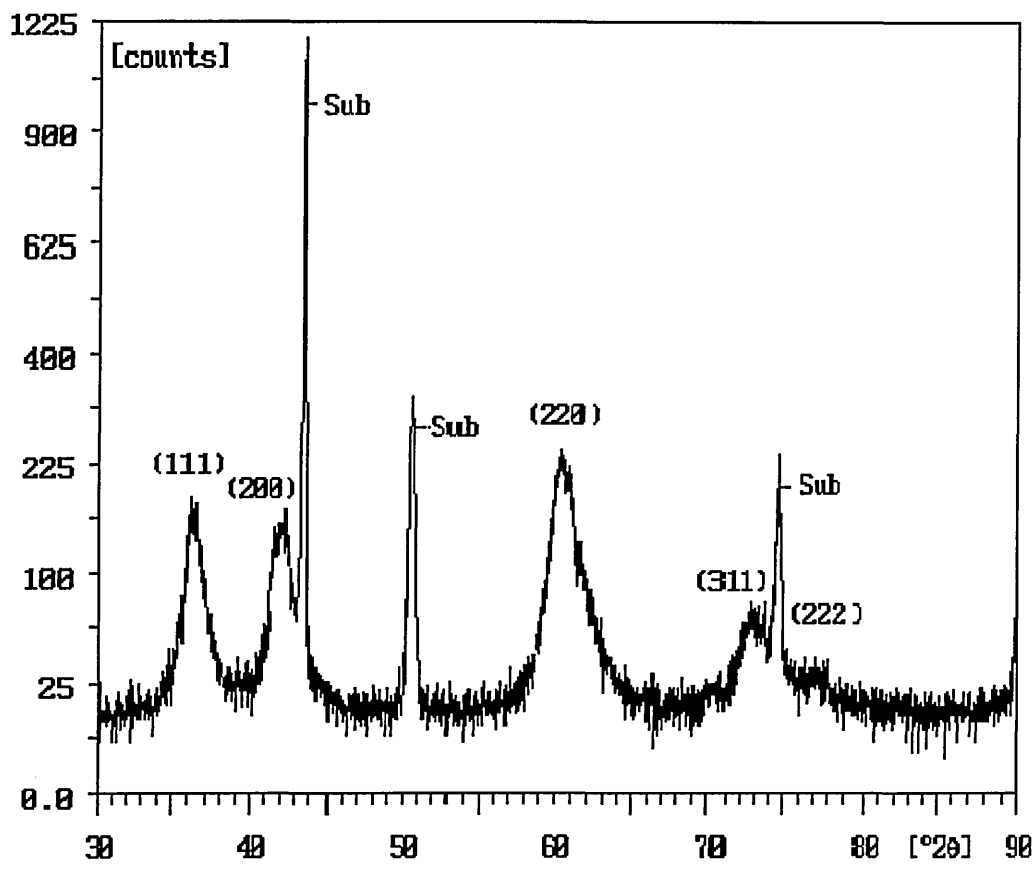


Fig 5.4.13 XRD pattern of TiCN coating deposited at 340°C (HT01)

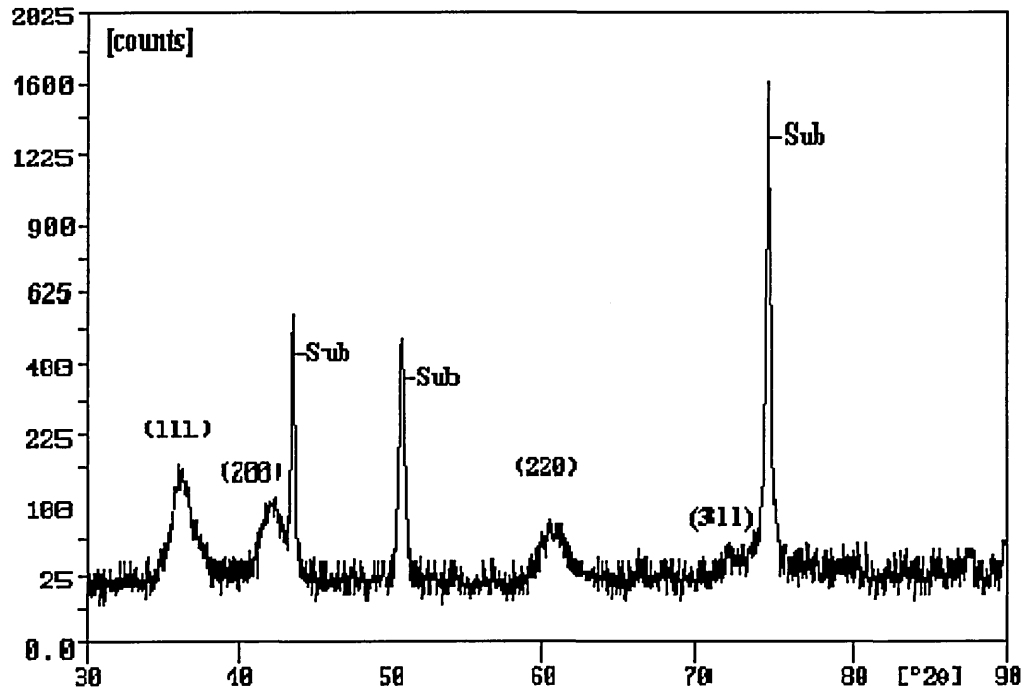


Fig 5.4.14 XRD pattern of TiCN coating deposited at 340°C (HT02)

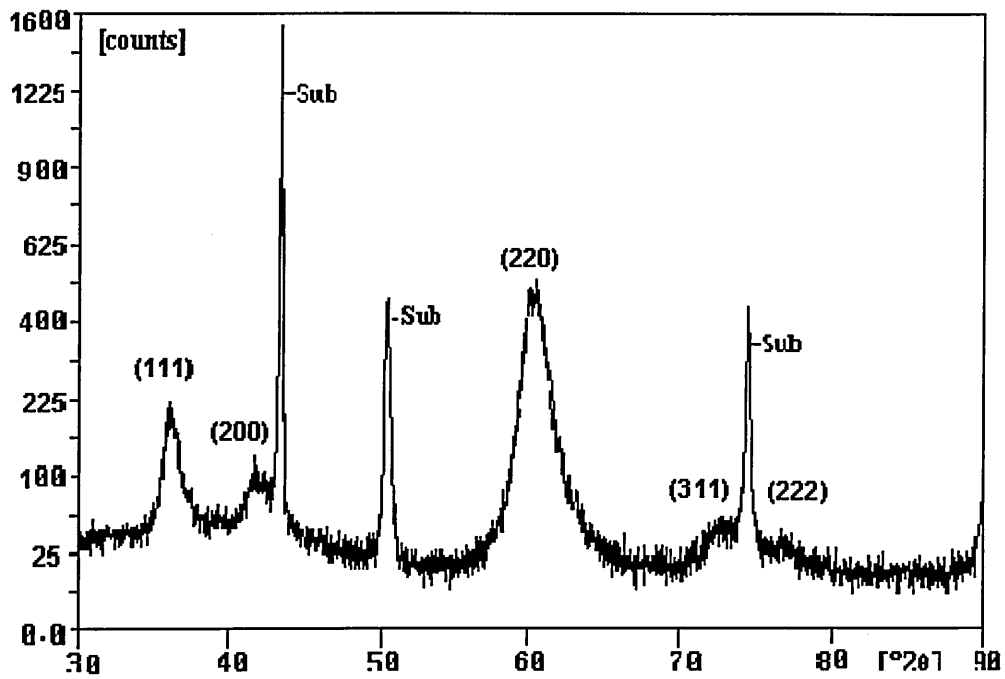
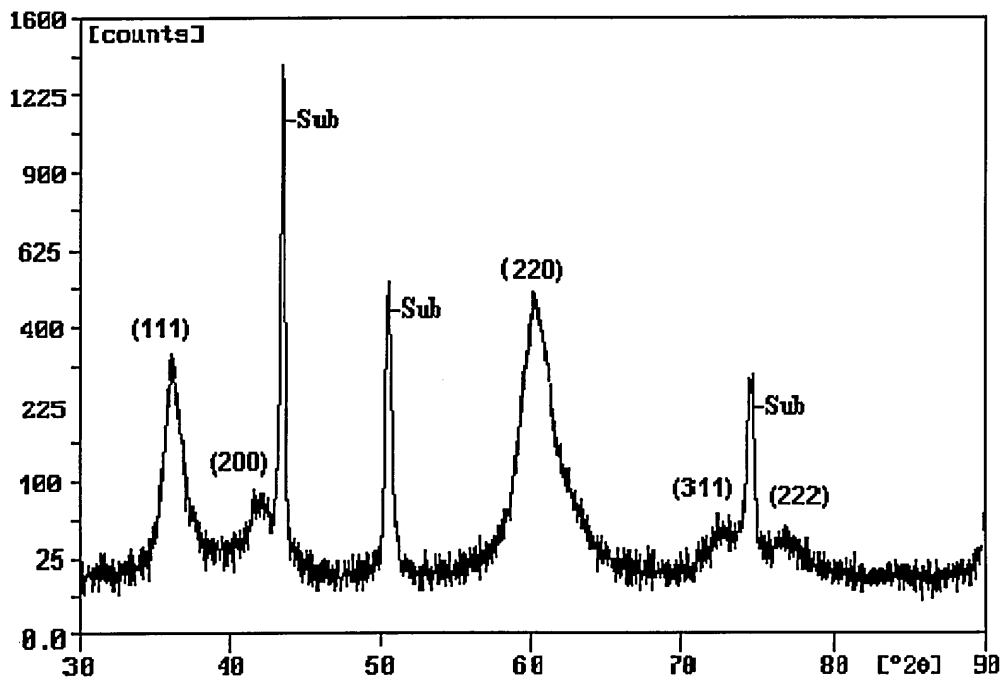
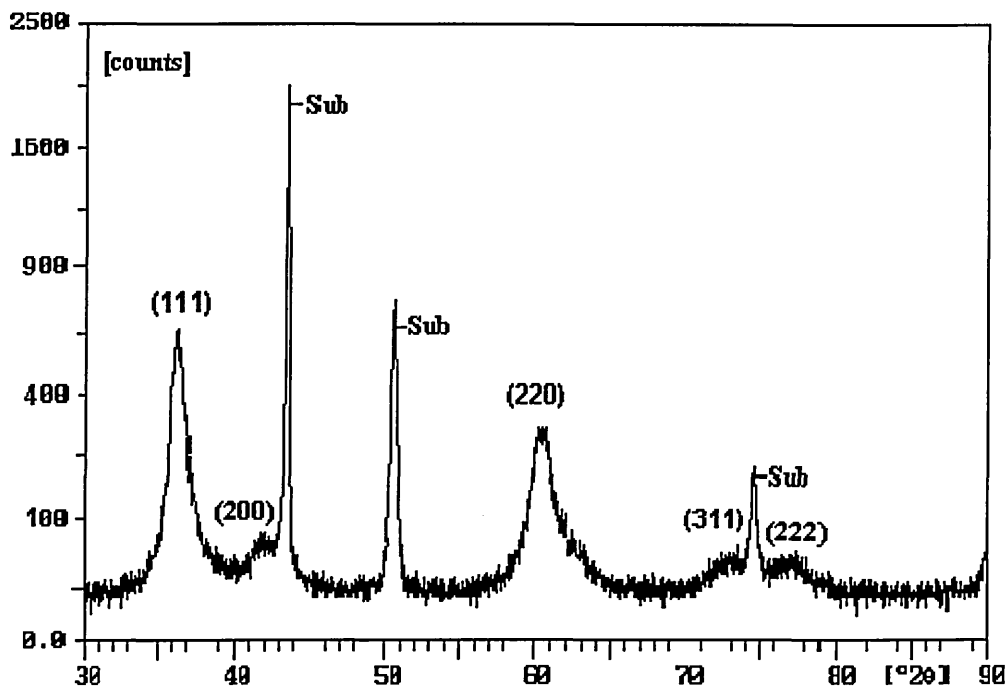


Fig 5.4.15 XRD pattern of TiCN coating deposited at 340°C (HT03)



5.4.16 XRD pattern of TiCN coating deposited at 340°C (HT04)



5.4.17 XRD pattern of TiCN coating deposited at 340°C (HT05)

Table 5.4.6 Texture and lattice parameters of TiCN coatings at 340°C

PN	plane	I	I _R	T (%)	d(Å)	a (Å)	a* (Å)
HT01	111	160.21	59	17.5	2.47085	4.27963	4.26441 or 4.29709
	200	161.13	100	10.4	2.14484	4.28968	
	220	358.57	46	50.3	1.52480	4.32192	
	311	84.42	25	21.8	1.29405	4.29911	
HT02	111	125.08	59	39.4	2.46437	4.26841	
	200	100.80	100	18.7	2.13781	4.27562	
	220	90.57	46	36.6	1.52482	4.31284	
	311	7.10	25	5.2	1.30950	4.34312	
HT03	111	134.45	59	9.5	2.47830	4.29250	
	200	130.99	100	5.5	2.14709	4.29418	
	220	821.66	46	74.4	1.53460	4.34050	
	311	63.56	25	10.6	1.30440	4.32620	
HT04	111	293.13	59	19.0	2.47401	4.28510	
	200	114.53	100	5.5	2.14747	4.29494	
	220	758.23	46	62.0	1.53055	4.32905	
	311	90.46	25	13.0	1.29907	4.30853	
HT05	111	572.92	59	45.6	2.47296	4.28329	
	200	106.99	100	5.1	2.14709	4.29418	
	220	391.24	46	39.9	1.52970	4.32660	
	311	50.25	25	8.7	1.30059	4.31357	

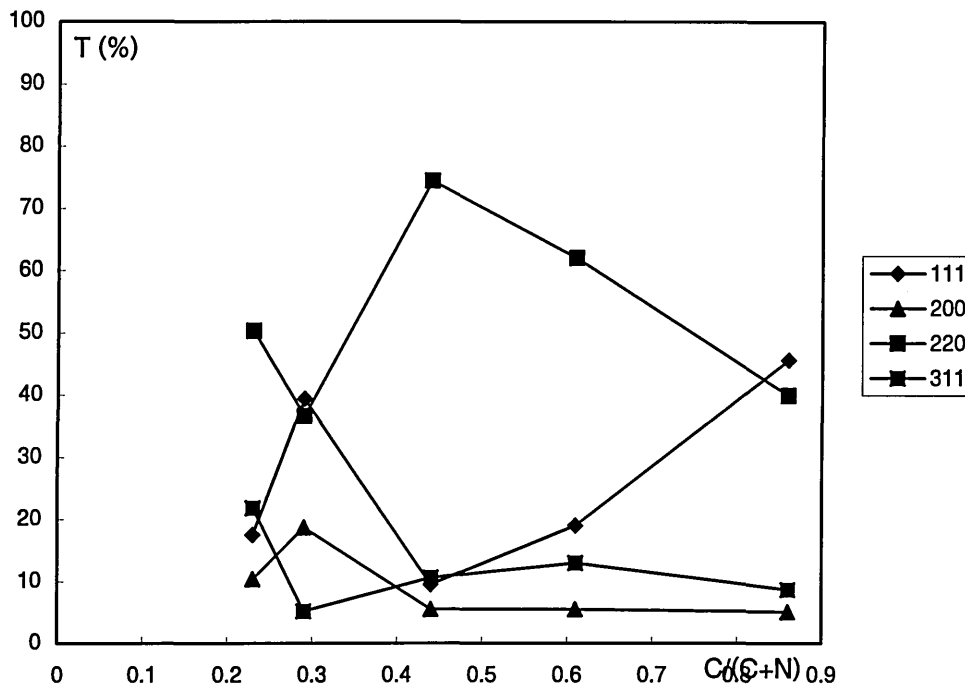


Fig 5.4.18 Texture coefficient dependence on composition of coating at 340°C

The lattice parameter dependency on composition is shown in fig 5.4.19 in which the lattice parameters calculated using (220) and (311) reflections were always larger than those calculated using (111) and (200) reflections. It can be seen that the lattice parameter value calculated using (111) and (200) reflections was smaller than that of the standard JCPDS files when composition was at a high carbon level, $C/(C+N) > 0.6$. When the composition was at low carbon level, $C/(C+N) < 0.6$, however, the value was larger than those of the standard JCPDS value.

In general (coatings deposited under both temperature conditions, 240°C and 340°C), the lattice parameters as calculated using different reflections were different. The lattice constants, a_0^{111} , a_0^{200} , a_0^{220} , and a_0^{311} were a menace of the lattice distortion. In the films investigated, both {111} and {110} texture were observed as the preferred orientations.

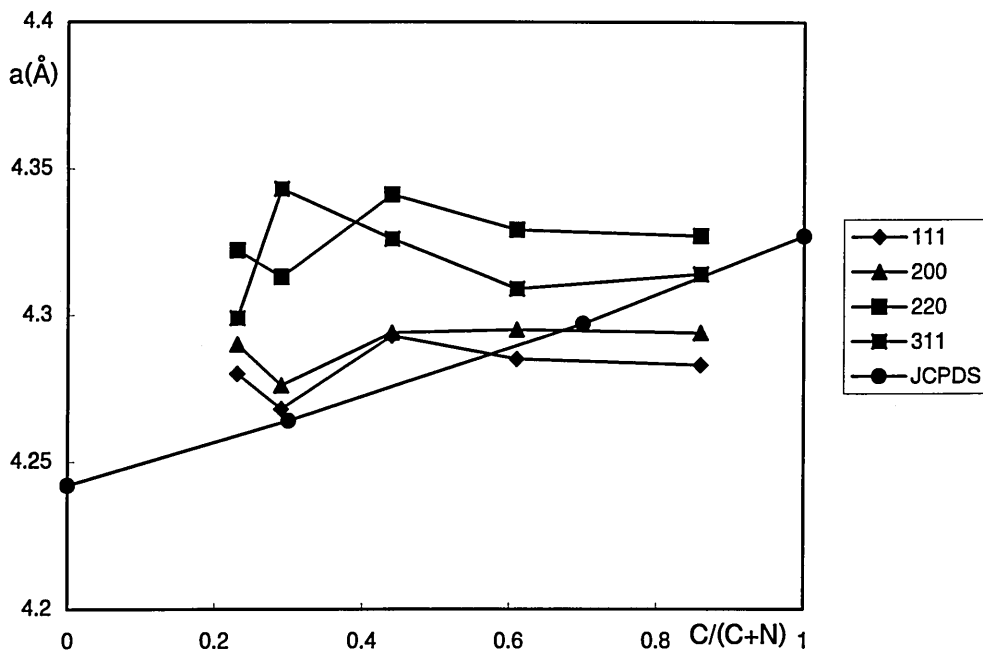


Fig 5.4.19 TiCN lattice parameter dependent on composition (deposited at 340°C)
a, b, c, and d are standard lattice parameters of TiN, TiC_{0.3}N_{0.7}, TiC_{0.7}N_{0.3}, and TiC

5.5 Triple layer TiCN coating

5.5.1 Experiment

A triple layer TiCN coating was produced by adjusting the reactive gas flow rates and keeping the argon flow rate constant. The process parameters are recorded in table 5.5.1.

Table 5.5.1 Process parameters of sandwich TiCN coating

Time (min)	N ₂ Flow (sccm)	CH ₄ flow (sccm)	N ₂ pressure (10 ⁻⁴ mbar)	CH ₄ pressure (10 ⁻⁴ mbar)	total pressure (10 ⁻³ mbar)
00-40	13.6	0	1.004	1.881x10 ⁻³	2.7541
40-80	4.0	7.8	0.2606	0.4984	2.7431
80-120	9.5	4.0	0.5513	0.2506	2.7538

Adjustment of the reactive gas flow rate during the process was carried out by using the relative intensity of the Ti plasma density as measured using a Ti⁺ emission optical spectrometer as a reference. The reactive gas flow rates, i.e. N₂ and CH₄, were adjusted

such that the Ti plasma density remained constant throughout the process. The amount of adjustment was considered to keep the Ti plasma density constant so that the sputtering rate would be also constant, and film growth would be uniform. In the first stage, nitrogen gas was introduced into the chamber; hence a TiN layer was deposited. In the last two stages, both N₂ and CH₄ were introduced and therefore two layers of TiCN with different C/N ratio were produced. The temperature was kept at 350°C. Cathode power, bias voltage, and coil current were kept at 4x10kW, 120V, and 4x10A respectively.

5.5.2 GDOES result

The titanium content was almost constant throughout the depth of coating as shown in fig 5.5.1 whilst the nitrogen and carbon concentration varied through the coating. The average atomic ratio (C+N)/Ti was about 43/57. Titanium nitride was formed in the region close the coating/substrate interface. Titanium carbonitride was deposited in both the middle and top layers. In the middle layer, the carbon to nitrogen ratio is high (C/N=1.44), whilst the top layer the carbon to nitrogen ratio is low (C/N=0.27).

(See page 128 for fig 5.5.1)

Fig 5.5.1 Composition depth profile of triple layer TiCN film

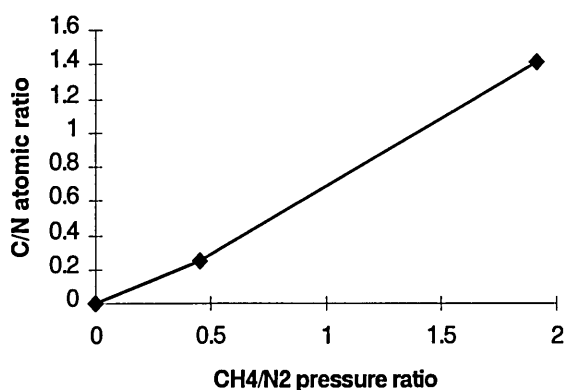


Fig 5.5.2 C/N of triple TiCN coating dependent on CH₄/N₂ pressure ratio

It can be seen in Fig 5.5.2 that the C/N ratio, as measured by GDOES, is a function of the ratio of reactive gas partial pressure, higher the CH_4/N_2 ratio the higher carbon content in the coating.

5.5.3 XRD result

The XRD pattern of sandwich TiCN coating is shown in fig 5.5.3 in which the (111), (200), (220), (311), and (222) reflections for TiCN were observed. Even though there was a layer TiN adjacent to the substrate, there were no obvious diffraction peaks belonging to the TiN phase. This may result from peak-overlaps peaks since the peaks for TiN are too close to those of TiCN. An other reason is that the carbon from the adjacent TiCN layer diffused into the TiN layer and therefore there was no TiN phase present in the film. The texture were 16.8%, 9.6%, 51.6%, and 22.1% as calculated using TiCN (111), (200), (220) and (311) reflections. The preferred orientation was {110} as compared with the standard XRD JCPDS file.

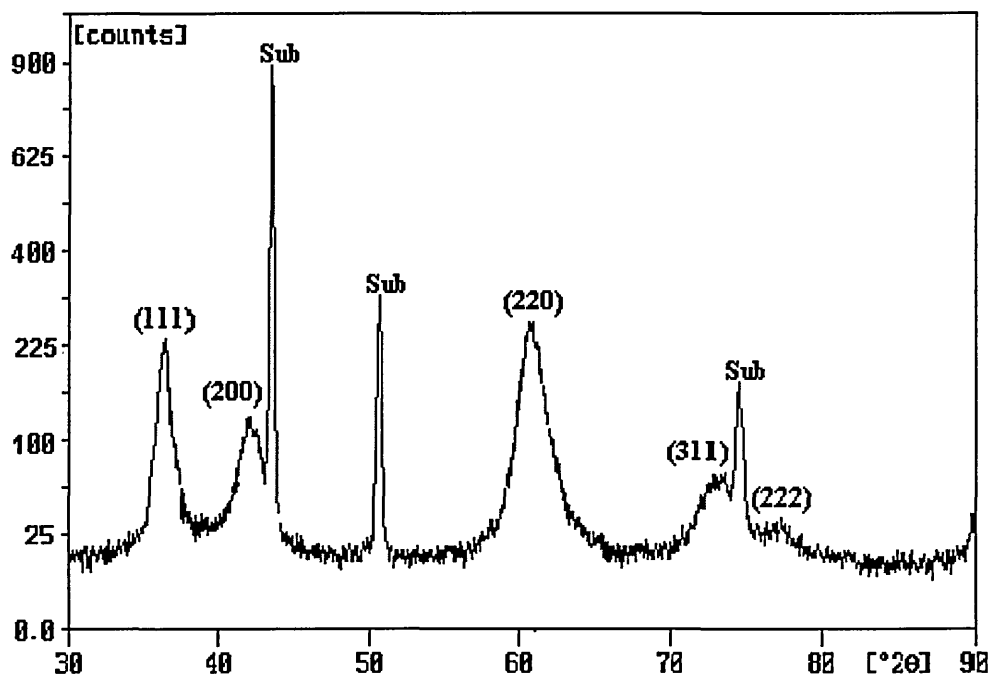


Fig 5.5.3 XRD pattern of sandwich TiCN coating

5.5.4 SEM and hardness result

A film of about 4 μ m thickness with different columnar layers was produced as shown in fig 5.5.4 a, b, and c. The columnar growth was normal to the substrate surface. It was clear that three distinct layers existed and with a different column size. The largest column size was found in the middle layer with the most understoichiometric composition as see fig 5.5.1 and 5.5.4. The finest columnar structure was found in the top layer with composition close to stoichiometry. In the TiN layer close to the coating/substrate interface, the variation of the cross section structure was similar to that of the middle and top layers. A cross section through the sandwich layered coating showing secondary electron image together with EDX X-ray distribution maps and line scans for Ck α , Nk α and Tik α is shown in fig 5.5.4. The results of the EDX X-ray maps and line-scans were similar to the that of the GDOES depth profile. The hardness was measured to be Hv 2861 using a load of 10g on the Vickers indenter.

(See page 129 for fig 5.5.4)

Fig 5.5.4 SEM cross sectional images of triple TiCN coating
a. Fracture cross section, b. X-ray map, c. X-ray line scan

5.6 Discussion of chapter 5

The relation between ratio of N/C in the TiCN coating and the ratio of the corresponding reactive gas flow N₂/CH₄ is noticeable and the variation is almost linear as see fig 4.4. This variation is in agreement with the report⁽⁵⁾ in the range of N₂/CH₄ from 1 to 3. In general, if the total chamber pressure is constant, the composition within the coating will proportional to the reactive gas flow. It can also be seen that when high target power (HT) is used during the deposition, the N/C within the coating is lower than that within the coating deposited using low target power (LT) deposition. This is may be associated with that the carbon in the plasma is more active than the nitrogen as the carbon can be deposited directly from the plasma⁽⁶⁾. High target power leads to high plasma density within the chamber and therefore high carbon concentration is formed in the coating.

TiCN coating was reported^(5,7) to be strongly textured by (111) planes as deposited by using cathodic arc and electron beam evaporation techniques. There are two planes, (111) and (220), however, are strongly textured in the TiCN coatings as deposited using unbalanced magnetron sputtering technology. The strong texture of TiCN (220) may be resulted from the bombardment of intensive energetic ions which are produced by the unbalanced magnetron sputtering technique. As the ion bombardment produces residual stress within the coating, the lattice parameters as calculated using the (220) as well as the other interplanar spacings are general larger than that referred to the JCPDS file.

The hardness of TiCN coating is a function of the stoichiometric coefficient. Even though the variation of hardness dependency on the stoichiometric coefficient intends to show high stoichiometric coefficient may results in high hardness, it does not mean the hardness will increase further when stoichiometric coefficient exceeds 1. In fact there may be two variations afterwards. One is that the hardness may increase if the composition is carbon rich. The extra carbon may be formed as diamond like film with hardness high up to Hv 7000 as reported using the ion-assistant deposition⁽⁶⁾. Another is that hardness may decrease if the composition is nitrogen rich. The hardness of over-stoichiometric TiN films decreases greatly with a increase of nitrogen within the coating⁽⁸⁾. The nitrogen rich film is resulted from high nitrogen partial pressure during a deposition. The high nitrogen partial pressure causes a compound formed on the target. As the target is poisoned, the sputtering yield is reduced which resulted in the deposits arrive at the substrate with less energy and therefore in-dense and pours film will be formed. As a result the hardness is greatly reduced. The TiCN coatings presented in this thesis have the hardness value in a range from HV 3500 to 4000 when the stoichiometric coefficient is near to 0.6. The TCN coatings with such high hardness may be the candidates used for wear resistant applications.

5.7 Conclusion of chapter 5

- TiCN coatings can be deposited using industrial sized unbalanced magnetron sputtering coating technique and the composition of TiCN coatings is dependent on the reactive gas partial pressures. The C/N ratio in the coating has a linear relationship with the CH_4/N_2 flow ratio.
- High target power process leads to higher substrate temperature by which higher carbon concentration is formed in the coating.
- Hardness is a function of stoichiometric coefficient. The maximum hardness is achieved when stoichiometric coefficient is 0.63.
- (111) and (220) are the dominant planes in most of the coatings. There is a large variation of texture dependent on composition as calculated using (111) and (220) reflections whilst the texture coefficients calculated using (200) and (311) reflections are relatively stable with composition.
- Multilayer TiN-TiCN coating can be produced using the reactive gas flow control during a deposition process. The coating has columnar structure with orientation normal to the substrate surface. The column size is dependent on composition and layer with composition close to stoichiometry leads to high density film.

References

- (1) W. D. Sproul, Surface and Coating Technology, V33(1987)73
- (2) W. D. Sproul and P. J. Rudnik, Thin Solid Films, V171(1989)171
- (3) J.-E. Sundgren, B.-O. Johansson, S.-E. Karlsson and H.T.G. Hentzell, Thin Solid Films, V105(1983)367
- (4) H.T.G. Hentzell, B. Andersson and S.E. Carlsson, Thin Solid Films, V85(1981)177
- (5) E. Damond and P. Jacquot, Materials Science and Engineering, A140(1991)838
- (6) J.E. Sundgren and H.T.G. Hentzell, Journal of Vacuum Science and Technology, A4(1986)2259
- (7) M. Tamura and H. Kubo, Surface and Coating Technology, V49(1991)194
- (8) J. Musil, S. Kadlec and J. Vyskocil, Thin Solid Films, V167(1988)107

List of figures referred to the chapter 5

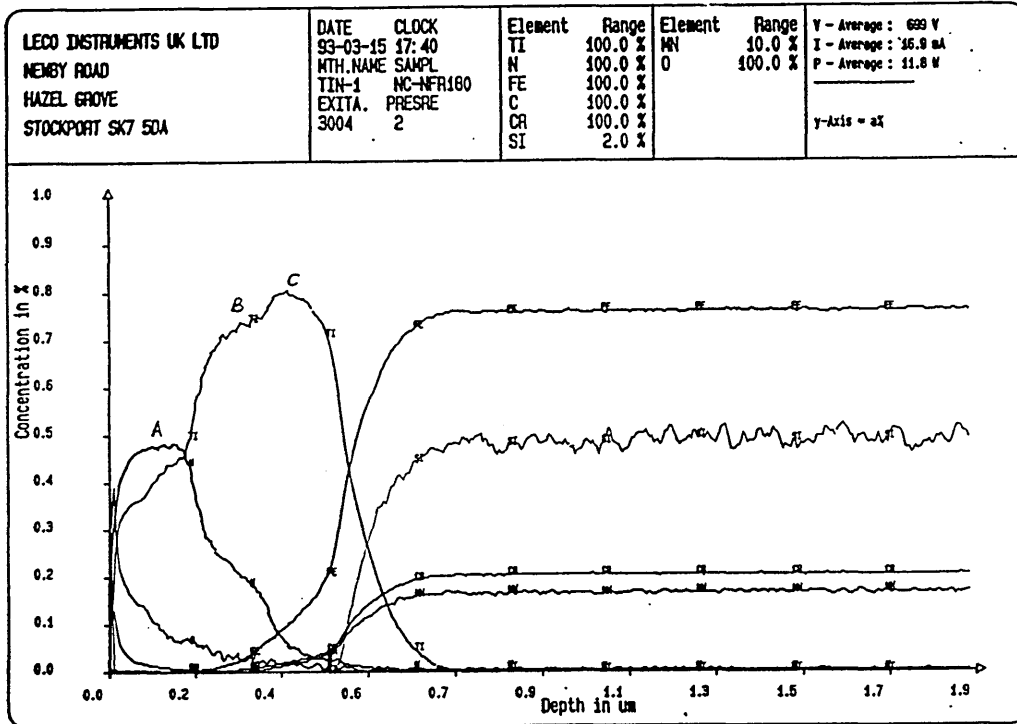


Fig 5.2.4 Concentration depth profile of film deposited using low target power

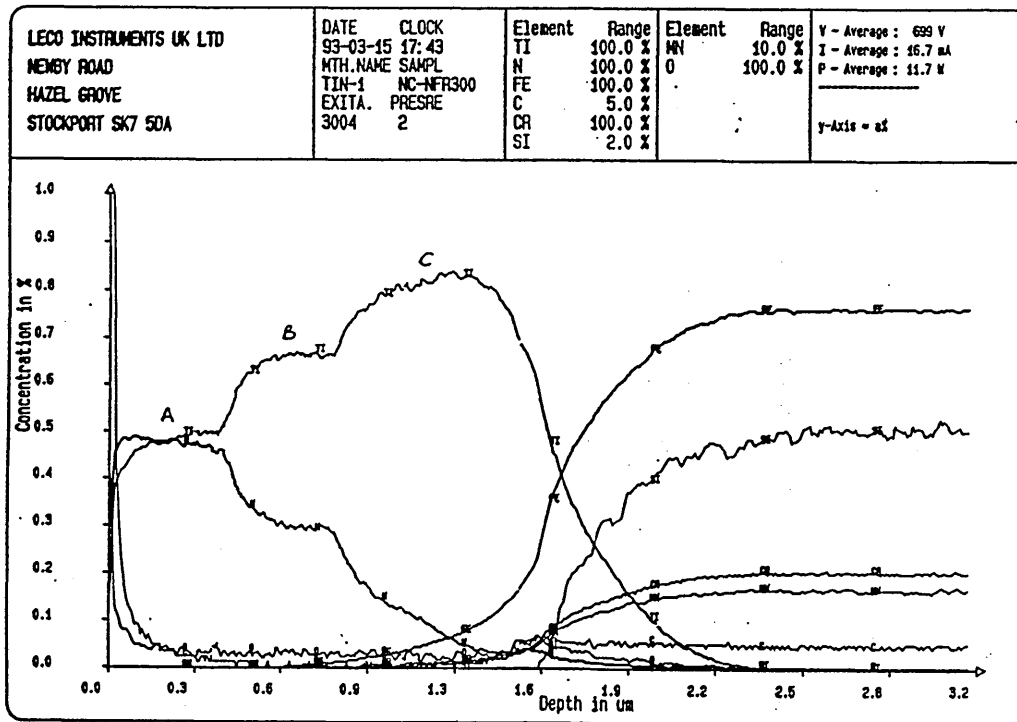


Fig 5.2.5 Concentration depth profile of film deposited using medium target power

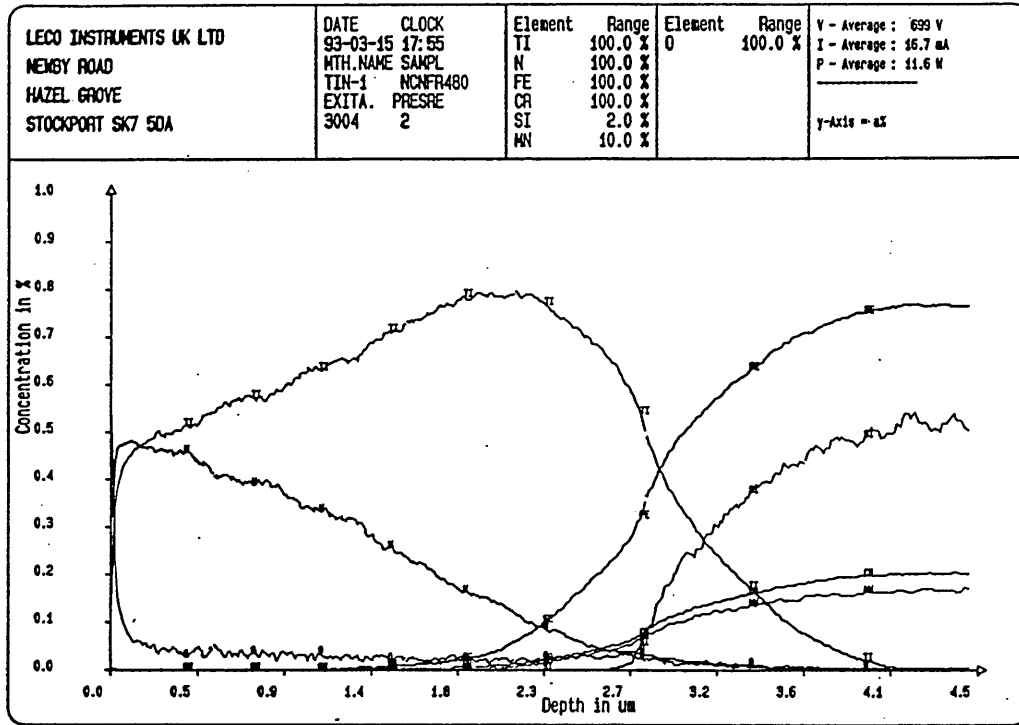


Fig 5.2.6 Concentration depth profile of film deposited using high target power

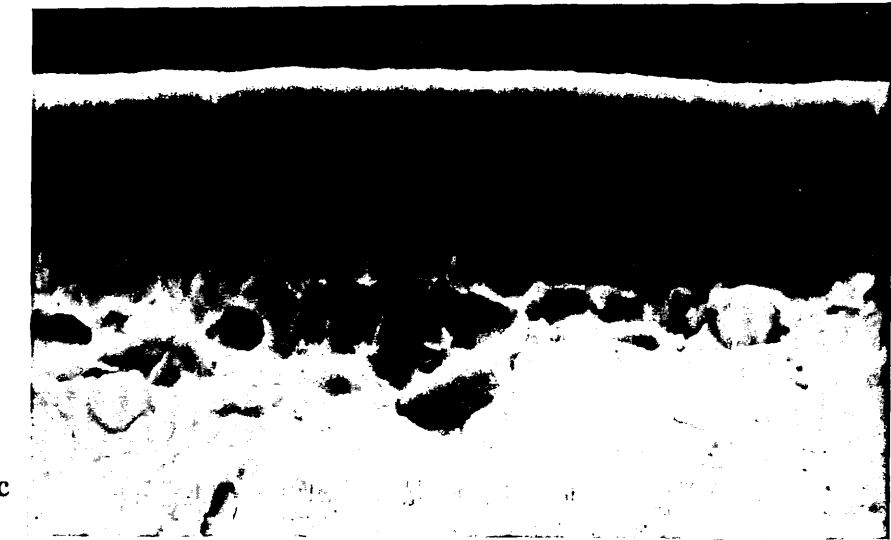
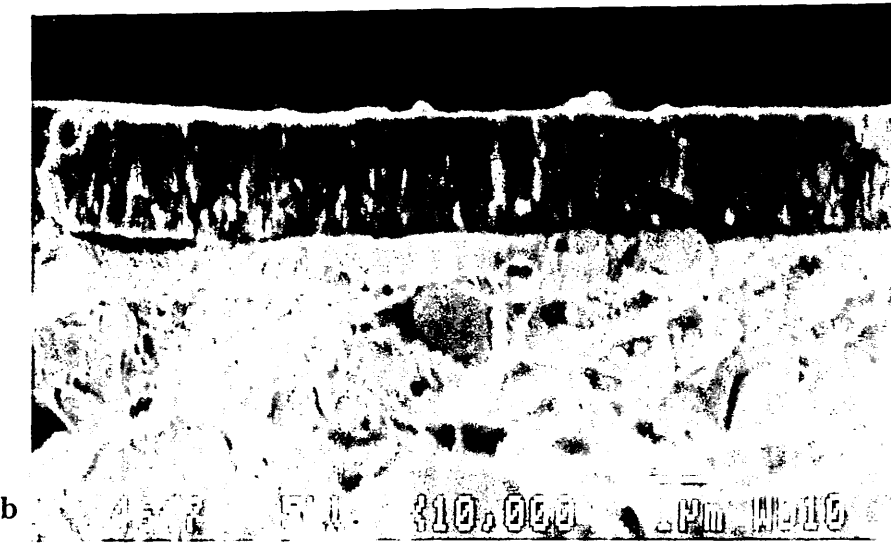
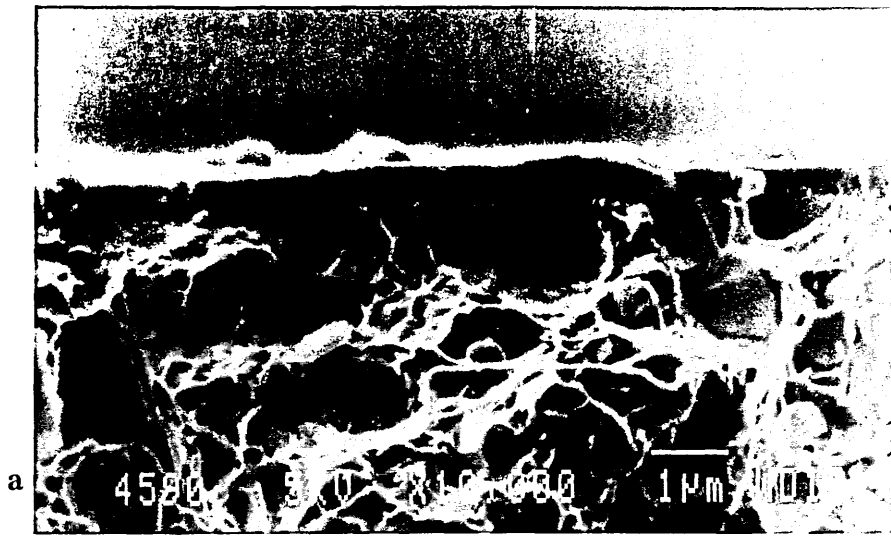


Fig 5.2.10 SEM fracture cross sectional images of stepwise TiN coatings
a. deposited at LP, b. deposited at MP, c. deposited at HP

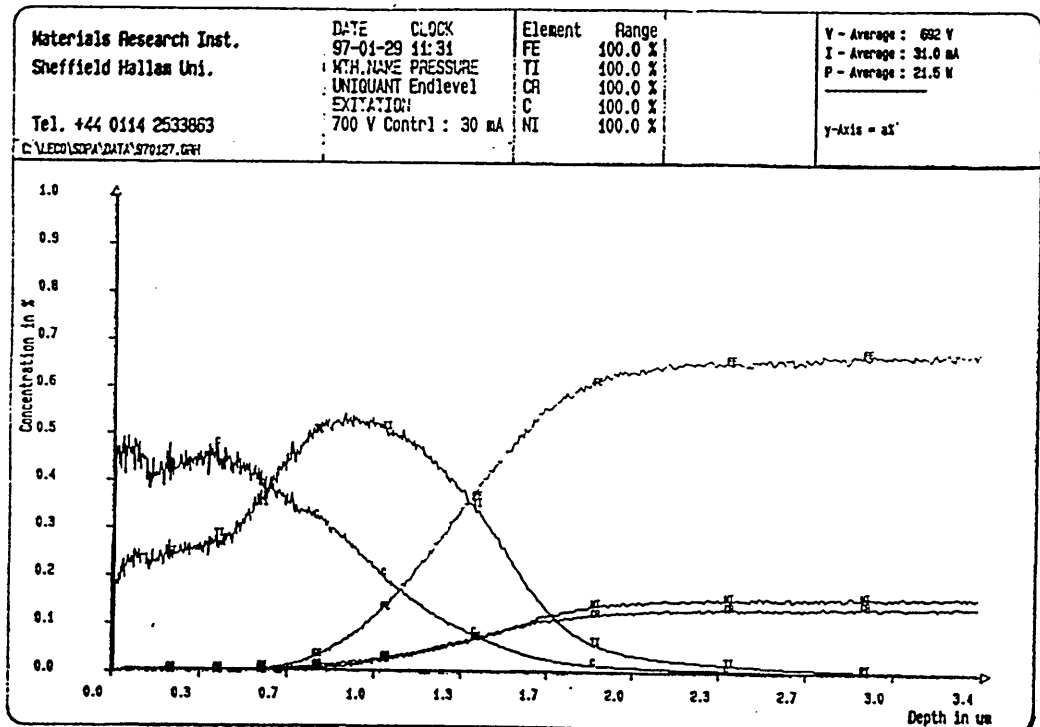


Fig 5.3.2 Concentration depth profile of stepwise TiC film deposited at LP

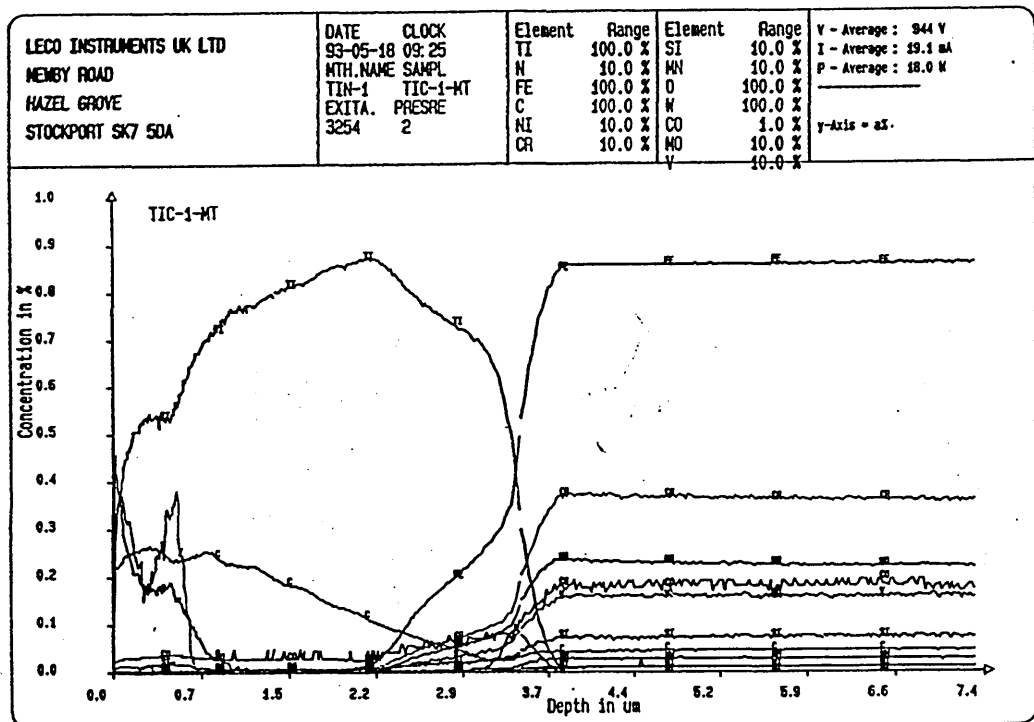


Fig 5.3.3 Concentration depth profile of stepwise TiC film deposited at MP

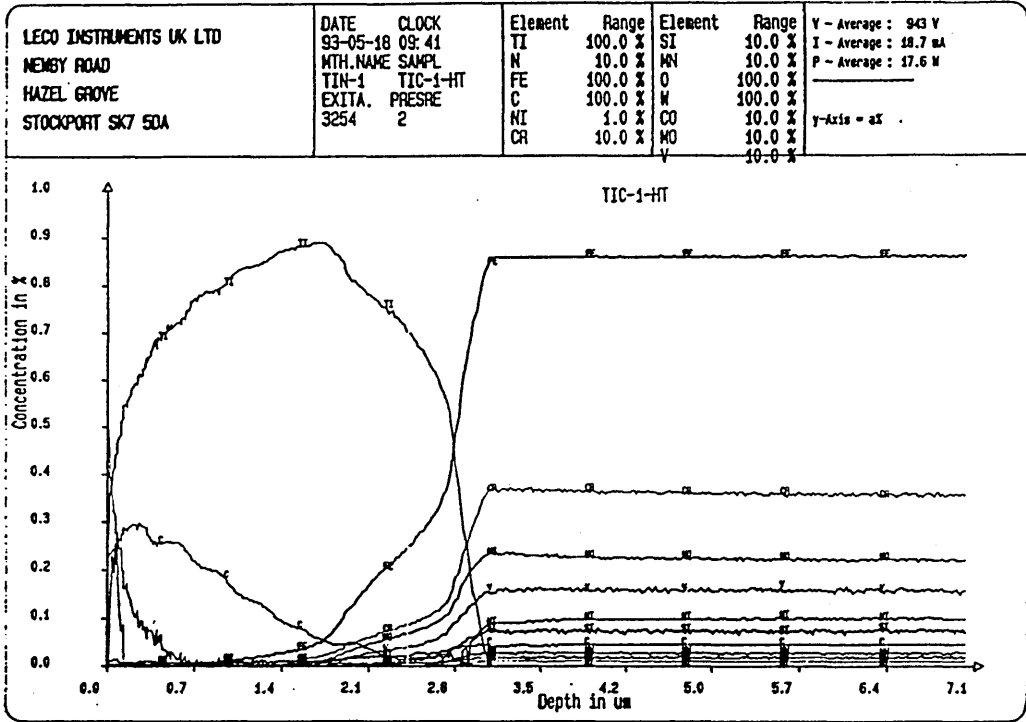


Fig 5.3.4 Concentration depth profile of stepwise TiC film deposited at HP



Fig 5.3.8 SEM images of the stepwise TiC coatings
deposited at a. LP, b. MP, c. HP

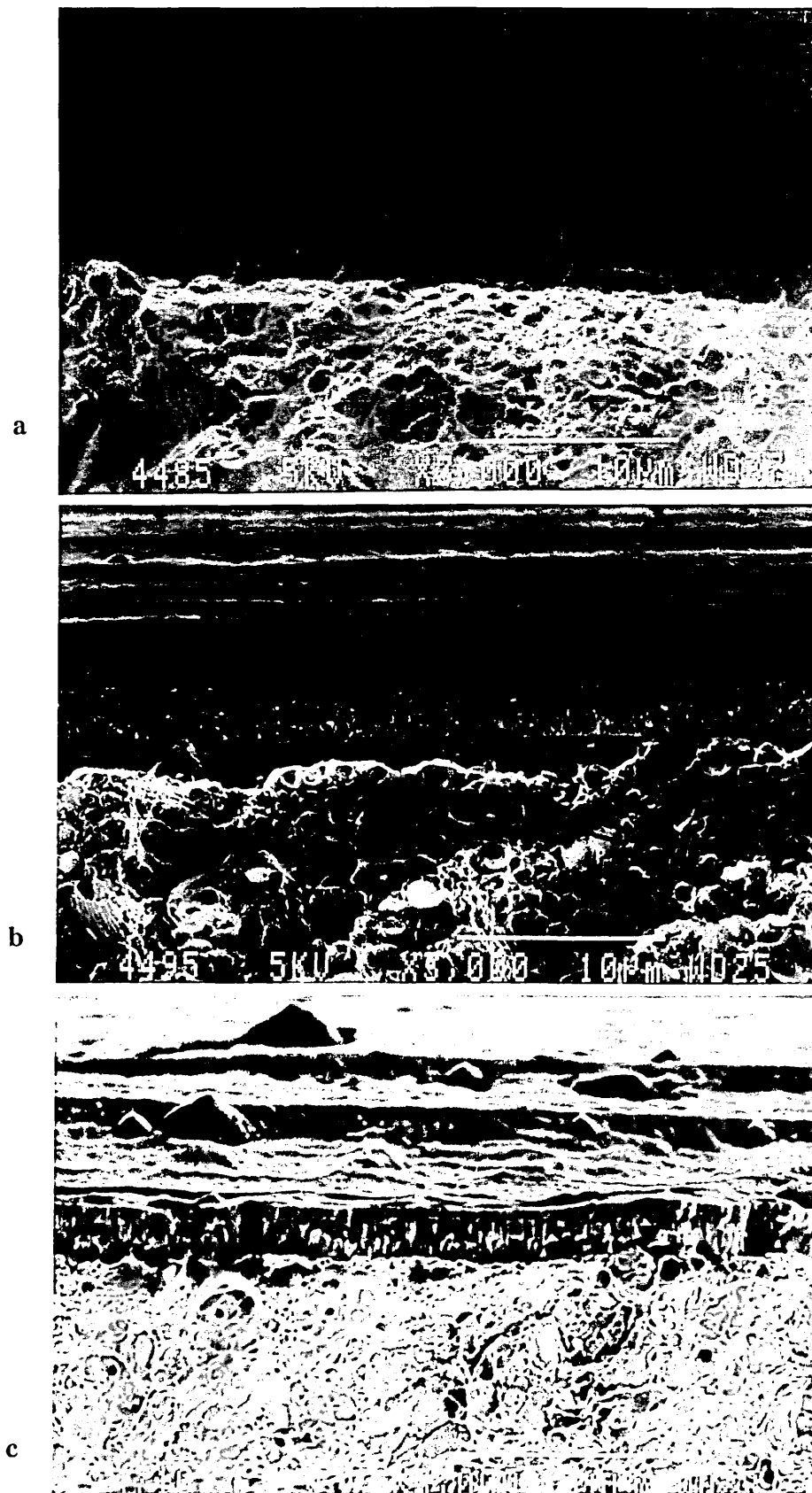


Fig 5.3.9 Outer edge images of the fracture cross section of the stepwise TiC coatings deposited at a. LP, b. MP, c. HP

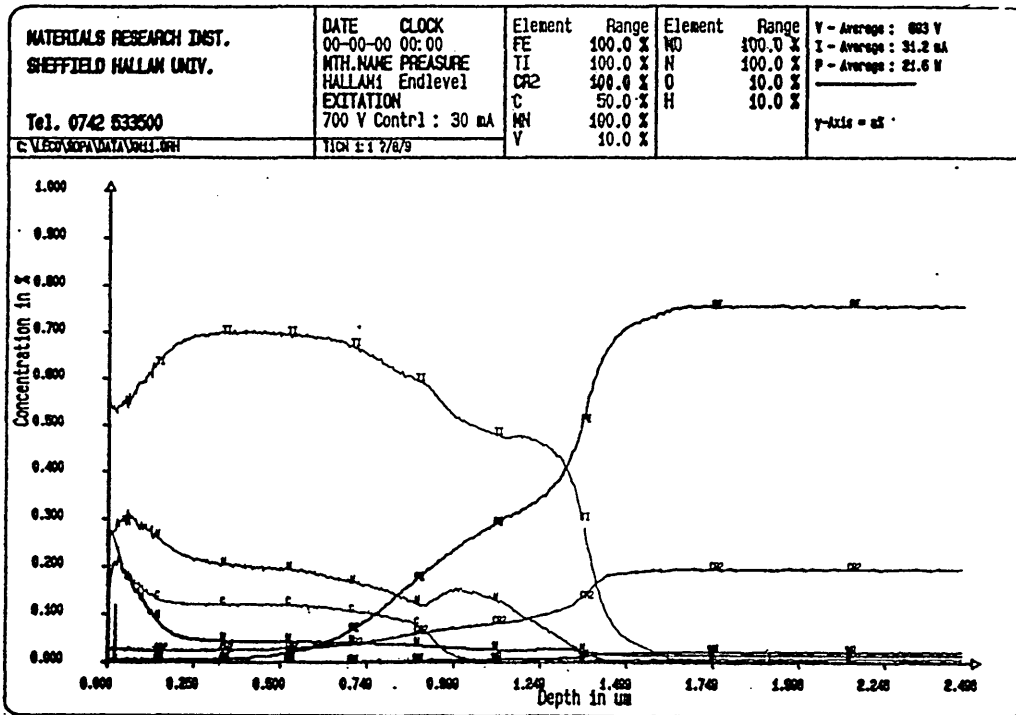


Fig 5.4.2 Composition depth profile of TiCN film deposited at LT temperature

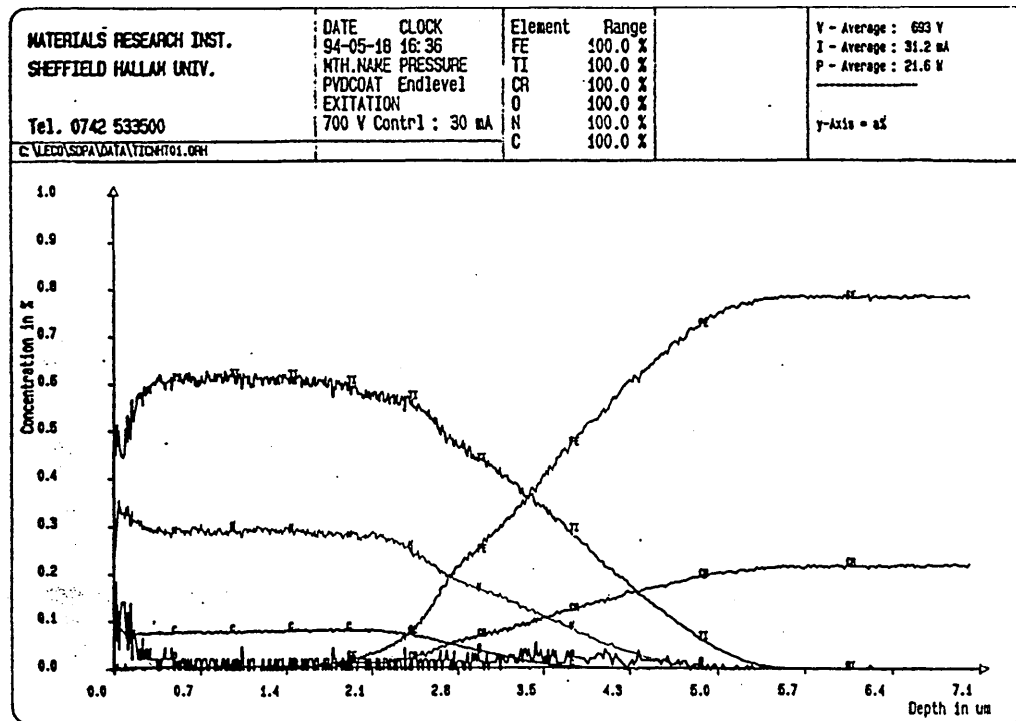


Fig 5.4.3 Composition depth profile of TiCN film deposited at HT temperature

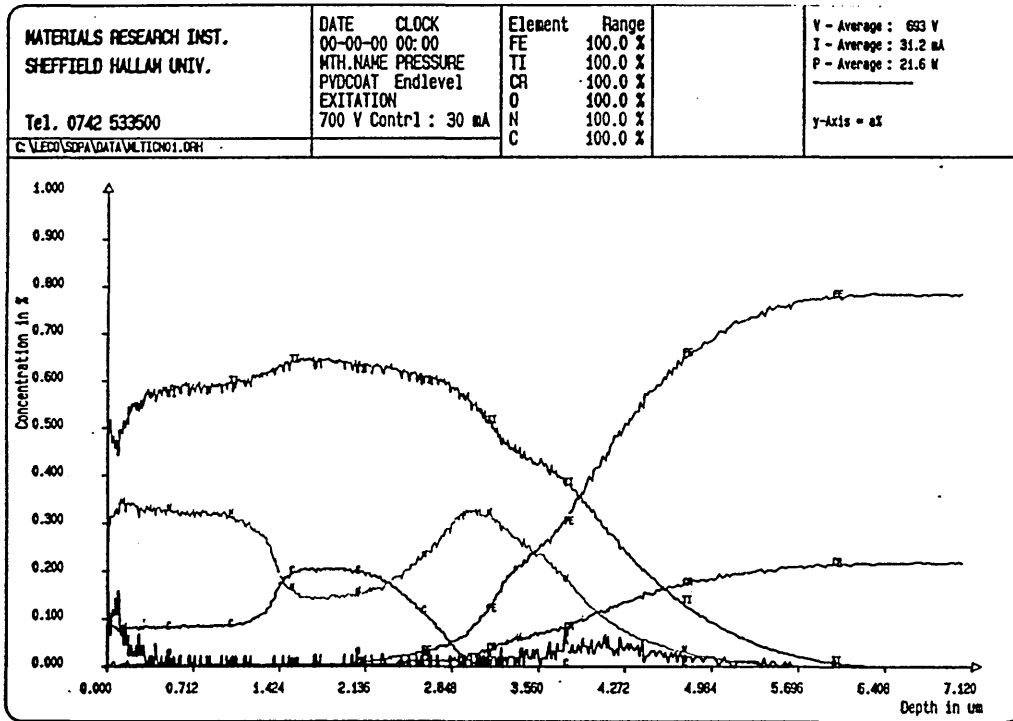


Fig 5.5.1 Composition depth profile of triple layer TiCN film

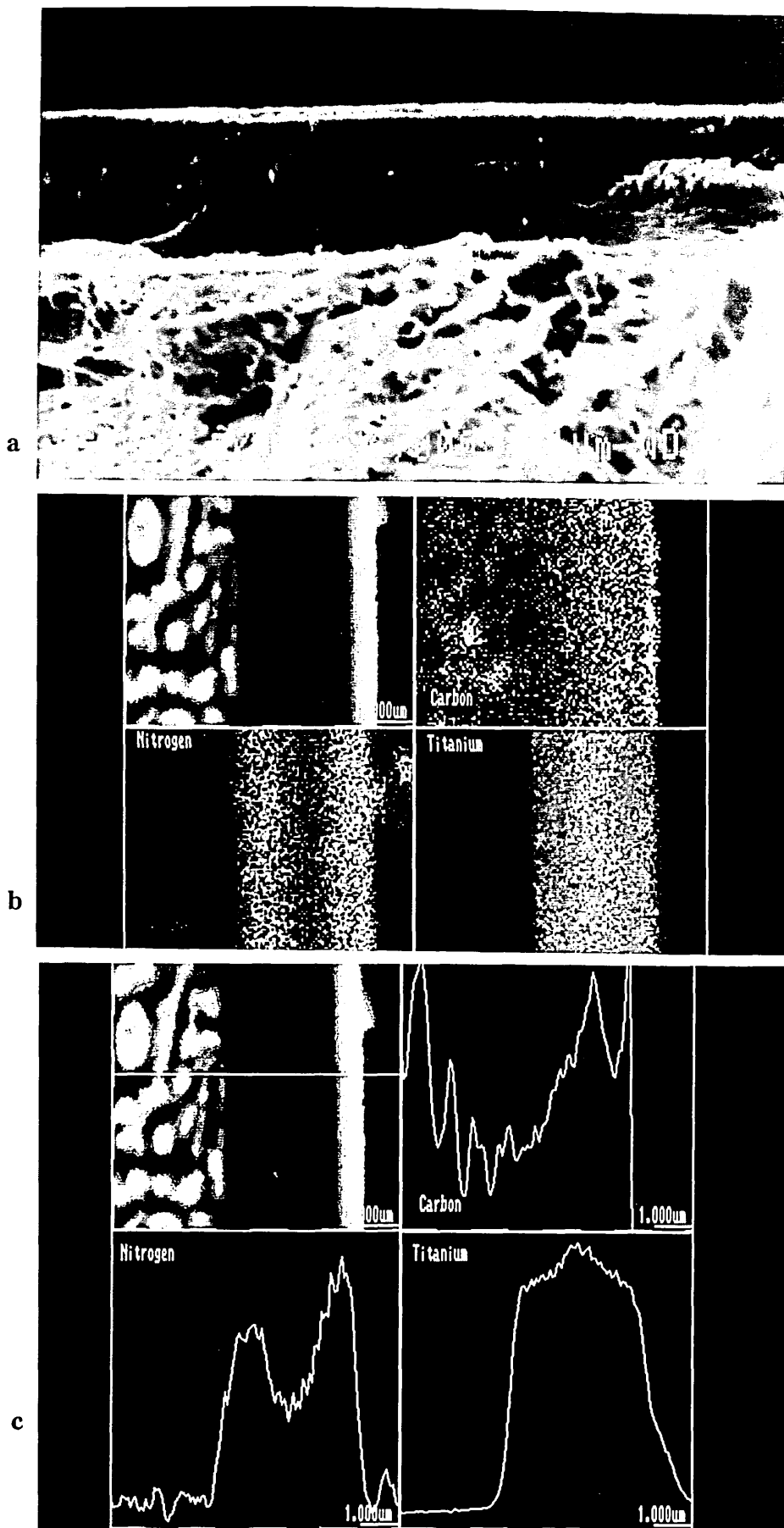


Fig 5.5.4 SEM cross sectional images of triple later TiCN coation
 a. Fracture cross section, b. X-ray map, c. X-ray line scan

6. Uniform Ti-N coatings deposited at 350°C

Uniform Ti-N coatings were deposited to study the phase development, especially the Ti_2N phase in the growing films with different compositions at a relative low temperature of 350°C. The development of Ti_2N phase was found to be critically dependent on the coating composition which was found to be sensitive to the nitrogen partial pressure during deposition. The physical properties, such as hardness, adhesion were investigated together with microstructure using cross sectional SEM. The practical application of the Ti-N coatings containing the Ti_2N phase composition was carried out using a drill test. The high speed steel twist drill coated films containing the Ti_2N phase composition had a very good drilling efficiency which was comparable with the drills coated with stoichiometric TiN film.

6.1 Experimental parameters and arrangement

Uniform Ti-N coatings (composition sub-stoichiometric to stoichiometric) were deposited at 350°C using the unbalanced magnetron sputtering process. A heater was used to warm the chamber and to heat the substrate up to a temperature of 350°C during the evacuating procedure. The heater was also used during the glow discharge target cleaning and deposition stages to keep the substrate at a constant temperature. The regular process parameters were that the target power was 4×5 kW, coil current 4×10 A, bias voltage was 120 V, bias current was 12 A, and argon flow rate 100 sccm. Parameters of a hysteresis process and the regular process are given in table 6.1.1 and 6.1.2 respectively.

Table 6.1.1 Parameters of stepwise Ti-N coating deposited at 350°C

Deposition time (Min)	N2 gas flow (SCCM)	N2 partial pressure (mbar)	Chamber total pressure (mbar)
0+20	0	2.19×10^{-6}	2.54×10^{-3}
(20)+20	30	3.99×10^{-6}	2.53×10^{-3}
(40)+20	60	8.05×10^{-6}	2.55×10^{-3}
(60)+20	90	5.36×10^{-4}	2.95×10^{-3}
(80)+20	120	9.10×10^{-4}	3.25×10^{-3}
(100)+20	150	1.30×10^{-3}	3.50×10^{-3}

Table 6.1.2 Parameters of Ti-N uniform coatings deposited at 350°C

PN	N ₂ Gas flow (SCCM)	N ₂ partial pressure (mbar)	Chamber total pressure (mbar)	Coating time (min)
01	35	4.001x10 ⁻⁶	2.6920x10 ⁻³	90
02	45	4.454x10 ⁻⁶	2.6854x10 ⁻³	120
03	50	4.731x10 ⁻⁶	2.6871x10 ⁻³	120
04	55	4.963x10 ⁻⁶	2.6858x10 ⁻³	120
05	65	5.534x10 ⁻⁶	2.6834x10 ⁻³	120
06	75	6.799x10 ⁻⁶	2.6865x10 ⁻³	120
07	85	9.595x10 ⁻⁶	2.7024x10 ⁻³	120

There were seven regular processes performed to produce uniform coatings with different compositions. Nitrogen gas flow rate was the only process parameter to be changed process to process, which resulted in the variations of nitrogen partial pressure in different coating process. The coating procedure was described in section 4.2.

The industrial application of the Ti-N film containing Ti₂N phase was carried out using a milling machine to test the coated high speed steel drills. The test was performed continuously drilling holes in bulk cast iron without cooling and lubricating until the drill failure was judged by hearing a sharp scream from the drilling. The improved quality of the coated drill was evaluated by counting the drilled holes of the coated drill as compared with that of un-coated drills. The cutting condition is given in table 6.1.3.

Table 6.1.3 Cutting conditions of high speed steel drills

Drill diameter (mm)	Material for drilling	Drilling speed (m/min)	Feed speed (mm/rev)	Drilled depth (mm)
6	Cast iron	50	0.2	25

6.2 Results of composition dependent on nitrogen partial pressure

6.2.1 Stepwise coating

A composition depth profile through the stepwise coating as measured using GDOES is shown in fig 6.2.1 which gave three distinct compositional layers, an outer layer of over

stoichiometric composition, an intermediate layer containing approximately 30 at % N and an inner layer adjacent to the coating/substrate interface with a titanium content greater than 80 at %. It would appear from a comparison of the composition with that of the partial pressure data for the stepwise coating, that the sub-stoichiometric TiN layer, composition increased from 0 to 30 at % N, was due to the nitrogen partial pressure increased from 2.19×10^{-6} mbar to 8.05×10^{-6} mbar and this resulted from the increasing of nitrogen gas flow rate from 0 to 60 sccm. The total chamber pressure, however, was kept almost constant with the increase of nitrogen gas flow rate. Whilst a sharp change in composition of the coating between 30 at % N and 50 at % N was due to an increase in nitrogen partial pressure from 8.05×10^{-6} mbar to 5.36×10^{-4} mbar and this resulted from a increase of nitrogen gas flow rate from 60 sccm to 90 sccm which caused the target poisoning and therefore total chamber pressure increased from 2.5×10^{-3} to 2.9×10^{-3} mbar.

(See page 149 for fig 6.2.1)

Fig 6.2.1 Composition depth profile of stepwise coating measured by GDOES

6.2.2 Uniform Ti-N coatings

The nitrogen concentrations of the uniform Ti-N coatings were a function of the reduced nitrogen partial pressure as shown in fig 6.2.2. There were two stages to describe the relation between concentration of nitrogen in coatings and nitrogen partial pressure within the main chamber. The nitrogen concentration increasing from 17 to 35% was the first stage in which the nitrogen partial pressure within the chamber was very sensitively to affect the nitrogen content of coating. In this stage, any small change in nitrogen partial pressure resulted in a big change in composition. The nitrogen partial pressures for coatings with concentration at 17, 20, 26, and 35 at % N were 4.0, 4.5, 4.7, and 5.0×10^{-6} mbar respectively. The composition over 35% at N was the second stage in which the variations of nitrogen concentration dependent on the nitrogen partial pressure are not as sensitive as that in the first stage. There was only a small change in the

nitrogen content of the coatings even though a big change in reduced nitrogen partial pressure was evidenced. The nitrogen partial pressures for coatings with concentration at 40, 46, and 50 at % N were 5.5, 8.0, and 9.6×10^{-6} mbar respectively.

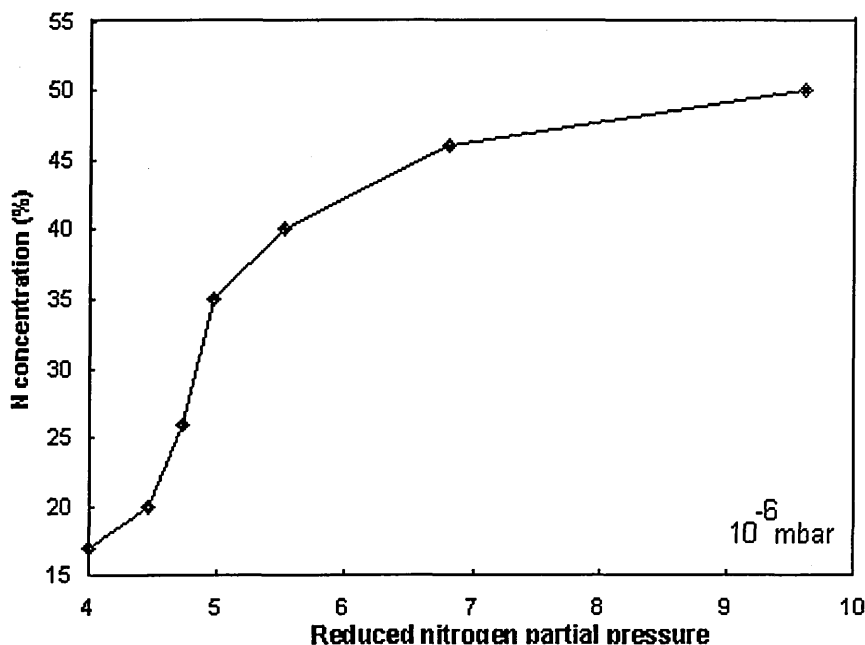


Fig 6.2.2 Concentration of Ti-N coating dependent on reduced N_2 partial pressure

6.3 XRD analysis of the coating

6.3.1 Compositional Stepped Coating

An X-ray diffraction pattern from the stepped coating is shown in fig 6.3.1. The diffraction pattern contained peaks at positions consistent with the face centred cubic δTiN (111), (200), (220), (311) and (222) (as referred to XRD JCPDS file number 38-1420), the tetragonal ϵTi_2N^* (112) and (224) (as referred to XRD JCPDS file number 23-1455), the hexagonal $\alpha TiN_{0.3}$ [$\alpha Ti(N)$] (10.0), (00.2) and (10.1) (as referred to XRD JCPDS file number 41-1352), as well as those from the substrate. There was considerable shift in the positions of the peaks of $\alpha Ti(N)$ relative to pure titanium, values for shifts of -0.27° , -0.21° , and -0.4° in 2θ for (10.0), (00.2) and (10.1) reflections respectively. This shift was due to the nitrogen atoms incorporated into the αTi lattice, which results in an expansion of the αTi lattice.

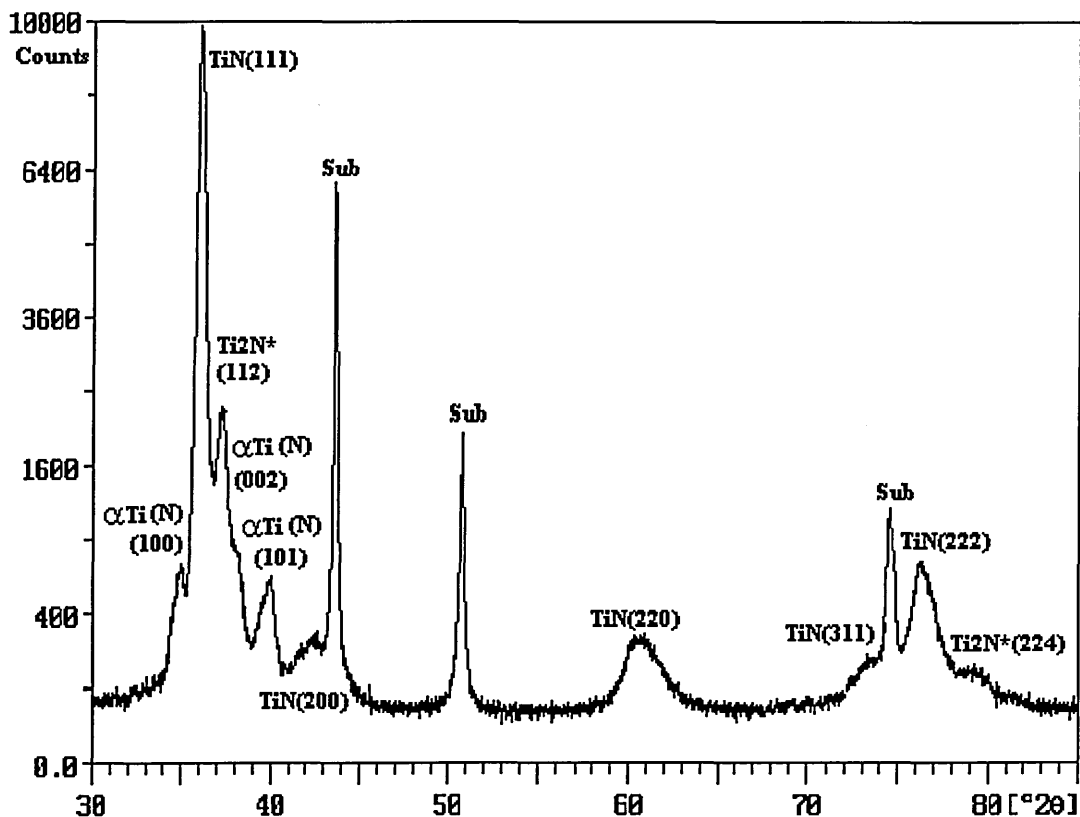


Fig 6.3.1 XRD pattern of the stepped Ti-N film

Values of interplanar spacings for fcc TiN and tetragonal Ti₂N together with standard data from the JCPDS files are respectively given in table 6.3.1. It could be seen values smaller and larger than the standard value were measured.

Table 6.3.1 TiN and Ti₂N* Interplanar Spacing of stepped coating

TiN Plane (hkl)	Interplanar Spacing (Å)	
	Specimen	Standard
(111)	2.491	2.449
(200)	2.118	2.121
(220)	1.533	1.499
(311)	1.279	1.279
Ti ₂ N* Plane (hkl)	Interplanar Spacing (Å)	
	Specimen	Standard
(112)	2.42	2.435
(224)	1.22	1.219

6.3.2 Coatings of Uniform Composition

The XRD pattern from the coating containing 17 at % N is shown in fig 6.3.2. The reflections present in the diffraction pattern gave the typical diffraction peaks corresponded to the $\alpha\text{TiN}_{0.3}$ [$\alpha\text{Ti(N)}$] JCPDS file number 41-1352 and the peaks were identified as the (10.0), (00.2), (10.1), (10.2), (11.0), (10.3), (20.0), (11.2), (20.1), and (00.4) planes. The $\alpha\text{Ti(N)}$ has the same hexagonal structure as that of the titanium. However the lattice parameters of $\alpha\text{Ti(N)}$ is larger than that of titanium due to the nitrogen atoms incorporated into the growing titanium lattices. It was obvious from fig 6.3.2 that the coating had a strong {00.1} texture.

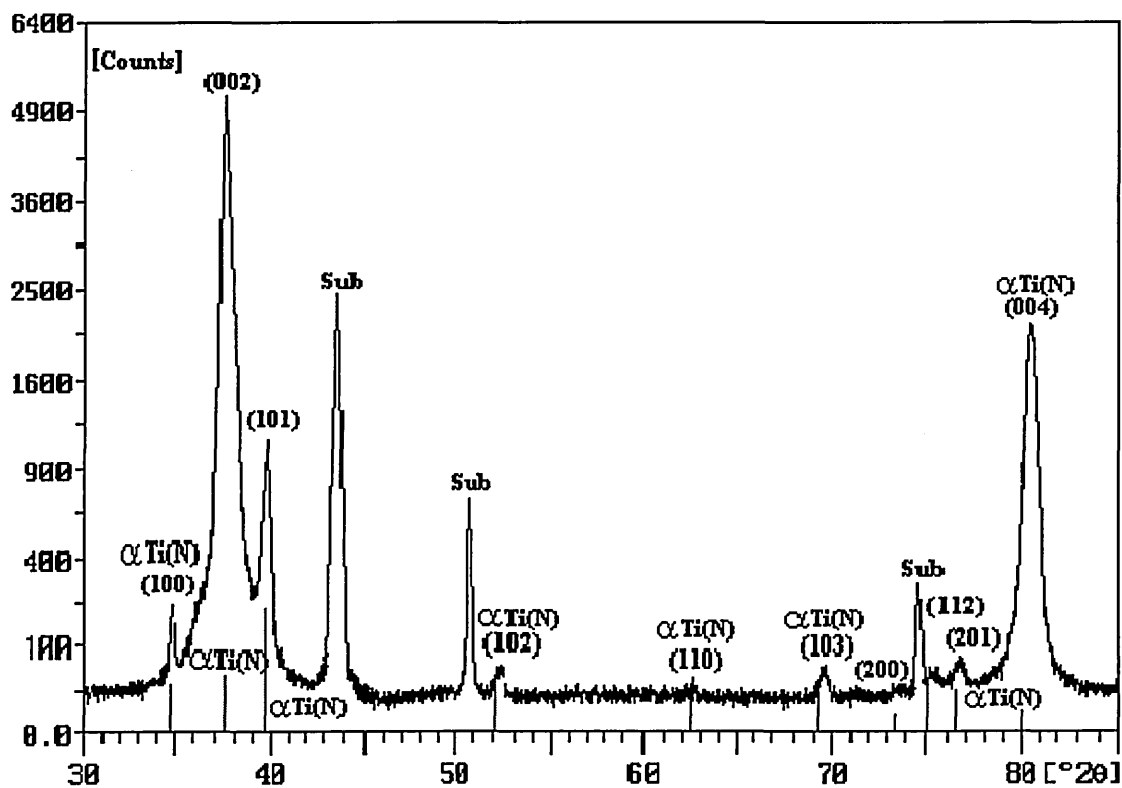


Fig 6.3.2 XRD pattern of coating at 17% N

When the composition of the coating was increased to 20% N, some peaks corresponding tetragonal $\epsilon\text{Ti}_2\text{N}^*$ could be identified resulting in a reduction in diffraction intensity of the $\alpha\text{Ti(N)}$ peaks. It can be seen in fig 6.3.3 that the reflections from (10.2), (11.0), (20.0), (11.2), and (20.1) planes for $\alpha\text{Ti(N)}$ as appeared in fig 6.3.2 not present. Also it was clear that the Ti_2N^* (204) was developed as composition of the coating increased up to 20% N. Although there was clear evidence to show the development of the $\epsilon\text{Ti}_2\text{N}^*$ phase, the dominant phase composition was still $\alpha\text{Ti(N)}$ with a {001} texture.

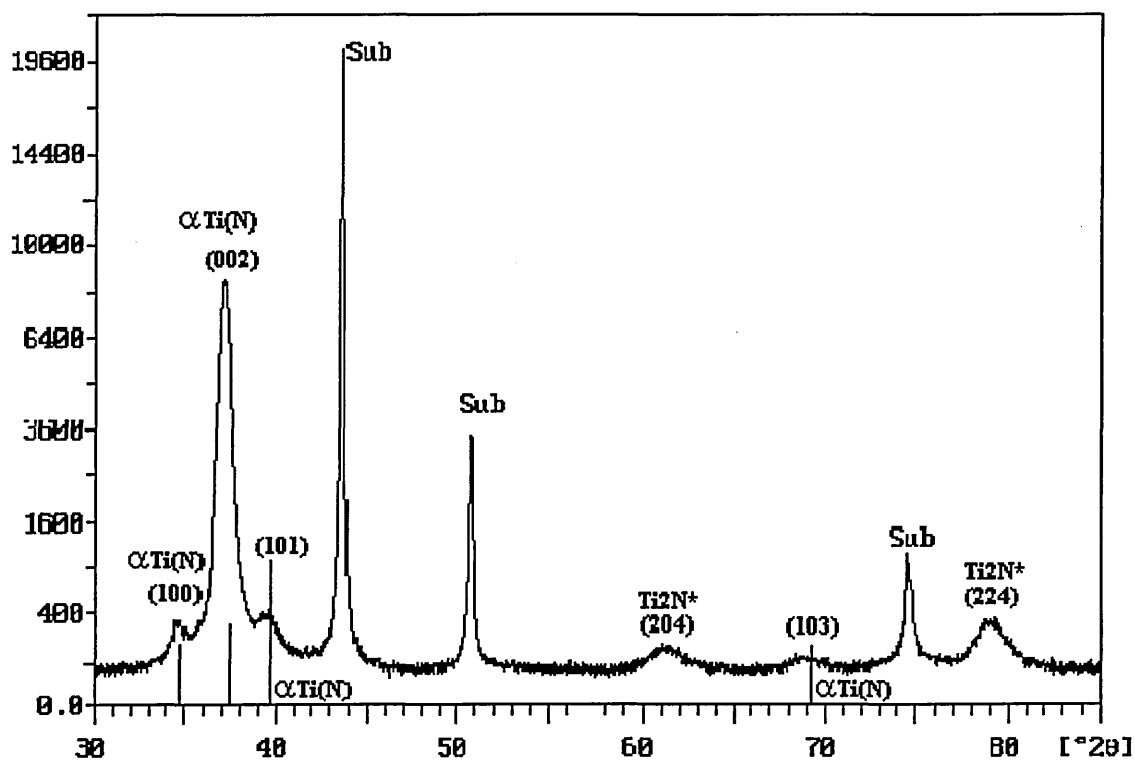


Fig 6.3.3 XRD pattern of coating at 20% N

When the composition of the coating increased to 26 at % N, the tetragonal $\epsilon\text{Ti}_2\text{N}^*$ phase was almost fully developed as shown in fig 6.3.4. The diffraction pattern contained peaks at positions corresponding to those of tetragonal $\epsilon\text{Ti}_2\text{N}^*$ and hexagonal $\alpha\text{Ti(N)}$, as well as those from the substrate.

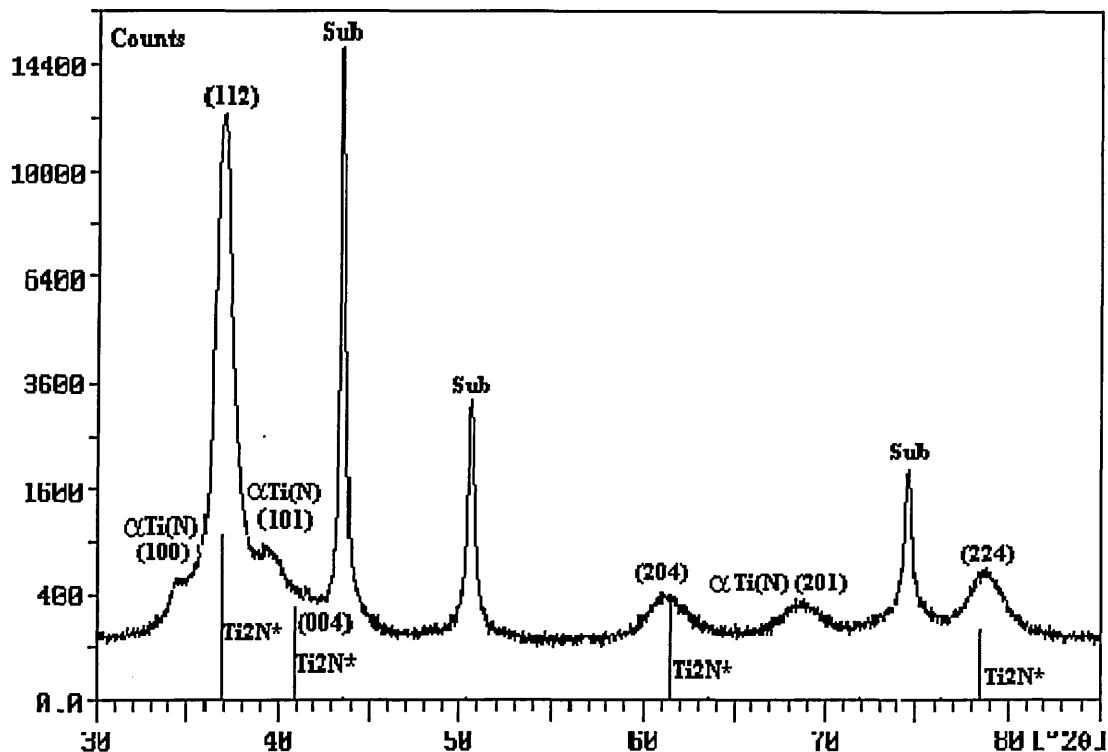


Fig 6.3.4 XRD pattern of coating at 26% N

The $\epsilon\text{Ti}_2\text{N}^*$ peak positions corresponded to the (hkl) reflections from (112), (004), (204) and (224) planes. The most intense $\epsilon\text{Ti}_2\text{N}^*$ reflection was the (112) which corresponded to the strongest intensity for a standard randomly oriented powder. However, the results from the pattern indicated that (112) plane parallel to the surface of the film was preferred, since the other reflections were less intense than those from a randomly oriented powder. The peak positions of the $\epsilon\text{Ti}_2\text{N}^*$ corresponded with those of the standard data, and the amount of peak broadening was significantly less than the films containing the TiN phase. The $\alpha\text{Ti(N)}$ reflections identified in the coating were from the (10.0), (10.1) and the (20.1) planes. However, there was considerable shift in the 2θ positions for the three peaks identified. Values of -0.36° , -0.55° and -2.03° in 2θ , compared with reference data of pure titanium, were found for the (10.0), (10.1) and (20.1) reflections. Calculation of the lattice parameters based on the 3 peak positions gave values of $a=2.983$ and $c=4.837$ Å for $\alpha\text{Ti(N)}$ with increases of 1.1% and 3.2% respectively in the lattice dimensions as comparing with the data from JCPDS file

number 5-682. It was clear that considerable peak broadening was associated with the titanium diffraction peaks.

The XRD pattern of a coating containing 35% N is shown in fig 6.3.5 which gave clear evidence that the face centred cubic (fcc) δ TiN was the dominant phase composition whilst the α Ti(N) phase had disappeared. The main reflecting planes in the diffraction pattern were (111), (200) and (220). It could be seen from the shoulders of the diffraction peaks for TiN(111) and (200) that reflections corresponding to peak positions for ϵ Ti₂N (hkl) planes (101), and (111) (JCPDS 17-386) were present.

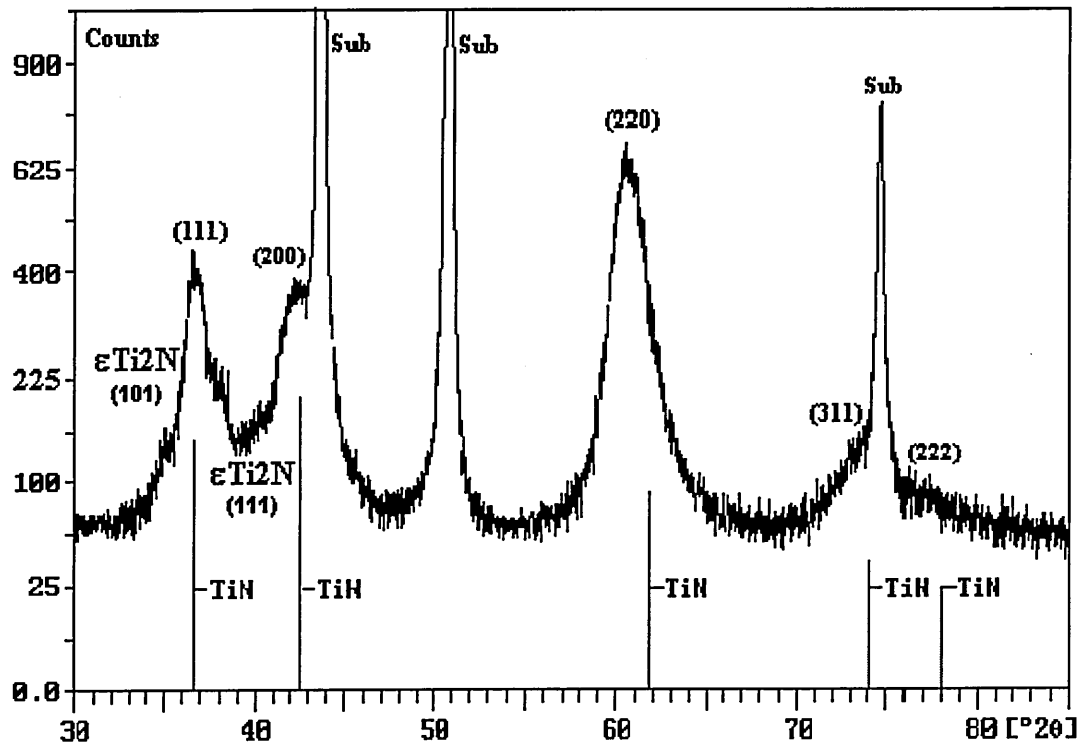


Fig 6.3.5 XRD pattern of coating at 35% N

XRD patterns from coatings above 40 at % N indicated that the coating contained only (fcc) δ TiN. There were however, significant differences between the traces obtained for TiN coatings with different nitrogen concentrations as shown in fig 6.3.6.

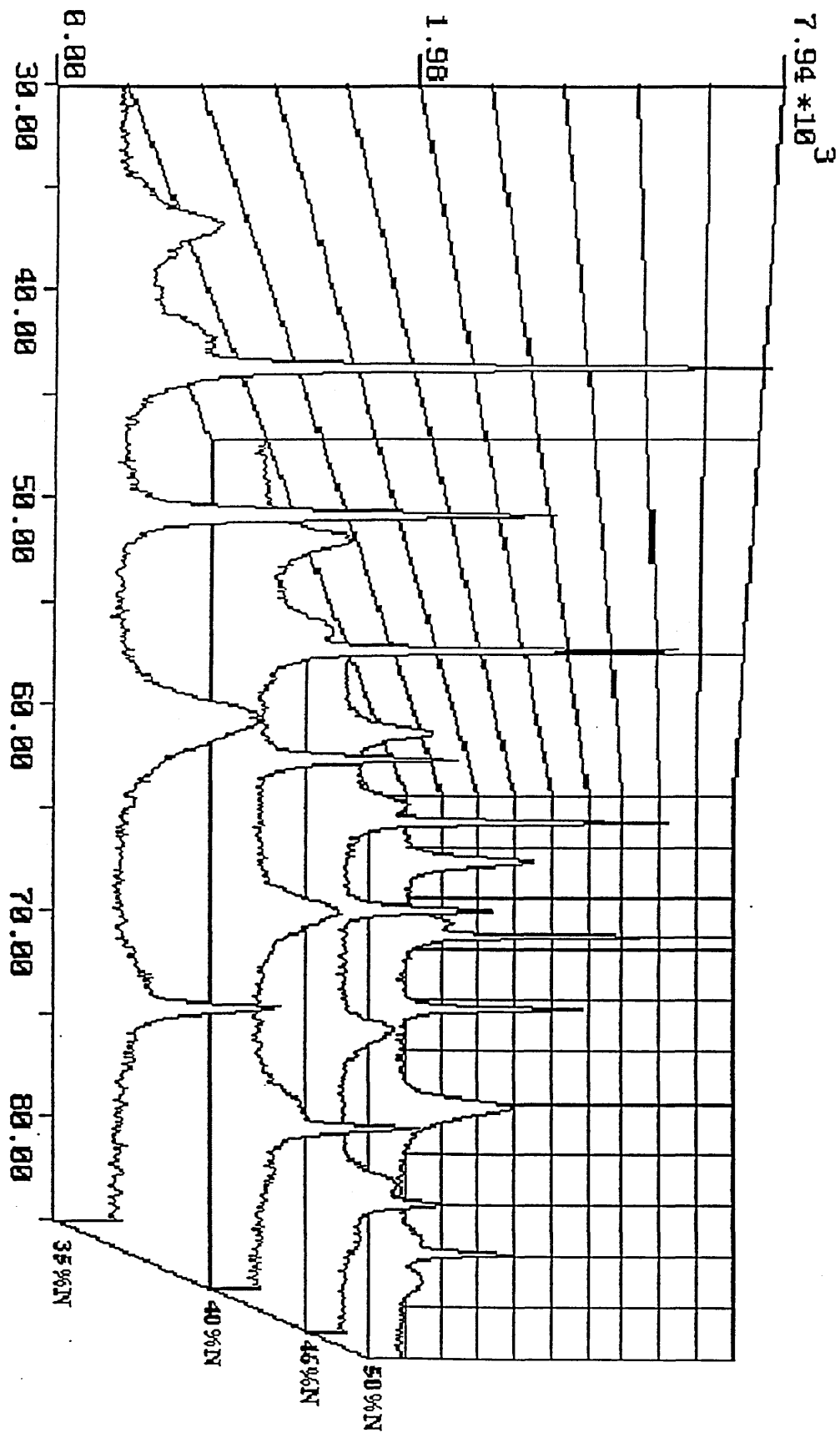


Fig 6.3.6 XRD patterns of coatings with composition from 35 to 50% N

It could be seen that extensive peak broadening was found in the pattern for the coating containing 35% N as compared with patterns for coatings containing above 40% N. With increasing nitrogen concentration the diffraction peaks became sharp and the peak for TiN (111) reflection increased in intensity. The intensity of the peak for δ TiN (311) reflection was also found increasing with the nitrogen concentration.

The interplanar spacing measurements and line broadening determinations for δ TiN (111), (200) and (220) reflections, together with standard data, at 35, 40, 46 and 50% N are given in table 6.3.2. The coatings exhibited a systematic increase in the interplanar spacing and decrease in peak broadening with increasing N:Ti ratio up to the stoichiometric composition. The percentage increase in the interplanar spacings for {110} oriented grains was always significantly greater than either {111} or {100} oriented grains, which differed only slightly from the equilibrium stress free levels. However, with the exception of {111} and {100} oriented grains in sample 04, there was lattice expansion above the equilibrium stress free level. In general the amount of peak broadening was the greatest in {100} oriented grains and the lowest in {111} oriented grains. The lattice parameter of {110} oriented grains also increased with increasing N:Ti ratio.

Table 6.3.2 Lattice parameter and line broadening of Ti-N coated specimens

Lattice parameter of standard is 4.2417Å							
sample No	N/Ti	lattice parameter (Å)			line broadening β (°)		
		(111)	(200)	(220)	(111)	(200)	(220)
04	35/65	4.23	4.23	4.31	1.33	3.23	2.11
05	40/60	4.26	4.25	4.32	1.28	2.66	1.82
06	46/54	4.27	4.26	4.32	0.93	1.68	1.63
07	50/50	4.27	4.27	4.33	0.72	1.12	1.48

The texture, micro strain and grain size of coatings deposited at 35, 40, 45 and 50 at % N are recorded in table 6.3.3. It was clear from table 6.3.3 that the {110} was the preferred orientation but the intensity of the {111} component increased with increasing N/Ti ratio. The micro strain and grain size decreased when the nitrogen content increased from 35 to 45% at N and then increased dramatically at stoichiometric TiN coating.

Table 6.3.3 Texture, strain and grain size results

% at N	Texture (%)						Strain (%)	Grain size (Å)
	(111)	(200)	(220)	(311)	(332)	(420)		
35	44	63	212	122	117	38	1.44	354
40	97	89	148	19	0	144	1.01	291
45	64	111	77	213	0	131	0.675	146
50	234	24	241	58	25	16	0.96	438

6.4 Thickness and hardness results of uniform Ti-N coatings

The results of coating thickness as measured using a calotest and the calculated deposition rates are shown in table 6.4.1. It can be seen that the deposition rate for process from number 1 to number 6 was almost the same value, about $2.0 \times 10^{-2} \mu\text{m}/\text{min}$ in average, whilst that for process number 7 reduced to $1.8 \times 10^{-2} \mu\text{m}/\text{min}$. The hardness values obtained using Vickers indentation measurement with a load of 10 g on coated stainless steel samples are also recorded in table 6.4.1 in which the hardness systematically increased with the nitrogen concentration within the coatings. The hardness for film containing 17 at % N was HV 942 whilst that for film containing 50 at % N was Hv 2008. The hardness for the coating containing 26 at % N (Ti_2N phase composition dominant) was Hv1233 which was lower than that for the stoichiometric TiN film.

Table 6.4.1 Thickness and hardness of uniform Ti-N coatings

Process number	01	02	03	04	05	06	07
Thickness (μm)	1.8	2.3	2.4	2.3	2.4	2.4	2.2
Deposition rate ($10^{-2} \mu\text{m}/\text{min}$)	2.0	1.9	2.0	1.9	2.0	2.0	1.8
Hardness (HV)	942	950	1233	1285	1569	1642	2008

6.5 Scanning Electron Microscopy

Scanning electron microscope images of fracture cross sections of the coatings are shown in fig 6.5.1 a-h. A fracture cross section through the stepped coating is given in

fig 6.5.1 a which shows three distinct layers. The morphologies at the surface of the deposit and adjacent to the coating/substrate interface are columnar. The structure at the centre of the deposit was rather indistinct. Fracture cross sections at low nitrogen, medium and stoichiometric composition levels are shown in fig 6.5.1 b-h respectively. The structures mirrored the stepped sample showing columnar structures at both the low nitrogen level and stoichiometric composition. At the medium nitrogen level (from 20% at N to 40% at N) the structure is similar to that at the centre of the stepped coating. It is clear from the micro-graph that the coatings with medium nitrogen concentrations had relatively dense and homogeneous films.

(See page 150 to 153 for fig 6.5.1)

Fig 6.5.1 Cross sectional structure of Ti-N coatings as measured by SEM

a. Stepwise film, b, c, d, e, f, g, h. composition at 17, 20, 26, 33, 40, 45, 50% N respectively.

6.6 Investigation of cutting test of the coated high speed steel drills

High speed steel twist drills were deposited with substoichiometric titanium nitride films (nitrogen contents from 0 to 29%). Composition, phase development and drilling tests were investigated.

6.6.1 Composition and phase analysis of the coatings using GDOES and XRD

The composition and phase development of the coatings are given in table 6.6.1. There were seven coating processes in which the nitrogen concentration in the coatings was 0, 12%, 23%, 26%, 28%, and 29% respectively. The main phase compositions within the coatings were hexagonal α Ti(N) and tetragonal ϵ Ti₂N. The reflecting planes (hkl) were identified as a function of the nitrogen concentration within the coatings. With increasing the nitrogen content, the intensity of reflections from the α Ti(N) phase decreased whilst those from the ϵ Ti₂N phase ϵ Ti₂N* (as referred to JCPDS file number 23-1455) started to develop when concentration was above 12% at N and it became the dominant phase as the concentration was more than 23% at N. Another ϵ Ti₂N phase (as

referred to JCPDS file number 17-386) was also found when concentration of the coating increased above 24% at N.

Table 6.6.1 phase analysis of XRD

PN	Concentration	compound	(hkl) plane					
			100	002	101	102	110	103
01	0% at N	Titanium	100	002	101	102	110	103
02	12% at N	$\alpha\text{TiN}_{0.3}$	100	002	101	102	103	
		$\epsilon\text{Ti}_2\text{N}^*$	204	312	107			
03	23% at N	$\alpha\text{TiN}_{0.3}$	100	101	110			
		$\epsilon\text{Ti}_2\text{N}^*$	112	224	107			
04	24% at N	$\alpha\text{TiN}_{0.3}$	002	200				
		$\epsilon\text{Ti}_2\text{N}$	101	002				
		$\epsilon\text{Ti}_2\text{N}^*$	112	004	204	224		
05	26% at N	$\alpha\text{TiN}_{0.3}$	100	110				
		$\epsilon\text{Ti}_2\text{N}$	111	002				
		$\epsilon\text{Ti}_2\text{N}^*$	112	004	215	224		
06	28% at N	$\alpha\text{TiN}_{0.3}$	100	110				
		$\epsilon\text{Ti}_2\text{N}$	111	002				
		$\epsilon\text{Ti}_2\text{N}^*$	112	004	215	224		
07	29% at N	$\alpha\text{TiN}_{0.3}$	100	110				
		$\epsilon\text{Ti}_2\text{N}$	111	002				
		$\epsilon\text{Ti}_2\text{N}^*$	112	004	215	224		

6.6.2 Physical properties of sub-stoichiometric Ti-N films and drilling test

Vickers hardness, Rockwell and scratch test of the coatings, as well as the results of drilling test of the coated high speed steel twist drills are shown in table 6.6.2.

Table 6.6.2 GDOES, Hardness and drill test Results

PN	at % N	Hardness (HV)	Rockwell adhesion (R_c)	Scratch $L_c(N) \leq$	Drilled holes		
					32	37	46
02	12	1000	1	12	32	37	46
03	23	1040	1	15	67	129	164
04	24	1270	1	20	22	131	153
05	26	1190	1	25	73	148	158
06	28	1108	1	25	134	179	215
07	29	1260	1	26	227	253	263
Uncoated		850			29	35	49

The hardness was increased from HV 1000 when coating was at 12% N, to HV 1260 when coating was at 29% N. All of the coatings had very good adhesion ($R_c=1$) as measured using Rockwell indentation test as shown in fig 6.6.1. The value of the critical load (L_c) of the scratch test, however, was not high (less than 26 N) which may be attributed to the relative low hardness value (HV 1200) as comparing with that (HV 2500) of stoichiometric TiN films. It was clear as seen from table 6.6.2 that drills deposited by $\epsilon\text{Ti}_2\text{N}$ film had better drilling performance than that deposited by $\alpha\text{Ti(N)}$ film. There was no improvement of the performance of the drills coated by $\alpha\text{Ti(N)}$ as comparing with the uncoated drills. The drills coated by $\epsilon\text{Ti}_2\text{N}$ film had the very good drilling giving up to 263 drilled holes which was 7 time that of the uncoated drills. This matched the performance of stoichiometric δTiN coated drills of approximately 250 holes.

(See page 154 and 155 for fig 6.6.1)

Fig 6.6.1 Rockwell test of the substoichiometric Ti-N coatings

a,b,c,d,e,f referred to composition of 12, 23, 24, 26, 28, 29% N respectively

6.7 Discussion of chapter 6

The compositional stepped specimen indicated a mixture of TiN, Ti_2N and titanium with a highly strained lattice. The GDOES depth profile shows three distinct compositional layers within the stepped coating (a surface layer of approximately stoichiometric composition, an intermediate layer containing 30 at % N, and a layer adjacent to the coating/substrate interface greater than 80 at % titanium). From the XRD results this clearly indicates a surface layer of TiN, an intermediate layer of Ti_2N , and a titanium layer near to the coating/substrate interface. The presence of both Ti_2N and Ti in coatings containing up to 30 at % nitrogen may be predicted from the titanium nitrogen phase diagram⁽¹⁾.

X-ray diffraction results from the 26 at % N specimen indicated that the structure was a mixture of $\epsilon\text{Ti}_2\text{N}$, and $\alpha\text{Ti(N)}$ with a highly strained lattice whilst the XRD pattern of

the film containing 35 at % N had the $\epsilon\text{Ti}_2\text{N}$ and δTiN multiphase without the $\alpha\text{Ti(N)}$. Comparing with the nitrogen partial pressures for the two specimen deposition processes, it is reasonable to say that the reduced nitrogen partial pressure for deposition of $\epsilon\text{Ti}_2\text{N}$ film is about 4.8×10^{-6} mbar.

It was known that the growth of Ti_2N phase was strictly dependent on the substrate temperature ($T \geq 500^\circ\text{C}$) and the deposition rate^(2,3,4). The coatings with approximate 30 at % N were always formed with multiphase compositions. It was often difficult to interpret the X-ray diffraction profile due to the overlap of lattice plane reflections. In the work presented here, all the specimens were coated using three fold rotation. When the substrate was facing the target, the growing film was rich in titanium, when the growing film was in the shadow region, the main activity was nitriding with bombardment of energetic particles. Therefore, multiphase compositions were always produced in the process This may explain why the overlap of different lattice plane reflections took place in the XRD pattern of coatings with low value of nitrogen concentration.

It is not always possible to unambiguously determine the presence of Ti_2N by X-ray diffraction, since some reflections belonging to this phase were not present in the trace. Also some of the reflections assigned to Ti_2N , such as $\epsilon\text{Ti}_2\text{N}^*(204)$, are close to those for unstrained TiN , such as $\delta\text{TiN}(220)$. However, no peaks were observed in the trace corresponding to positions of the reflections from (200) and (311) planes in TiN . Furthermore, the trace for the 26 at % N was significantly different from those for the TiN deposits containing above 35 at % N, in terms of line broadening and peak position, thus further substantiating the evidence for the presence of Ti_2N .

Despite the low deposition temperature (350°C) there is sufficient adatom mobility to allow the formation of Ti_2N rather than $\alpha\text{-Ti(N)}$. This is due to the high ion bombardment of the films during growth made possible by the ABS magnetron design. Following the definition proposed by Poulek et al⁽⁵⁾ of a deposition parameter S_E values in the 10^6 Jcm^{-3} range were obtained for these coatings. Despite deposition

temperatures in the range 450-500°C only for bias voltages in excess of -250V was Ti₂N formed when using a single magnetron static deposition process^(4,6).

The presence of α titanium in deposition up to 26 at % N is clearly predictable from the Ti-N phase diagram⁽¹⁾. However, the results of the X-ray diffraction indicate that the lattice of the α titanium is heavily distorted resulting in increases in both a and c values. This is because nitrogen dissolves in the α titanium and expands the lattice^(7,8).

The amount of line broadening present in the film of stoichiometric composition is consistent with that of a film deposited at -120V bias⁽⁹⁾. The percentage increases in the interplanar spacings of (220) oriented grains were always systematically greater than other orientations. High d (interplanar spacing) for the (220) planes was often characteristic of TiN coatings⁽⁹⁾. The amount of strain broadening was also found to decrease for all (hkl) orientations with increase in the nitrogen content from 35 at % to 50 at %. Strain broadening resulted from a non-uniform distribution of strain within the lattice such as. an increase in lattice distortion and disorder. The lattice parameters calculated by the formula of cubic lattice as shown in table 6.3.2 were, in general, different. These differences of a_0^{111} , a_0^{200} , and a_0^{220} were the consequence of lattice distortion. According to the Ti-N phase diagram, δ TiN forms a stable solid solution between 40 at % N and 50 at % N. It is a cubic nitride with the metal atoms at the face centred cubic sites and the nitrogen at the interstitial positions in a structure of the NaCl type. TiN with compositions less than stoichiometric contain vacancies in the interstitial positions, the number of vacancies decreases as the nitrogen content increases. Since, the deposition process is random the distribution of vacancies is not uniform and hence an increase in disorder and lattice distortion. This results in an increase in line broadening in the TiN phase with decreasing N:Ti ratio. The systematic increase in the lattice parameter with increasing N:Ti ratio is consistent with increase in the equilibrium value from 0.422nm at the low N phase boundary to 0.424nm at the stoichiometric composition⁽¹⁾.

The experiments documented that the hardness of the Ti-N films is a function of the nitrogen concentration within the films. The film with the highest hardness do not correspond to the $\epsilon\text{Ti}_2\text{N}$ phase. On the contrary, the hardest film was found only containing δTiN phase. It is very common that the deposited films containing Ti_2N phase have very good adhesion with the substrate since the measurements made by Rockwell test always indicate the $R_c=1$ results. However, the critical load of the scratch test on the same kind of films is not high as compared with the scratch test on stoichiometric TiN films. As the performance of Ti_2N coated cutting tools can match that of the stoichiometric TiN coated components, the advantage of using Ti_2N film instead of stoichiometric TiN film is obvious. The deposition of Ti_2N film is operated at the un-poisoned mode and therefore the deposition rate is high, this is very important for the industrial mass production as more time and energy are saved as comparing with the deposition of stoichiometric TiN film. In addition the films containing Ti_2N phase composition have more dense packed structure as compared with the stoichiometric TiN films. This is also an advantage to produce pin-hole free film for the corrosion resistant applications.

6.8 Conclusion of chapter 6

- (1) The X-ray diffraction results indicate the presence of almost pure Ti_2N in the specimens containing approximately 30 at % N. The nitrogen partial pressure for depositing Ti_2N film is about 4.7×10^{-6} mbar. The nitrogen gas flow for Ti_2N process is 50 sccm.
- (2) The presence of α titanium was identified in deposits containing up to 26 at % N. There was considerable displacement in the peak position for titanium because of lattice expansion by dissolved nitrogen.
- (3) The texture of TiN {111} tends to increase as the N content increased from 35 at % N to 50 at % N, at the same time, but the {220} is always the preferred orientation.
- (4) The relative increase in interplanar spacings of (111), (220), and (222) oriented grains are systematically greater than in other orientations. The amount of peak

broadening and hence non-uniform strain distribution decrease as the N content increased from 35 at % N to 50 at % N.

- (5) The ABS chamber allows Ti_2N to be deposited at lower temperatures due to the high ion bombardment.
- (6) The Ti_2N coated high speed steel twist drills have very good practical performance due to the dense columnar structure, relative high hardness, and good adhesion to the substrate.

References

- (1) M. Hansen, Constitution of Binary Alloys, McGraw Book Co., Inc. New York, 1st edi., 1958
- (2) B.E. Jacobson, R. Nimmagadda and R.F. Bunshah, *Thin Solid Films*, V63 (1979)333
- (3) M. Van Stappen, Fourth International Conference on Plasma Surface Engineering, Garmisch-Partenkirchen September 19-23, 1994
- (4) V. Poulek, J. Musil, V. Valvoda, L. Dobiasova *Materials Science and Engineering*, A140 (1991) 660
- (5) V. Poulek, J. Musil, R. Cerny, R. Kuzel *Thin Solid Films*, V170(1989)L55
- (6) V. Valvoda, R. Cerny, R. Kuzel Jr, J. Musil, V. Poulek *Proc. First International Conference on Plasma Surface Engineering 1988, Garmisch-Partenkirchen*
- (7) RF. Mehl, MB. Bever, Metallurgy and Metallurgical Engineering Series McGRAW-HILL BOOK COMPANY, INC. New York (1958) 989
- (8) H.T. Clark *Trans. AIME*, 185, (1949) 588
- (9) A.J. Perry, M. Jagner, W.D. Sproul and P.J. Rudnik, *Surf. Coat. Technol.*, V42 (1990)49

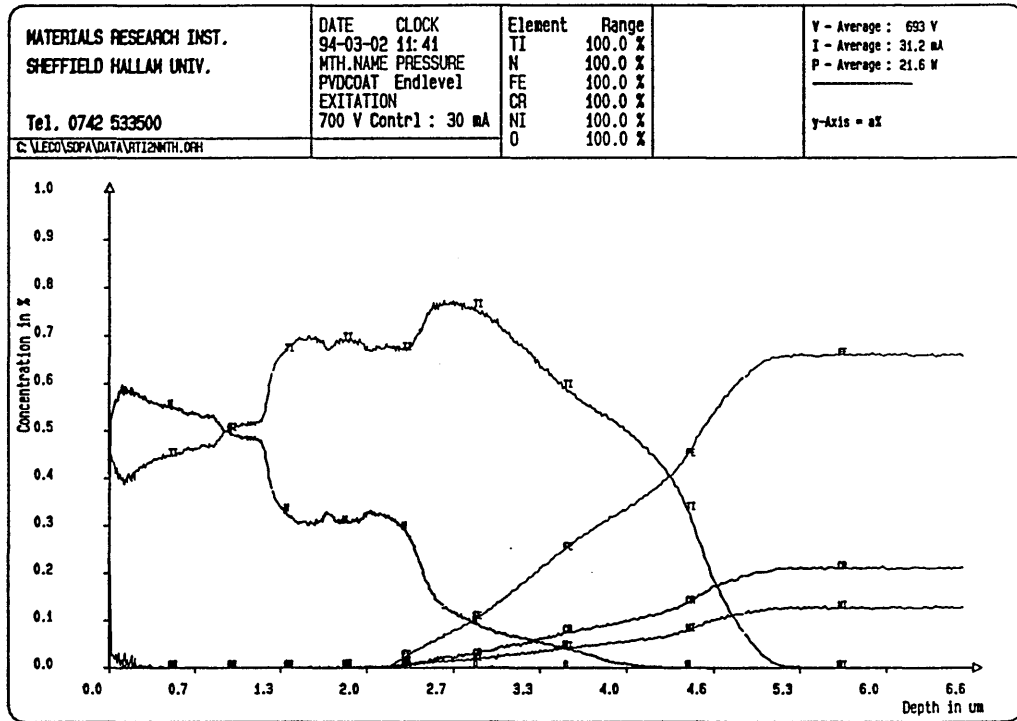


Fig 6.2.1 Composition depth profile of stepwise coating measured by GDOES

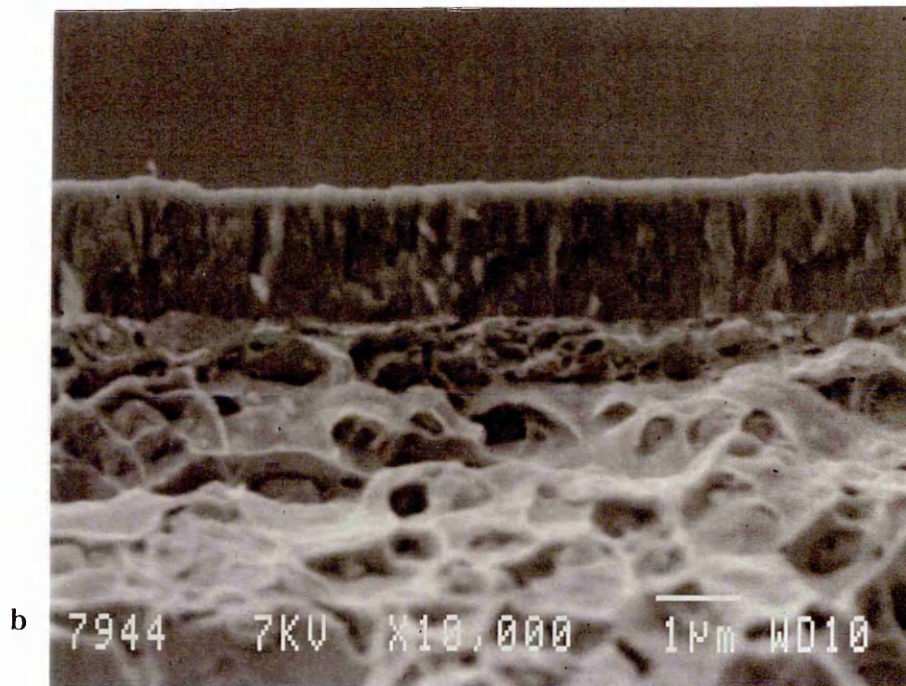
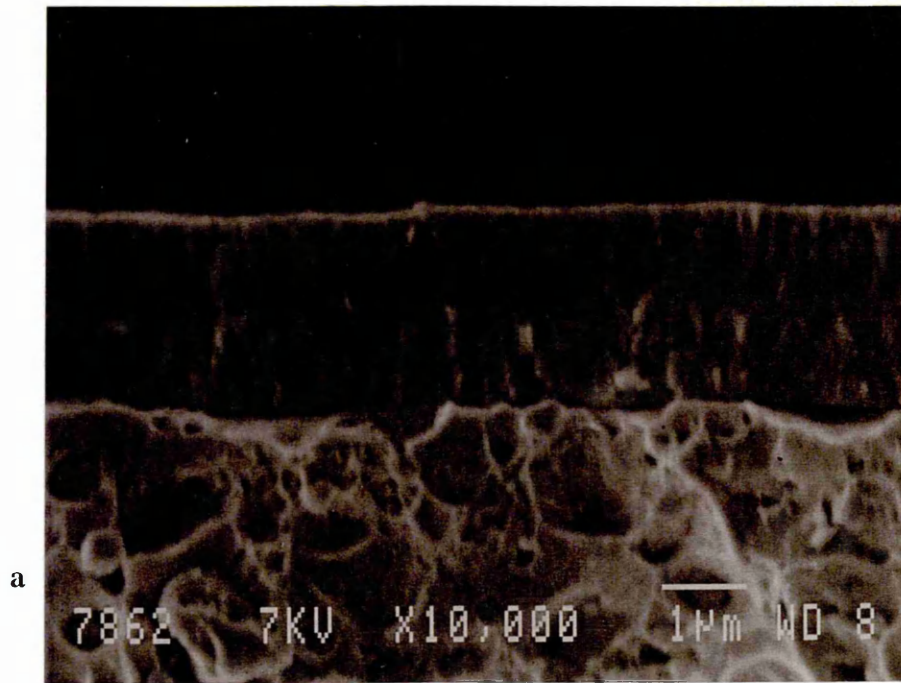


Fig 6.5.1 Cross sectional structure of Ti-N coatings as measured by SEM
a. Stepwise film, b, c, d, e, f, g, h. composition at 17, 20, 26, 33, 40, 45, 50% N respectively.

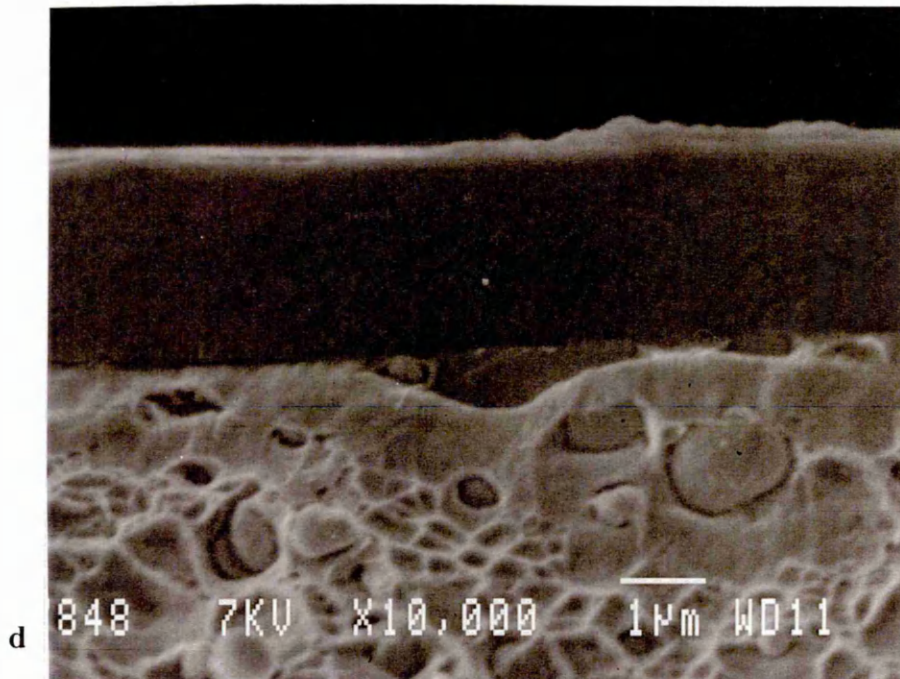
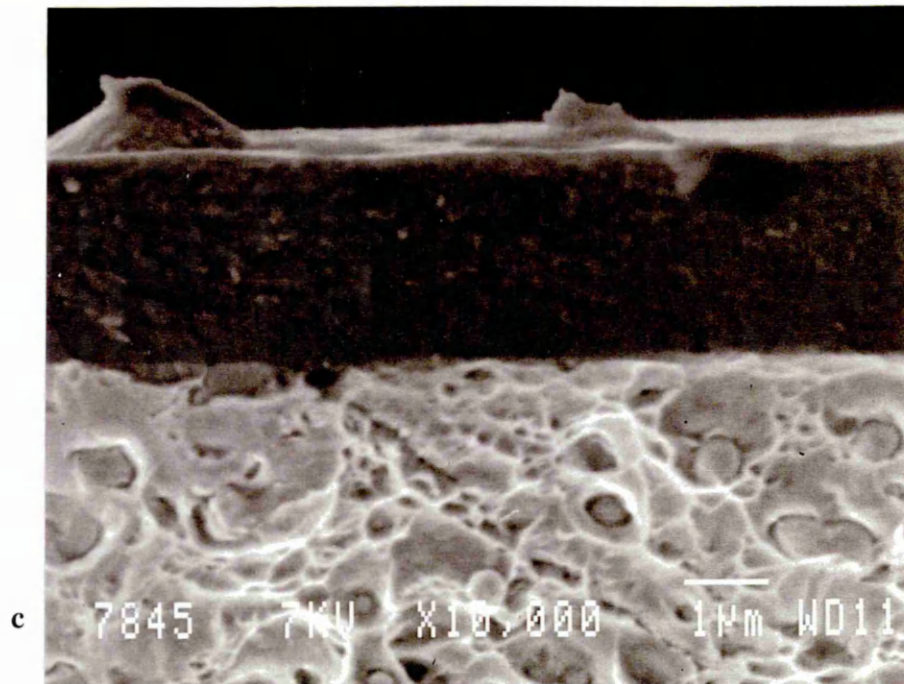


Fig 6.5.1 Cross sectional structure of Ti-N coatings as measured by SEM
a. Stepwise film, b, c, d, e, f, g, h. composition at 17, 20, 26, 33, 40, 45, 50% N respectively.

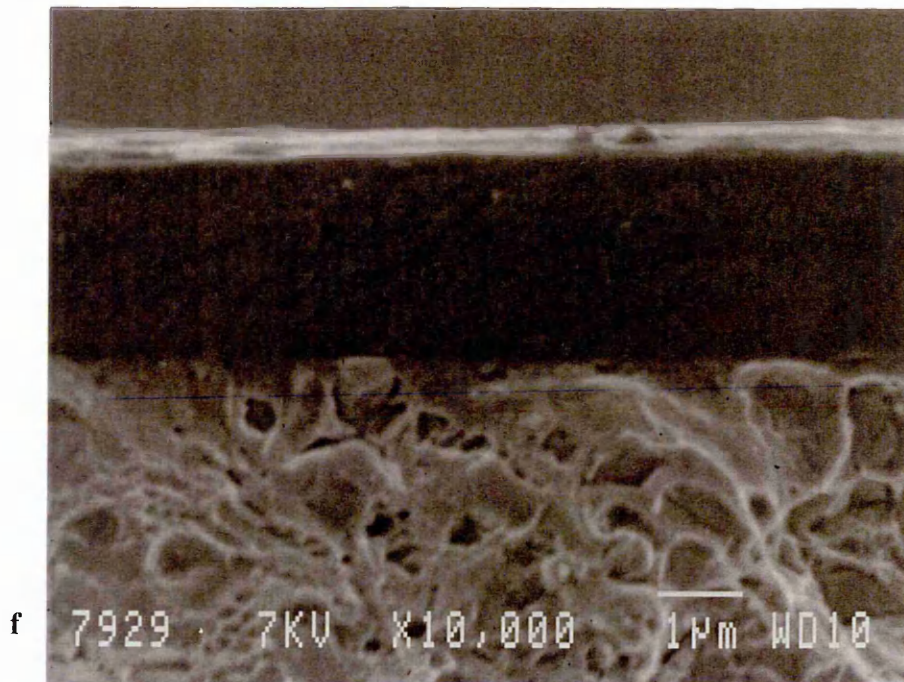
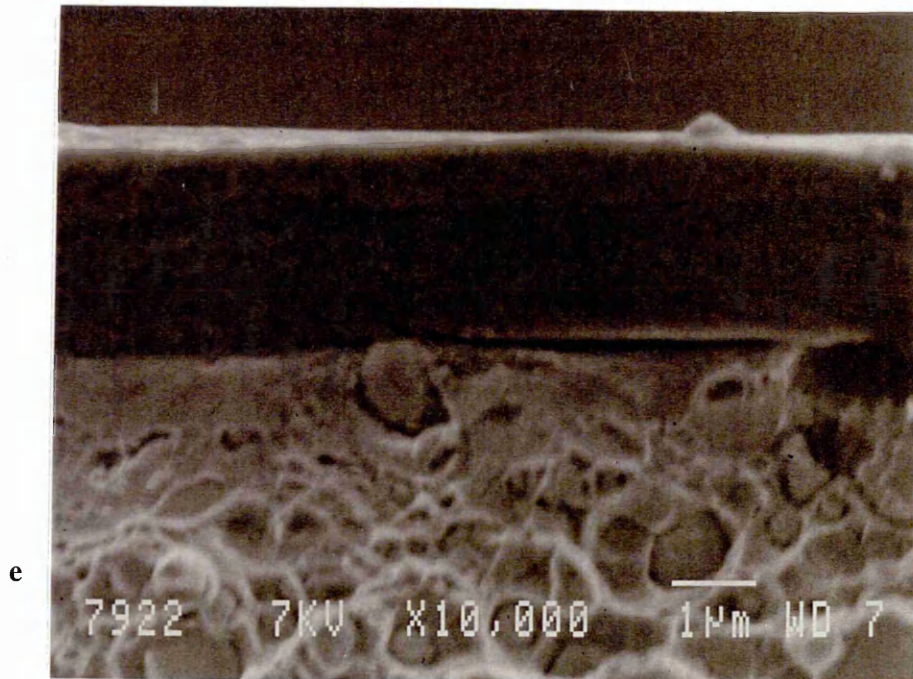


Fig 6.5.1 Cross sectional structure of Ti-N coatings as measured by SEM
a. Stepwise film, b, c, d, e, f, g, h. composition at 17, 20, 26, 33, 40, 45, 50% N respectively.

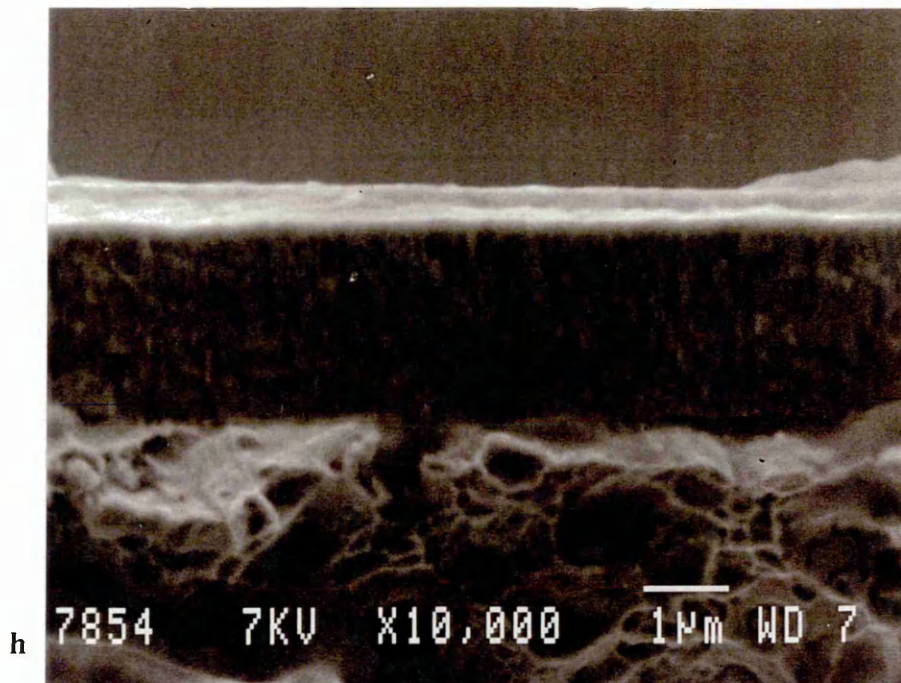
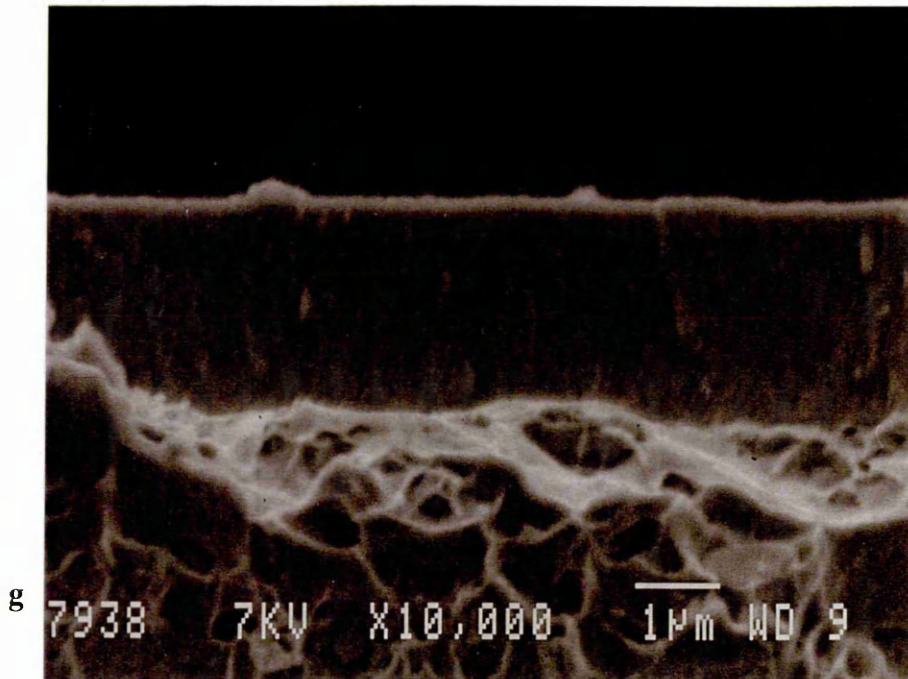


Fig 6.5.1 Cross sectional structure of Ti-N coatings as measured by SEM
a. Stepwise film, b, c, d, e, f, g, h. composition at 17, 20, 26, 33, 40, 45, 50% N respectively.

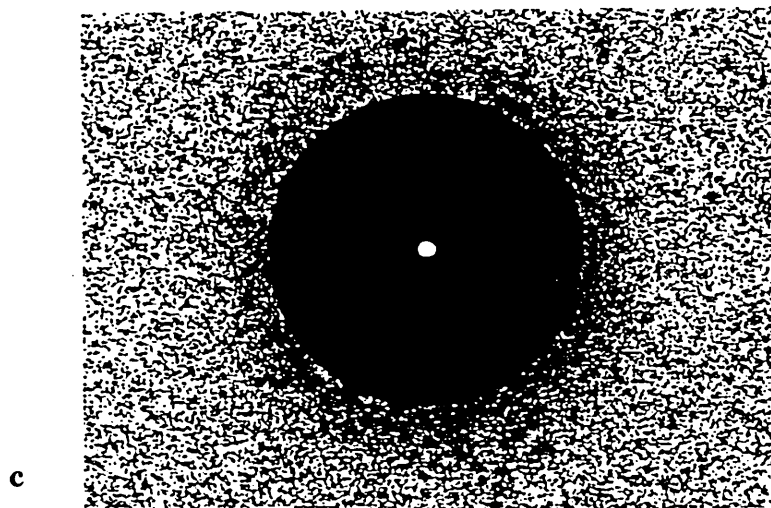
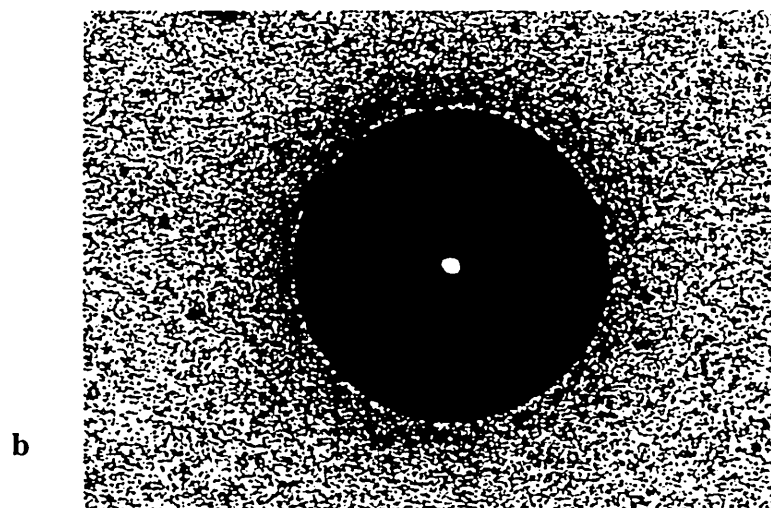
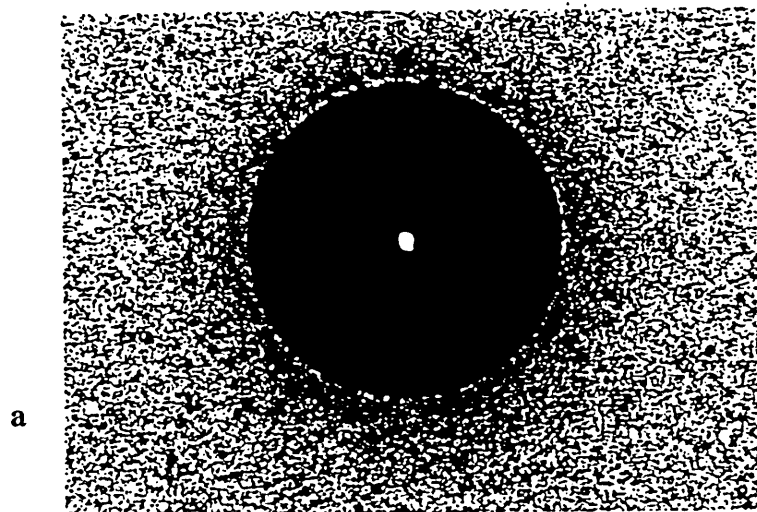


Fig 6.6.1 Rockwell test of the substoichiometric TiN coatings
a,b,c,d,e,f referred to composition of 12, 23, 24, 26, 28, 29% N respectively

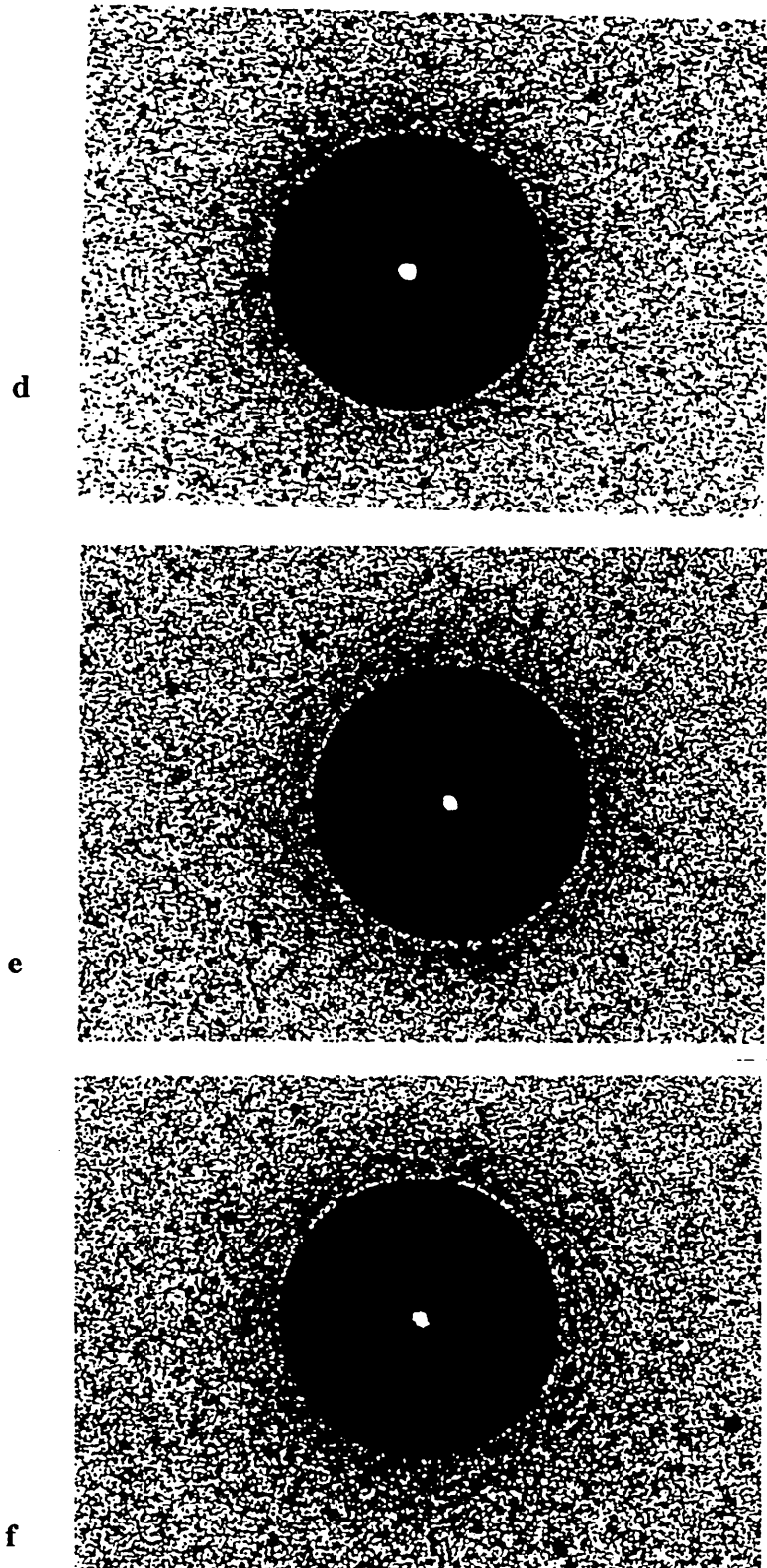


Fig 6.6.1 Rockwell test of the substoichiometric TiN coatings
a,b,c,d,e,f referred to composition of 12, 23, 24, 26, 28, 29% N respectively

7. Process study of static Ti-N coatings deposited at 480°C

Uniform titanium nitride films (concentration from 0 to 50 % N) were deposited at 480°C without substrate rotation using an unbalanced magnetron sputtering (UBMS) technique. This was considered to investigate the development of $\epsilon\text{Ti}_2\text{N}$ phase dependent on nitrogen partial pressure under high temperature condition. Therefore accurate description of production of Ti_2N films and better understanding of the phase formation in the static coating process could be obtained. The aim of investigating the static processes was to obtain more information in order to carry out production of $\epsilon\text{Ti}_2\text{N}$ films using the substrate rotation coating process.

7.1 Experimental arrangement of the static deposition process

The test pieces were high speed steel and stainless steel samples prepared according to the regular steps as described in section 4.2. The test pieces were placed in the vacuum chamber facing the target at a distance of 25 cm without rotation and were heated up to 450°C. The coating procedure is the same as mentioned in section 4.2 except that the substrate is not rotated in this case. After etching the substrate temperature was increased to 480°C and the deposition process started using a target power of 10kW. A bias voltage of -80V was applied to the substrates. The substrate temperature was maintained precisely at 480°C using the adjustable radiator heaters in the main chamber.

Table 7.1.1 Nitrogen gas flow and partial pressures for the static Ti-N coatings

Process number	1	2	3	4	5	6	7	8
N_2 flow rate (sccm)	0	2.0	2.8	3.4	3.0	3.6	5.0	6.5
N_2 partial pressure (10^{-5} mbar)	0.03	0.50	1.26	1.86	2.01	2.19	5.09	21.25
Deposition time (minute)	30	30	30	60	120	30	30	30

The nitrogen gas flow rate was kept constant during a single process, but varied from process to process from zero to a equilibrium level, in order to give a range of nitrogen gas partial pressures and hence films with different Ti:N ratios could be deposited. The

reduced nitrogen partial pressure was measured by using a differentially pumped mass spectrometer. The nitrogen gas flow rate and the related partial pressure for each process is shown in table 7.1.1.

7.2 Experimental results

7.2.1 Composition dependence on the nitrogen partial pressure

The variation of film composition (as measured by GDOES) with the reduced nitrogen partial pressure (as estimated by a mass spectrometer) is shown in fig 7.2.1. The total chamber pressure was constant at about 2.4×10^{-3} mbar during each process. It can be seen from this figure that the resulting curve is similar to that obtained in section 6.2.2 showing two different stages in which the nitrogen gas partial pressure in a process affects the nitrogen concentration in the coating.

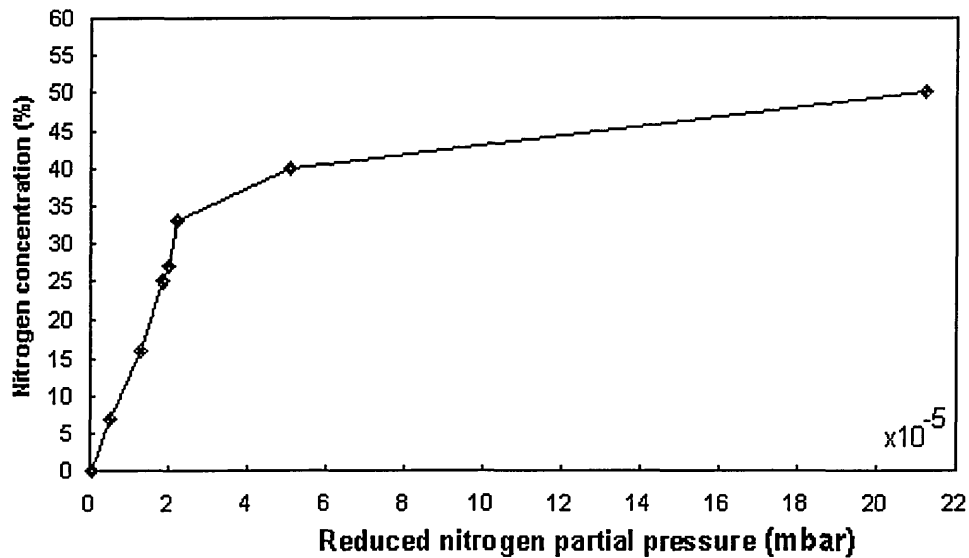


Fig 7.2.1 Composition dependence on nitrogen partial pressure

The concentration of nitrogen in the films increased rapidly with an increase in nitrogen partial pressure before the reactive gas partial pressure reached 2.2×10^{-5} mbar, where approximately 33 % N in the coating was produced. Beyond this point, the composition was not as sensitive to the reactive gas partial pressure, and the concentration of nitrogen within the coating changed very slowly with change of nitrogen partial pressure. The

stoichiometric TiN (at 50% N) coating was produced in the nitrogen partial pressure range of 2.1×10^{-4} mbar.

7.2.2 Crystal phases dependent on composition of the coatings

The XRD pattern for pure titanium (at 0 % N) coating is shown in fig 7.2.2, which gave very sharp diffraction peaks at almost identical positions as those referred in the JCPDS file 5-682 to indicate that the film was produced little stress.

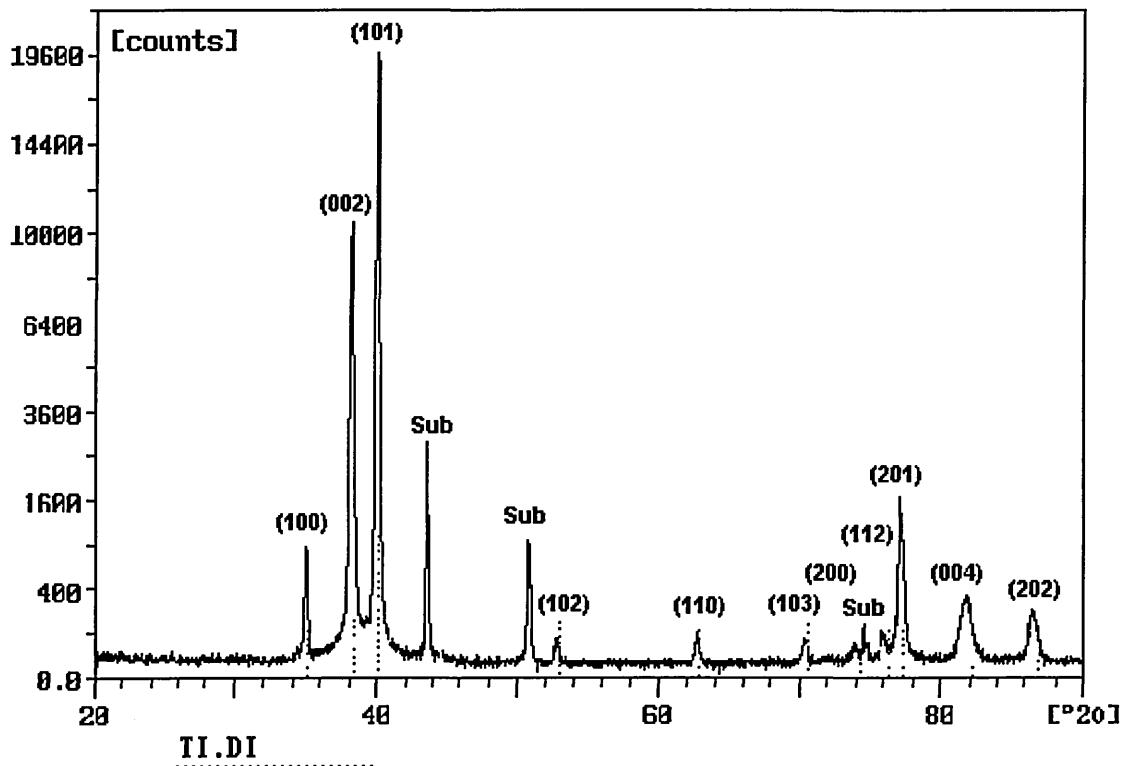


Fig 7.2.2 XRD pattern of pure titanium coating

The calculated texture, the measured interplanar spacings and diffraction intensities of the specimen and those referred in the JCPDS file, are shown in table 7.2.1. The average difference in the interplanar spacings was $\Delta d = 0.01 \text{ \AA}$, as compared with the standard interplanar spacing values of the JCPDS file. The coating exhibited a strong $\{001\}$ texture (54.2%) with minor $\{101\}$ and $\{201\}$ components.

Table 7.2.1 Texture calculation of the pure titanium coating

(hkl)	100	002	101	102	110	103	200	112	201	004	202
d*(Å)	2.557	2.342	2.244	1.726	1.475	1.332	1.276	1.247	1.233	1.171	1.122
d (Å)	2.562	2.357	2.251	1.732	1.481	1.338	1.271	1.252	1.236	1.177	1.125
Δd (Å)	0.01	0.02	0.01	0.01	0.01	0.01	0.01	0.01	<0.01	0.01	<0.01
I	170.5	4004.5	4865.4	17.7	30.2	24.8	39.91	37.38	654.3		
I*	30	26	100	19	17	16	2	16	13		
I/I*	5.7	154.0	48.7	0.9	1.8	1.6	20.0	2.3	50.3		
T(%)	2.0	54.2	17.1	0.3	0.7	0.6	7.0	0.8	17.7		

d* and I* are interplanar spacing and diffraction intensity of titanium phase referred to JCPDS file 5-682.

When a film containing at 7 % N was deposited, the XRD pattern (shown in fig 7.2.3) exhibited diffraction peaks systematically shifted to the left as compared with the XRD pattern of pure titanium coating. Compared with the positions of the $\alpha\text{TiN}_{0.3}$ phase of the JCPDS file 41-1352 however, the diffraction peaks of the specimen were located to the right side of the positions for $\alpha\text{TiN}_{0.3}$ phase, indicating a smaller interplanar spacing than that of the $\alpha\text{TiN}_{0.3}$ phase. This obviously indicated an incorporation of the nitrogen atoms in the hcp titanium lattices at a lower concentration than that of $\alpha\text{TiN}_{0.3}$.

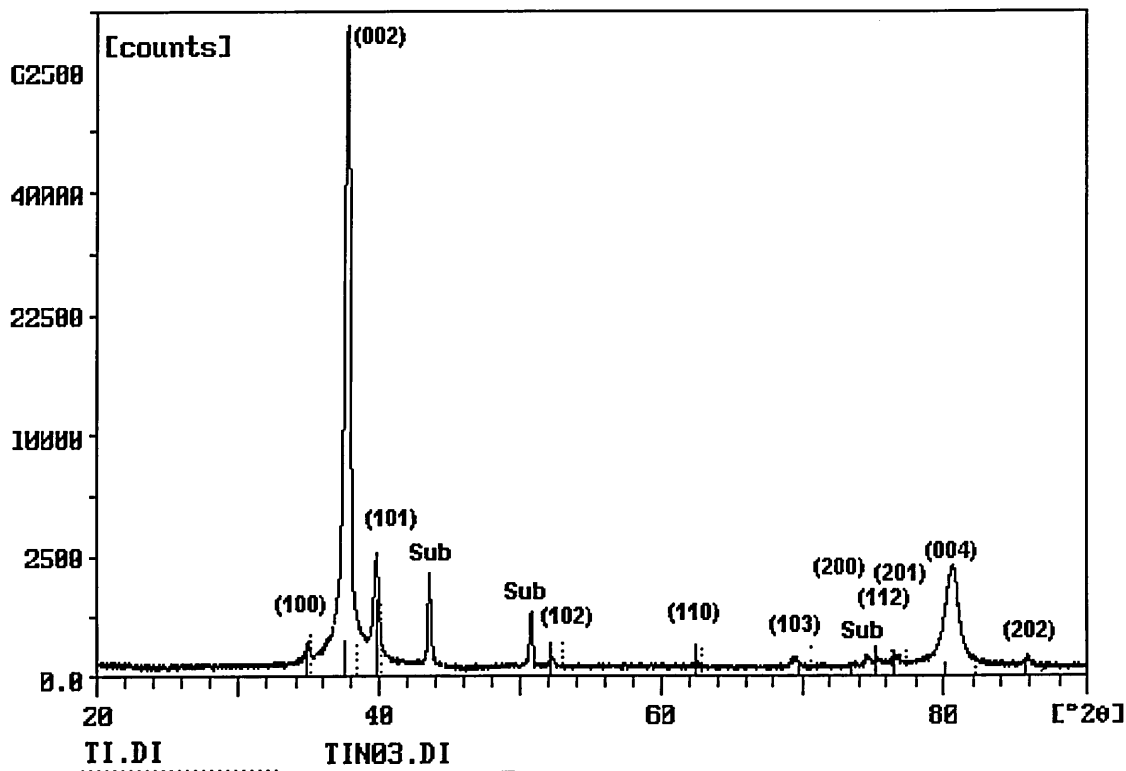


Fig 7.2.3 XRD pattern of coating at 7 % N

The reflections were identified as $\alpha\text{TiN}_{0.3}$ (10.0), (00.2), (10.1), (10.2), (11.0), (10.3), (20.0), (11.2), (20.1), (00.4), and (20.2). The calculation of texture parameter, interplanar spacings and the related diffraction intensities of specimen and standard data from the XRD JCPDS file, are recorded in table 7.2.2. The average difference between the measured interplanar spacings and that from the JCPDS file (41-1352) was $\Delta d = 0.01 \text{ \AA}$. It was found that the {00.1} was the most preferred orientation. The texture parameters of the (10.1) and (11.2) were clearly reduced compared with those of pure titanium coating.

Table 7.2.2 Texture calculation of the coating at 7 % N

(hkl)	100	002	101	102	110	103	200	112	201	004	202
d*(Å)	2.575	2.396	2.268	1.754	1.487	1.357	1.288	1.263	1.244	1.198	1.134
d (Å)	2.566	2.381	2.263	1.750	1.485	1.351	1.271	1.259	1.241	1.191	1.131
Δd (Å)	0.01	0.02	0.01	<0.01	<0.01	0.01	0.02	0.01	<0.01	0.01	<0.01
I	15.4	27016.4	846.2	15.3	5.6	20.7	15.5	18.1	25.7		
I*	17	22	100	19	18	16	2	15	12		
I/I*	0.9	1145.9	8.3	0.8	0.3	1.3	7.8	1.2	2.2		
T(%)	0.1	97.9	0.7	0.1	<0.1	0.1	0.7	0.1	0.2		

With increasing nitrogen in the coating, the diffraction peaks were further shifted to the left. An X-ray diffraction profile of film containing 16 % N is shown in fig 7.2.4. However the diffraction peaks of the sample were slightly shifted to the left side of the peak positions for the $\alpha\text{TiN}_{0.3}$ phase. The reflections identified were $\alpha\text{TiN}_{0.3}$ (10.0), (00.2), (10.1), (10.2), (11.0), (10.3), (11.2), (20.1), (00.4), and (20.2).

The texture calculation as well as the interplanar spacings and diffraction intensities of both the specimen and the JCPDS file are shown in table 7.2.3. The average difference of the measured interplanar spacings and the standard values referred to the JCPDS file was $\Delta d = 0.01 \text{ \AA}$. The most preferred orientation was $\alpha\text{TiN}_{0.3}$ {00.1}.

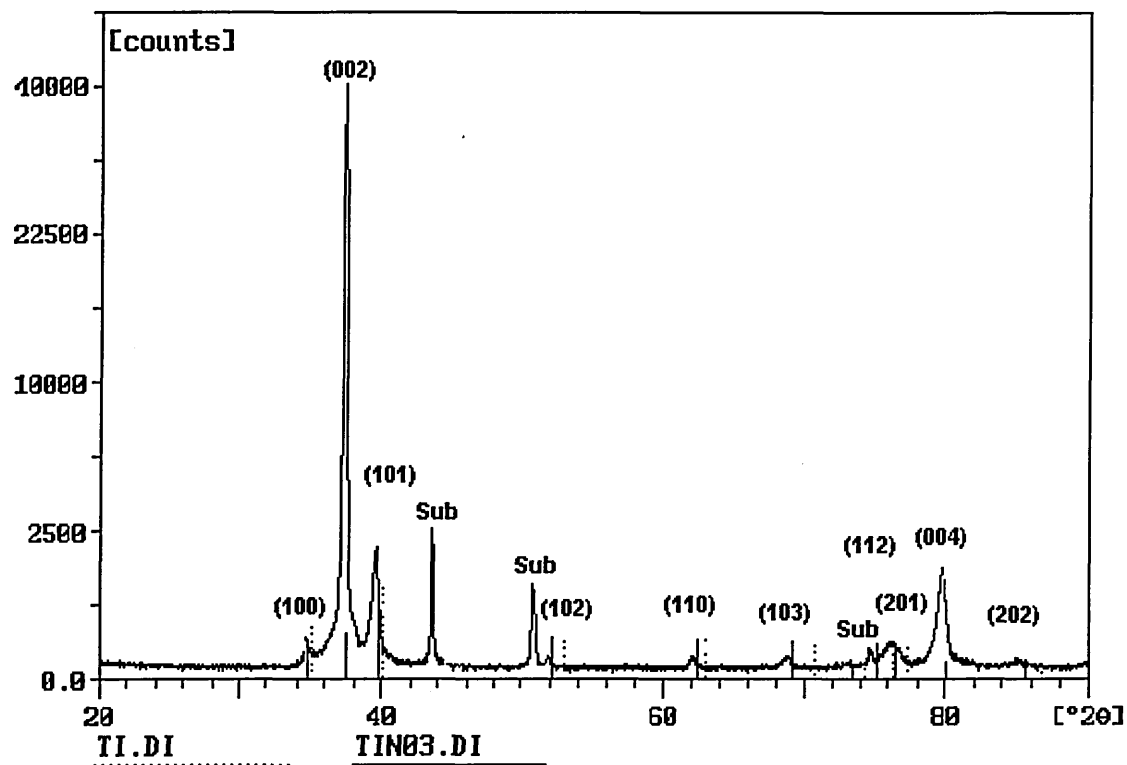


Fig 7.2.4 XRD pattern of coating at 16 % N

Table 7.2.3 Texture calculation of the coating at 16 % N

(hkl)	100	002	101	102	110	103	112	201	004	202
d*(Å)	2.575	2.396	2.268	1.754	1.487	1.357	1.263	1.244	1.198	1.134
d (Å)	2.580	2.403	2.277	1.761	1.494	1.363	1.269	1.248	1.201	1.139
Δd (Å)	0.01	0.01	0.01	0.01	0.01	0.01	0.01	<0.01	<0.01	0.01
I	30.9	12053.7	930.7	9.9	19.1	24.9	19.9	118.0		
I*	17	22	100	19	18	16	15	12		
I/I*	1.8	547.9	9.3	0.5	1.1	1.6	1.3	9.8		
T(%)	0.4	95.6	1.6	0.1	0.3	0.3	0.3	1.8		

When the nitrogen content of the coating was increased to 25 % N, the X-ray diffraction profile still indicated that the reflections corresponded to the $\alpha\text{TiN}_{0.3}$ phase; however, the positions for these peaks were clearly shifted further to the left as compared with that of the reference data as shown in fig 7.2.5. The identified reflections were $\alpha\text{TiN}_{0.3}$ (10.0), (00.2), (10.1), (10.2), (11.0), (10.3), (20.1), and (00.4). Texture calculations together with the interplanar spacings and diffraction intensities of both the specimen and the JCPDS file are given in table 7.2.4. The average difference between the measured interplanar spacings and the standard values referred to the JCPDS file was Δd

= 0.02 Å. The most preferred orientation was still the $\alpha\text{TiN}_{0.3}$ {00.1}; however, the texture was weaker than the other $\alpha\text{Ti(N)}$ films containing nitrogen of 7 and 16%. It was found that the reflections, $\alpha\text{TiN}_{0.3}$ (20.0), (11.2) and (20.2), which appeared in the XRD profile for the specimen at 7 % N were not present in the XRD pattern for the sample at 25 % N. It was also found the intensity of the $\alpha\text{TiN}_{0.3}$ (11.0) reflection was systematically increased with increasing nitrogen concentration in the coatings.

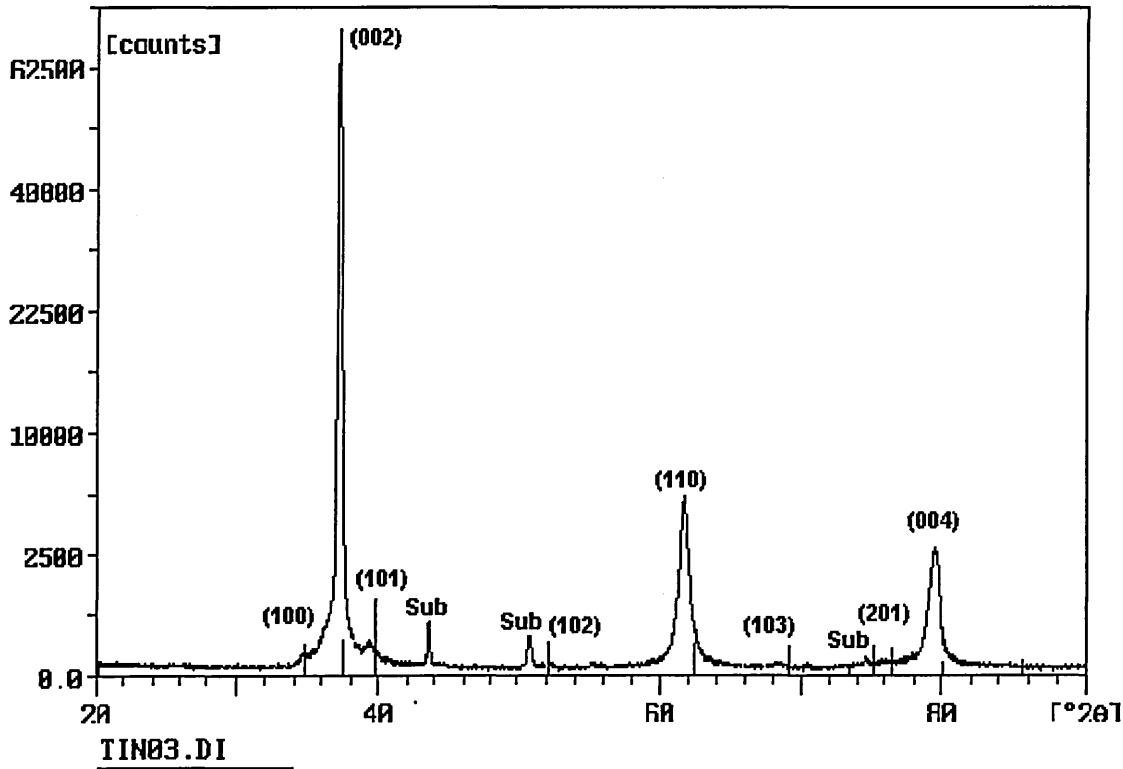


Fig 7.2.5 XRD pattern of coating at 25 % N

Table 7.2.4 Texture calculation of the coating at 25 % N

(hkl)	100	002	101	102	110	103	201	004
d*(Å)	2.575	2.396	2.268	1.754	1.487	1.357	1.244	1.198
d (Å)	2.581	2.412	2.293	1.748	1.505	1.372	1.251	1.206
Δd (Å)	0.01	0.02	0.03	0.01	0.02	0.02	0.01	0.01
I	93.4	23173.0	422.6	10.73	3780.3	8.5	1.9	
I*	17	22	100	19	18	16	12	
I/I*	5.5	1053.3	4.2	0.6	210.0	0.5	0.2	
T(%)	0.4	82.7	0.3	0.1	16.4	<0.1	<0.1	

As the composition of the coating increased to 27% N, the phase composition suddenly changed from $\alpha\text{TiN}_{0.3}$ to $\epsilon\text{Ti}_2\text{N}$, as shown in fig 7.2.6. Two $\epsilon\text{Ti}_2\text{N}$ phases were identified. The dominant phase was $\epsilon\text{Ti}_2\text{N}$, as referred to JCPDS file 17-386. The other phase was $\epsilon\text{Ti}_2\text{N}^*$ as referred to JCPDS file 23-1455. The reflections identified were $\epsilon\text{Ti}_2\text{N}$ (110), (101), (200), (111), (210), (211), (220), (002), (301), (311), (202), (212), and $\epsilon\text{Ti}_2\text{N}^*$ (200), (204), (107). These diffraction peaks were at almost the same positions as those referred to by the JCPDS file, indicating that the film was formed of $\epsilon\text{Ti}_2\text{N}$ phase and free of residual stress.

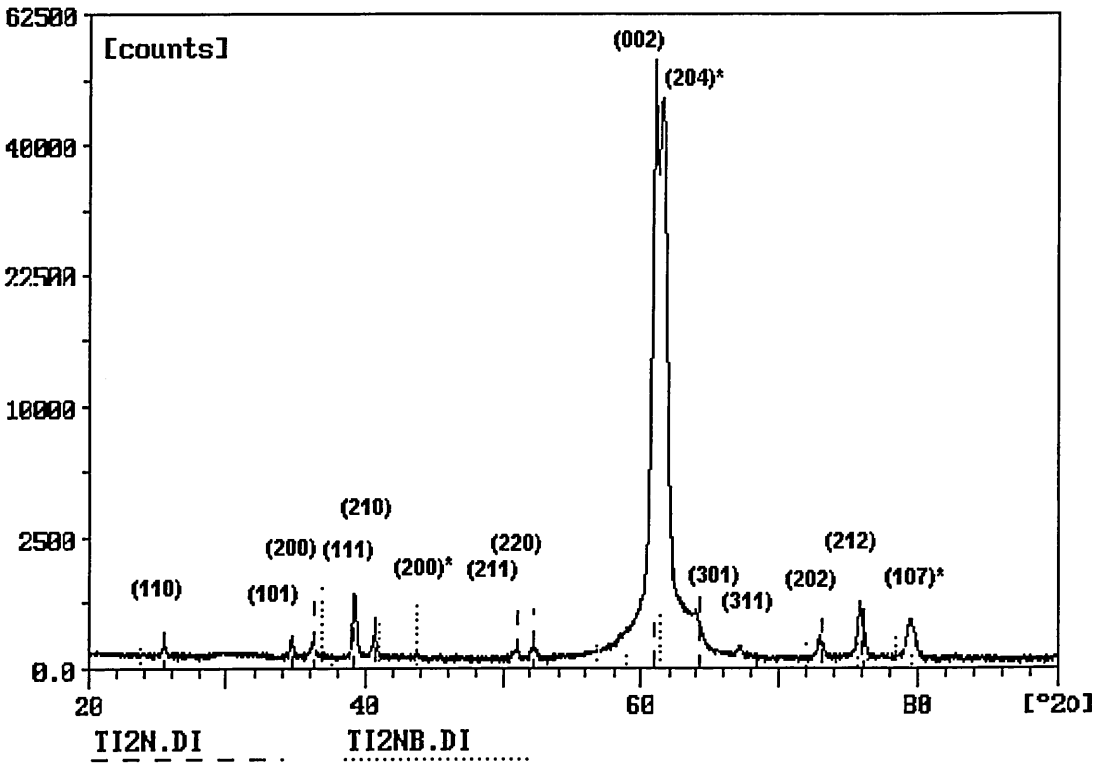


Fig 7.2.6 XRD pattern of coating at 27 % N

The positions for diffraction peaks of $\epsilon\text{Ti}_2\text{N}$ (110), (200), (111), (210), (211), and (311) were far away from those for the peaks of Ti, $\alpha\text{TiN}_{0.3}$ and δTiN phases, thus further proving that the film was pure $\epsilon\text{Ti}_2\text{N}$ phase in composition. The calculated texture values, interplanar spacings and related diffraction intensities of both the specimen and the JCPDS file are shown in table 7.2.5. The average difference between the measured interplanar spacings and the standard values referred to the JCPDS file was Δd less than

0.01 Å. The coating was formed with an extremely strong {001} texture with a minor {102} component.

Table 7.2.5 Texture calculation of specimen of 27 % N

(hkl)	d* (Å)	d (Å)	Δd (Å)	I	I*	I/I*	T(%)
(110)	3.500	3.490	0.01	13.3	20	0.7	0.2
(101)	2.586	2.585	<0.01	21.5	10	2.2	0.5
(200)	2.473	2.477	<0.01	31.1	80	0.4	0.1
(111)	2.292	2.293	<0.01	185.6	100	1.9	0.4
(210)	2.211	2.214	<0.01	41.2	50	0.8	0.2
(211)	1.788	1.789	<0.01	14.8	50	0.3	0.1
(220)	1.749	1.751	<0.01				
(002)	1.517	1.519	<0.01	23416.0	50	468.3	96.9
(301)	1.448	1.453	0.01	327.3	80	4.1	0.9
(311)	1.390	1.393	<0.01	10.2	80	0.1	0.1
(202)	1.293	1.296	<0.01				
(212)	1.251	1.254	<0.01	215.8	50	4.3	0.9
(200)*	2.069	2.070	<0.01	3.0	65	0.05	0.3
(204)*	1.508	1.504	<0.01	24888.5	40	622.2	88.0
(107)*	1.204	1.205	<0.01	168.8	2	84.4	11.7

When the composition of the coating was increased to 33 % N, the XRD pattern showed that the coating was formed with a multiphase composition of $\epsilon\text{Ti}_2\text{N}$ + δTiN phases as shown in fig 7.2.7. Even though overlapping of the diffraction peaks exist, the diffraction pattern could still indicate that the corresponding reflections were $\epsilon\text{Ti}_2\text{N}$ (101), (200), (111), (210), (220), (311), (320), (212); $\epsilon\text{Ti}_2\text{N}^*$ (103), (204), (107); and δTiN (111), (200). It could be seen from this XRD profile that the dominant phase was Ti_2N (JCPDS 17-386 and 23-1455) whilst the TiN phase was just starting to develop.

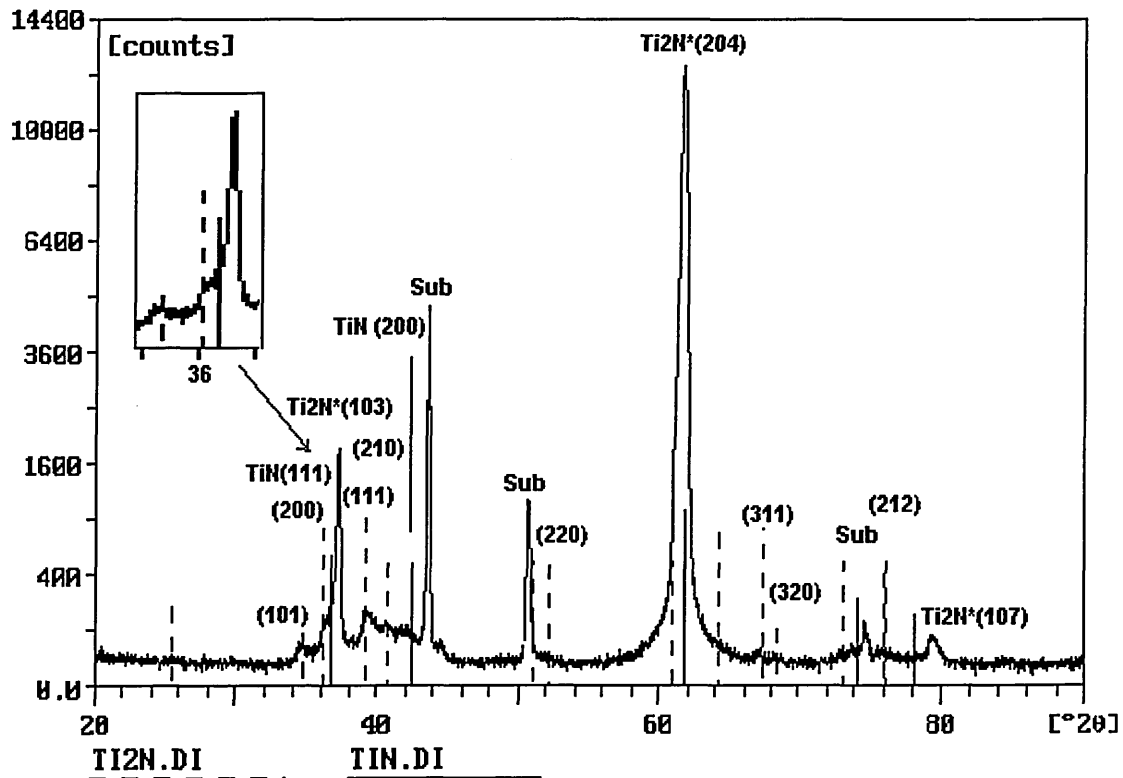


Fig 7.2.7 XRD pattern of coating at 33 % N

When the composition of the coating increased to 40 % N, the stoichiometric δ TiN phase composition was fully developed. The X-ray diffraction peaks corresponded with the reflections from δ TiN (111), (200), (220), (311), and (222) as shown in fig 7.2.8 in which the profiles for specimens with composition at 40, and 50 % N were given.

The texture calculations, measured interplanar spacings and diffraction intensities of the specimens and the related values referred to the JCPDS file 38-1420, are given in table 7.2.6 The average difference between the measured interplanar spacings and standard values of the JCPDS file was $\Delta d = 0.01 \text{ \AA}$ for coating at 40 % N, and $\Delta d = 0.02 \text{ \AA}$ for coating at 50 % N. The preferred orientation of the coating at 40 % N was {110} and $\langle 311 \rangle$ whilst that of the coating at 50 % N was only {110}.

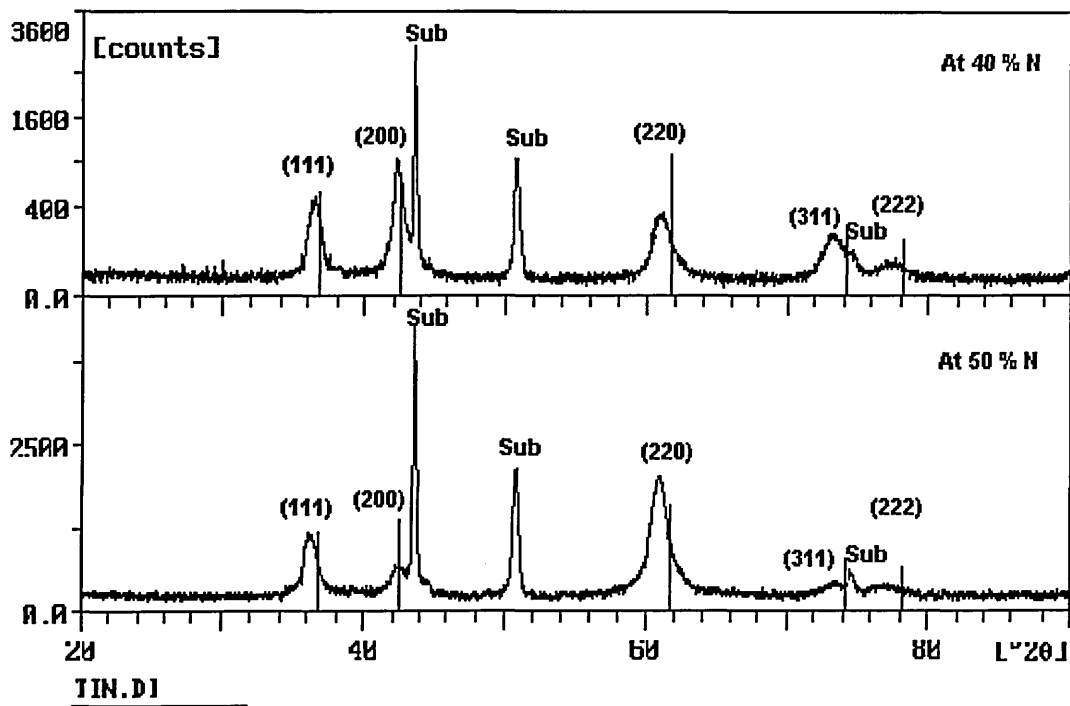


Fig 7.2.8 XRD patterns of coating at 40 and 50 % N

Table 7.2.6 Texture calculation of the coating at 40 and 50 % N

At % N	(hkl)	111	200	220	311	222
JCPDS	d*(Å)	2.4492	2.1207	1.4997	1.2789	1.2245
Data	I*	72	100	45	19	12
40	d (Å)	2.4552	2.1390	1.5173	1.2958	1.2271
	Δd (Å)	0.006	0.018	0.018	0.017	0.003
	I	456.6	677.0	447.9	269.1	83.9
	I/I*	6.3	6.8	10.0	14.2	6.4
	T(%)	14.4	15.6	22.9	32.5	14.6
50	d (Å)	2.4864	2.1210	1.5156	1.2886	1.2489
	Δd (Å)	0.037	<0.001	0.016	0.010	0.024
	I	503.1	176.4	1869.2	74.6	81.6
	I/I*	7.0	1.8	41.5	3.9	6.8
	T(%)	11.5	3.0	68.0	6.4	11.1

7.2.3 Thickness, micro hardness, and adhesion measurement

The thickness as measured using SEM was 3.7, 3.6, 3.6, 7.3, 15.0, 3.5, 3.5, and 3.0 μm for the coatings containing 0, 7, 16, 25, 27, 33, 40, and 50% N respectively. The hardness values of these coatings were measured using knoop indentation with a load of

25 g giving that the hardness is a function of nitrogen concentration as shown fig 7.2.9. It can be seen that hardness increased linearly up to approximately 26000N/mm^2 as the concentration changed from 0 to 25 at % N. The hardness reduced to a value of 22000N/mm^2 when the concentration of the film (the pure Ti_2N film as measured by XRD) was 27% N, followed by an increasing hardness to a maximum of 32000N/mm^2 when the N concentration of the coating increased to 40 at %. The hardness decreased to approximately 27000N/mm^2 when the coating contained 50 at % N. The hardness value of the pure Ti_2N coating was less than that of coatings with stoichiometric TiN phase composition as expected. However Poulek et al.⁽¹⁾ conducted similar experiments and reported the result shown in fig 7.2.9 which also fits with other reported results for the hardness of Ti_2N . In interpreting the results obtained in this work, it is speculated that the operating conditions, particularly the choice of nitrogen partial pressure, were not sufficiently discriminating to optimise the production of single phase stoichiometric Ti_2N . Thus the dotted lines shown on fig 7.2.9 suggest that this work could be in agreement with that of Poulek et al.

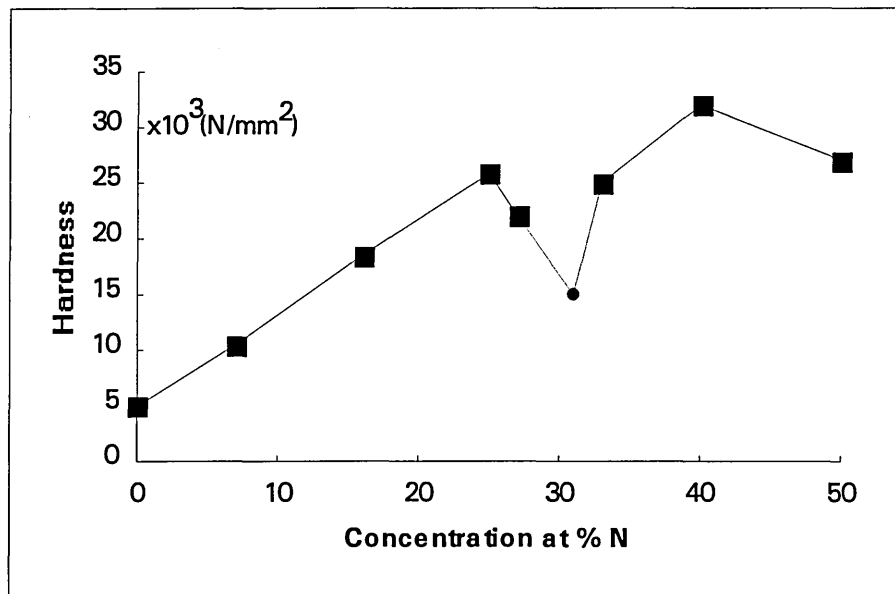


Fig 7.2.9 Hardness dependence on composition

● Reference (1) for the hardness of $\epsilon\text{Ti}_2\text{N}$ phase

The adhesion measurements using the Rockwell indentation test are shown in fig 7.2.10. Indentations of $R_c=1$ were obtained for films with concentrations from 0 to 40 at % N. An indentation of $R_c=2$ was found on the coating of 50 at % N. It could be seen from the edge of the indentation that all the coatings showed good quality of resistance to propagation of cracks along the interface between coating and substrate.

(See page 174-176 for fig 7.2.10)

Fig 7.2.10 Rockwell indentation tests on the Ti-N films

a, b, c, d, e, f, g, h. refer to coating at 0, 7, 16, 25, 27, 33, 40, 50% N respectively

The adhesion measurements using the scratch test are given in fig 7.2.11, in which the critical load (L_c) increased from 6.6 N to 12 N with increasing nitrogen concentration from 0 to 16%. A large increase of L_c (from 16 to 39.3 N) was found when N concentration increased from 16 to 25%. Then the critical load decreased to 25.3 N as nitrogen increased to 33%. Afterwards the critical load increased to a maximum of 49.7 N when the composition increased to 40% of nitrogen. Finally the critical load decreased to 37.2 N when the coating was deposited at stoichiometric TiN composition. The large increase of L_c value at composition of 25 and 27% N as resulted from the effect of thickness as the films were twice as thick as the others.

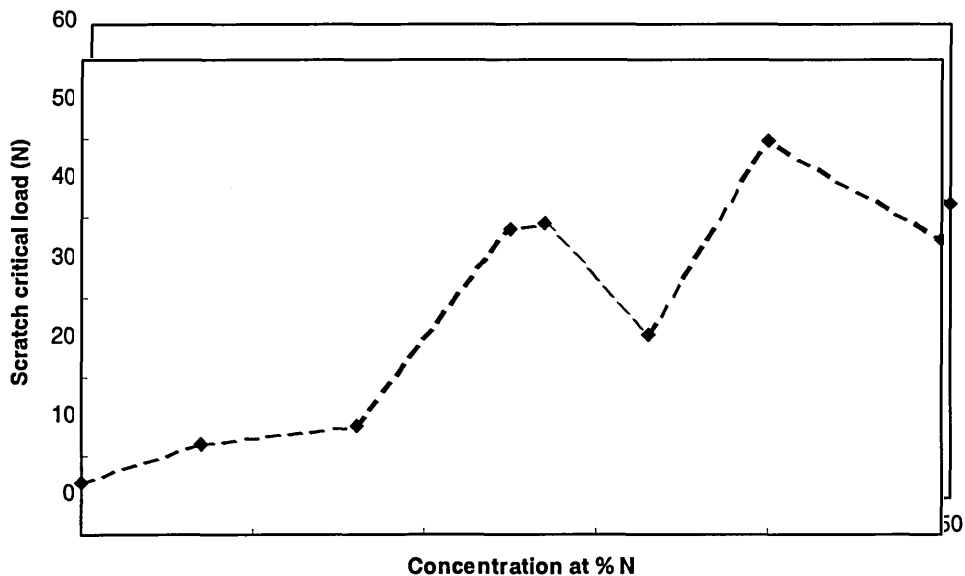


Fig 7.2.11 Scratch critical load dependent on composition

7.2.4 Surface roughness dependence on composition of the films

The roughness results of the Ti-N films are shown in fig 7.2.12, which gives the variation of film roughness with film composition. It can be seen that the pure Ti_2N film (composition at 27% N) had the lowest roughness ($R_a=0.11\mu m$, $R_z=0.89\mu m$, $R_t=1.5\mu m$). The films produced with $\alpha TiN_{0.3}$ phase (composition at 25% N) or multiphase ($\epsilon Ti_2N + \delta TiN$, composition at 33% N) had a higher roughness ($R_a=0.23$ or $0.20\mu m$, $R_z=2.41$ or $3.10\mu m$, $R_t=3.92$ or $5.00\mu m$ respectively). The films produced by single titanium phase, $\alpha TiN_{0.3}$ phase (composition at 7 and 16% N), and stoichiometric δTiN phase (composition at 40 and 50% N) had lower roughness compared with films produced at 25 and 33% N.

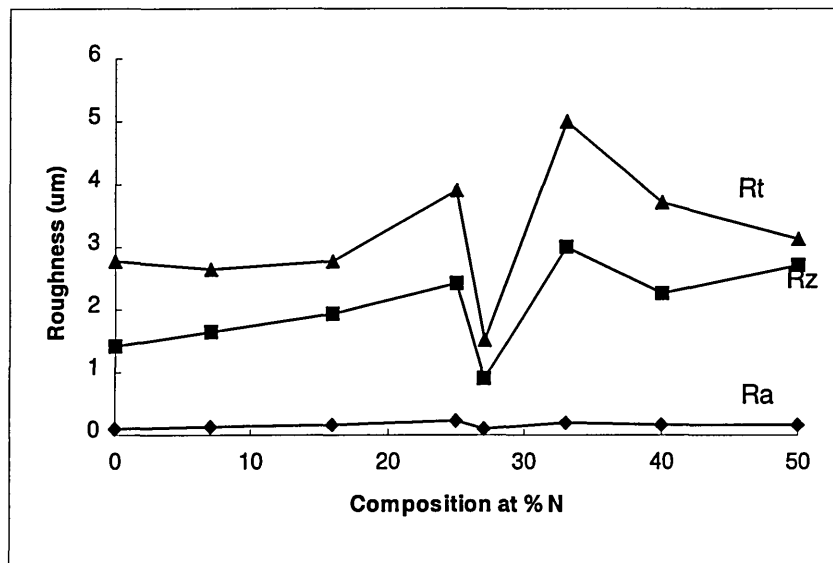


Fig 7.2.12 Dependence of film roughness on film composition

The surface morphologies of the films were a function of the film composition as investigated by scanning electron microscopy, as shown in fig 7.2.8. It could be seen that many droplets and defects were found on the surface of the films (containing pure Ti phase and $\alpha TiN_{0.3}$ phase) with composition $\leq 25\%$ N as well as films (containing multiphase, $\epsilon Ti_2N + \delta TiN$, and single phase δTiN) with composition $\geq 33\%$ N. When the film was produced as pure ϵTi_2N phase composition (about 27% N), however, there

were hardly any droplets and defects to be seen on the surface of the film and the film surface was extremely smooth.

(See page 177-180 for fig 7.2.13)

Fig 7.2.13 Top-graphic SEM images of the static Ti-N films
a, b, c, d, e, f, g, h. refer to coating at 0, 7, 16, 25, 27, 33, 40, 50% N respectively

7.3 Discussion of chapter 7

The characteristics of these coatings were examined by glow discharge optical emission spectrum (GDOES), x-ray diffraction (XRD), micro hardness, Rockwell (R_C indentation), roughness (R_a , R_z , and R_t), scanning electron microscope, and transmission electron microscope investigative techniques. The nitrogen content of the film was very sensitive to variations in nitrogen partial pressure and the nitrogen concentration influenced the phases developed in the films. α Ti(N) was found in the films containing up to 25% N. The pure ϵ Ti₂N film was deposited at 27% N and both ϵ Ti₂N phases were identified as shown by X-ray diffraction. Multi-phase compositions (ϵ Ti₂N and δ TiN) were produced in film of 33% N. Single phase δ TiN was formed in films containing 40 and 50% N. It is clear that the composition for formation of pure ϵ Ti₂N film is located in a small range of N concentration. The N-rich and N-poor films compared with this range will result in formation of δ TiN and α Ti(N) respectively.

In general as the composition for pure ϵ Ti₂N film is only at a very narrow range, the presence of ϵ Ti₂N phase always accompanied with either α Ti(N) or δ TiN. Sundgren⁽²⁾ investigated the Ti-N film system and found that the α Ti(N) presented in film containing composition less than 15% N; above 15% N the ϵ Ti₂N began to appear and the single phase ϵ Ti₂N was present only at 33% N; δ TiN started to develop at compositions above 30%N and above 35% N only single phase δ TiN was present in the film. Matthews⁽³⁾ applied ion plating techniques to deposit ϵ Ti₂N film containing δ TiN phase. Kiuchi⁽⁴⁾ obtained the similar result in which the film consisted of multi-phase (α Ti(N) + ϵ Ti₂N + δ TiN) when composition ratio, Ti/N, was large than that (2/1) for ϵ Ti₂N; for lower Ti/N,

$\epsilon\text{Ti}_2\text{N} + \delta\text{TiN}$ present in the film; for further lower Ti/N, only δTiN was developed in the films. The concentration of pure Ti_2N phase film as presented here was 27% N. This discrepancy, compared with the literature (33% N), may result from the quantitative inaccuracy of the GDOES technique. Nevertheless the X-ray diffraction showed a very unique pattern for the film of 27% N, which indicated that there was no trace of $\alpha\text{Ti(N)}$ and δTiN thus pure Ti_2N film was proved to be produced.

The most important aim in producing pure Ti_2N coating was to obtain the right concentration at a certain temperature⁽⁵⁾, deposition rate⁽⁶⁾ and in a critical nitrogen partial pressure regime⁽⁷⁾ during the coating process. Here the temperature of the deposition process can be precisely controlled since a heater was used in the main chamber, the sputtering rate was determined by the target power and the deposition rate is fully controlled. As can be seen from fig 7.2.1 the composition of nitrogen was sensitive to the nitrogen partial pressure before the nitrogen concentration reached to 33% N. During this stage, the target was not poisoned so that the sputtering rate of titanium was constant and high plasma density was produced in front of the target. As the consumption of the nitrogen in the plasma was proportional to the nitrogen gas flow during this stage, there was no distinct change in total chamber pressure. Therefore the nitrogen partial pressure is the crucial process parameter which has to be controlled accurately in order to produce pure Ti_2N coatings. However, the nitrogen partial pressure control was a complicated problem which was influenced by several parameters such as the chamber base pressure, the chamber total pressure, target sputtering rate, loading of the chamber, substrate bias voltage, nitrogen gas flow and consumption of the nitrogen during the process. These inter-related parameters affected the reproducibility of pure Ti_2N films. The partial pressure as monitored here was measured by a mass spectrometer which was differentially pumped from the main coating chamber and therefore the measured nitrogen partial pressure was only proportionally related to that of main chamber. From the static coating process for production of pure Ti_2N coating presented in this thesis, the nitrogen partial pressure must be precisely controlled in the range of 2.0×10^{-5} mbar by the nitrogen gas flow-meter. If the nitrogen partial pressure is

below or above that range, either the $\alpha\text{Ti(N)}$ or δTiN phases will be present in the coating respectively, and the Ti_2N phase disappears.

The enhanced hardness of the Ti-N films ($\text{Ti}_2\text{N} + \text{TiN}$) were reported^(8,9) when the Ti_2N phase was present in the film. The work presented here, however, indicated that the Ti_2N did not correspond to the highest hardness. The highest hardness (320000 N/mm^2) corresponded to the sub-stoichiometric TiN film containing 40% N and single phase δTiN . In fact the high hardness is mainly caused by the specific microstructure that can develop rather than by the Ti_2N phase itself⁽¹⁰⁾. The highest value of adhesion ($R_c = 1$, $L_c = 49.7 \text{ N}$) was achieved for the film containing 40% N and single phase δTiN with the highest hardness value. The films containing low nitrogen level ($\leq 33 \text{ at } \% \text{ N}$) were characterised by low L_c value compared with the single phase δTiN film. The low L_c of the low nitrogen level films does not mean the poor adhesion between film and substrate because these films are not as hard as δTiN and hence are less able to resist the scratch of the diamond tip. As the hardness for those films is in different level, it is not fair to judge the adhesion using the same scratch criteria. In fact these films have been shown excellent adhesion as measured using Rockwell indentation tests. The pure Ti_2N film was characterised as having excellent adhesion and relatively high hardness, being extremely smooth and having an almost droplets free surface. These excellent properties may make Ti_2N film a candidate for wear and corrosion applications.

7.4 Conclusion of chapter 7

1. The development of the coating phase structure was critically dependent on the concentration of nitrogen within the plasma.
2. The optimised nitrogen partial pressure for deposition of pure Ti_2N film was $2.0 \times 10^{-5} \text{ mbar}$. Any deviation from this value resulted in formation of either the $\alpha\text{Ti(N)}$ phase or the stoichiometric TiN phase.
3. The highest hardness and adhesion were characterised the film containing 40% N and single phase δTiN . The low L_c value for the low nitrogen film was because of the

lower hardness. Measurements of these low nitrogen films by Rockwell indentation test appeared to show excellent adhesive properties ($R_C=1$).

4. The pure Ti_2N film was characterised as having relatively high hardness, excellent adhesion to the substrate, and an exceptionally smooth and droplet free surface.

References

- (1) V.Poulek, J. Musil, V. Valvoda, and R. Cerny, *Journal of Physics*, D21 (1988)1657
- (2) J.-E. Sundgren, B.-O. Johansson, S.-E. Karlsson and H.T.G. Hentzell, *Thin Solid Films*, V105 (1983)367
- (3) A. Matthews and D.G. Teer, *Thin Solid films*, V72 (1980)541
- (4) M. Kiuchi, K. Fujii, H. Miyamura, K. Kadono and M. Satou, *Nuclear Instruments and Methods in Physics Research*, B37/38 (1989)701
- (5) V. Poulek, J. Musil, V. Valvoda, and L. Dobiasova, *Materials Science and Engineering*, A140 (1991)660
- (6) B. Zega, M. Kornmann and J. Amiguet, *Thin Solid Films*, V45 (1977)577
- (7) J.-E. Sundgren, B.-O. Johansson and S.-E. Karlsson, *Thin Solid Film*, V105 (1983)353
- (8) B.E. Jacobson, R. Nimmagadda and R.F. Bunshah, *Thin Solid Films*, V63 (1979)333
- (9) H. Yoshihara and H. Mori *J. Vac. Technol.* V16 (1979)1007
- (10) J.-E. Sundgren, *Thin Solid Films*, V128 (1985)21

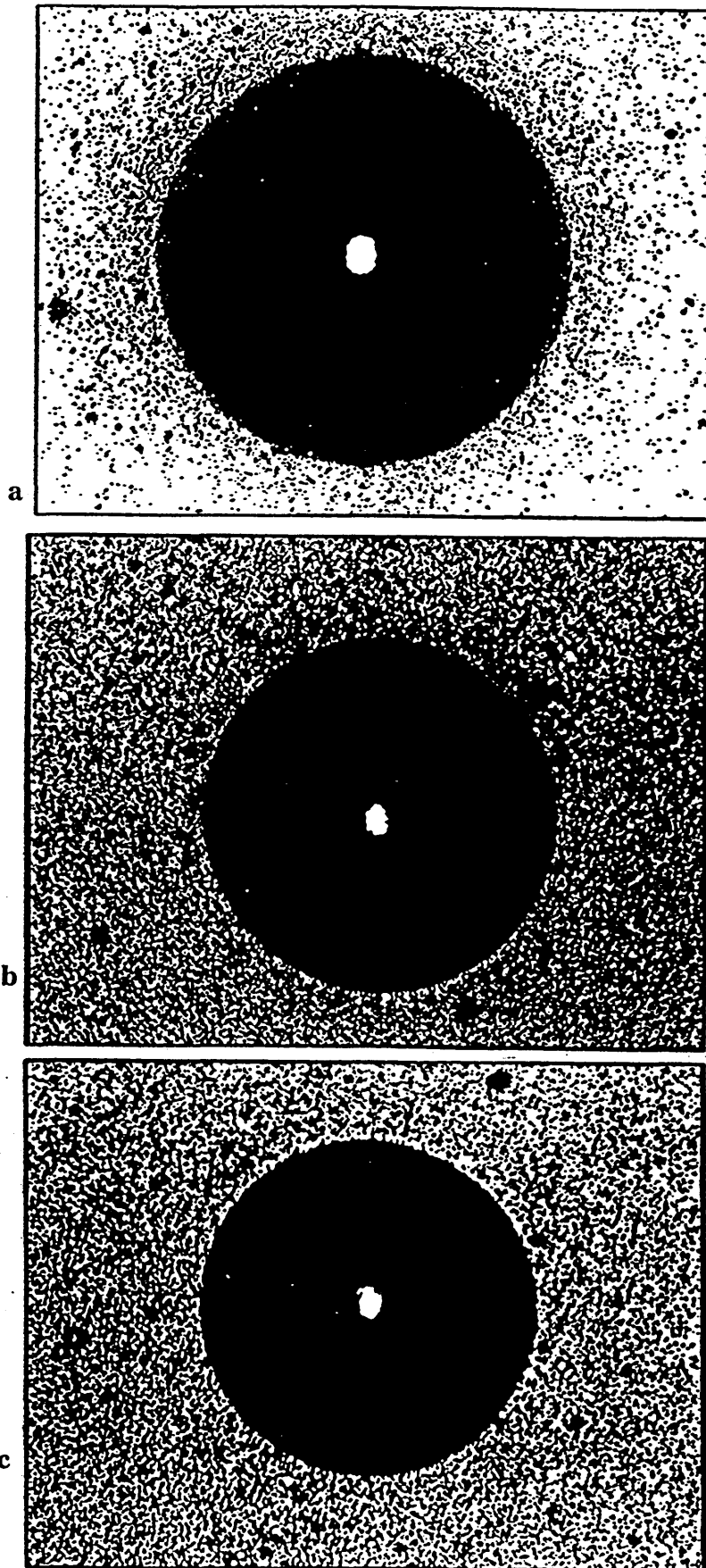


Fig 7.2.10 Rockwell indentation tests on the Ti-N films
a, b, c, d, e, f, g, h. refer to coating at 0, 7, 16, 25, 27, 33, 40, 50% N respectively

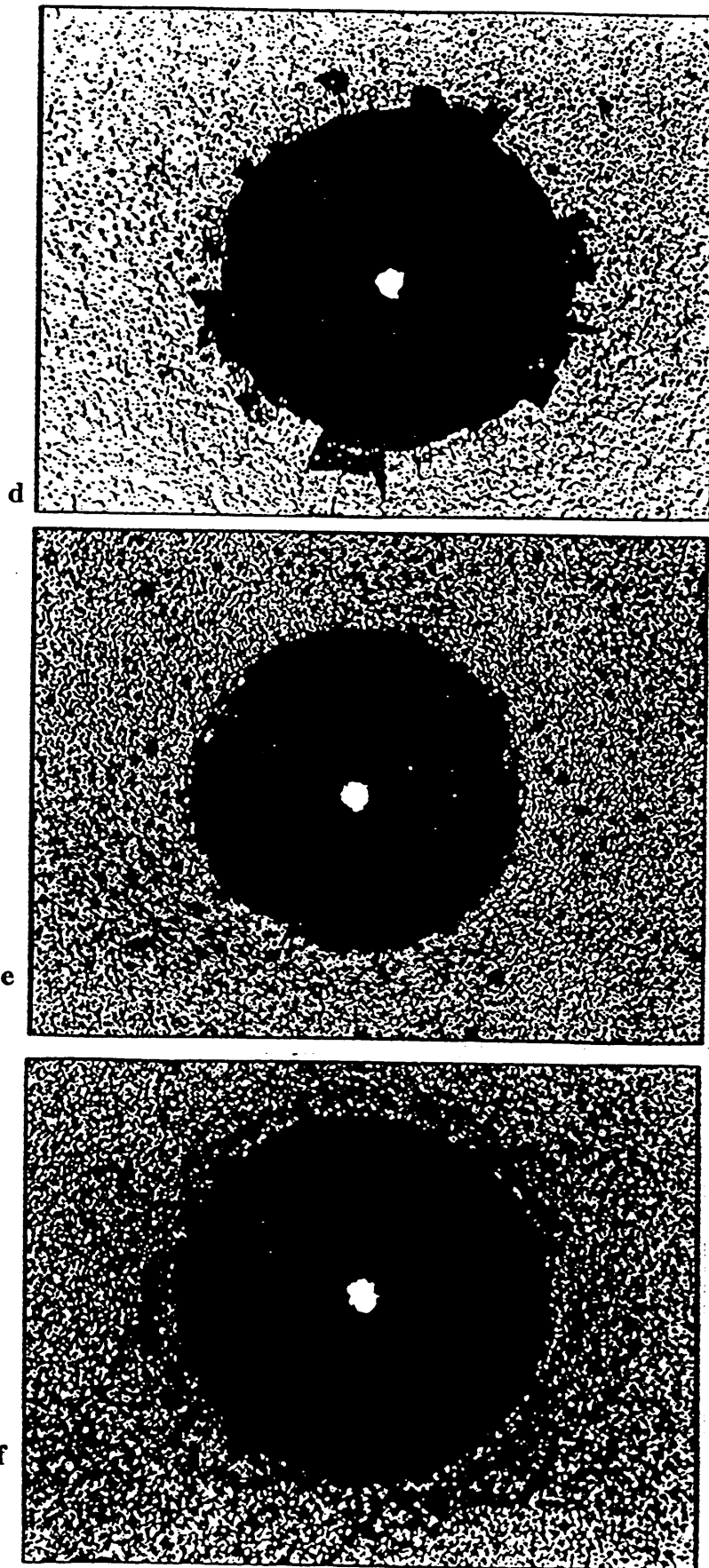


Fig 7.2.10 Rockwell indentation tests on the Ti-N films
a, b, c, d, e, f, g, h. refer to coating at 0, 7, 16, 25, 27, 33, 40, 50% N respectively

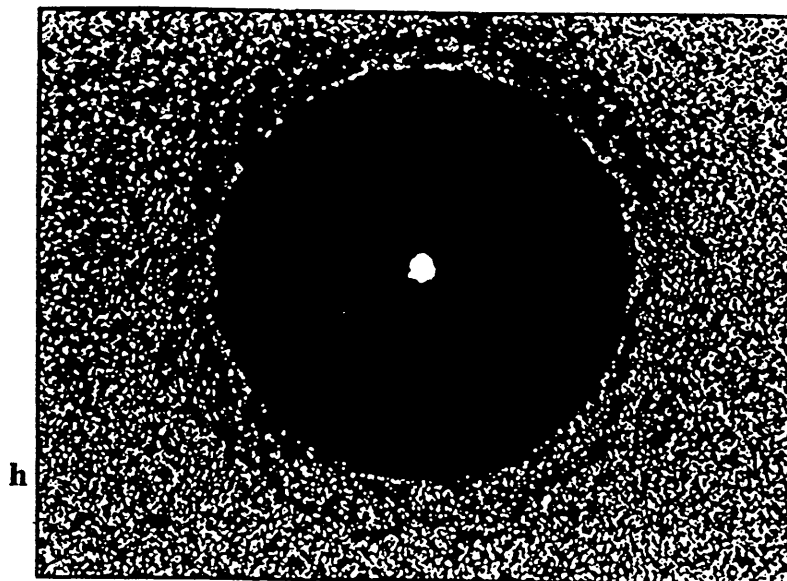
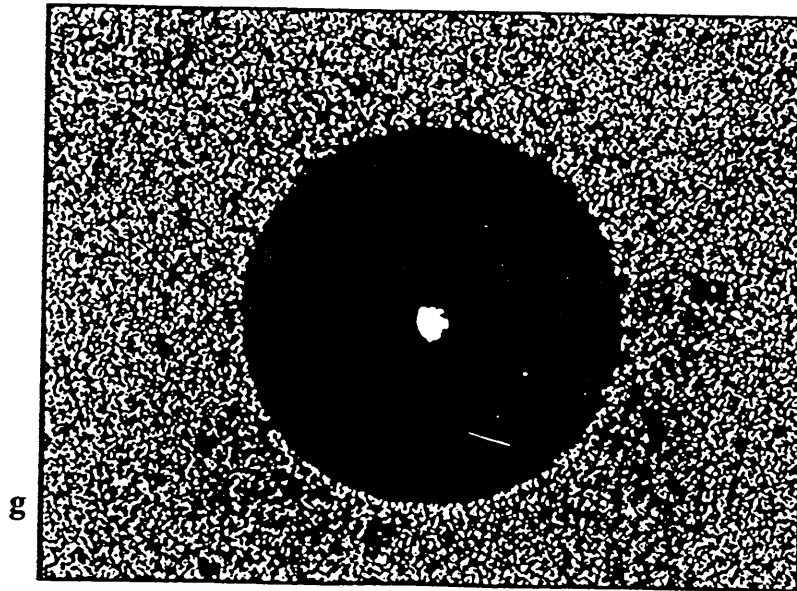


Fig 7.2.10 Rockwell indentation tests on the Ti-N films
a, b, c, d, e, f, g, h. refer to coating at 0, 7, 16, 25, 27, 33, 40, 50% N respectively

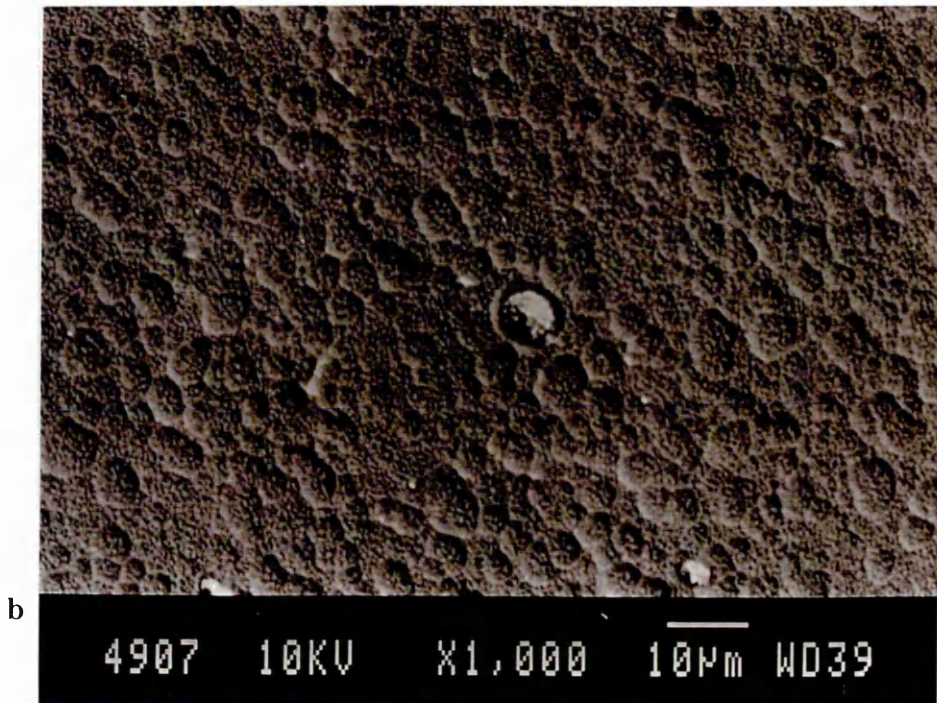
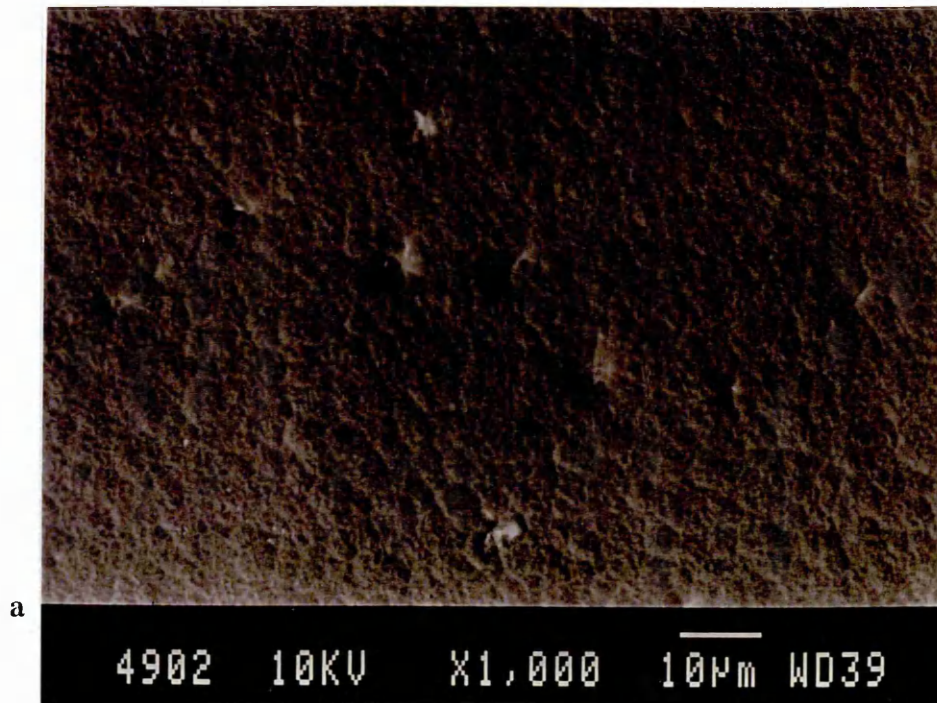


Fig 7.2.13 Top-graphic SEM images of the static Ti-N films
a, b, c, d, e, f, g, h. refer to coating at 0, 7, 16, 25, 27, 33, 40, 50% N respectively

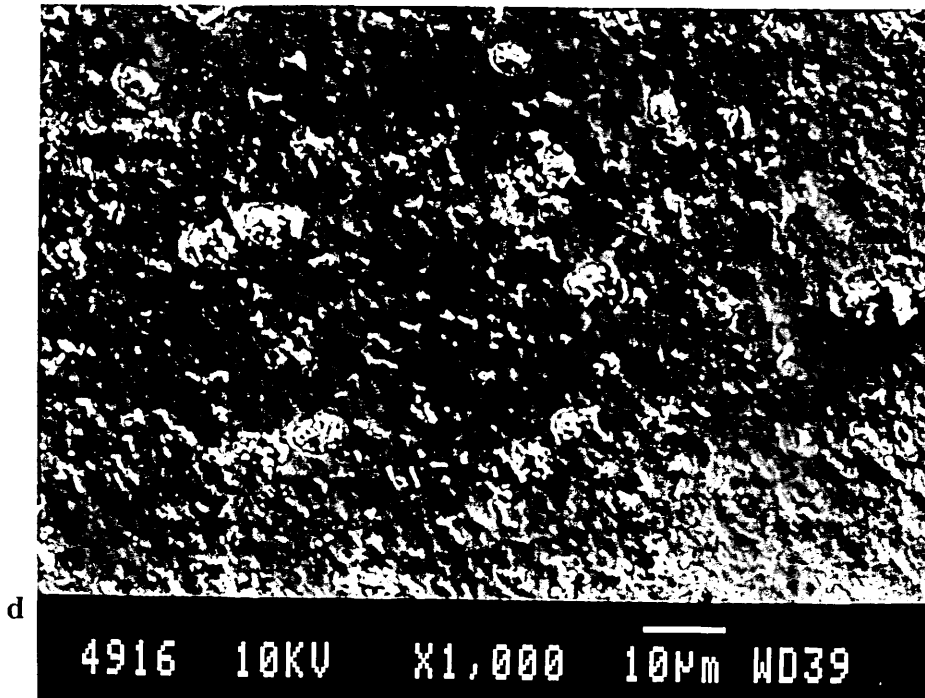
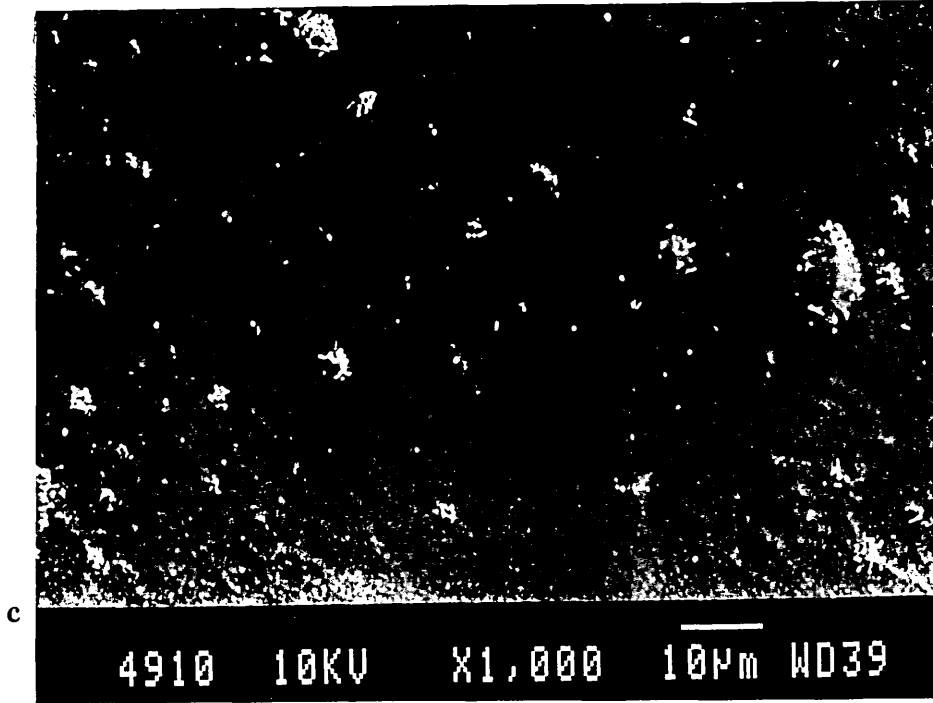


Fig 7.2.13 Top-graphic SEM images of the static Ti-N films
a, b, c, d, e, f, g, h. refer to coating at 0, 7, 16, 25, 27, 33, 40, 50% N respectively

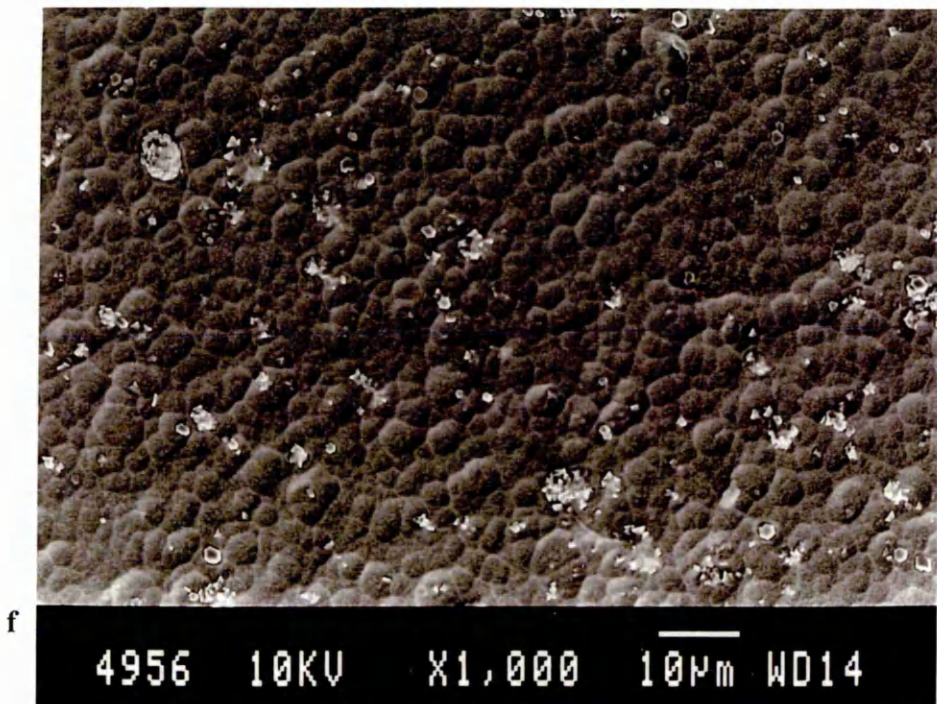
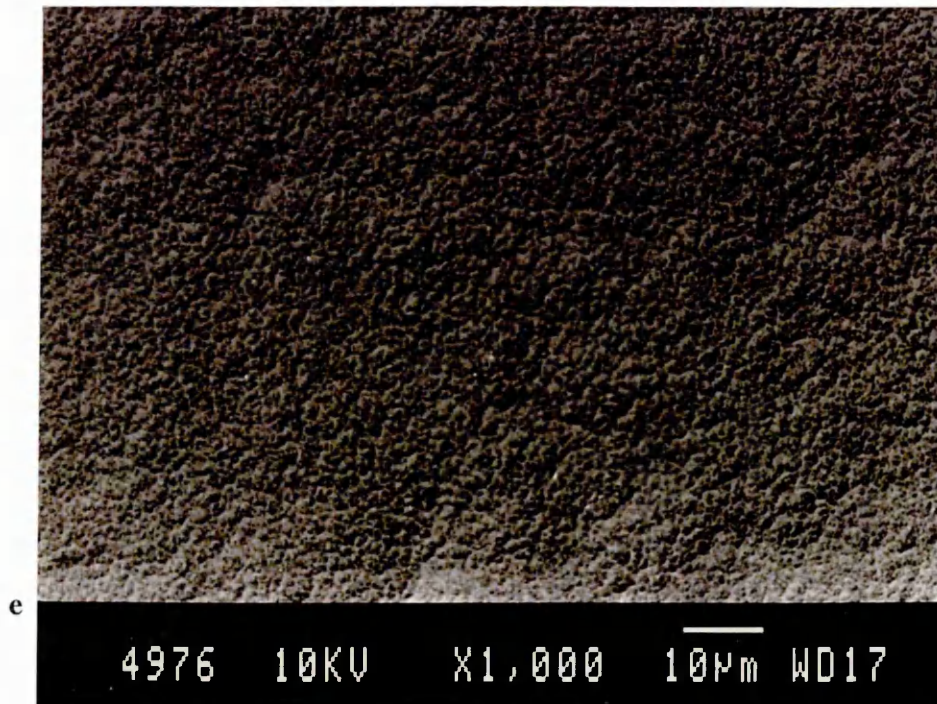


Fig 7.2.13 Top-graphic SEM images of the static Ti-N films
a, b, c, d, e, f, g, h. refer to coating at 0, 7, 16, 25, 27, 33, 40, 50% N respectively

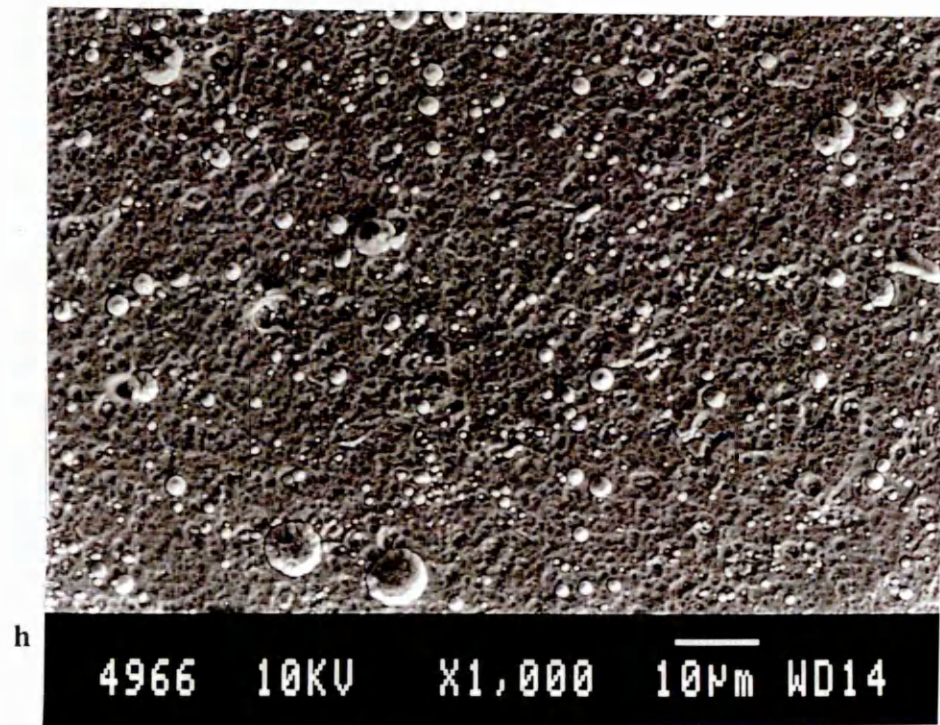
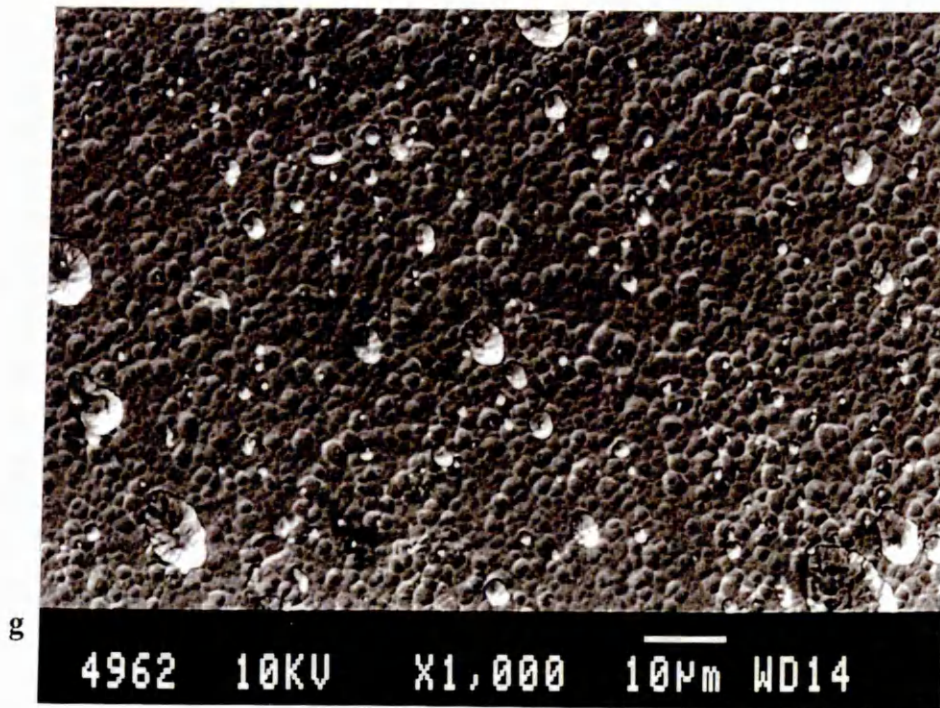


Fig 7.2.13 Top-graphic SEM images of the static Ti-N films
a, b, c, d, e, f, g, h. refer to coating at 0, 7, 16, 25, 27, 33, 40, 50% N respectively

8. Investigation of $\epsilon\text{Ti}_2\text{N}$ films using substrate table rotation

TiN_x (stoichiometric factor, $x = 0.2$ to 0.4) films were deposited at a substrate temperature of typically 480°C using an industrial sized unbalanced magnetron sputtering PVD coating machine. The stoichiometric factor, x , depended on the manner of substrate rotation as well as the reactive gas flow during deposition. This was considered in order to study the production of pure $\epsilon\text{Ti}_2\text{N}$ films for commercial purposes using an unbalanced magnetron sputtering machine. The substrates underwent single, double, and triple fold rotations during the deposition to match the real industrial coating process. The effect of substrate rotation on the development of phase composition in the film was investigated. The effect of nitrogen gas flow rate on the composition was also studied. The introduced nitrogen gas flow rate was considered as 70, 75 and 80 sccm in order to deposit films containing dominant Ti_2N phase compositions.

8.1 Experimental arrangement

There were three processes carried out and the process parameters recorded in table 8.1.1. All the processes used the same parameters except for the nitrogen gas flow rate (N_2 F.R.), which was changed from process to process. A heater was used during a process to combine the heating effects of applied target power, coil current, and bias voltage keeping the substrate temperature at a constant 480°C . The sample preparation and coating procedure is the same as described in section 4.2.

Table 8.1.1 Process parameters to produce Ti_2N film using substrate rotation

N_2 F.R. (sccm)	Ar F.R. (sccm)	P_t (kW)	I_{coil} (A)	V_{bias} (V)	I_{bias} (A)	T_s ($^\circ\text{C}$)	Rotation (Fold)
70	100	4×10	4×8	80	19	480	1, 2, 3
75	100	4×10	4×8	80	19	480	1, 2, 3
80	100	4×10	4×8	80	19	480	1, 2, 3

SNMS (secondary neutral mass spectrometry) was used to determine composition within the coating^(1,2). This measurement was carried out by penetrating the sample to a depth of $0.5 \mu\text{m}$ after reaching a sputter equilibrium and the average value was used to

determine the surface concentration. The concentration data as measured by SNMS was also used to revise that estimated by GDOES. XRD (X-ray Diffraction) was applied to determine the phase composition by comparing the diffraction peak positions with standard data⁽³⁾. SEM and TEM were used to investigate the morphology of the film fracture cross sectional structure and the interface structure between coating and substrate. Knoop hardness and Rockwell adhesion testers were used to measure the hardness and adhesion of the coatings.

8.2 Composition and hardness as a function of substrate rotation

The SNMS measurement was done on samples deposited in a process using a nitrogen flow rate of 75 sccm. The results of cps (counts per second from the spectrum of the elements in the coating) and the concentration in % N are shown in table 8.2.1. It can be seen that the titanium, carbon, and argon were systematically reduced whilst the nitrogen was increasing from one to three fold rotation. There was no evidence that the oxygen in the coating was increasing or reducing systematically. The atomic concentration of nitrogen in the coatings was at 14, 18, and 25% in samples using one, two, and three fold rotation to give the stoichiometric factor $x = 0.16, 0.22, \text{ and } 0.33$ respectively.

Table 8.2.1 SNMS analysis of Ti₂N films deposited using nitrogen flow 75 sccm

Fold	O (cps)	C (cps)	N (cps)	Ar (cps)	Ti (cps)	Fe (cps)	At % N	x
One	12.1	8.4	158.1	0.8	17072.2	10.0	14	0.16
Two	21.2	6.7	162.7	0.6	15079.2	9.2	18	0.22
Three	16.7	3.1	227.6	0.2	14335.6	10.8	25	0.33

The composition depth profile was made by SNMS using the nitrogen/titanium cps ratio vs time as plotted in fig 8.2.1. This indicated that the nitrogen distributions in growth direction of the coatings from one to three fold rotations were extremely uniform, thus giving rise to the assumption that the microstructures and mechanical properties should be also uniform through the coatings.

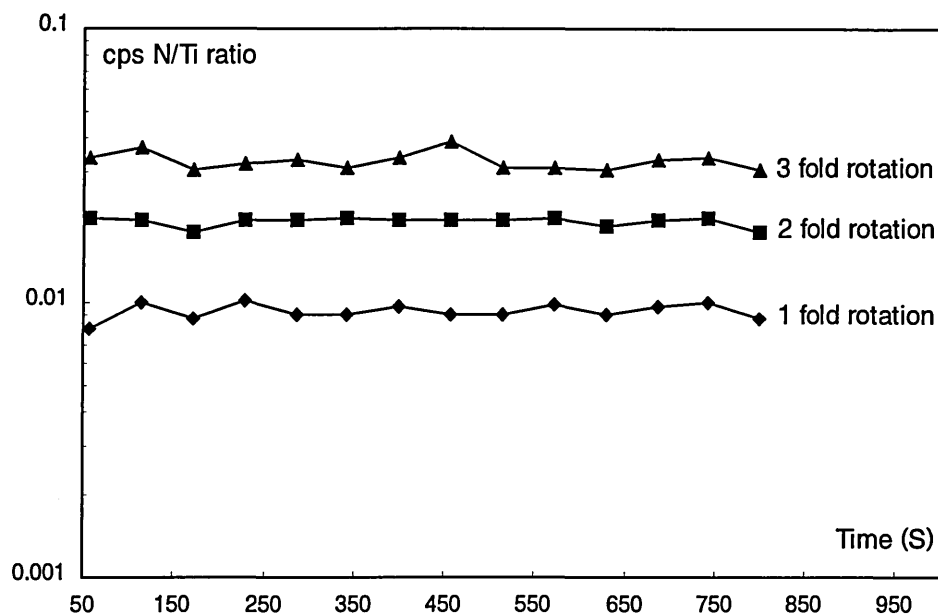


Fig 8.2.1 Composition depth profile of cps N/Ti ratio

It can also be assumed that the coatings deposited using 70 sccm and 80 sccm nitrogen gas flow rate should give a similar variation of composition values dependent on substrate rotation. The concentration ratio of one fold rotation to two and three fold rotation, which was measured by SNMS for process using nitrogen flow 75 sccm, can be used as the reference value for the coated samples using nitrogen flow of either 70 sccm or 80 sccm. The concentrations of coated samples of one fold rotation using 70 sccm and 80 sccm nitrogen flow rate were determined by GDOES. Then the concentration of the coatings using two and three fold rotation were estimated as shown in table 8.2.2. It can be seen that the stoichiometric factor increased as expected with the nitrogen gas flow rate and the substrate fold rotation.

Table 8.2.2 Composition dependent on gas flow and substrate rotation

Rotation	One fold		Two fold		Three fold	
	at % N	x	at % N	x	at % N	x
70 sccm	10	0.11	13	0.15	18	0.22
75 sccm	14	0.16	18	0.22	25	0.33
80 sccm	16	0.19	21	0.27	29	0.41

The hardness measurement of these samples are shown in fig 8.2.2. It can be seen that the hardness is systematically increased with nitrogen gas flow and the substrate fold rotation. The hardness for samples deposited using 70 sccm nitrogen gas flow was increased from Hk1500 to Hk1780 as the rotation increased from one to three fold rotation; the hardness for samples deposited using 75 sccm nitrogen flow was Hk1800, Hk 1900, and Hk 2100 for coatings deposited using one, two, and three fold rotation respectively; when 80 sccm nitrogen flow was used, the hardness increased from Hk 2070 to Hk 2250 as rotation increased from one to three fold respectively.

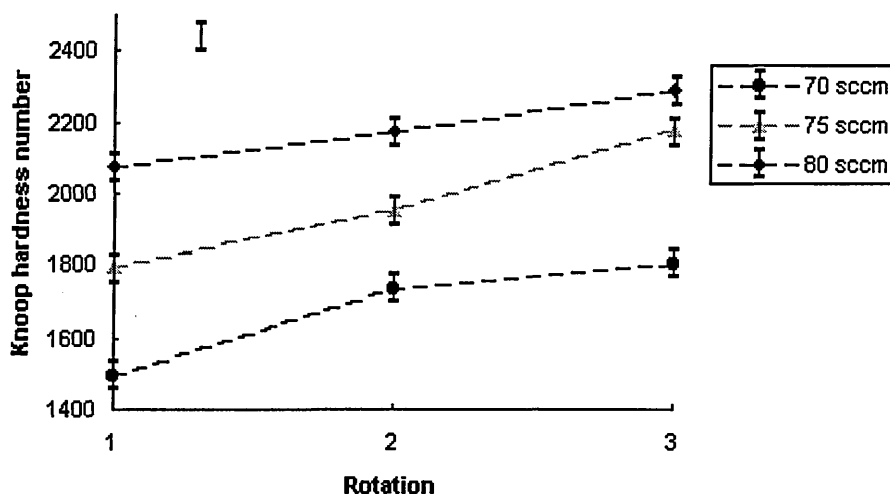


Fig 8.2.2 Hardness as a function of substrate rotation

8.3 Crystal phase dependent on nitrogen gas flow and substrate rotation

8.3.1 X-ray diffraction pattern from coatings using 70 sccm nitrogen gas flow rate

The X-ray diffraction profiles for samples deposited using 70 sccm nitrogen flow rate are shown in figs 8.3.1, 2, and 3. It was found that the diffraction peaks were systematically shifted to the left as rotation increased from one to two and three fold. This indicated that the nitrogen content within the coatings increased with fold rotation.

The diffraction pattern of one fold rotation indicated that the dominant phase was α TiN_{0.3}. However, issue of traces of ϵ Ti₂N was also addressed. The identified reflections were corresponded to α TiN_{0.3} (10.0), (00.2), (10.1), (11.0), (10.3), (11.2), (20.1), and (00.4); and ϵ Ti₂N (110), (211) and (220).

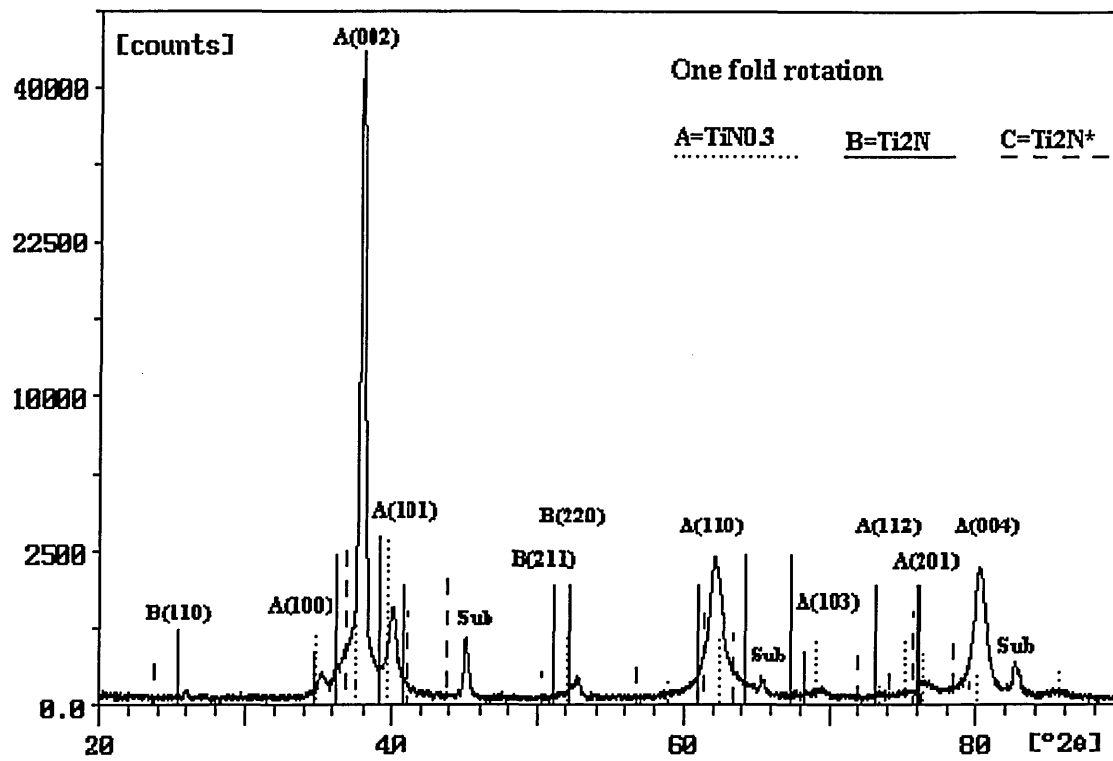


Fig 8.3.1 XRD pattern of Coating using 70 sccm nitrogen flow

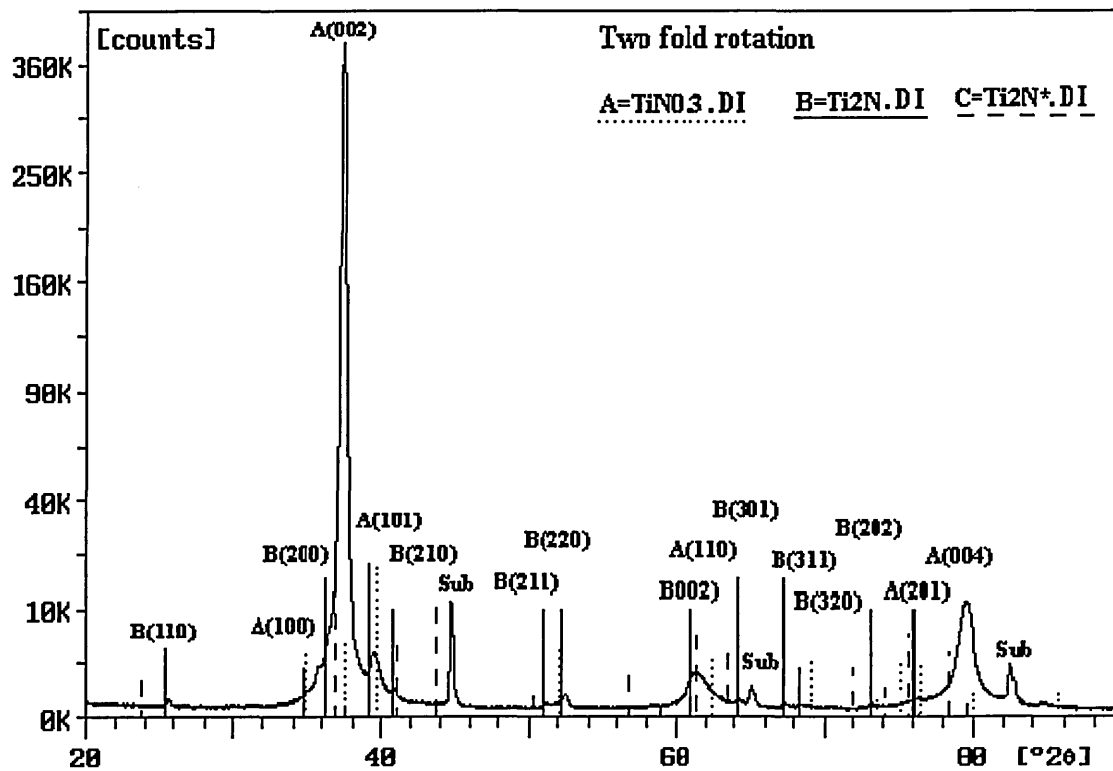


Fig 8.3.2 XRD pattern of Coating using 70 sccm nitrogen flow

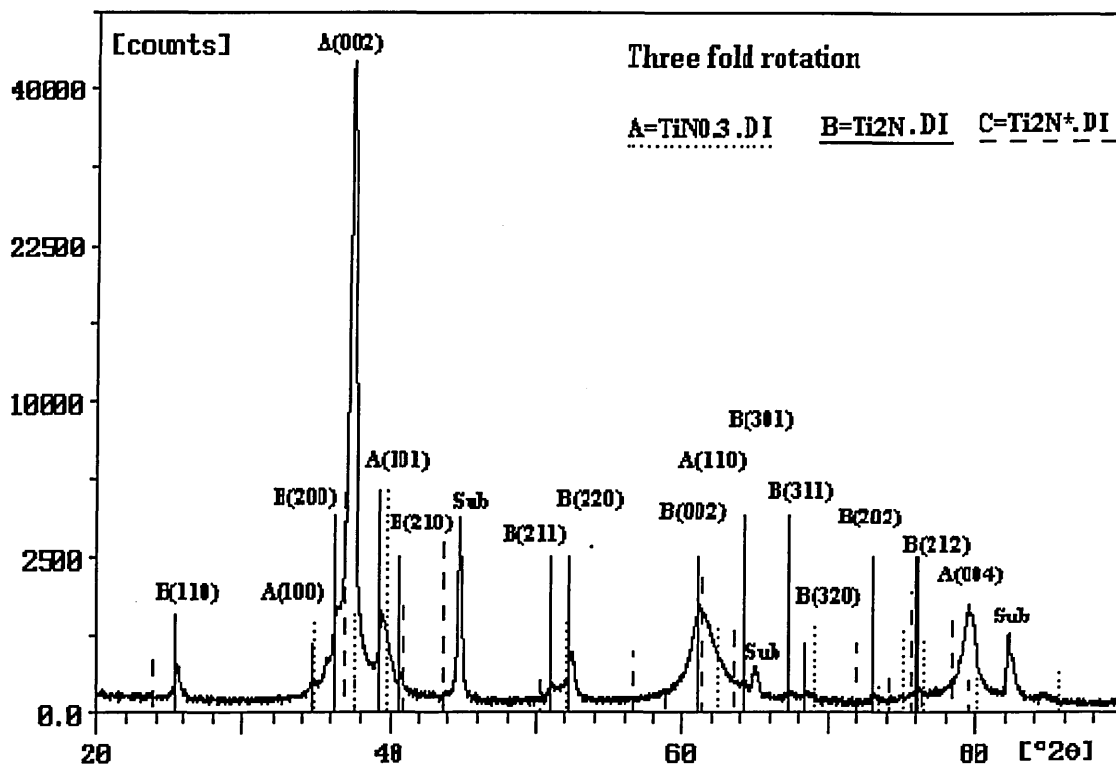


Fig 8.3.3 XRD pattern of Coating using 70sccm nitrogen flow

When the mode of rotation was changed from one to two and three fold, the number of reflections for the $\epsilon\text{Ti}_2\text{N}$ phase was increased whilst those for $\alpha\text{TiN}_{0.3}$ phase was decreasing. The XRD pattern of specimen using two fold rotation demonstrated presentation of $\alpha\text{TiN}_{0.3}$ (10.0), (00.2), (10.1), (11.0), (20.1) and (00.4); $\epsilon\text{Ti}_2\text{N}$ (110), (200), (210), (211), (220), (002), (301), (311), (320) and (202).

The diffraction peaks of the three fold rotation sample were shifted further to the left as compared with that of the two fold rotation sample. It was obvious that the strongest reflection was still $\alpha\text{TiN}_{0.3}$ whilst most of the diffraction peaks corresponding to the $\epsilon\text{Ti}_2\text{N}$ phase started to develop in the same X-ray diffraction profile. The diffraction peaks were corresponding to $\alpha\text{TiN}_{0.3}$ (10.0), (00.2), (10.1), (11.0) and (00.4); $\epsilon\text{Ti}_2\text{N}$ (110), (200), (210), (211), (220), (002), (301), (311), (320), (202), and (212).

The dependency of intensity of the reflections on substrate rotation is given in table 8.3.1. The relative intensities as referred to the JCPDS data are also given in this table.

Table 8.3.1 Apparent percentage of phase dependent on substrate rotation (70 scm N₂)

Rotation	Phase	(hkl)	I	R	I/R	Apparent %			
One fold	$\alpha\text{TiN}_{0.3}$	100	43.8	17	2.6	99.6			
		002	13470.5	22	612.3				
		101	590.8	100	5.9				
		110	2053.6	18	114.1				
		103	17.1	16	1.1				
		112	0.2	15	0.01				
		201	74.6	12	6.2				
	$\epsilon\text{Ti}_2\text{N}$	110	3.61	20	0.2	0.4			
		211	20.1	50	0.4				
220		24.7	50	0.5					
Two fold	$\alpha\text{TiN}_{0.3}$	100	2899.0	17	170.5	0.994			
		002	161984.0	22	7362.9				
		101	5343.4	100	534.3				
		110	1286.0	18	71.4				
		201	367.2	12	30.6				
	$\epsilon\text{Ti}_2\text{N}$	110	51.5	20	2.6	0.6			
		200	1031.3	80	12.9				
		210	27.0	50	0.5				
		211	93.1	50	1.9				
		002	1277.0	50	25.5				
		301	99.6	80	1.3				
		311	34.6	80	0.4				
		320	53.6	10	5.4				
		202	22.6	50	0.5				
		Three fold	$\alpha\text{TiN}_{0.3}$	100	6.7		17	0.4	94.1
				002	16605.8		22	754.8	
				101	667.2		100	6.7	
110	941.0			18	52.3				
$\epsilon\text{Ti}_2\text{N}$	110		63.6	20	3.2	5.9			
	200		1841.7	80	23.0				
	210		57.6	50	1.2				
	211		58.1	50	1.2				
	002		937.4	50	18.8				
	301		49.6	80	0.6				
	311		16.8	80	0.2				
	320		15.2	10	1.5				
	202		7.7	50	0.2				
	212		81.3	50	1.6				

The percentage of $\epsilon\text{Ti}_2\text{N}$ phase within the film is estimated using the apparent percentage epsilon₂ which is written as

$$\epsilon_{Ti_2N} = \frac{\sum_0^n \frac{I_{hkl}^\epsilon}{R_{hkl}^\epsilon} \frac{1}{n}}{(\sum_0^n \frac{I_{hkl}^{\alpha Ti}}{R_{hkl}^{\alpha Ti}} \frac{1}{n}) + (\sum_0^n \frac{I_{hkl}^\epsilon}{R_{hkl}^\epsilon} \frac{1}{n})} \text{-----} 3.1$$

where n is the number of (hkl) reflections considered in the alpha and epsilon phases; $I_{(hkl)}$ are the integrated intensities of the (hkl) reflections from alpha and epsilon; $R_{(hkl)}$ are the integrated intensities of the (hkl) reflections from alpha and epsilon phases in a random powder determined from the JCPDS file. The intensities of reflections referred to the JCPDS file and the calculation of the apparent percentage are also given in table 8.3.1. It can be seen that the apparent percentage of ϵTi_2N phase is 0.4, 0.6, and 5.9% for the reflections from samples using one, two, and three fold rotation respectively.

8.3.2 X-ray diffraction pattern from coatings using 75 sccm nitrogen gas flow rate

The X-ray diffraction patterns from coatings deposited using the 75 sccm nitrogen flow rate are given in figs 8.3.4, 5, and 6. It was found that the diffraction peaks for the ϵTi_2N phase developed rapidly whilst those for the $\alpha TiN_{0.3}$ decreased quickly with increase of rotation from one to two and three fold. The dominant phase composition for coating deposited using one fold rotation was $\alpha TiN_{0.3}$. For coating deposited using two fold rotation, however, the ϵTi_2N began to be the dominant phase.

The diffraction profile of one fold rotation indicated reflections corresponding to both $\alpha TiN_{0.3}$ and ϵTi_2N . It was also clear that the $\alpha TiN_{0.3}$ (00.2) and (11.0) were strongly textured. The reflections as identified by this diffraction pattern corresponded to $\alpha TiN_{0.3}$ (10.0), (00.2), (10.1), (11.0) and (00.4); ϵTi_2N (110), (101), (200), (210), (211), (220), (202) and (212).

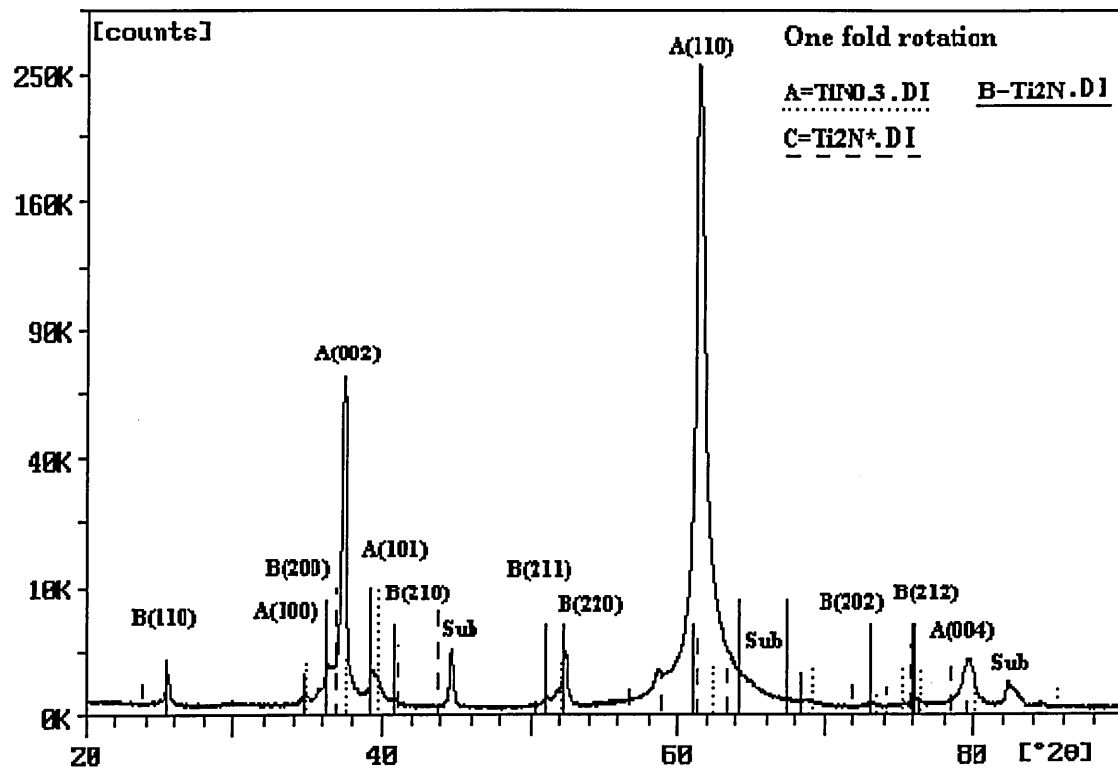


Fig 8.3.4 XRD pattern of coating using 75 sccm nitrogen flow

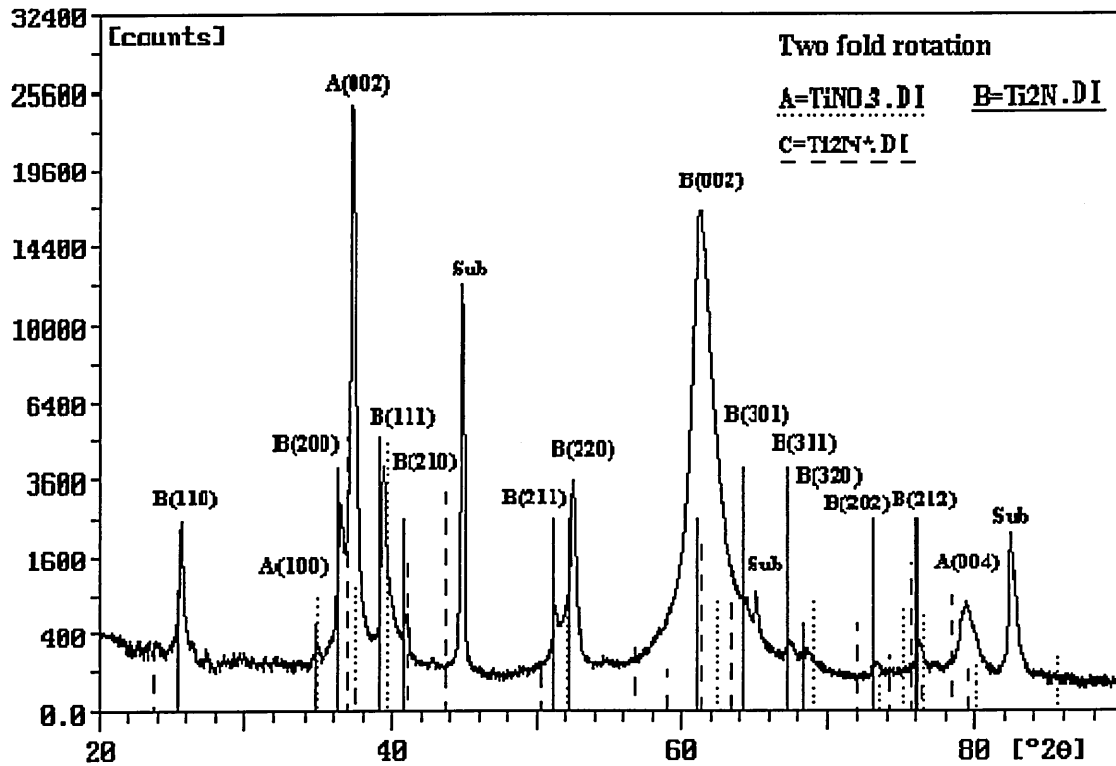


Fig 8.3.5 XRD pattern of coating using 75 sccm nitrogen flow

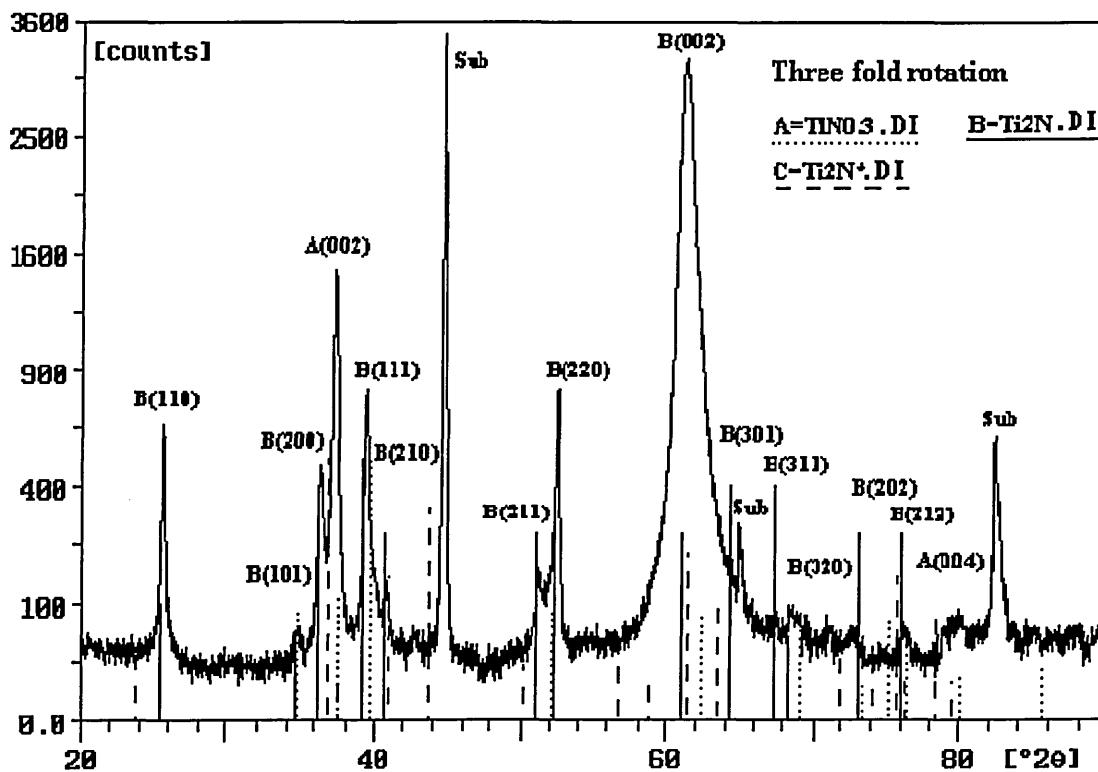


Fig 8.3.6 XRD pattern of coating using 75 sccm nitrogen flow

The XRD pattern of specimen using two fold rotation suggested that the $\epsilon\text{Ti}_2\text{N}$ became to be the dominant phase. Traces of $\alpha\text{TiN}_{0.3}$ phase were also found in this diffraction pattern. The identified reflections were $\alpha\text{TiN}_{0.3}$ (10.0), (00.2), and (00.4); $\epsilon\text{Ti}_2\text{N}$ (110), (200), (111), (210), (211), (220), (002), (301), (311), (320), (202) and (212). It was clear that the diffraction peaks of the $\epsilon\text{Ti}_2\text{N}$ reflections were very sharp and their positions matched perfectly those of the JCPDS file 17-386; this may be a indication that the $\epsilon\text{Ti}_2\text{N}$ could be deposited as a film without stress. It should also be mentioned that some positions for $\epsilon\text{Ti}_2\text{N}$, such as $\epsilon\text{Ti}_2\text{N}$ (111), (220), (002) and (202), were close to those for $\alpha\text{TiN}_{0.3}$ (101), (102), (110) and (200) and this may bring into question the existence of dominant $\epsilon\text{Ti}_2\text{N}$ phase. Comparing the XRD profile from the sample using one fold rotation, and the XRD pattern shown in fig 7.2.3 (typical $\alpha\text{TiN}_{0.3}$ pattern) however, the XRD profile from the sample using two fold rotation was obviously different. Firstly the peak position at 2θ 25.6° only corresponded to $\epsilon\text{Ti}_2\text{N}$ (110). Secondly there were two

peaks, at 2θ equals 51 and 53°, corresponding to $\epsilon\text{Ti}_2\text{N}$ (211) and (220) if the phase was $\epsilon\text{Ti}_2\text{N}$, whilst only one peak, $\alpha\text{TiN}_{0.3}$ (10.2), would appear at this area if the phase was $\alpha\text{TiN}_{0.3}$. Thirdly the peaks positions at 2θ equals 39, 61 and 73° could be clearly identified as belonging to $\epsilon\text{Ti}_2\text{N}$ phase. Therefore it is reasonable to say that the $\epsilon\text{Ti}_2\text{N}$ phase was become the dominant phase in the film deposited using two fold rotation.

The diffraction profile for three fold rotation clearly indicated that the $\epsilon\text{Ti}_2\text{N}$ phase was mainly developed. The relative intensities of the reflections corresponding to $\epsilon\text{Ti}_2\text{N}$ phase increased more whilst those corresponding to $\alpha\text{TiN}_{0.3}$ were reduced further as compared with the XRD pattern from two fold rotation. The identified reflections were $\alpha\text{TiN}_{0.3}$ (00.2) and (00.4); $\epsilon\text{Ti}_2\text{N}$ (110), (101), (200), (210), (211), (220), (002), (301), (311), (320), (202), and (212).

The calculations of apparent percentage for the reflections dependent on substrate rotation are given in table 8.3.2. The apparent value fraction of $\epsilon\text{Ti}_2\text{N}$ phase increased dramatically when the mode of rotation was changed from one to two fold. From two to three fold rotation, however, the increase of apparent percentage of the $\epsilon\text{Ti}_2\text{N}$ phase was not as dramatic as that from one to two fold rotation. The value of $\epsilon_{\text{Ti}_2\text{N}}$ was 0.5, 57.0, and 80.4% for the one, two, and three fold rotation respectively. It is clear that the $\epsilon\text{Ti}_2\text{N}$ phase has more chance to develop in this case as compared with the films deposited using 70 sccm nitrogen gas flow.

The lattice parameters of the tetragonal $\epsilon\text{Ti}_2\text{N}$ crystal were calculated using the interplanar spacings of $\epsilon\text{Ti}_2\text{N}$ (101), (111) and (211) from the XRD profile of three fold rotation sample. The calculation gave the average values, $a = 4.946\text{\AA}$, $c = 3.022\text{\AA}$, which were almost identical to the JCPDS file ($a^* = 4.945\text{\AA}$, and $c^* = 3.034\text{\AA}$). This is clearly indicates that the $\epsilon\text{Ti}_2\text{N}$ film can be produced with little residual stress.

Table 8.3.2 Apparent percentage of phase dependent on substrate rotation (75 sccm N₂)

Rotation	Phase	(hkl)	I	R	I/R	Apparent %
One fold	α TiN _{0.3}	100	96.2	17	5.7	99.5
		002	21863.8	22	993.8	
		101	628.4	100	6.3	
		110	146009.0	18	8111.6	
	ϵ Ti ₂ N	110	223.4	20	11.2	0.5
		200	1190.5	80	14.9	
		210	29.6	50	0.6	
		211	51.6	50	1.0	
		220	871.4	50	17.4	
		202	18.3	50	0.4	
Two fold	α TiN _{0.3}	100	55.9	17	3.3	43.0
		002	10517.0	22	478.1	
	ϵ Ti ₂ N	110	627.9	20	31.4	57.0
		200	1156.1	80	14.5	
		111	1192.0	100	11.9	
		210	935.1	50	18.7	
		211	572.9	50	11.5	
		220	1389.2	50	27.8	
		002	24773.0	50	495.5	
		301	871.1	80	10.9	
		311	63.3	80	0.8	
		320	33.2	10	3.3	
		202	8.7	50	0.2	
		212	111.1	10	11.1	
Three fold	α TiN _{0.3}	002	658.8	22	30.0	19.6
	ϵ Ti ₂ N	110	168.8	20	8.4	80.4
		101	11.3	10	1.1	
		200	192.3	80	2.4	
		111	291.1	100	2.9	
		210	37.9	50	0.8	
		211	114.4	50	2.3	
		220	320.0	50	6.4	
		002	4620.8	50	92.4	
		301	431.9	80	5.4	
		311	11.4	80	0.1	
		320	0.8	10	0.1	
		202	20.3	50	0.4	
		212	24.3	50	0.5	

8.3.3 X-ray diffraction pattern from coatings using 80 sccm nitrogen gas flow rate

The X-ray diffraction profiles from coatings deposited using 80sccm nitrogen flow rate are given in figs 8.3.7, 8, and 9. The relative intensities and positions as referred to JCPDS files for ϵ Ti₂N, ϵ Ti₂N* and δ TiN phases are also given in these figures. It was

found that the diffraction peaks within the profile from the one fold rotation sample were sharp and these peaks clearly corresponded to those of $\alpha\text{TiN}_{0.3}$ and $\epsilon\text{Ti}_2\text{N}$ reflections. The relative intensities of peaks for $\alpha\text{TiN}_{0.3}$ phase were largely reduced for the two and three fold rotation sample. When the mode of rotation was changed from one to three fold, the diffraction peaks of XRD patterns expanded and overlapped. The overlapped area from the profiles of two and three fold rotation was identified as belonging to the weak reflections from the $\alpha\text{TiN}_{0.3}$ phase, and the strong reflections from the dominant $\epsilon\text{Ti}_2\text{N}$ phase. Although the weak reflections of the $\alpha\text{TiN}_{0.3}$ were present in the XRD pattern of the three fold rotation sample, there was no evidence to the presence of δTiN reflections. Thus, the XRD profile for three fold rotation may suggest mainly a $\epsilon\text{Ti}_2\text{N}$ phase within the film.

The reflections of one fold rotation indicated that the dominant phase was $\alpha\text{TiN}_{0.3}$. It was also clear that the reflections of $\epsilon\text{Ti}_2\text{N}$ were present in this profile. The identified reflections corresponded to $\alpha\text{TiN}_{0.3}$ (00.2), (10.1), (11.0) and (00.4); $\epsilon\text{Ti}_2\text{N}$ (110), (101), (200), (210), (211), (220), (301), (311), (320), (202) and (212).

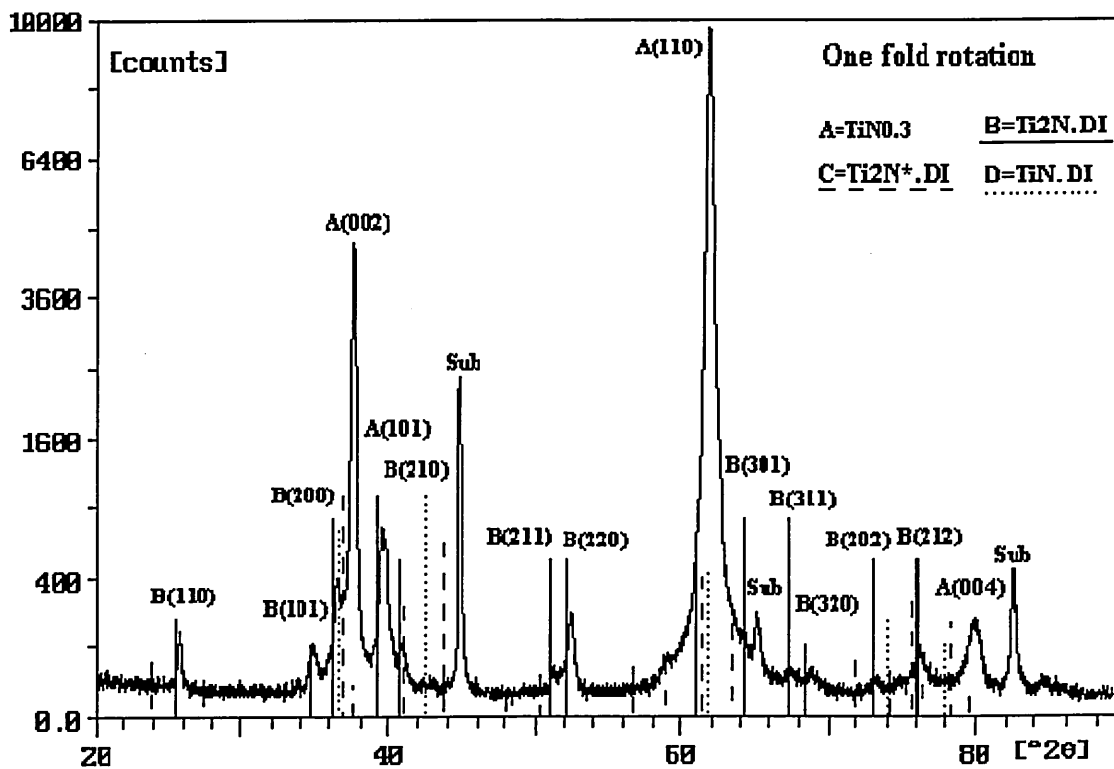


Fig 8.3.7 XRD pattern of Coating using 80 sccm nitrogen flow

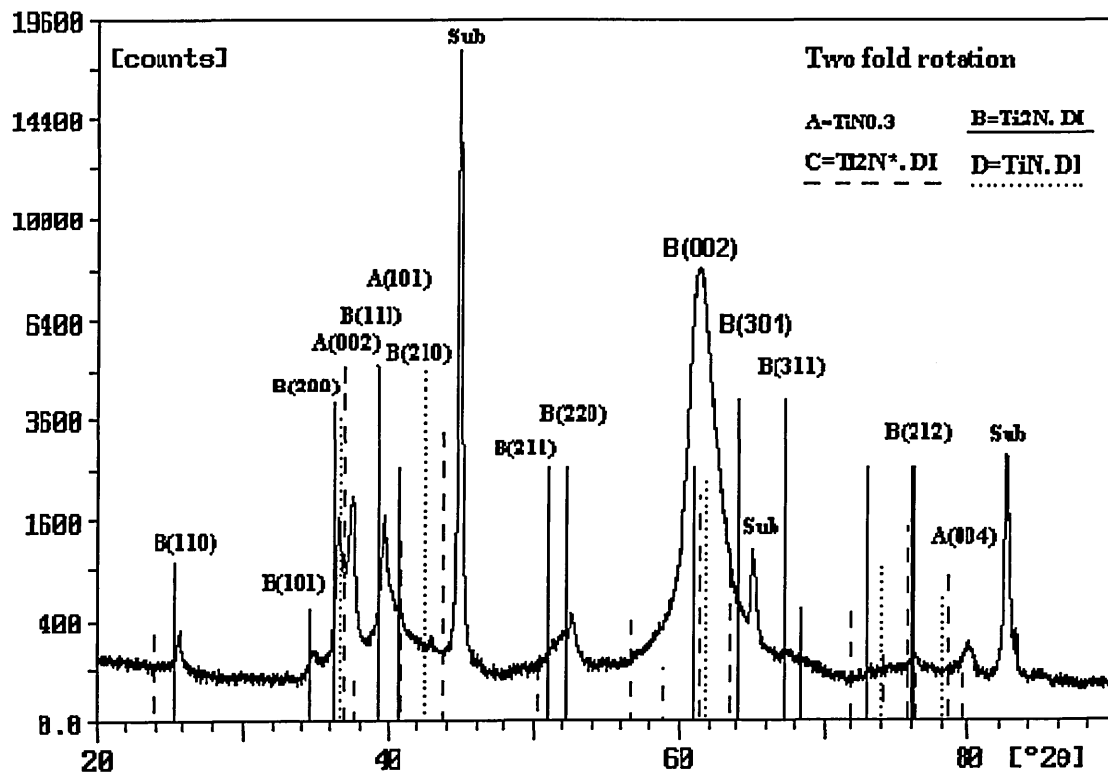


Fig 8.3.8 XRD pattern of coating using 80 sccm nitrogen flow

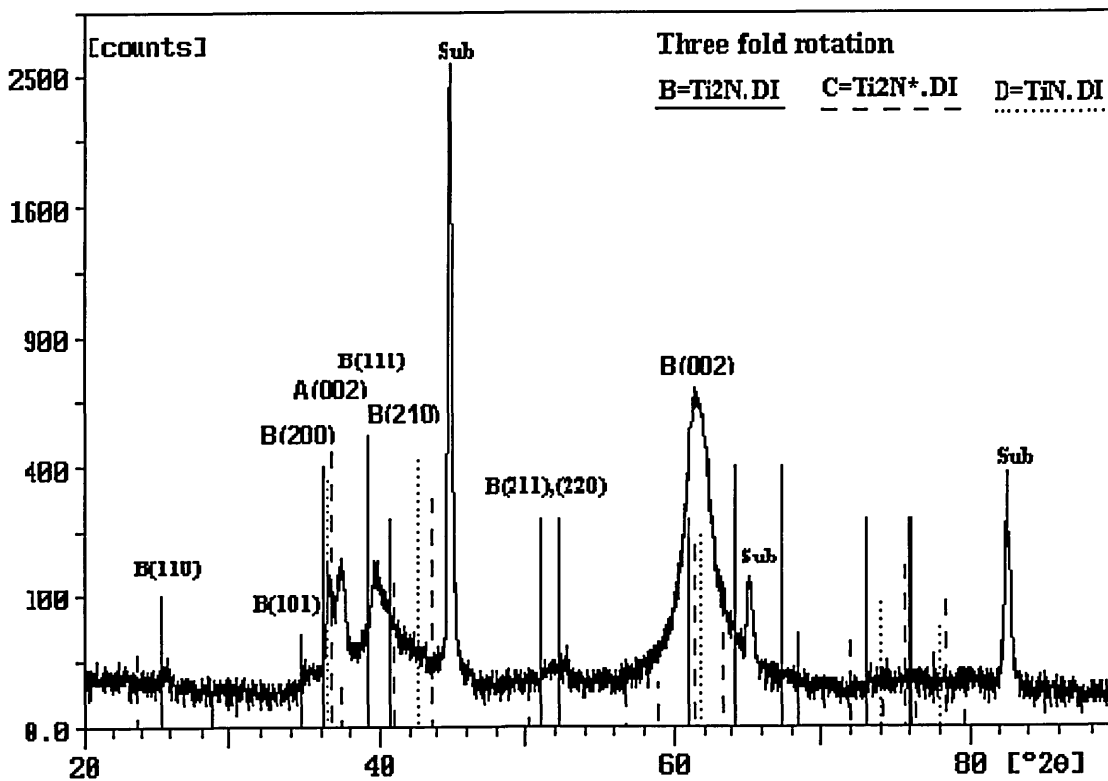


Fig 8.3.9 XRD pattern of coating using 80 sccm nitrogen flow

The peaks of XRD pattern were clearly broadened from the two fold rotation sample; even so, the reflections for $\alpha\text{TiN}_{0.3}$ and $\epsilon\text{Ti}_2\text{N}$ are still clear to see. The identified reflections were (00.2), (10.1) and (00.4) for $\alpha\text{TiN}_{0.3}$; and (110), (101), (200), (111), (210), (211), (220), (002), (301) (311), and (212) $\epsilon\text{Ti}_2\text{N}$.

The diffraction pattern of the sample subjected to three fold rotation clearly indicates a weak reflection from $\alpha\text{TiN}_{0.3}$ phase and strong reflections of the $\epsilon\text{Ti}_2\text{N}$ phase. It can be seen from the XRD profiles of one fold rotation sample that there was a strong peak for $\alpha\text{TiN}_{0.3}$ (002) at 2θ 37.5° , and this peak was accompanied by its second order diffraction (004) at 2θ 80° . In the three fold rotation case, the peak present at 2θ 37.5° was obviously reduced in intensity and there was no peak at 2θ 80° . Therefore, it is clear that in this XRD pattern a small amount $\alpha\text{TiN}_{0.3}$ phase was present. At the positions of 2θ 36.7 , 42.6 and 61.8° the peaks could belong reflections from δTiN (111), (200) and (220). Typical XRD patterns from the stoichiometric δTiN films (as seen from chapters 6 and chapter 7), however, indicate that these reflections do not correspond to the δTiN phase. Although the broadening and overlapping of the diffraction peaks made it difficult to analysis the XRD pattern, peak stripping using de-convolution software enable reflections from $\alpha\text{TiN}_{0.3}$ (002), $\epsilon\text{Ti}_2\text{N}$ (110), (101), (200), (111), (210), (211), (220) and (002) to be identified.

The calculations of apparent percentage $\alpha\text{TiN}_{0.3}$ and $\epsilon\text{Ti}_2\text{N}$ for different substrate rotations using 80 sccm nitrogen gas flow rate are given in table 8.3.3. The variation of the apparent percentage in this case was similar to that using nitrogen flow 75 sccm. The apparent percentage of $\epsilon\text{Ti}_2\text{N}$ phase was 3.4, 84.4, and 90.0% for the samples using one, two, and three fold rotation respectively. This suggested that the films were mainly formed by the $\epsilon\text{Ti}_2\text{N}$ phase when two or three fold rotation was used during the deposition process.

Table 8.3.2 Apparent percentage of phase dependent on substrate rotation (80 sccm N₂)

Rotation	Phase	(hkl)	I	R	I/R	Apparent %
One fold	α TiN _{0.3}	002	1665.7	22	75.7	96.6
		101	515.7	100	5.2	
		110	6240.5	18	346.7	
	ϵ Ti ₂ N	110	33.0	20	1.7	3.4
		101	42.7	10	4.3	
		200	277.1	80	3.5	
		210	37.6	50	0.8	
		211	49.3	50	1.0	
		301	156.7	80	2.0	
		311	3.9	80	0.1	
		320	1.8	10	0.2	
		212	70.5	50	1.4	
		Two fold	α TiN _{0.3}	002	1212.0	
101	1213.8			100	12.1	
ϵ Ti ₂ N	110		68.9	20	3.5	84.4
	101		62.0	10	6.2	
	200		640.6	80	8.0	
	111		532.7	100	5.3	
	210		3.1	50	0.1	
	211		783.4	50	15.7	
	002		14659.5	50	293.2	
	301		1323.3	80	16.5	
	311		20.1	80	0.3	
	212		153.4	10	15.3	
	Three fold		α TiN _{0.3}	002	84.0	
ϵ Ti ₂ N		110	4.3	20	0.2	90.0
		101	9.1	10	0.9	
		200	69.9	80	0.9	
		111	97.4	100	1.0	
		210	192.5	50	3.9	
		211	3.1	50	0.1	
		002	1425.8	50	28.5	

The apparent percentage of the ϵ Ti₂N phase was a function of both the nitrogen gas flow rate and the substrate rotation. This function is given in fig 8.3.10. The apparent percentage could be used to estimate the dominant phase composition in the coatings. It can be seen that the percentage of ϵ Ti₂N phase within the coatings increased with both the nitrogen gas flow rate and the substrate rotation. The dominant phase composition for one, two, and three fold rotation samples deposited using nitrogen gas flow 70 sccm was α TiN_{0.3} as the percentage of ϵ Ti₂N phase in these coatings was less than 6%. Alpha TiN_{0.3} was the dominant phase for the one fold rotation samples deposited using

75 and 80 sccm nitrogen gas flow. When samples were deposited using two fold rotation however, the percentages of $\epsilon\text{Ti}_2\text{N}$ phase within the coatings increased to 57% and 84% for the processes using nitrogen flow 75 sccm and 80 sccm respectively. At 75 and 80 sccm, the percentage of $\epsilon\text{Ti}_2\text{N}$ phase within the coatings using three fold rotation increased to 80% and 90% respectively.

From the above XRD profile analysis, it can be seen that very sharp diffraction peaks for the $\epsilon\text{Ti}_2\text{N}$ phase were developed from samples using nitrogen flow 75 sccm. Whilst the XRD reflections became expanded and overlapped as the nitrogen flow increased to 80 sccm. Even through there was no clear evidence to indicate the presence of δTiN phase, It would be expected that the δTiN phase would develop if the nitrogen flow rate was increased further. In fact the multiphase ($\epsilon\text{Ti}_2\text{N} + \delta\text{TiN}$) film was characterized as to have the overlapped diffraction profile as shown in fig 7.2.7. As the $\alpha\text{TiN}_{0.3}$ (002) was strongly textured, it was difficult to produce the pure $\epsilon\text{Ti}_2\text{N}$ phase without the reflection of $\alpha\text{TiN}_{0.3}$ (002) especially when the substrate was rotated. Nevertheless, the nitrogen gas flow rate used to produce the dominant $\epsilon\text{Ti}_2\text{N}$ film was determined in a range between 75 and 80 sccm.

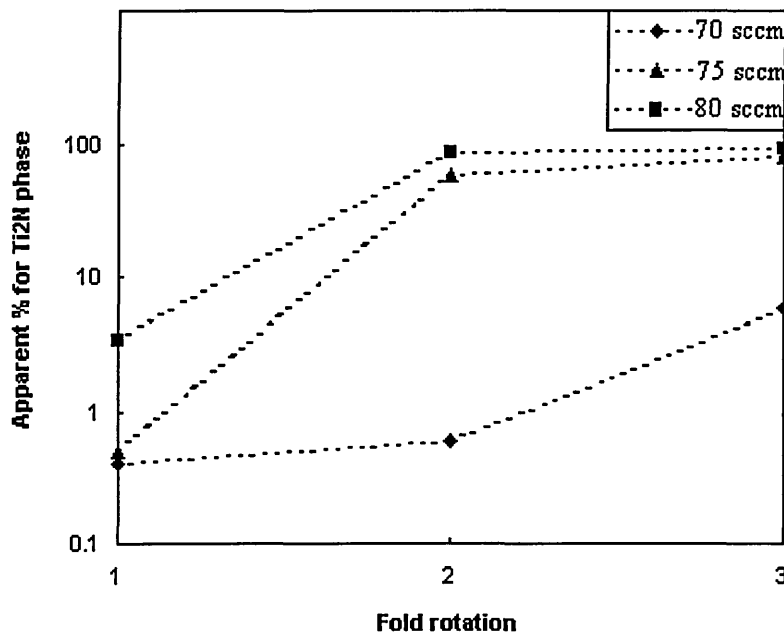


Fig 8.3.10 Apparent percentage as a function of N_2 flow and rotation

8.4 Cross sectional structure of the $\epsilon\text{Ti}_2\text{N}$ films

The cross sectional structure of the films containing $\epsilon\text{Ti}_2\text{N}$ phase was examined using scanning electron microscopy (SEM) for analysis of the morphology of the fracture cross sectional structure and transmission electron microscopy (TEM) for investigation of the interface structure, phase composition of a particular area within the coating, and the grain orientation within the film cross section. Only the samples deposited using 75 sccm nitrogen flow rate were used for the cross sectional analysis.

8.4.1 Cross sectional analysis using SEM

The analysis of fracture cross sectional structure is given in figs 8.4.1 a, b, and c , which refer to samples of one, two and three fold rotation. It can be seen that a clear columnar structure was found throughout the coating using one fold rotation. The direction of the columnar structure was parallel to the film growing direction. The structure of the coatings using two and three fold rotation, however, was rather indistinct as it was difficult to see the columnar structure using the SEM. This is because that the coating was formed by dense packed fine grains which are finer than the resolution of the SEM. In fact these coating structures are still columnar as seen from the following TEM analysis. The thickness of the coatings reduced with increasing fold rotation and this indicated that the deposition rate decreased with increase of fold rotation. The thickness values were 2.5, 3.8, and 5.0 μm for coatings deposited using one, two and three fold rotation respectively.

(See page 212 for fig 8.4.1)

Fig 8.4.1 Fracture cross sectional analysis using SEM

a, b and c refer to one, two and three fold rotation samples respectively

8.4.2 Cross sectional investigation using TEM

8.4.2.1 Results from sample deposited using three fold rotation

The cross sectional structure of the coating/substrate interface area is given in fig 8.4.2 in which, a is the image of the interface area and b is the electron diffraction pattern from the interface. It was found that there was a 50 nm primary layer close to the interface where very fine and densely packed equi-axed grains were formed and these grains were randomly distributed within the interface. After this thin layer the columnar structure was formed with orientation parallel to the growing direction. The growing columns encountered strong competition for survival and the largest column size was up to 100

nm. The termination of an individual column was observed to indicate that re-nucleation occurred during the deposition. The columns within the coating were inter-locked to form a dense packed structure.

(See page 213 for fig 8.4.2)

Fig 8.4.2 TEM analysis at interface area from three fold rotation sample

a and b refer to TEM image of interface area and electron diffraction at interface respectively

The electron diffraction pattern at the interface showed a pattern of spots on a line and a pattern of spots on rings with different radius. The line spots indicated the information from the stainless steel substrate whilst the ring pattern suggested that film at the coating/substrate interface had a very fine grain size. It was measured that the ring pattern was a indication of the $\alpha\text{TiN}_{0.3}$ phase. The first ring with radius from 9.6 to 10.4 mm suggested a overlap reflection of $\alpha\text{TiN}_{0.3}$ (10.0) and (00.2) with a interplanar spacings 2.615 and 2.413 Å. Then the rings with radius 13.6, 15.7, 18.5 (very weak), 19.3, 24.5 (very weak), and 26.2 mm, indicated the reflections of $\alpha\text{TiN}_{0.3}$ (102), (110), (103), (200), (203) and (211) with interplanar spacing 1.845, 1.599, 1.357, 1.301, 1.024, and 0.958 Å respectively. Compared with the standard data of the $\alpha\text{TiN}_{0.3}$ from JCPDS file, the differences of interplanar spacings, as measured above, were $\Delta d = 0.04, 0.02, 0.09, 0.11, 0.00, 0.01, 0.02, 0.00$ Å respectively.

About 400 nm above the coating/substrate interface, the columns gradually became very finer, uniform and of dense inter-locked fibre structure as shown in figs 8.4.3 a and b. It can be seen that the individual column size was less than 10 nm and this structure was present throughout all the film. At top of the film the surface was extremely smooth.

(See page 214-216 for fig 8.4.3)

Fig 8.4.3 TEM cross sectional images of three fold rotation sample

a, b and c refer to image at middle, image at top and electron diffraction pattern respectively

The electron diffraction pattern from the middle columnar area of the coating is given in fig 8.4.3 c, which indicates that the columnar structure was formed by the $\epsilon\text{Ti}_2\text{N}$ phase. There was no distinctive change in the electron diffraction profiles from the areas of the columnar structure throughout the coating. The indication of the electron diffraction pattern for fig 8.4.3 c is scheduled in fig 8.4.4. It is clear that there are two sets of reciprocal lattice points belonging to zone axis $[1\bar{1}0]$ and $[0\bar{1}0]$. The reciprocal lattice points of the $[1\bar{1}0]$ correspond the $\epsilon\text{Ti}_2\text{N}$ (002), (004), (113), (111), (222), (331), (220) and (440). Whilst the set reciprocal lattice points belonging to the $[0\bar{1}0]$ are reflections

of $\epsilon\text{Ti}_2\text{N}$ (002), (004), (103), (101), (202), (301), (200) and (400). The two set reciprocal lattice points are overlapped at (002). It was found a strong orientation on the $\langle 001 \rangle$ direction which was parallel to the direction of the columnar structure of the film. The spots profile of the zone axis $[0\bar{1}0]$ was perfectly matched the typical tetragonal structure with the axial ratio of $c/a = 0.6$ as referred by Andrews⁽⁴⁾. The direction of $\langle 101 \rangle$ was found about 31° away from $\langle 001 \rangle$. The directions of $\langle 301 \rangle$ and $\langle 100 \rangle$ appeared on the 61 and 90° away from $\langle 001 \rangle$ respectively. The set of reciprocal lattice points for zone axis $[\bar{1}\bar{1}0]$ was matched the tetragonal structure with the axial ratio of $c/a = 0.7$ rather than that of $c/a = 0.6$. The $\langle 111 \rangle$ and $\langle 110 \rangle$ were 44° and 90° away from the $\langle 001 \rangle$ respectively.

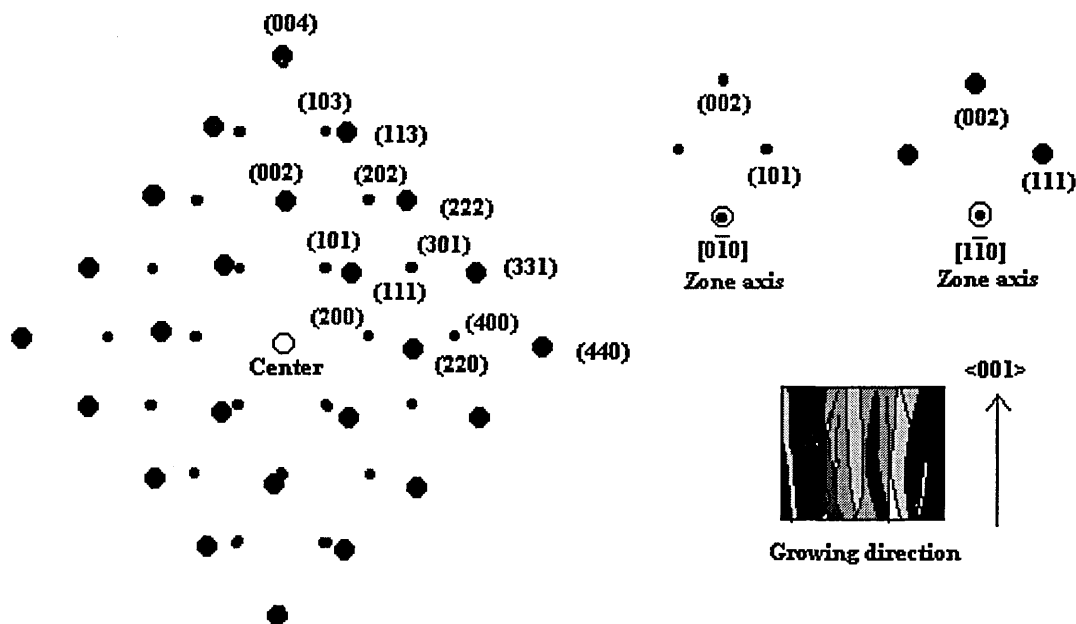


Fig 8.4.4 Indication of the spots on diffraction pattern from the middle columnar area

The measured distances (r) of the spots from the centre of the diffraction pattern, calculated interplanar spacings of the diffraction spots, the angles between r and the direction of the columnar structure, and the interplanar spacings referred to the JCPDS file 17-386 ($c/a=0.61$) are given in table 8.4.1. Taking the d^* values referred to JCPDS file as the standard, the average difference between the measured d value and the standard value was not more than 0.07 \AA . Therefore it was confirmed that the columnar structure within the film was formed of pure $\epsilon\text{Ti}_2\text{N}$ phase.

Table 8.4.1 Measurement of interplanar spacings from diffraction pattern in fig 8.4.3

Zone	$\bar{[1\ 1\ 0]}$			$\bar{[0\ 1\ 0]}$		
	1	2	3	4	6	7
spots						
r (mm)	16.6	11.5	16.3	9.9	17.0	10.1
φ ($^{\circ}$)	0	44	90	32	61	90
d (Å)	1.512	2.183	1.552	2.535	1.476	2.485
d* (Å)	1.517	2.292	1.749	2.586	1.448	2.473
Δd (Å)	0.01	0.11	0.20	0.05	0.03	0.01
(hkl)	002	111	220	101	301	200

d* referred to JCPDS file, d calculated by $L\lambda/r$, L=1m (camera length), $\lambda=0.251\text{Å}$ (electron wave length)

Some metal grains were occasionally found within the columnar area as shown in figs 8.4.5 a and b. The size of those particles could be up to hundreds nanometers. However, it seems that there was no effect of these metal grains on the formation of those $\epsilon\text{Ti}_2\text{N}$ columnar grains as the columnar grains could grow freely apart from the metal grains and some columns could even penetrate through the metal grain without any change in the growth direction as shown in fig 8.4.5 b.

(See page 217-218 for fig 8.4.5)

Fig 8.4.5 Metal grains randomly located within the three fold rotation film

a. Large metal grain b. Column penetrates through the grain

The electron diffraction on the metal grain in fig 8.4.5a indicates that this grain was formed with a single crystal structure and identified as a titanium metal particle as shown in fig 8.4.6. The diffraction pattern gave the typical hexagonal pattern based on $c/a=1.59$, which was identified by both the angle between planes $(h_1k_1l_1)$ and $(h_2k_2l_2)$ as referred to Andrews and the interplanar spacing (d) values as referred the data from the JCPDS file.

(See page 219 for fig 8.4.6)

Fig 8.4.6 Diffraction pattern of the metal grain within the three fold rotation film

The indication of the reciprocal lattice spots from fig 8.4.6 is given in fig 8.4.7. The zone axis was $\bar{[010]}$ as calculated using any two reciprocal lattice spots. The identified reflections corresponded to the Ti (001), (002), (003), (004), (005), (100), (200), (300), (101), (102), (103), (104), (105), (201), (202), (203), (204), and (302). There were also some spots which could not be referred to the standard data. However as this reciprocal lattice points are single crystal pattern and the zone axis is determined, it is not difficult to index the whole spots compared with the other lattice points. Therefore the spots which can not find reference from Andrews and JCPDS file are considered as Ti (205), (301), (303), (304) and (305).

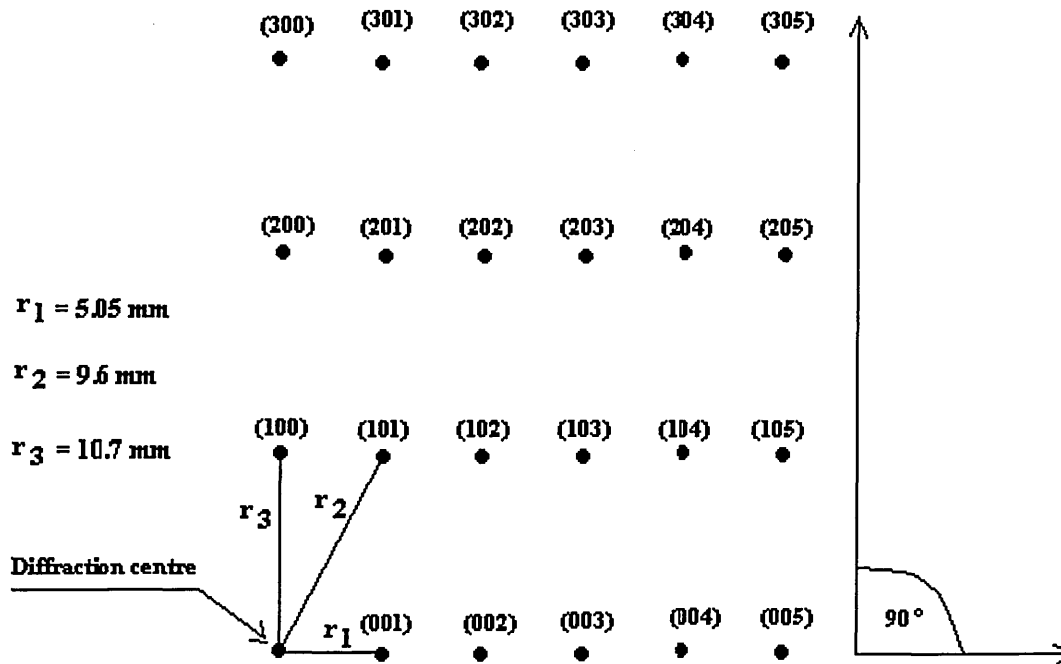


Fig 8.4.7 The reciprocal lattice spots of titanium grain

Table 8.4.2 Identification of the metal grains as Ti particle

Ti (hkl)	r (mm)	φ (°)	d (Å)	d* (Å)	Δd (Å)
001	5.05	0	4.9702	<u>4.683</u>	0.29
002	10.1	0	2.4851	<u>2.342</u>	0.14
003	15.2	0	1.6513	<u>1.561</u>	0.09
004	20.2	0	1.2425	<u>1.171</u>	0.07
005	25.3	0	0.992	<u>0.937</u>	0.06
100	9.6	90	2.6146	2.557	0.06
200	19.2	90	1.3072	1.276	0.03
300	28.8	90	0.8715	0.8514	0.02
101	10.8	63	2.3139	2.244	0.07
102	13.9	44	1.8012	1.726	0.08
103	17.9	33	1.3944	1.332	0.06
104	22.4	26	1.1222	1.0653	0.06
105	27.0	22	0.9291	0.8796	0.05
201	19.9	76	1.2642	1.233	0.03
202	21.7	63	1.1568	1.1220	0.04
203	24.5	53	1.0262	0.9895	0.04
204	27.9	44	0.9006	0.8634	0.04
205	31.7	38	0.7912		
301	29.2	79	0.8584		
302	30.5	70	0.8224	0.8927	0.07
303	32.5	63	0.7713		
304	35.2	56	0.7135		
305	38.3	49	0.6553		

d* referred to Andrews data, d* referred to data from JCPDS file

The measured data of the diffraction spots is given in table 8.4.2, in which the measured angle for plane (hkl) was referred to the direction of <001>; the radius of the spots was measured from the diffraction centre; the difference Δd was considered as compared with the measured interplanar spacing (d) and the standard d^* as referred to Andrews and the JCPDS file. It could be seen that the largest difference Δd of the interplanar spacing as referred to data from Andrews (d^* values with a dash line) was less than 0.3 Å whilst that as referred to the JCPDS file (d^* values without dash line on the bottom) was less than 0.08 Å.

8.4.2.2 Result from sample deposited using one fold rotation

The cross sectional TEM analysis from the coating/substrate interface of the sample deposited using one fold rotation is given in figs 8.4.8a and b for the image and the electron diffraction respectively. The image was similar to that from the three fold rotation sample. There was a primary layer between substrate and columnar region of the coating. This layer was about 50 nm thick, and was randomly and densely packed with equi-axed grains. After this primary layer the columnar layer started to grow and the direction of the columns was normal to the substrate surface. The individual growing columns appeared to show competition for survival. After one column was fully developed, this column tended to be terminated and a new column grain began to grow.

(See page 220 for fig 8.4.8)

Fig 8.4.8 TEM analysis at interface area from one fold rotation sample

a. TEM image, b. Electron diffraction pattern

The electron diffraction pattern from the interface area was formed by a set of spots distributed on rings with different radius due to the diffraction come from a group of fine crystal grains with random orientation. There were at least five rings formed by diffraction spots as seen from the diffraction pattern. The measured radius for each ring was 10.5, 13.8, 16.2, 19.0, and 25.9 mm, which suggested that the interplanar spacing (d) for each reflection was 2.3904, 1.8188, 1.5493, 1.321 and 0.9691 Å respectively. Compared with the data from the JCPDS file, these ring spots corresponded to $\alpha\text{TiN}_{0.3}$ (002), (102), (110), (103) and (211).

The cross sectional analysis from the middle area of the one fold rotation coating is shown in fig 8.4.9. It was found that the coating layer was formed by both columnar grains and metal grains. The direction of the columns was parallel to the film growing

direction. The metal grains were regularly distributed in strips between columnar areas and these strips were clearly parallel to the columnar direction.

(See page 221 for fig 8.4.9)

Fig 8.4.9 TEM analysis of one fold rotation coating

a. Image at middle area b. Electron diffraction pattern from columnar area

The electron diffraction pattern of the columnar area formed from the one fold rotation sample was similar to that formed from the three fold rotation sample to indicate a tetragonal $\epsilon\text{Ti}_2\text{N}$ phase composition. There were two sets of diffraction spots. One set of the strong reciprocal lattice points belonged to zone axis $[0\bar{1}0]$ and the other set of weak reciprocal lattice points belonged to zone axis $[\bar{1}\bar{1}0]$ as shown in fig 8.4.10. The reciprocal lattice points of zone axis $[\bar{1}\bar{1}0]$ corresponded $\epsilon\text{Ti}_2\text{N}$ (002), (004), (113), (111), (222), (331), (220) and (440) whilst that of zone axis $[0\bar{1}0]$ were $\epsilon\text{Ti}_2\text{N}$ (002), (103), (101), (202), (301), (200) and (400).

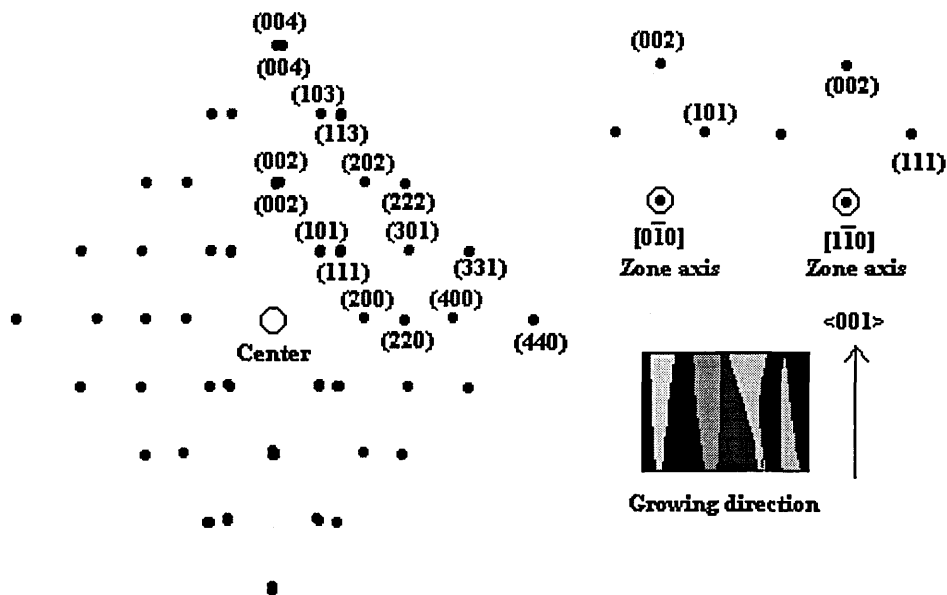


Fig 8.4.10 Reciprocal lattice points of columnar area from one fold rotation

The measured interplanar spacings from fig 8.4.9b are given in table 8.4.3. The largest different value of the Δd is less than 0.2\AA and the average Δd value is about 0.07\AA as referred to the standard interplanar spacing values of the $\epsilon\text{Ti}_2\text{N}$ phase. Thus the electron diffraction pattern indicated that the columnar grains were belonged to $\epsilon\text{Ti}_2\text{N}$.

Table 8.4.3 Calculation of interplanar spacings from diffraction pattern in fig 8.4.3

Zone	[1 $\bar{1}$ 0]			[0 $\bar{1}$ 0]		
	1	2	3	4	6	7
spots	1	2	3	4	6	7
r (mm)	16.6	11.4	16.2	10.0	17.1	10.2
φ (°)	0	43	90	33	62	90
d (Å)	1.512	2.202	1.549	2.510	1.468	2.461
d* (Å)	1.517	2.292	1.749	2.586	1.448	2.473
Δd (Å)	0.01	0.07	0.20	0.08	0.02	0.01
(hkl)	002	111	220	101	301	200

The structure of the metal grains within the one fold rotation coating was similar to that within the three fold rotation sample. The image at one grain area is shown in fig 8.4.11. It could be seen that the metal grain had little influence at the columnar structure. The nucleation direction for the individual metal grain was random whilst that for the columnar grain was normal to the substrate surface no matter how the closed metal grain was nucleated.

(See page 222 for fig 8.4.11)

Fig 8.4.11 Metal grain within the one fold rotation film

a. Image at the metal grain area, b. Electron diffraction from the metal grain

The electron diffraction pattern from the metal grain appeared to show both the single crystal structure of the alpha titanium and the columnar structure from $\epsilon\text{Ti}_2\text{N}$ phase. The diffraction spots of the single crystal structure were similar to those of the three fold rotation film whilst the spots of the columnar film corresponded to the $\epsilon\text{Ti}_2\text{N}$ phase. The interpretation of the diffraction spots is given in fig 8.4.12. The identified reflections for single crystal structure were Ti (001), (002), (003), (004), (005), (100), (101), (102), (103), (104), (105), (200), (201), (202), (203), (204), and (205). The diffraction spots from columnar film were assessed to be $\epsilon\text{Ti}_2\text{N}$ (002), (101), (111) and (200). The direction of $\epsilon\text{Ti}_2\text{N}$ (002) was parallel to the direction of columnar orientation.

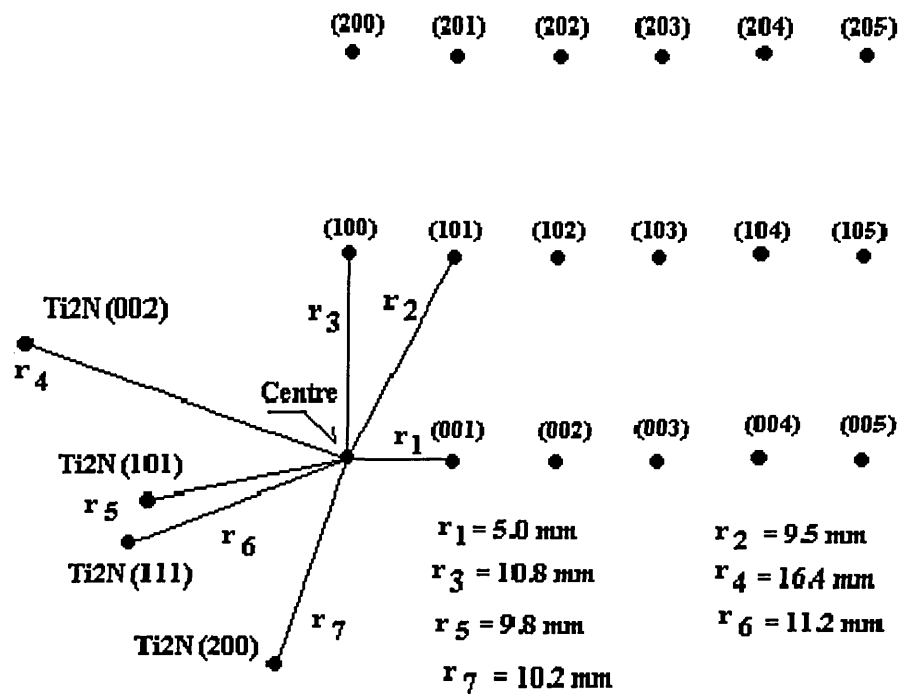


Fig 8.4.12 The diffraction spots from Ti metal grain using one fold rotation

8.5 Discussion of chapter 8

All the coatings were deposited using the commercially designed industrial sized coater which has an excellent substrate table rotation system⁽⁵⁾. When the deposition was carried out using un-poisoned model (low nitrogen partial pressure), the film composition was obvious a function of substrate rotation. The titanium content within the coatings decreased from the samples using one to three fold rotation due to the deposition rate reduced respectively. This is because of the shadow effect which is caused by the line of sight sputtering deposition. The sample using one fold rotation was always facing the sputtering source when it passed through in front of the target whilst the samples using two or three fold rotation were in period coming into the shadow area of the sputtered titanium flux. There was more titanium concentration in the one fold rotated sample because there was less shadow effect and more sputtered titanium atoms contributed to the film growth. The samples using two and three fold rotation, however,

evidenced more shadow effect and therefore there was less sputtered titanium to contribute to the film growth; the titanium content within the coating was reduced accordingly.

The magnetic geometry of the chamber was designed as a close field using unbalanced magnetron sputtering techniques^(6,7,8). The effect of unbalanced magnetron was enhanced by the electromagnetic coil behind each target so that high density plasma was confined in the chamber and ion bombardment on the substrate was high. Even though the energy of the ions may slightly higher when the ions arrived at the sample using one fold rotation as compared with that using two and three fold rotation, the intensity of ion bombardment was not very much different for the substrate using one, two, or three fold rotation. There was no shadow effect of the nitrogen and argon plasma on the samples within the confined area. This could give rise to the assumption that the nitrogen contributed to the film growth was not different for the substrate exposed in the plasma region of the chamber. The results made by SNMS indicated that the nitrogen/titanium ratio increased in the samples using from one to three fold rotation owing to the fact that the titanium was reduced accordingly. The argon content reduced in the samples from one to three fold rotation due to the resultant decrease in titanium deposition rate. As the deposition rate decreased, the chance for argon to be trapped in the vacancy reduced^(9,10) and therefore the argon content in the film decreased.

The nitrogen partial pressure is lower within the Ti₂N coating process as compared with that within the stoichiometric TiN process. Under such a nitrogen pressure multiphase compositions could have the chance to be developed and this corresponding with the fact that most of the X-ray diffraction analysis of the low nitrogen partial pressure Ti-N coatings suggests the coexistence of multiphase compositions in one film. The development of the phase within the coatings using one, two, and three fold rotation is very complicated. Taking the sample using three fold rotation as an example, when it passes through the sputtering source and faces the target, the metal deposition is the major process for the growing film. As the sample faces away from the target, there is no, or very little metal deposition happening on the surface owing to the sputtering

shadow effect. In this situation the sample is still undergoing bombardment of the energetic nitrogen and argon particles and therefore nitriding of the growing film becomes the major process. These phenomena are changing periodically with time as the substrate table turns cyclically. It is reasonable to assume that in a low nitrogen partial pressure coating process, metal titanium is deposited, and $\alpha\text{Ti(N)}$ may be developed during the stage when the growing film is facing the sputtering source, whilst the $\epsilon\text{Ti}_2\text{N}$ phase begins to develop as the growing film goes off the source. With increasing fold rotation the time during which the sample faces away from the target increases so that there is more chance for $\epsilon\text{Ti}_2\text{N}$ phase to develop on the sample using three fold rotation. With increasing nitrogen gas flow up to 80 sccm the chance for developing $\alpha\text{Ti(N)}$ phase is largely decreased whilst the $\epsilon\text{Ti}_2\text{N}$ phase is mainly developed, especially on the sample using three fold rotation. If the nitrogen gas flow is increased further, it can be expected that there is no chance for $\alpha\text{Ti(N)}$ to develop and the formation of $\epsilon\text{Ti}_2\text{N}$ will reduce, accompanied by development of δTiN phase.

The deposition temperature for $\epsilon\text{Ti}_2\text{N}$ films has to be high up to 480°C. This temperature is attributed to the intensity of ion bombardment and the heaters. It is estimated that about 60% of energy used to heat the substrate is contributed by the ion bombardment. As the targets are operated in an un-poisoning mode, the growing film is exposed to an intensive ion bombardment and therefore a high densely packed film can be produced⁽¹¹⁾. This ion bombardment enhancement of film density is particular effective on the sample deposited using three fold rotation because the arrival ions/metal-atoms ratio at the surface of this sample is higher than that for samples deposited using one and two fold rotation. This ion bombardment effect also influences to the mobility of surface adatoms and the enhancement of surface diffusion. As a result, very smooth surface is produced during the deposition.

It has been seen from cross sectional TEM analysis of the one and three fold rotation samples that there is a thin layer between substrate and columnar coating, and the phase composition of this thin layer corresponds to $\alpha\text{Ti(N)}$. This undesirable layer is produced by the un-poisoned deposition process. As the targets are fully cleaned by 10 minutes

glow discharge sputtering prior to the deposition and the nitrogen partial pressure for deposition of $\epsilon\text{Ti}_2\text{N}$ film is low, the arrival ratio of titanium to nitrogen at the substrate surface is higher in the first few minutes than later during the deposition. This may be the main reason that the interface is formed by $\alpha\text{Ti(N)}$. The melting point of $\alpha\text{Ti(N)}$ is much lower than δTiN or $\epsilon\text{Ti}_2\text{N}$ and therefore the equi-axed crystal grains are produced⁽¹²⁾ during the first few minutes as the surface temperature of the growing film is high enough to produce equi-axed crystal grains. After a few minutes deposition, the targets are slightly poisoned and the deposit ratio of titanium to nitrogen is lower than the beginning and therefore the film is deposited with $\epsilon\text{Ti}_2\text{N}$. The melting point of $\epsilon\text{Ti}_2\text{N}$ may be higher than that of $\alpha\text{Ti(N)}$ so that the columnar structure is formed. The $\alpha\text{Ti(N)}$ is brittle with less hardness, this may account for that the scratch tests on the $\epsilon\text{Ti}_2\text{N}$ film have not shown the expected L_c values.

The electron diffraction pattern from the columnar area was formed by two sets of reciprocal lattice points with the zone axis $[1\bar{1}0]$ and $[0\bar{1}0]$ respectively. The reciprocal lattice points with zone axis $[0\bar{1}0]$ were perfectly matched the tetragonal $\epsilon\text{Ti}_2\text{N}$ structure as referred to the JCPDS file 17-386 and Andrews's book⁽⁴⁾ by both the interplanar spacing values and the angles between different planes. The measured lattice parameters were $a = 4.97 \text{ \AA}$, $c = 3.04 \text{ \AA}$, $c/a = 0.6$, whilst the referred data from JCPDS file is $a = 4.945 \text{ \AA}$, $c = 3.034 \text{ \AA}$, $c/a = 0.6$. The reciprocal lattice point with zone axis $[1\bar{1}0]$ was matched the tetragonal structure with axis ratio $c/a = 0.7$ as referred to Andrews. The measured lattice parameters, however, were $a = 4.378 \text{ \AA}$, $c = 3.042 \text{ \AA}$, $c/a = 0.695$. Compared with data from JCPDS file, a large different value was found on lattice parameter a , $\Delta a = 0.6 \text{ \AA}$. It seems that this difference is caused by expanding the interplanar spacing of (220) which has a vector \mathbf{d}_{110} normal to the growing direction. This expansion may be resulted from tensile stain along the $\langle 110 \rangle$ direction to enlarge the interplanar spacing.

In general the result from the electron diffraction analysis agrees with that from the XRD analysis. Most of the $\epsilon\text{Ti}_2\text{N}$ planes as identified by electron diffraction are also present from the XRD profile. There are three reflections, $\epsilon\text{Ti}_2\text{N}$ (103), (113) and (331), as identified by electron diffraction, not presented in XRD pattern. Also there are five reflections, $\epsilon\text{Ti}_2\text{N}$ (110), (210), (211), (311), (320) and 212 which presented in XRD profile, but did not present in the electron diffraction pattern. This difference is because that the electron diffraction is used to investigate a particular small area within the coating whilst the XRD is used to study a relative large area from both the substrate and the coating. Nevertheless the analysis of both electron diffraction and XRD from the three fold rotation sample deposited using 75 sccm nitrogen flow is intended to show that almost pure $\epsilon\text{Ti}_2\text{N}$ film is produced.

For the samples deposited using 70 and 80 sccm nitrogen flow, there is no TEM analysis to give further identification of the phase composition of the coating depends on the substrate rotation and the nitrogen gas flow rate. From all the results of chapter 8 and the discussion above, however, there is no difficult to indicate that the optimistic nitrogen gas flow rate for deposition of films containing dominant $\epsilon\text{Ti}_2\text{N}$ phase is between 75 sccm and 80 sccm. As the nitrogen gas flow rate can be accurately controlled by the coating machine mentioned above, the deposition of almost pure $\epsilon\text{Ti}_2\text{N}$ films for commercial application is fully reproducible.

8.6 Conclusion of chapter 8

1. Films containing dominant $\epsilon\text{Ti}_2\text{N}$ films can be produced using the industrial sized unbalanced coating machine.
2. Nitrogen concentration within the coating was dependent on the manner of substrate rotation and the nitrogen gas flow rate.
3. The hardness increases with nitrogen gas flow and substrate rotation. The $\epsilon\text{Ti}_2\text{N}$ phase film is characterised to have a hardness value about HK 2200.
4. Multiphase compositions are produced in parallel as the substrate is rotated.

5. The electron diffraction give evidence that the columnar grains are formed by $\epsilon\text{Ti}_2\text{N}$ phase which agree with the analysis of the X-ray diffraction.
6. Very uniform columnar and fine grain structure is found within the $\epsilon\text{Ti}_2\text{N}$ film and the surface of the film is extremely smooth.
7. The deposition of $\epsilon\text{Ti}_2\text{N}$ film is reproducible by accurate control of the nitrogen gas flow rate during a process.

References

- (1) Leybold INA 3, Electron Gas SNMS (1986)
- (2) D. Briggs and M.P. Seah, Practical Surface Analysis V2 (Ion and Neutral Spectroscopy), John Wiley & Sons (1992)
- (3) Powder Diffraction File, JCPDS International Centre for Diffraction Data, Swarthmore, PA 1991.
- (4) K. W. Andrews, D. J. Dyson and S. R. Keown, Interpretation of Electron Diffraction Patterns, Adam Hilger LTD (1968)
- (5) W-D. Münz, D. Schulze, F. J.M. Hauzer, Surf. Coat. Technol., 50 (1992)169
- (6) B. Window and N. Savvides, Journal of Vacuum Science and Technology, A4 (1986)196
- (7) B. Window and N. Savvides, Journal of Vacuum Science and Technology, A4 (1986)453
- (8) N. Savvides and B. Window, Journal of Vacuum Science and Technology, A4 (1986)504
- (9) A. G. Dirks, H. J. Leamy, Thin Solid Films, V42 (1977)219
- (10) K. H. Müller, Journal of Applied Physics, V58 (1985)2573
- (11) I. Petrov, L. Hultman, U. Helmersson, J.E. Sundgren and J. Greene, Thin Solid Films, V169 (1989)299
- (12) B.A. Movchan and A.V. Demshishin, Fiz. Metal. Metalloved. V28 (1969)653

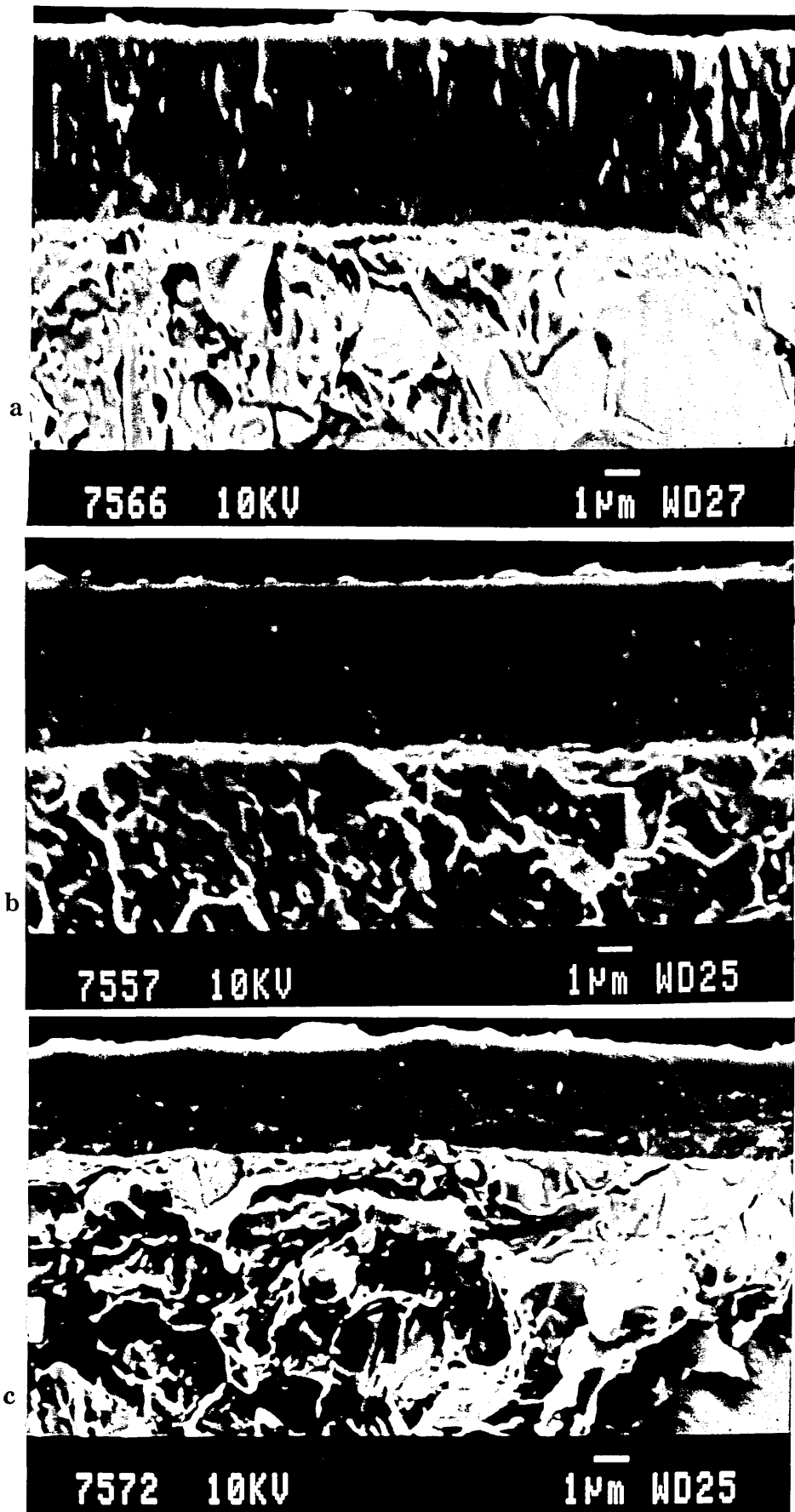


Fig 8.4.1 Fracture cross sectional analysis using SEM
a, b and c refer to one, two and three fold rotation samples respectively



Fig 8.4.2 TEM analysis at interface area from three fold rotation sample
a and b refer to TEM image of interface area and electron diffraction at interface respectively

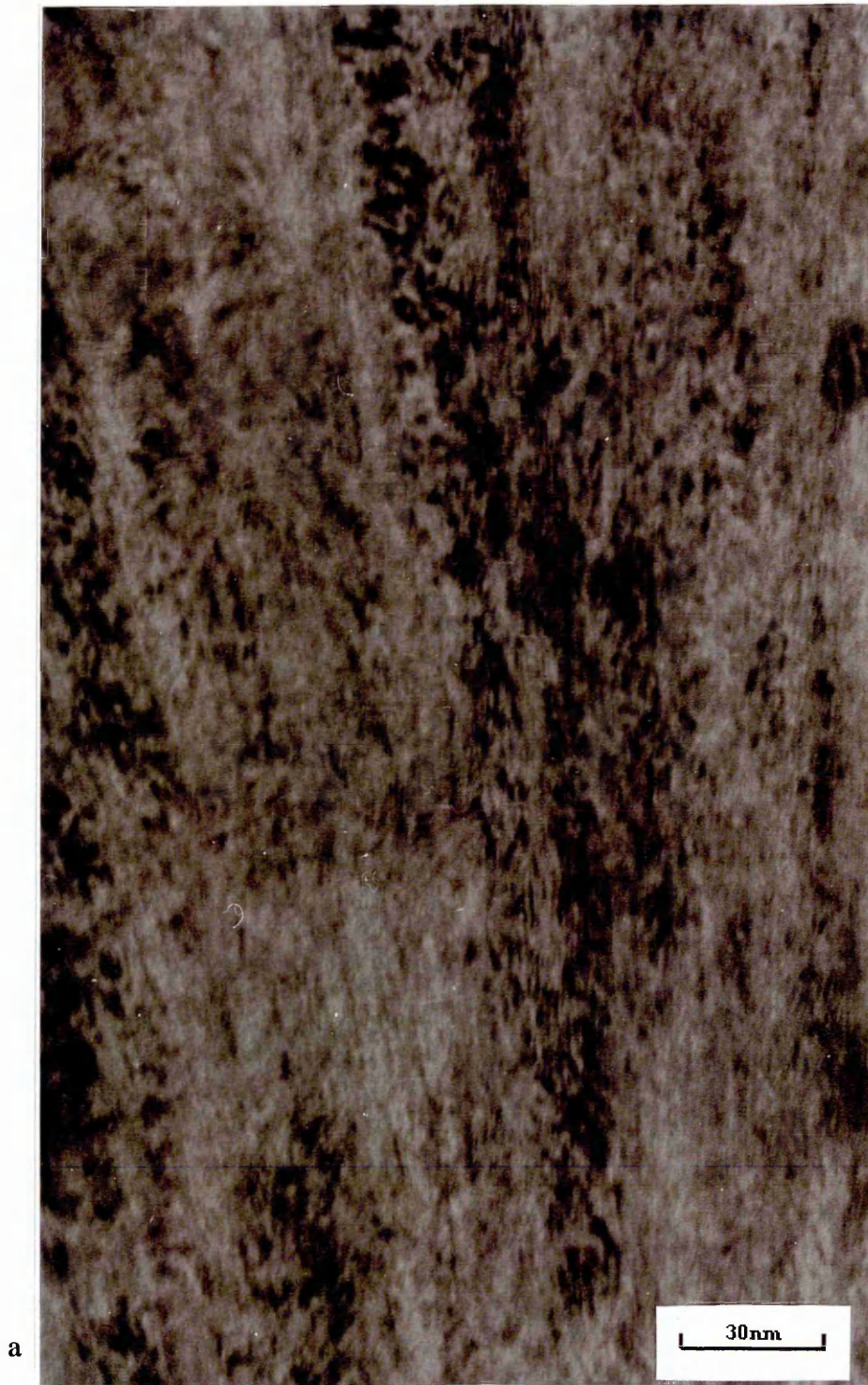


Fig 8.4.3 TEM cross sectional images of three fold rotation sample
a, b and c refer to image at middle, image at top and electron diffraction pattern respectively



Fig 8.4.3 TEM cross sectional images of three fold rotation sample
a, b and c refer to image at middle, image at top and electron diffraction pattern respectively

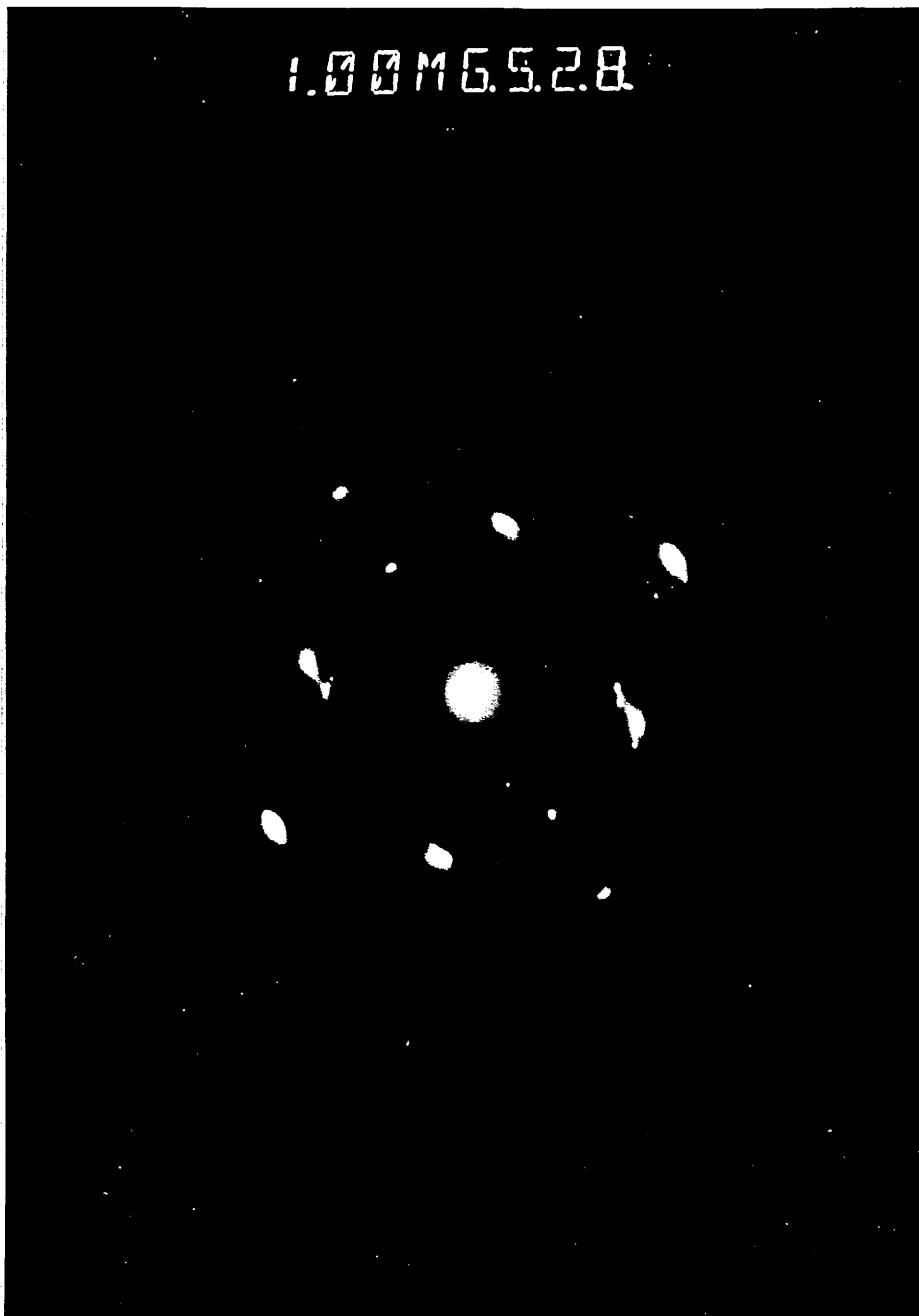


Fig 8.4.3 TEM cross sectional images of three fold rotation sample
a, b and c refer to image at middle, image at top and electron diffraction pattern respectively



Fig 8.4.5 Metal grains randomly located within the three fold rotation film
a. Large metal grain b. Column penetrates through the grain



Fig 8.4.5 Metal grains randomly located within the three fold rotation film
a. Large metal grain b. Column penetrates through the grain

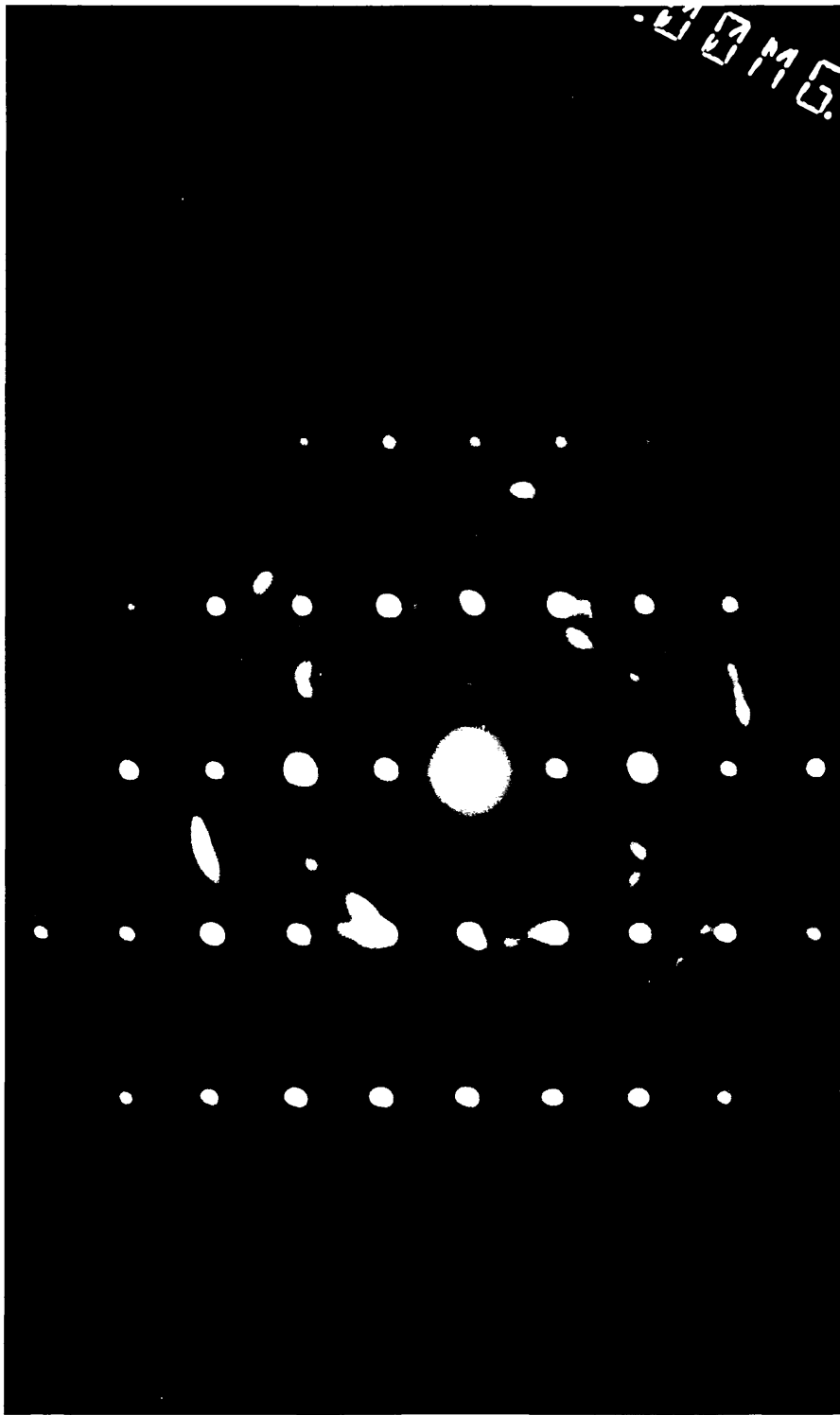


Fig 8.4.6 Diffraction pattern of the metal grain within the three fold rotation film



**Fig 8.4.8 TEM analysis at interface area from one fold rotation sample
a. TEM image, b. Electron diffraction pattern**

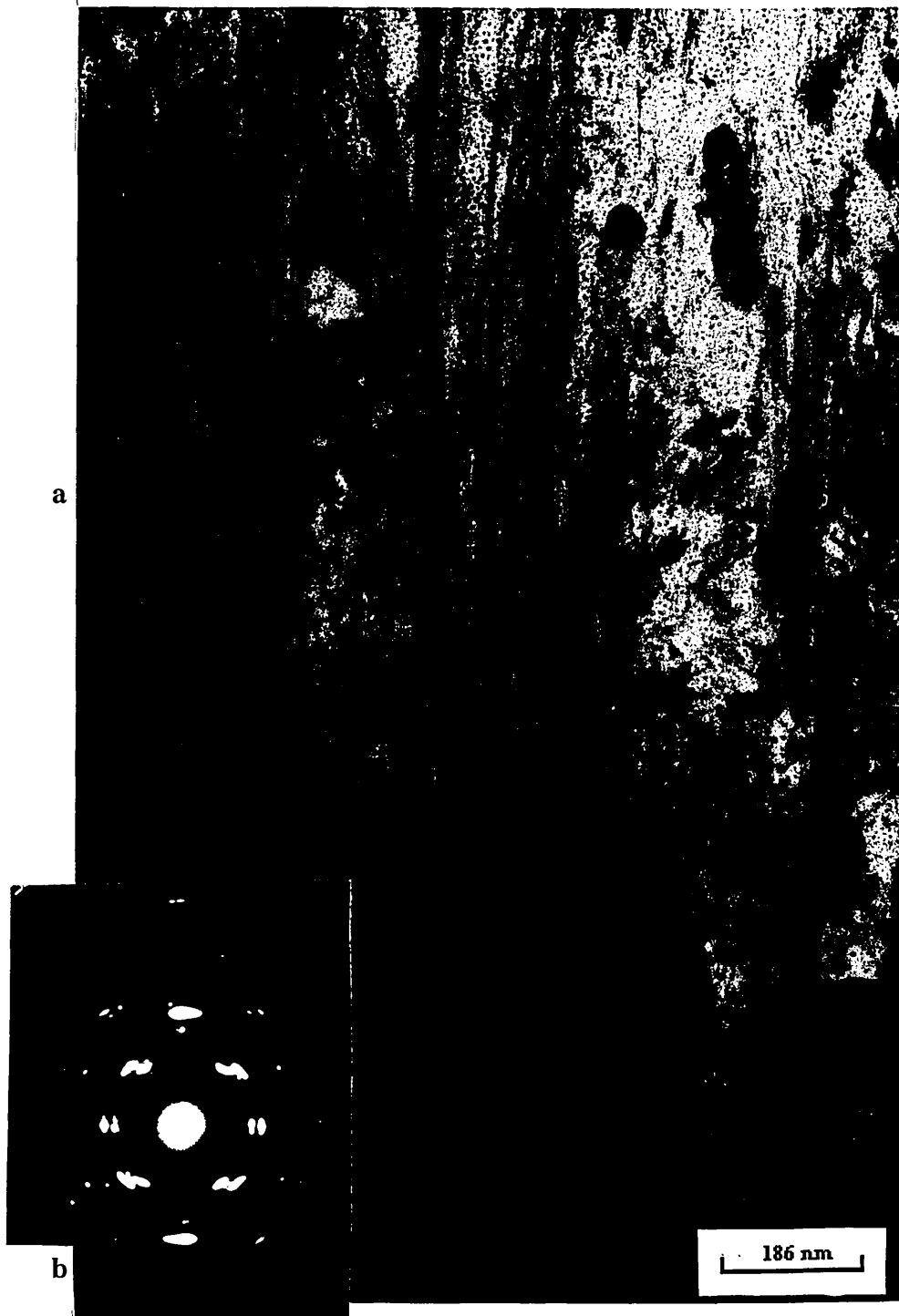


Fig 8.4.9 TEM analysis of one fold rotation coating
a. Image at middle area b. Electron diffraction pattern from columnar area

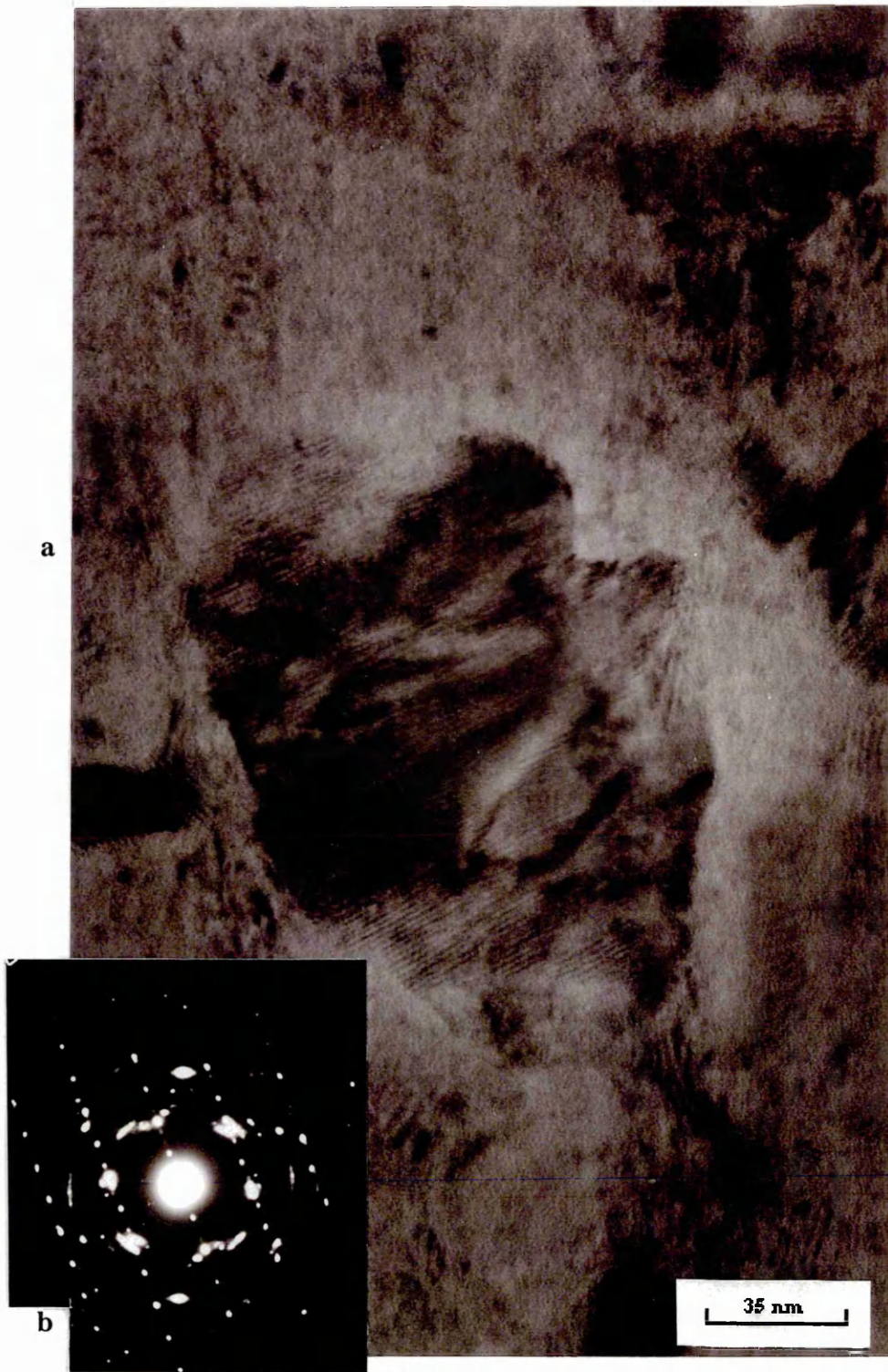


Fig 8.4.11 Metal grain within the one fold rotation film
a. Image at the metal grain area, b. Electron diffraction from the metal grain

9. Investigation of practical applications of $\epsilon\text{Ti}_2\text{N}$ films

The practical applications of $\epsilon\text{Ti}_2\text{N}$ films were studied using pin-on-disc sliding wear test, thermogravimetric analysis, electrochemical corrosion/erosion test, and test of drilling through holes on stainless steel bulk material. The parameters used for these experiments were chosen to match practical industrial applications. A comparison of result of different coatings and materials is also presented in this chapter.

9.1 Result of using pin-on-disc sliding wear test*

9.1.1 Experimental program

The $\epsilon\text{Ti}_2\text{N}$ coated high speed steel discs were analyzed using pin-on-disc sliding wear test⁽¹⁾ to establish the wear rate (k) of the coated discs and the loaded pin balls (tungsten carbide, WC). The test diagram is given in fig 9.1.1 in which the coated disc was held on a rotated turntable with a constant speed against the fixed ball with a loading normal to the disc.

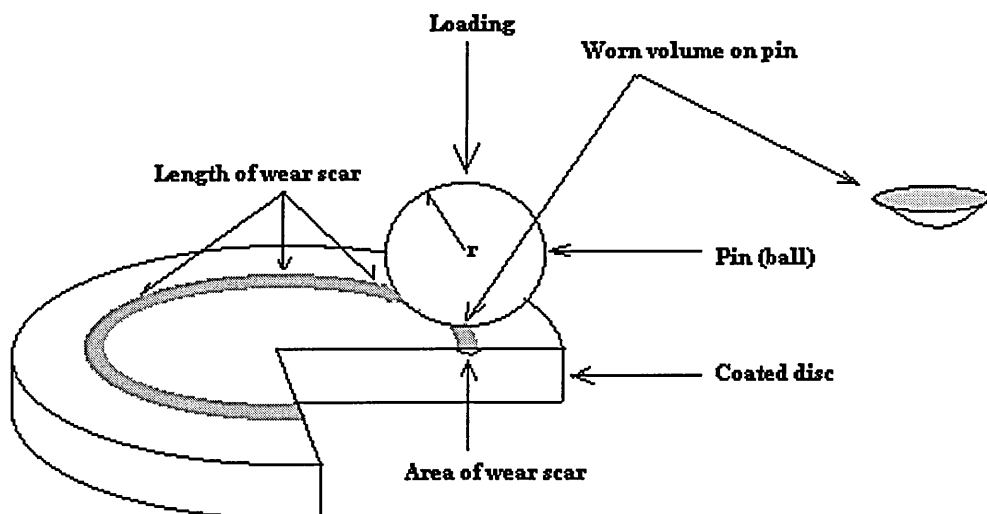


Fig 9.1.1 Pin-on-disc sliding wear test

* Test carried out at Research Center in Surface Engineering, University of Hull

Track dimensions of the wear of coated disc and pin ball were investigated using a surface profilometer in order to calculate the worn volumes. The wear rates were calculated for both the coating (k_c) and the pins (k_p). The k_c is expressed as

$$k_c = V_d / w s \text{-----} (1)$$

where V_d , w , and s is the volume of worn disc material, normal loading, and sliding distance respectively. The k_p is written as

$$k_p = V_p / w s \text{-----} (2)$$

where V_p is the volume of worn pin material. The test samples are $\epsilon\text{Ti}_2\text{N}$ coated high speed steel discs and δTiN coated high speed steel discs. The test parameters are given in table 9.1.1.

Table 9.1.1 Pin-on-disc test parameters

Test No	Normal load (N)	Speed (m/s)	Sliding distance (m)	Pin material
1	10	0.1	500	WC
2	20	0.1	1000	WC

9.1.2 Result of pin-on-disc sliding wear test

The resistance of sliding wear of $\epsilon\text{Ti}_2\text{N}$ and δTiN (arc deposited by Hauzer Coating center in the Netherlands) coated high speed steel discs against the tungsten carbide pin are shown in fig 9.1.2 and 3 referred to test number 1 and 2 for both $\epsilon\text{Ti}_2\text{N}$ and δTiN coatings respectively. In test number 1, the normal load, sliding speed, and sliding distance was 10 N, 0.1 m/s, and 500 m. It was found that loss of materials from both coated discs and pin indicated a dominant abrasive wear mechanism^(2,3). The volume of the worn material from the $\epsilon\text{Ti}_2\text{N}$ coating was much less than that

from the δTiN coatings whilst the value of worn materials from the WC pin in the $\epsilon\text{Ti}_2\text{N}$ sliding case was larger than that in the δTiN sliding case. It was obvious that the $\epsilon\text{Ti}_2\text{N}$ coating provided much better wear performance than the δTiN coating in the case of sliding against the tungsten carbide pin.

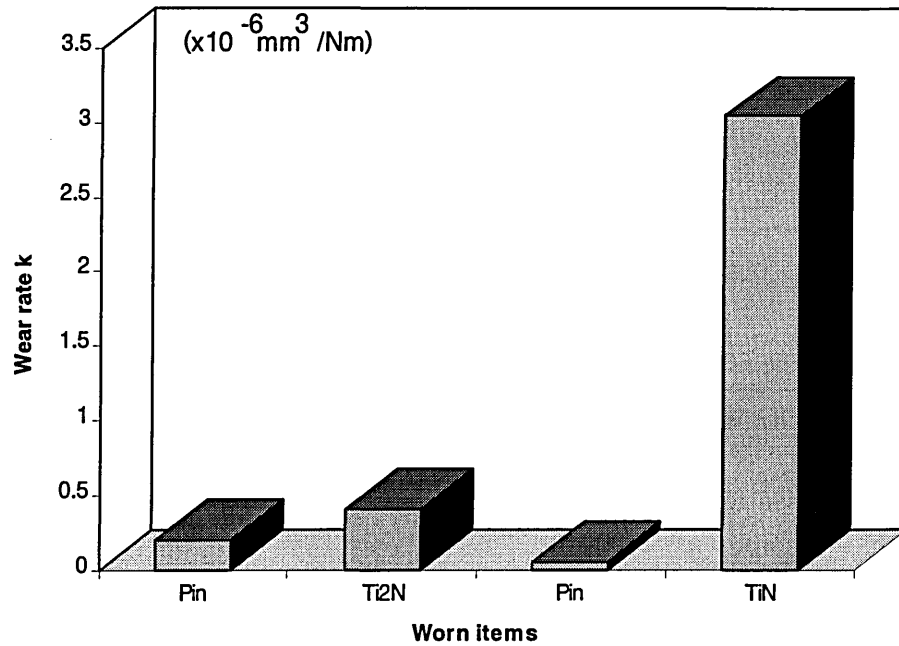


Fig 9.1.2 Test No 1 WC 500m 10N

With the normal load and sliding distance increased as shown in fig 9.1.3, the increased worn materials from both the coatings and the pin balls was found. In this case, the $\epsilon\text{Ti}_2\text{N}$ coating was still showing better wear performance than the δTiN film. However when load and sliding distance was increased, the value of wear rate for $\epsilon\text{Ti}_2\text{N}$ coating appeared to approach that for δTiN coating. This may indicated that the $\epsilon\text{Ti}_2\text{N}$ coating had much better wear resistance under the lower load condition.

The δTiN coating exhibited a smooth abraded surface with deeper breakthrough areas where adhesive failure occurred at the edge of the track profiles. The $\epsilon\text{Ti}_2\text{N}$ coating appeared to have a rougher wear track profile, however, when failure occurred the areas were not as deep as that with δTiN . This may be the evidence that δTiN is more

brittle than $\epsilon\text{Ti}_2\text{N}$. When pin is sliding on δTiN film, the film will be broken and spalled off due to high shear stress between pin and film. Whilst the $\epsilon\text{Ti}_2\text{N}$ film is tough and capable to resist the stress, and therefore, there is not failure of the coating adhesion, but the material is worn off when the abrasive wear took place.

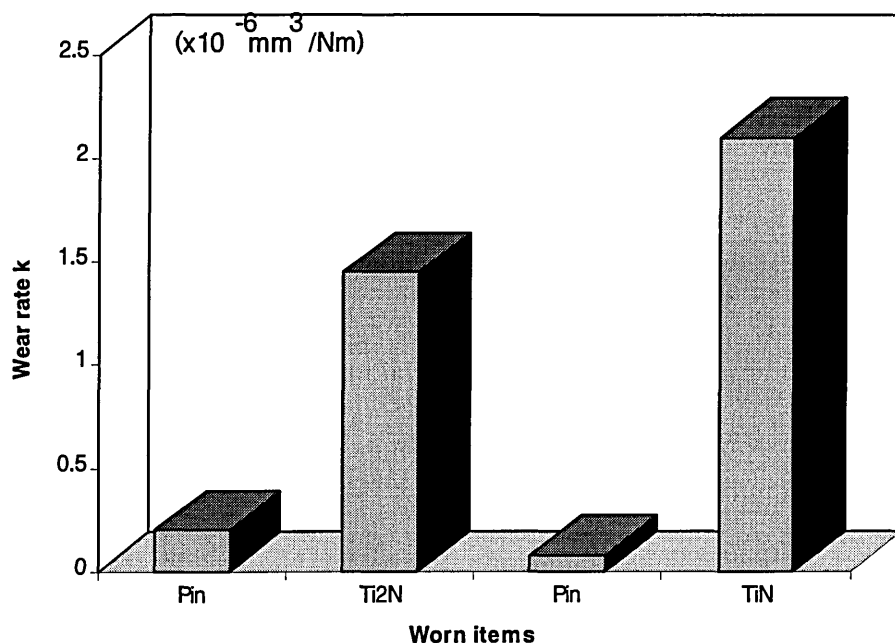


Fig 9.1.3 Test No 2 WC 1000m 20N

9.2 Result of thermal stability of $\epsilon\text{Ti}_2\text{N}$ film (Tested by Synergic Chemical Analysis Laboratory, MRI, SHU)

Thermal stability of $\epsilon\text{Ti}_2\text{N}$ film was investigated using thermogravimetry (TG) to measure the weight gain of the $\epsilon\text{Ti}_2\text{N}$ coated sample against the increase in temperature. The principle of TG can be shown in fig 9.2.1⁽⁴⁾. When the sample is heated in atmosphere, the surface of the sample will react with the oxygen in the air at the elevated temperature to form a loose bonded thin oxide layer and as indicated by weight gain of the sample. If the temperature rises up to the melting point, evaporating of the materials will take place accompanied by weight loss. The

instrument consists of a precision CAHN quartz balance, a furnace controlled by a temperature programmer, and a recorder for data acquisition. The sample container inside the furnace is suspended directly from the balance. The instrument used for this analysis is a CAHNTG131 instrument which allow a resolution of 1 μg .

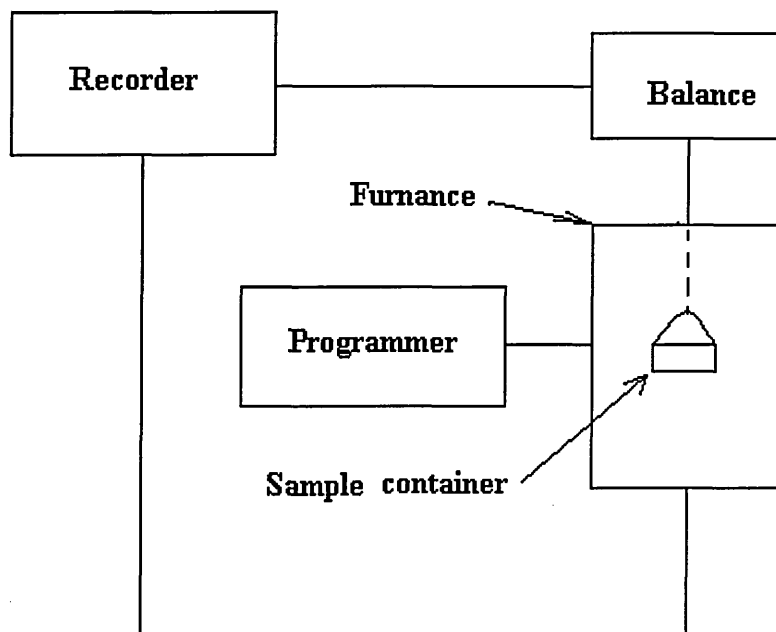


Fig 9.2.1 diagram of thermogravimetry

The result of weight gain of the $\epsilon\text{Ti}_2\text{N}$ film against the temperature is given in fig 9.2.2. It can be seen that the weight gain is almost negligible before the temperature reaches 600°C . Then the weight gain increases slowly with the temperature until the temperature rises up to 700°C . At this point the weight gain increased rapidly with the increase of temperature from 700 to 900°C . Afterwards there was not much variation of the weight gain to indicated a stable weight gain against the temperature. The stable weight gain at temperature 950°C was about $15\text{g}/\text{m}^2$. It is clear as seen from the weight gain vies temperature curve that the $\epsilon\text{Ti}_2\text{N}$ film was stable in the temperature range lower than 600°C . When the temperature was higher than 600°C , the film began to react with the oxygen resulting in the increase of weight gain. As the temperature was higher than 700°C , the reaction between film and the oxygen in the air was rapidly increased with the temperature. After the temperature reached at 900° , a stable and intensive reaction between film and oxygen was established to

indicate a stable weight gain with the temperature. Therefore the maximum temperature at which the $\epsilon\text{Ti}_2\text{N}$ film can keep its thermal stability is 600°C

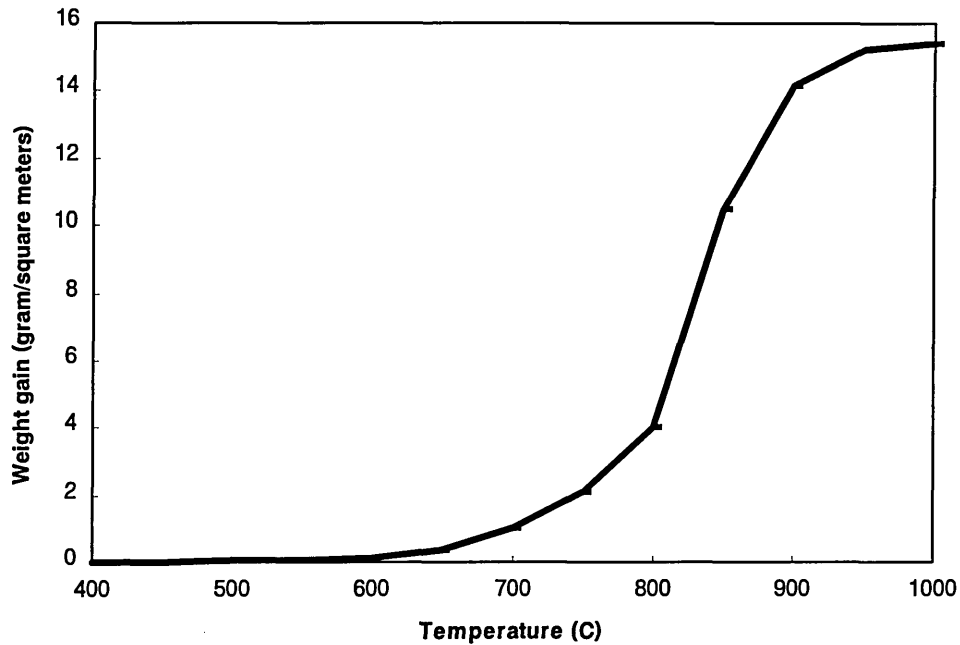


Fig 9.2.2 Weight gain of $\epsilon\text{Ti}_2\text{N}$ film dependent on temperature

The application of $\epsilon\text{Ti}_2\text{N}$ as a diffusion barrier against Fe and Cr was further investigated using heat treatment. The heat treatment was carried out using a furnace to heat the sample (stainless steel coated $3\mu\text{m}$ by $\epsilon\text{Ti}_2\text{N}$ film and $1\mu\text{m}$ $\text{Ti}_{0.43}\text{Al}_{0.52}\text{Cr}_{0.03}\text{Y}_{0.02}\text{N}^{(5)}$ as top layer) up to 950°C in the air and to keep this temperature for one hour. Afterwards the composition was investigated by SNMS. The result is shown in fig 9.2.3. It can be seen that the materials (Fe and Cr) from the substrate diffused into the $\epsilon\text{Ti}_2\text{N}$ film and penetrated through the TiAlCrYN over layer. The aluminum from the over layer was diffused into the $\epsilon\text{Ti}_2\text{N}$ film and met the substrate materials at the $\epsilon\text{Ti}_2\text{N}$ film/substrate interface. Oxygen was found through all of the coatings and the coating/substrate interface. This evidence clearly indicated the coated film was heavily oxidized at this temperature. The only

unaffected element was the yttrium in the TiAlCrYN over layer, which was not likely found in the $\epsilon\text{Ti}_2\text{N}$ film and this may indicate that the yttrium was still stable at this temperature. Therefore, $\epsilon\text{Ti}_2\text{N}$ is not suitable as a diffusion barrier against the Fe and Cr.

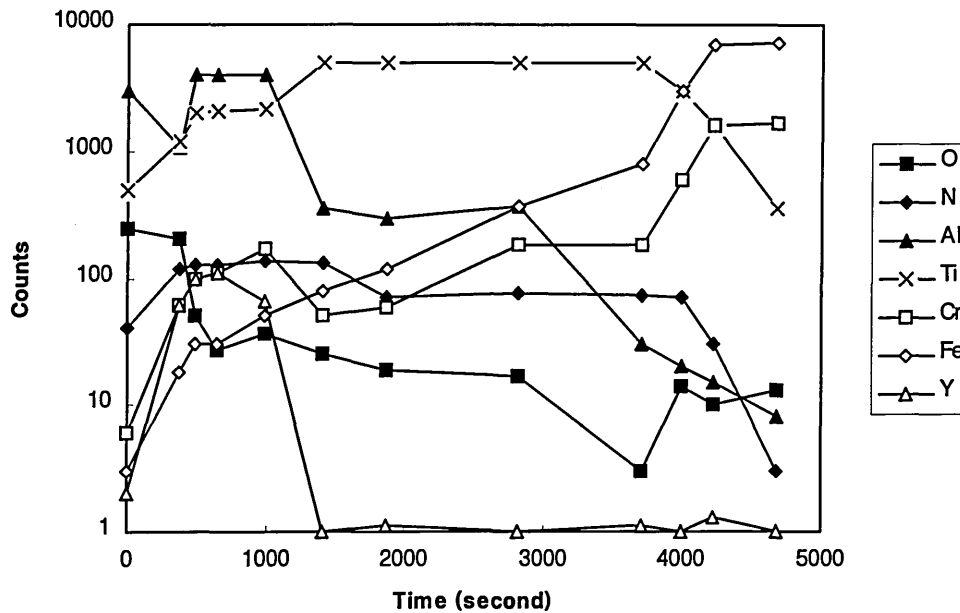


Fig 9.2.3 Composition change of the $\epsilon\text{Ti}_2\text{N}+\text{TiAlCrYN}$ over layer after heat treatment

9.3 Electrochemical corrosion test of the $\epsilon\text{Ti}_2\text{N}$ film (Tested at Corrosion and Protection Center, UMIST)

9.3.1 Experimental

Electrochemical corrosion test of the $\epsilon\text{Ti}_2\text{N}$ coated mild steel (BS6323), uncoated mild steel and austenitic stainless steel (AISI 304) were investigated by potentiodynamic polarization technique which was used to develop a curve by measuring the corrosion potential against the current and therefore the corrosion property of the materials can be described by the corrosion potential E_{corr} , critical current i_{crit} , and passivation current density i_{pass} . When the potential increases, the current (corrosion rate) will also increase until a critical value i_{crit} where the related

potential is called E_{corr} . If the potential increases further, the corrosion rate suddenly decreases owing to the formation of a protective film on the surface and this is called as the passivity. The current (corrosion rate) keeps at the same value as the potential increases more. When the potential is increased up to a certain level, the current will start to increase again and this current is called as the passivation current i_{pass} .

The corrosion test was carried out using a rotating cylinder, three electrode system⁽⁶⁾ which consists of a hollow cylindrical working electrode (specimen, stationary for corrosion, or rotated for corrosion/erosion) and an auxiliary electrode (platinum) contained in the electrolyte cell, and a outside standard reference electrode (saturated calomel electrode, SCE) connected to the solution through salt bridging. Ring samples with dimensions of outer diameter of 38 mm, height of 10 mm, and wall thickness of 2 mm, were cleaned, dried, and weighed prior to and after each test. The electrolyte, an 0.5 M mixed solution, 1:1 by volume of NaHCO_3 and Na_2CO_3 , was prepared out of de-ionized water and sufficiently deaerated using pressurized nitrogen. Linear potential sweep range is usually from - 1.0 to + 1.2 V at a potential ramp of 2.5 mV/s. The response to applied potential of specimen (referred to SCE, V_{sce}) and electrical current were directly measured against running time, and polarization curves further obtained.

9.3.2 Result of electrochemical corrosion test

The electrochemical corrosion behavior of the mild steel, austenitic stainless steel and $\epsilon\text{Ti}_2\text{N}$ coated mild steel samples were studied using the potentiodynamic polarization techniques. The pure corrosion case was first made using stationary sample in the 0.5 M solution containing alumina particles of 150 μm in size. The result of pure corrosion test is shown in fig 9.3.1. The corrosion potential, E_{corr} for the coated sample was - 0.5 V whilst that for austenitic stainless steel and mild steel was - 0.82 and - 0.88 V respectively. The critical current density, i_{crit} , defined as the maximum current density before passivation, was about $1\mu\text{A}/\text{cm}^2$ for coated sample,

9uA/cm² for austenitic stainless steel, and 400uA/cm² for mild steel. The passivation current density, i_{pass} , was 1~2uA/cm² for coated sample, ~10ua/cm² for stainless steel, and 20~30uA/cm² for the mild steel. It is clear that the ϵ Ti₂N coated sample had higher E_{corr} , lower i_{crit} , i_{pass} , and therefore it appeared to show superior corrosion resistance to austenitic stainless steel and mild steel.

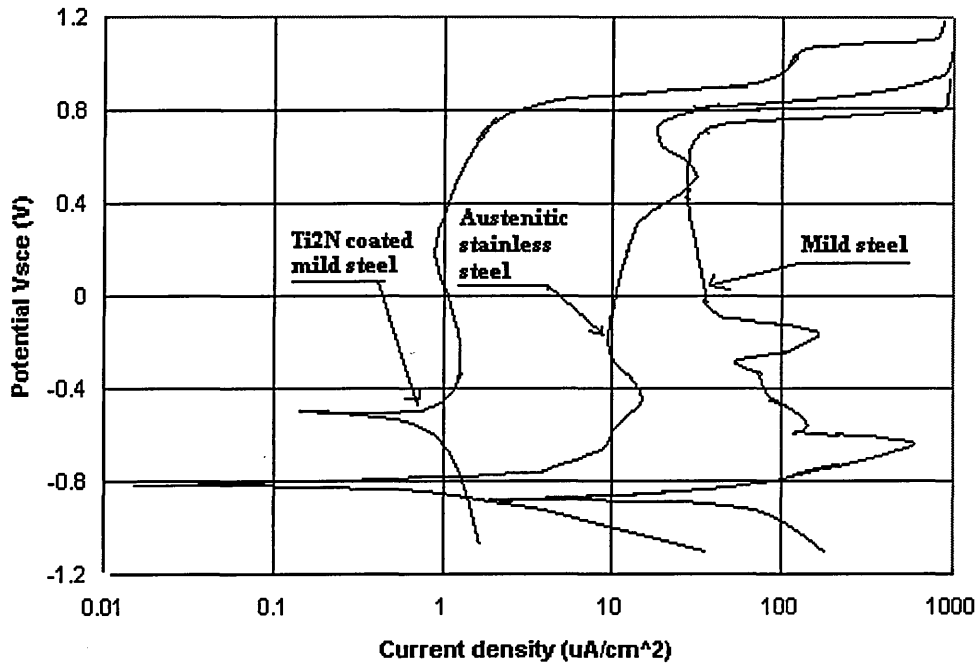


Fig 9.3.1 Polarization curves of the tested samples

The corrosion under conditions of particles erosion was studied using the erodent speed at 2, 4, and 8m/s. In general the effect of erosive particles on the corrosion was obvious because that all the polarization curves were shifted to the right with a increase of erodent speed indicating a large critical current density. The polarization curve of the tests using erodent speed of 8m/s is shown in fig 9.3.2. It could be seen that in the mild steel case, not only the polarization curve was shifted to the right, but also the passive region was suppressed with the increase of erodent speed. This indicated that the protective film could not be formed when the erodent taken into the corrosion and therefore the corrosion current i_{corr} was largely enhanced. The corrosion behavior of the stainless steel also indicated a erosion enhanced effect on

the active and passive regions. Even though the passive region was survive at erodent speed up to 8m/s, a greatly enhanced dissolution was evident as the i_{pass} was increased ten time ($100\mu\text{A}/\text{cm}^2$) that of no particle erosions. The effect of moving particles on the corrosion behavior of the $\epsilon\text{Ti}_2\text{N}$ coated sample, however, was similar to the coating under pure corrosion only. The average corrosion current density (i_{pass}) of the coating under erodent speed (8m/s) in the passive region, was only $\sim 5\mu\text{A}/\text{cm}^2$ which was much less than that in the stainless steel case. It was clear that the corrosion behaviors of the stainless steel and mild steel were critical dependent on the intensity of solid particle erosion whilst that of the $\epsilon\text{Ti}_2\text{N}$ film was much less affected by the erodent particles. The latter again appeared to superior corrosion resistance than the uncoated steels in the case of synergistic effect of the erosion on corrosion.

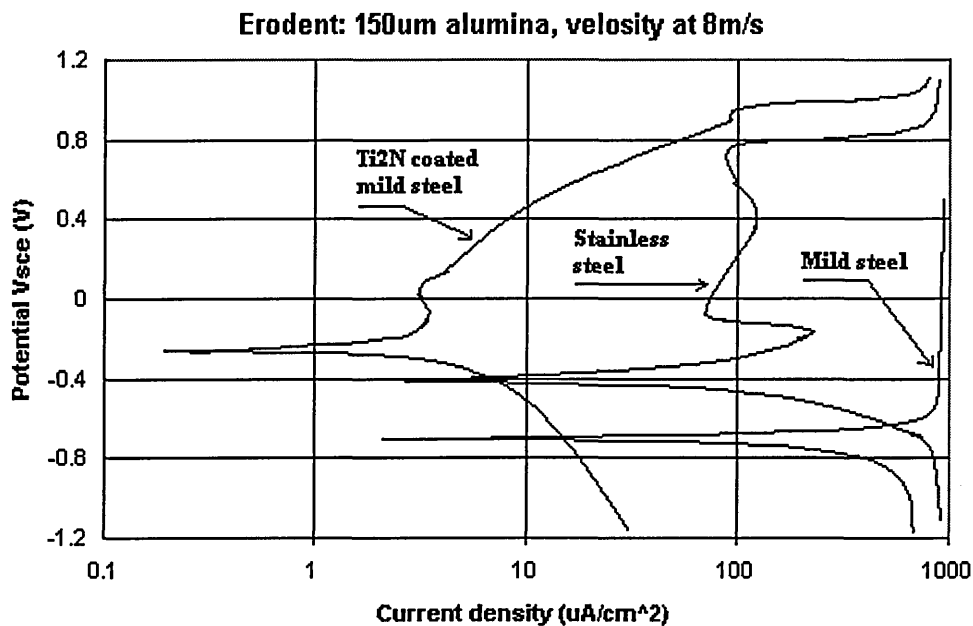


Fig 9.3.2 Corrosion behavior affected by erodent particles

The weight loss of the test samples was a function of the erodent speed as shown in fig 9.3.3 which mirrored the erosion-corrosion behavior as described by the polarization technique to indicate a enhanced corrosion of the uncoated specimens under erodent conditions whilst the weight loss of the coated sample was only slightly affected by the moving of the solid particles. It could be seen that the loss of weight was systematically increased with the erodent speed. It was measured that the

weight loss under no erosion condition (erodent speed 0m/s) was 290, 65, and 10 ug whilst that under maximum erosion intensity (erodent speed 8m/s) was 8450, 4930, and 100 ug for the mild steel, stainless steel and $\epsilon\text{Ti}_2\text{N}$ coated mild steel respectively.

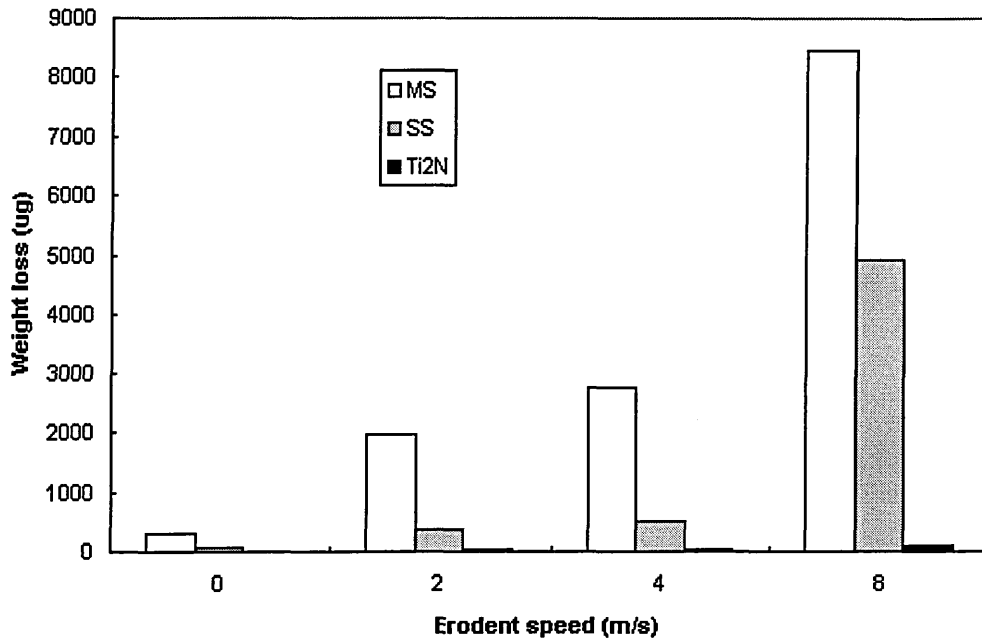


Fig 9.3.3 Weight loss as a function of the erodent speed

9.4 Investigation of the practical performance of the $\epsilon\text{Ti}_2\text{N}$ coated drills (Experiment carried out in School of Engineering, SHU)

The practical performance of the $\epsilon\text{Ti}_2\text{N}$ films was carried out using a milling machine (Beaver NC5) to test the improvement of the cutting efficiency of coated high speed steel twist drill as compared with the uncoated drills. The test was performed continuously drilling through holes on the bulk austenitic 316 stainless steel with water cooling until the drill failed which was judged by hearing a sharp scream from the drilling. The parameters of the drilling test were chosen for a commercially application purpose which is given in table 9.4.1

Table 9.4.1 Parameters of drilling test

Drill diameter (mm)	Material for drilling	Drilling speed (m/min)	Feed speed (mm/rev)	Coolant	Drilled depth (mm)
8	Stainless steel	15	0.22	Water	32

9.4.1 Result of drilling test using simple cooling

The drilling test using simple cooling applied only one coolant jet during the drilling as shown in fig 9.3.1. The angle (θ) of the jet can be adjusted from 0 to 70°. In the practical drilling performance, however, the angle has to be $\theta > 45^\circ$ in order to get a reasonable cooling condition. The coolant water was re-circulated.

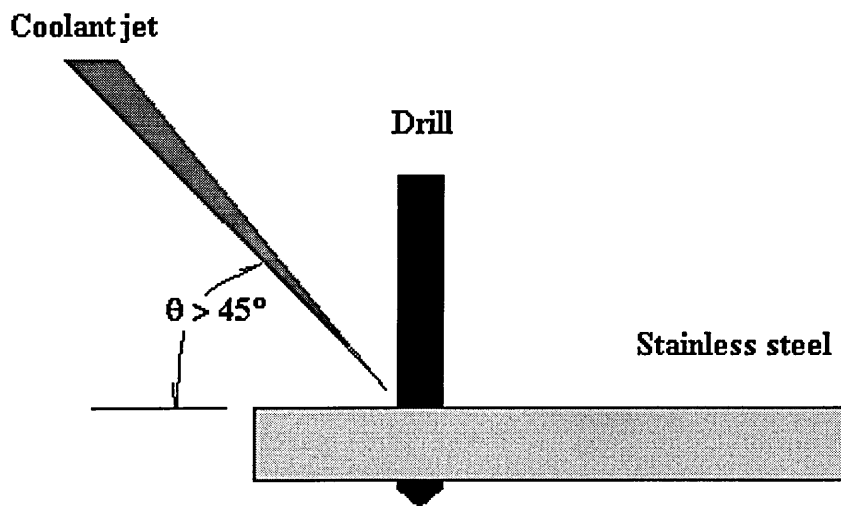


Fig 9.4.1 Diagram of drilling test using simple cooling

The result of the drilling test using simple cooling is given in table 9.4.2. It can be seen that there was no obvious improvement of the performance of the coated drills compared with that of the uncoated drills. The drilled holes for each type of drill appeared to show a large fluctuation which indicated unstable cutting conditions incorporated during the drilling test.

Table 9.4. 2 Result of drilling test using simple cooling

Type of drill	Jet angle (°)	Finished holes			Comments
D _{70*}	<65	9	20	55	Failure found
D ₇₅	<65	7	28	75	Failure found
D ₈₀	<65	15	36	82	Failure found
D _{Cr1}	<65	32	50	79	Failure found
D _{Cr2}	<65	28	107	145	Failure found
D _{un}	<65	12	38	90	Failure found

* The sub-font specify the nitrogen flow rate , Cr metal ion etch of the coating process and the blank drill respectively.

It was found that high temperature ($> 600^{\circ}\text{C}$) was produced during drilling process as the local area at the bottom of the stainless steel block became red at the moment when the lip of the drill was coming through . The chips and the drill lips were occasionally welded each other to indicate extremely elevated temperatures produced at the interface between chip and cutting edge. This evidence appeared to show that the simple cooling was not effective enough to transfer heat from the chip/cutting-edge interface.

The austenitic stainless steel was regarded as one of the materials most difficult to machine⁽⁷⁾ as the chips were often remaining stuck to the surface of the cutting edge resulted in the extreme stress, strain and temperature at the chip/cutting edge interface. As the drill was in a constant speed making holes, the chips must be removed by extremely force which was required to overcome the interlocking and bonding between chip and cutting edge. It was reported⁽⁷⁾ that the maximum stress was found near the cutting edge, this was one of the important facts to deform the cutting edge.

Coolant jet was often used⁽⁸⁾ to flood the local cutting area in order to extract heat from the work-piece, tool and chips during cutting process. For the drilling process carried out here however, the use of coolant jet was not effective to remove the heat from the drill-lip/workpiece interface because the coolant could not reach the cutting edge due to the chips continuously came out from slots of the drill and blocking the way between the drill tip and the cutting cooling fluid. As the poor cooling method was applied for the drilling test of stainless steel and the cutting speed and feeding were unusually high, a

large heat was produced and this heat could not efficiently removed by the coolant, and therefore, high temperature was unavoidable. The elevated temperature at the drill tip resulted from sticking of the chips at the cutting edge, and this was the main cause of intensive stress at the cutting edge and the work-piece as the chips must be pushed out by drilling holes. The high temperature and stress on the workpiece caused hardening effect on the local area as shown in fig 9.4.2. The drilled area was more than two times harder than the bulk material as measured using Knoop microhardness indenter with a load of 25 g.

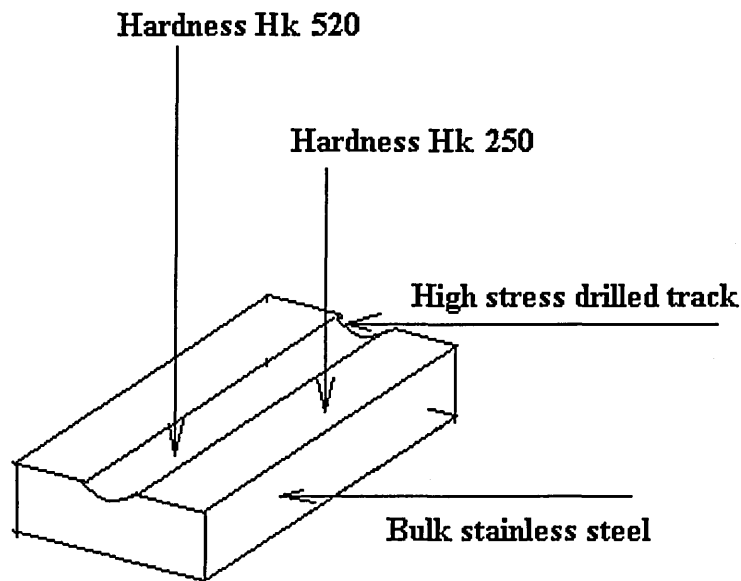


Fig 9.4.2 Hardening effect of the high stress drilled workpiece

Under a high stress cutting condition the drill was experienced two critical conditions. One was that both the coating and the substrate of the drill tip were surrounded in high temperature as a result, the oxidation of the coating and soft of the substrate were unavoidable. Another was that the drill was continuously cutting a severely hardened surface, which caused the drilling is highly inefficient. As both the coating and the substrate of the drill were rapidly damaged, there was not clear evidence to show the improvement of the coated drills. Therefore, when cutting parameters are chosen, the

drilling test for coated twist high speed steel drills on stainless steel is critically dependent on the cooling condition.

9.4.2 Result of drilling test using enhanced cooling

The basic design of the enhanced cooling is shown in fig 9.4.2. There were three coolant jets arranged around the drill (here only one was drawn) instead of only one used in simple cooling. The stainless steel block was fitted as a tray with 1.5 cm high sides around the workpiece. A wood plate was fitted at the bottom of the stainless steel block. The drilling process was carried out only under the condition that the three coolant jets were operated in maximum flow rate and the tray was flooded over. As the gravity force can direct the coolant to reach the surface very close to the cutting-edge/workpiece interface, the heat from the interface was rapidly and efficiently removed. Therefore much better cooling condition was obtained using the enhanced cooling method. There was no evidence related to elevated temperature as no weld was found between drill lip and chips. During the drilling process the temperature was estimated not more than 500°C because there was not found thermal oxidation on the chips and the stainless steel block.

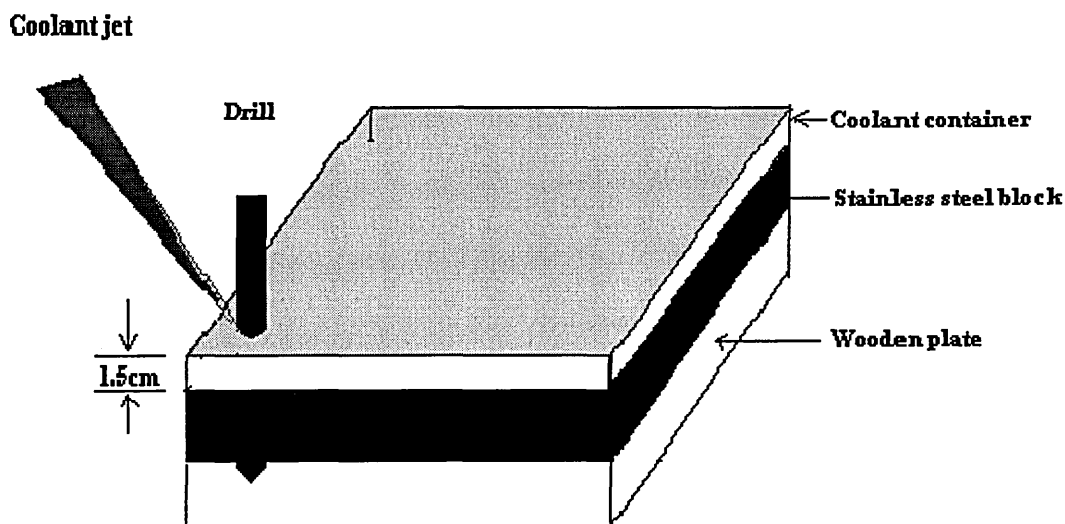


Fig 9.4.3 Diagram of enhanced cooling

The enhanced cooling method can be used as a standard condition for the practical cutting test of the coated twist drills. This is particularly necessary when tough materials, such as austenitic stainless steel, is used as the workpiece. When stainless steel is drilled, the workpiece is hardened because of high stress incorporated during the cutting. The stress is the result of thrust and torque. The thrust is produced by the axial pressure of feed rate and extruding effect of the drill point. The torque is directly produced by the rotational motion of the drill. Both of these forces affect the hardness of the workpiece and the cutting edge of the drill. The result of work hardening of drilling austenitic stainless steel is shown in fig 9.4.4.

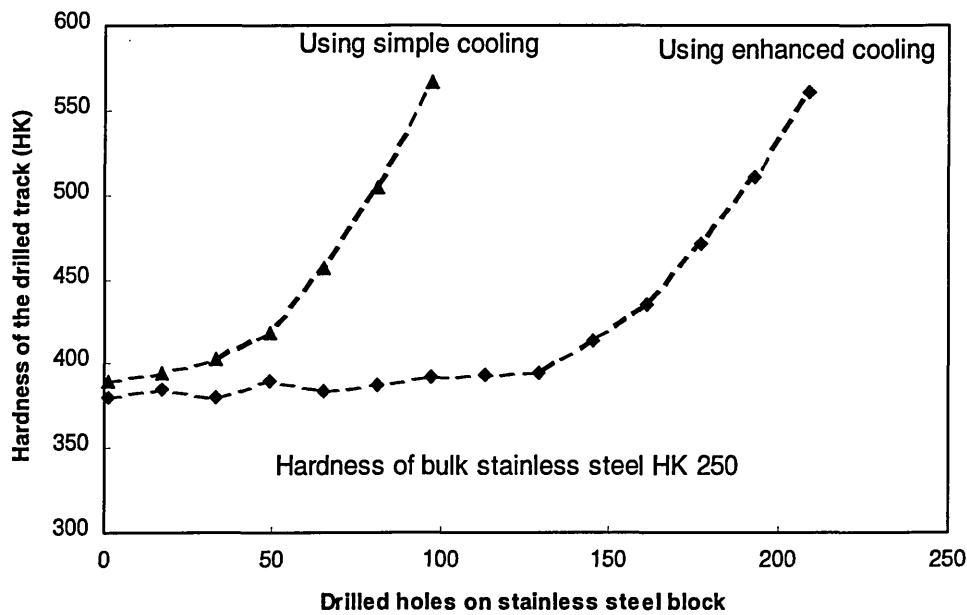


Fig 9.4.4 Work hardening effect of the drilling test

The hardness of bulk material was Hk 250. The hardness of the track surface of the first drilled hole (sharp cutting edge was used) was about Hk 380 for both the tests using simple and enhanced cooling. Afterwards the hardness of the drilled track for test using simple cooling increased slowly from the first to thirty holes, and then increased rapidly from thirty to one hundred holes. The hardness of the drilled track produced by the

almost failed drill (dull cutting edge was used) was about Hk 570 which was two times more than that of the bulk material. There was no obvious variation of the hardness of the drilled track from 1 to 150 holes when enhanced cooling was used for the test. After 150 holes the hardness of the drilled track increased rapidly from about Hk 410 to Hk 560. The point, at which the hardness of the drilled track increased rapidly, indicated the point at which cutting edge of the drill was badly worn. As large stress was produced using the dull drill, the work hardening on drilled component was enhanced and the drill was failed rapidly.

The result of drilling test using enhanced cooling is given in table 9.4.2 in which different types of drills made by different manufacturers were tested. It can be seen that TiN coated drill is the best candidate for stainless steel cutting, and then the TiCN coated drill also had the excellent performance. The Ti₂N coated drills had the better cutting performance than the TiAlN coated drills.

Table 9.4.2 Results of drilling test using enhanced cooling

Type	Manufactured	Finished holes	Comments
TiN	Balzars or Multiarc	435	No failure found
TiCN	Balzars or Multiarc	362	Failed
Ti ₂ N	SHU	210	failed
Ti ₂ N	SHU	175	failed
Ti ₂ N	SHU	168	failed
Ti ₂ N	SHU	162	failed
TiAlN	Multiarc	158	failed
TiAlXN	SHU	138	failed
Uncoated	Dormer	80	failed

9.5 Discussion of chapter 9

Compared with stoichiometric δTiN film, the $\epsilon\text{Ti}_2\text{N}$ coating has better wear resistant behavior as demonstrated by pin-on-disc sliding wear tests. This may be resulted from the fact that the $\epsilon\text{Ti}_2\text{N}$ film has a very dense packed grain structure, smooth surface, and excellent adhesion between coating/substrate surface. In addition there is less residual stress produced in the $\epsilon\text{Ti}_2\text{N}$ whilst the δTiN produced by PVD is normally characterized by a large residual stress. In fact the wear mechanism of the coatings and the wear environment is a complicated topic which can not be explained by just a few parameters and this topic is beyond the scope of this chapter. The thermal stability of $\epsilon\text{Ti}_2\text{N}$ coating is similar to that of the δTiN film which can keep the physical properties at temperature not more than 600°C . The corrosion behavior of the $\epsilon\text{Ti}_2\text{N}$ film is superior to mild steel and stainless steel especially when the case of erodent particles is taken affect into the corrosion. There are some reports^(9,10) which indicate that the limitation of corrosion resistance using the δTiN films deposited by PVD techniques is due to the open pores and pin-holes within the coatings. The $\epsilon\text{Ti}_2\text{N}$ film produced by unbalanced magnetron sputtering technique however, has the dense fine packed grains with fabric like interlocking columns to provide a pin-hole free structure. This may be the advantage to other films used for corrosion resistant applications. The cutting test on austenitic stainless steel of the coated drills is critically dependent on the cooling condition during the cutting process. The $\epsilon\text{Ti}_2\text{N}$ coated drills have not better performance than the δTiN and TiCN coated drills may be due to the over heating on the cutting edge during the deposition process. The $\epsilon\text{Ti}_2\text{N}$ film has to be produced at a temperature more than 480°C which is the equilibrium temperature recorded from the thermocouple. In fact the local temperature on the cutting edge may be much higher than the reading from the thermocouple because of the bombardment of energetic particles from the nearby plasma region. This bombardment will produce elevated temperature at the surface of the cutting edge to soften the substrate nearby the cutting edge. The soft cutting edge will be worn rapidly during the cutting test on stainless steel as a large stress produced between cutting-edge/workpiece interface. Therefore further work should be done to improve the performance of $\epsilon\text{Ti}_2\text{N}$ films. The future work may be

considered to use more power of the radiate heater rather than the power of target. This will reduce the bombardment of the energetic particles and keep the temperature up 480°C

9.6 Conclusion of Chapter 9

- $\epsilon\text{Ti}_2\text{N}$ film has better wear resistant performance than δTiN film using the pin-on-disc sliding wear test.
- The thermal stability temperature for $\epsilon\text{Ti}_2\text{N}$ film is 600°C and this indicates that the $\epsilon\text{Ti}_2\text{N}$ coated components should be used at temperature not more than the thermal stability temperature in order to get the best performance of the film
- Corrosion resistance of $\epsilon\text{Ti}_2\text{N}$ films is superior to the uncoated steels especially when the erodent particles have an affect on corrosion.
- The superior corrosion resistant behavior of the $\epsilon\text{Ti}_2\text{N}$ film are due to the chemical stability, high dense packed fine grains, and pin-hole free structure.
- Drilling test of the coated drills on austenitic stainless steel is critically dependent on the cooling condition and enhanced cooling method has to be used in order to obtain a efficiently heat removing from the cutting-edge/workpiece interface.
- All the coated drills have better performance than the uncoated drills. δTiN coated drills, however, have the best drilling performance and then the TiCN , $\epsilon\text{Ti}_2\text{N}$ and TiAlN coated drills respectively
- Further deposition process to produce $\epsilon\text{Ti}_2\text{N}$ films should be investigated to improve the performance of both coating and substrate.

References

- (1) A. Wilson, Report on Tribological Testing of Arc Deposited Coatings on HSS, Research Centre in Surface Engineering, University of Hull, Feb. 1997
- (2) R.D. Arnell, P.B. Davies, J. Halling and T.L. Whomes, *Tribology (Principles and Design Applications)*, M Macmillan (1991)70
- (3) M.J. Neale, *Tribology Handbook*, London Butterworths (1973)F6
- (4) J. W. Dodd, K. H. Tonge, *Thermal Methods*, JOHN WILEY & SONS, (1987)41
- (5) L.A. Donohue, I.J. Smith, W-D. Münz, I. Petrov, J.E. Greene, Presented at ICMCTF-97 San Diego, USA, April 1997-in press Surface and Coating Technology
- (6) H.W. Wang and M.M. Stack, Technical Report: Erosion-Corrosion Protection by PVD Hard Coatings.
- (7) E.M. Trent, *Metal Cutting*, Butterworths, (1984)204
- (8) G.T. Smith, *Advanced Machining: The Handbook of Cutting Technology*, IFS Publications, (1989)190
- (9)I. Milosev and B. Navinsek, *Surface and Coating Technology*, V63 (1994)173
- (10) B. Matthes, E. Broszeit, J. Aromaa, H. Ronkainen, S.P. Hannula, A. Leyland and A. Matthews, *Surface and Coating Technology*, V49(1991)489

10. Discussion and conclusions of the deposition of Ti₂N and TiCN films

10.1 Discussion

10.1.1 TiCN coatings

The most important results can be seen in the fact that very dense TiCN structures grow if the coating is stoichiometric and the N to C ratio is about 3.7 as it can be seen from fig 5.5.1 and fig 5.5.4. In contrast under-stoichiometric compositions lead to a rather coarse film growth. The same is observed from the under-stoichiometric TiN coating (fig 5.5.4). Finally it could be shown in all experiments, that precise flow control in combination with the high pumping speed generated by two turbo-molecular pumps (4400l/s) allow the deposition of coatings with sharply formed interfaces when the reactive gases varied stepwise.

10.1.2 Ti₂N coatings

Most of the results published in the literature indicate a very narrow window of process parameters. Palty⁽¹⁾ even demands a line phase composition of 33% N for the existence of bulk ϵ Ti₂N. In the field of PVD deposition, however, multiphase compositions seems to be allowed^(2,3,4,5,6). The experiments carried out in the special sputtering system used in this work confirm this experience. Alone the behaviour of the reactive gases needed to form stoichiometric ϵ Ti₂N show in a striking manner, how careful the setting of the partial pressure of N₂ has to be considered, however. Fig 6.2.2 and fig 7.2.1 demonstrate very clear, how sensitive the nitrogen concentration of the films reacts on the partial pressure of N₂ in the range of low nitrogen content. This is valid for both 3 fold rotation (fig 6.2.2) and static deposition (fig 7.2.1). Tables 8.2.1 and 8.2.2 as well as figs 8.2.1 and 8.2.2 emphasise how critical the question of gas content and the question of stoichiometry and film properties, e.g. hardness have to be seen in this very special parameter window. It is extremely surprising how sudden the sensitivity on N incorporation changes when the N content in the deposited films exceeds the critical value of 33% . Fig 6.2.2 shows that the incorporation of 17 to 35% N is accomplished in reduced partial pressure of 4 to 5×10^{-6} mbar, whilst a more than 5 times increase in the partial pressure (5 to 9.6×10^{-6}

mbar) is demanded to incorporate further 15% of N to form stoichiometric TiN. This behaviour gives a clear impression, how much less critical it is to control the δTiN process in comparison to the $\epsilon\text{Ti}_2\text{N}$ process.

It can be concluded also very clearly that the most sharp X-ray diffraction spectra of Ti_2N can be generated if the method of static deposition is chosen. In this case the used experiment set up allows the deposition of coating with very narrow XRD peaks (fig 7.2.6). Even the two Ti_2N phases (JCPDS 17-386 and JCPDS 23-1455) can be clearly registered. Introducing substrate motion, the peak width increases steadily from 1 fold to 3 fold rotation (fig 8.3.7 to 8.3.9). In parallel a decrease of the peak height is to observe. This result has to be attributed to the line of sight nature of the PVD process and the related permanent changes of deposition rate and ion bombardment during deposition.

The most interesting results may be seen in the microstructure of the deposited Ti_2N films. An extremely fine structured almost fibrous appearing film has been observed by TEM. Such a structure has not been reported before in literature. Obviously this microstructure is responsible for the smooth SEM fracture cross section images (fig 8.4.1), and for the low surface roughness of Ti_2N film (fig 7.2.12 and fig 7.2.13e)

The experiments at 350°C and 480°C confirm the experiments of the other authors^(7,8,9,10,11) how important the choice of the apparent substrate temperature has to be treated. In this context, it may be speculated that the powerful radiant heaters as well as the degree of ionisation, which allows an average bias current density of 2 to 5 mA/cm², may have supported the generation of unambiguously Ti_2N textured coatings. The influence of the ionisation has been reported by^(12, 13) also.

It was described in chapter 6, 7, and 8 that the phase composition within the film deposited at 350°C was obviously different from that deposited at 480°C even though the nitrogen concentration of these coatings was at the same level. The $\epsilon\text{Ti}_2\text{N}$ films deposited at low temperature corresponded to the data as referred to the random powder diffraction JCPDS file 23-1455 and the number of reflections appeared in the XRD pattern were

limited and broaden. The $\epsilon\text{Ti}_2\text{N}$ film deposited at high temperature corresponded to the data referred to the JCPDS file 17-386, almost every crystal line referred to this file presented in the XRD pattern, the diffraction peaks were sharp and almost without shift. The hardness of the $\epsilon\text{Ti}_2\text{N}$ films deposited at different temperatures is also effected. The hardness of $\epsilon\text{Ti}_2\text{N}$ film is about 1200 kg/mm^2 at low deposition temperature. At high temperature, however, $\epsilon\text{Ti}_2\text{N}$ film has hardness of 2100 kg/mm^2 . The high substrate temperature condition is beneficial to improve the crystallisation, to reduce the residual stress, and to enhance dense packed films.

The $\epsilon\text{Ti}_2\text{N}$ films appear to show very good corrosion resistance especially when erosion forms part of the corrosion process (fig 9.3.1, 9.3.2 and 9.3.3). The thermal stability of $\epsilon\text{Ti}_2\text{N}$ films is approximately 600°C (fig 9.2.2). The wear resistant of $\epsilon\text{Ti}_2\text{N}$ film as measured by pin-on-disc is better than that of stoichiometric δTiN film (fig 9.1.2 and fig 9.1.3). These properties let appear $\epsilon\text{Ti}_2\text{N}$ films as candidate to replace δTiN films used for wear and corrosion/erosion resistant applications at temperature below 600°C .

The production of films containing dominantly $\epsilon\text{Ti}_2\text{N}$ phase using the industrial sized PVD coating machine is critically dependent on the essential parameters such as composition, temperature, and ion bombardment. The equipment used in the research project has appropriate control means of all the process variables needed for the production of $\epsilon\text{Ti}_2\text{N}$ films. The working gas and reactive nitrogen gas can be accurately controlled by the gas flow meters combined with the powerful pumping system to keep the chamber total pressure and the consumption of nitrogen at the desired level. The substrate temperature can be precisely adjusted from 200 to 500°C using the radiant heaters within the chamber. During the deposition, the plasma is well confined over all the substrate region by the unbalanced magnetron geometry field and the ion bombardment can be fully controlled using the substrate bias potential and the current of the electromagnetic coil around the cathodes. From the results, problems and discussions presented in this thesis, it is clear that the films of $\epsilon\text{Ti}_2\text{N}$ can be deposited and reproduced using the industrial sized unbalanced magnetron coater and the $\epsilon\text{Ti}_2\text{N}$ films may be optimised for specific wear, and corrosion/erosion resistant applications.

10.2 Conclusions

- TiCN coatings can be produced using industrial sized unbalanced magnetron sputtering coater. The low carbon content TiCN coating may be the candidate used for wear and corrosion resistant applications because of the high hardness and densely packed structure.
- The industrial sized ABS unbalanced magnetron sputtering coating machine can be used to deposit films containing dominantly $\epsilon\text{Ti}_2\text{N}$ phase because the process parameters are fully controlled using the accurate gas flow meters, the powerful pumping system, efficient radiant heaters, substrate bias potential and close magnetic field techniques by electromagnetic coils.
- The essential parameters for the formation of $\epsilon\text{Ti}_2\text{N}$ films are composition of the coating, the substrate temperature during deposition, and the bombardment of the substrate surface with energetic particles.
- The $\epsilon\text{Ti}_2\text{N}$ films produced at temperature of 480°C are characterised as having relatively high hardness, very little residual stress, very smooth surface, and very densely packed with extremely fine and almost fibrous columnar grains.
- The $\epsilon\text{Ti}_2\text{N}$ film has similar thermal stability as the stoichiometric δTiN film. The wear resistant property of $\epsilon\text{Ti}_2\text{N}$ seems to be superior to that of δTiN . The property of corrosion/erosion resistance of pure $\epsilon\text{Ti}_2\text{N}$ film is much better than the austenitic AISI 304 stainless steel.
- The reproduction of $\epsilon\text{Ti}_2\text{N}$ films is possible in the industrial sized PVD coater only by the condition that the optimised process parameters are used, and the chamber has to be loaded by the same capacity as well as the same sized geometry substrates from run to run.

10.3 Future work

Pure $\epsilon\text{Ti}_2\text{N}$ films have not yet been reported to be produced by industrial sized PVD coaters for commercial applications. From the results and discussion of above chapters, it is necessary leading to further investigation of the following areas:

1. Nitriding the sputtering cleaned target before the formal deposition process started for pure $\epsilon\text{Ti}_2\text{N}$ films for the purpose of quenching the growth of $\alpha\text{Ti}(\text{N})$ at the initial coating stage.
2. Investigation the effect of substrate temperature on the formation of pure $\epsilon\text{Ti}_2\text{N}$ film and the physical properties of the films.
3. Studies on the effect of deposition rate (target power) on the phase development and the crystal structure of pure $\epsilon\text{Ti}_2\text{N}$ films.
4. Investigation of bombardment of the energetic particles for the purpose to obtain the optimised microstructure of the pure $\epsilon\text{Ti}_2\text{N}$ films.
5. Transmission electron microscope analysis of the cross sectional microstructure; coating/substrate interface structure; the orientation, distribution, and composition of the global and local columnar grains.
6. The practical applications of pure $\epsilon\text{Ti}_2\text{N}$ films as investigated using wear, corrosion/erosion, and cutting tool tests and the comparing with the result of the other hard coatings.

References

- (1) A.E. Palty, H. Margolin and J.P. Nielsen, "Titanium-nitrogen and Titanium-boron Systems," Trans. ASM, V46 (1954)312
- (2) B.E. Jacobsson, R. Nimmagadda and R..F. Bunshah, Thin Solid Films, V63 (1979)333
- (3) T. Sato, M. Tada, Y.C. Huang and H. Takei, Thin Solid Films, V40 (1978)61
- (4) M.K. Hibbs, J.E. Sundgren, B.E. Jacobsson and B.O. Johansson, Acta Metall., V33 (1985)797
- (5) A. Matthews and D.G. Teer, Thin Solid Films, V73 (1980)367
- (6) H. Yoshihara and H. Mori, J. Vac. Sci. Technol., V16 (1979)1007
- (7) J. Musil, S. Kadlec, J. Vyskocil and V. Poulek, Surface and Coatings Technology, V39/40 (1989)301
- (8) M.V. Stappen, K.D. Bruyn, C. Quaeyhaegens, L. Stals, V. Poulek, Surface & Coating Technology, V74-75 (1995)143
- (9) V. Valvoda, R. Kuzel, R. Cerny and J. Musil, Thin Solid Films, V156 (1988)53
- (10) V. Valvoda, R. Cerny, R. Kuzel, L. Doblasova, J. Musil, V. Poulek and J. Vyskocil, Thin Solid Films, V170 (1989)201
- (11) M. Erola, Thin Solid Films, V156 (1988)117
- (12) A. Mathhews and D.G. Teer, Thin Solid Films V72 (1980)541
- (13) T. Cerwiec, M. Remy and H. Michel, Surface and Coating Technology, V59 (1993)91

Appendix 1 The capillary model for the nucleation of spherical cap atomic group

The capillary model predicts that the free energy of formation of a condensed aggregate goes through a maximum; i.e., the aggregate has a stability minimum with respect to dissociation as it grows through its critical size. This maximum in free energy arises from the large surface-volume ratio of the small aggregates, tending to decrease their stability, and the condensation energy, tending to increase it, as they grow in size.

As shown in fig 1, when the aggregation of atomic group of the spherical cap take place on the substrate, the surface energy and volume energy will change. The change in free energy can be expressed as:

As shown in fig 1, when the aggregation of atomic group of the spherical cap take place on the substrate, the surface energy and volume energy will change. The change in surface free energy can be expressed as:

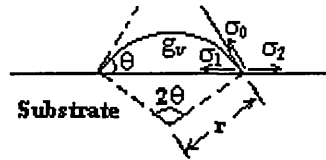


Fig 1 spherical cap nucleation

$$\Delta G_0 = \sigma_0 2\pi r^2 (1 - \cos\theta) + (\sigma_1 - \sigma_2)\pi r^2 \sin^2 \theta \quad \text{-----1}$$

where r is the radius, θ is the contact angle between the cap and the substrate, σ_0 is the density of surface energy of the aggregate exposed to the vapour, σ_1 is the density of surface energy of the contact area between aggregate and substrate. In a balanced state, the density of surface energy between substrate and vapour is

$$\sigma_2 = \sigma_1 + \sigma_0 \cos\theta$$

so $\sigma_1 - \sigma_2 = -\sigma_0 \cos\theta$ -----2

from equation 1 and 2 the change of surface free energy can be written as:

$$\Delta G_0 = \sigma_0 4\pi r^2 f(\theta) \text{ -----3}$$

where $f(\theta) = \frac{2 - 3\cos\theta + \cos^3\theta}{4}$ ----- 4

the volume of the cap aggregate is $4\pi r^3 f(\theta) / 3$, the change in volume free energy of condensation of the film material in the bulk is negative which can be expressed as

$$\Delta G_v = g_v 4\pi r^3 f(\theta) / 3 \text{ -----5}$$

where g_v is the density of the volume free energy of the aggregation which can be

written as $g_v = (-) \frac{KT}{V} \ln\left(\frac{P}{P_e}\right)$, where P is the vapour pressure of the source, P_e is the

balanced vapour pressure on the substrate, P/P_e is the super-saturation ratio. Then the total free energy can be expressed as:

$$G = 4\pi f(\theta) (\sigma_0 r^2 + g_v r^3 / 3) \text{ -----6}$$

the free energy of the aggregate is a maximum for an aggregate of critical size can be

obtained by $\frac{dG}{dr} = 0$, then the critical radius is

$$r^* = (-) \frac{2\sigma_0}{g_v} \text{ -----7}$$

which leads to the maximum free energy written as

$$G^* = \frac{16\pi f(\theta)\sigma_0^3}{3g_v^2} \text{-----} 8$$

The dependence of the free energy of the aggregate on its radius is shown in fig 2. The condition for maximum free energy corresponds to the minimum stability of the aggregate which occurs at r^* . For $r > r^*$, the r^3 term in equation 6 is dominate, leading to negative free energy and therefore, the aggregate tends to be more stable.

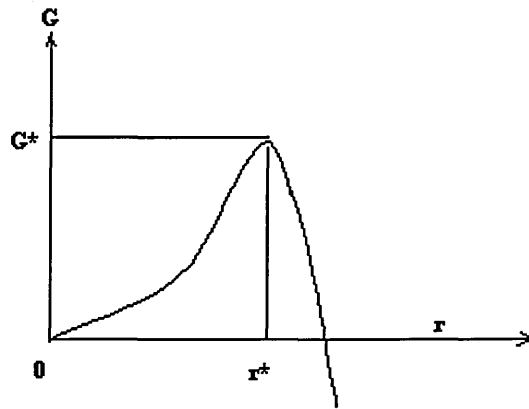


Fig 2 Free energy dependence on size of the aggregate